REFERENCE ONLY

UNIVERSITY OF LONDON THESIS

Degree PhD Year 2005 Name of Author DIXON S

COPYRIGHT

This is a thesis accepted for a Higher Degree of the University of London. It is an unpublished typescript and the copyright is held by the author. All persons consulting the thesis must read and abide by the Copyright Declaration below.

COPYRIGHT DECLARATION

I recognise that the copyright of the above-described thesis rests with the author and that no quotation from it or information derived from it may be published without the prior written consent of the author.

LOANS

Theses may not be lent to individuals, but the Senate House Library may lend a copy to approved libraries within the United Kingdom, for consultation solely on the premises of those libraries. Application should be made to: Inter-Library Loans, Senate House Library, Senate House, Malet Street, London WC1E 7HU.

REPRODUCTION

University of London theses may not be reproduced without explicit written permission from the Senate House Library. Enquiries should be addressed to the Theses Section of the Library. Regulations concerning reproduction vary according to the date of acceptance of the thesis and are listed below as guidelines.

A. Before 1962. Permission granted only upon the prior written consent of the author. (The Senate House Library will provide addresses where possible).

B. 1962 - 1974. In many cases the author has agreed to permit copying upon completion of a Copyright Declaration.

C. 1975 - 1988. Most theses may be copied upon completion of a Copyright Declaration.

D. 1989 onwards. Most theses may be copied.

This thesis comes within category D.

☑ This copy has been deposited in the Library of UCL.

☐ This copy has been deposited in the Senate House Library, Senate House, Malet Street, London WC1E 7HU.

Instrumental Development for Understanding Atmospheric Chemistry and Kinetic Studies of Chlorine Oxide Dimerisation

by

Sarah Louise Dixon

A thesis submitted for the degree of Doctor of Philosophy

University of London
2004

Department of Chemistry,
University College London

ProQuest LLC
789 East Eisenhower Parkway
P.O. Box 1346
Ann Arbor, MI 48106-1346

Abstract

Numerous current environmental problems result from changes to the trace gas composition of the Earth's atmosphere. Issues such as smog formation, acid rain and stratospheric ozone depletion all result from the chemical transformation of pollutants in the atmosphere and understanding the nature and rapidity of these chemical changes is consequently an important goal of atmospheric science. Laboratory studies of the kinetics and product channels of important atmospheric reactive species - atoms and free radicals - aim to provide data for inclusion into numerical models to simulate changing atmospheric composition. Typically, the limitation of such laboratory studies is the sensitivity required for monitoring very low concentrations of very short-lived gas phase species. The work described in this thesis addresses this limitation in new instrument development and in application of an existing instrument to studies of reactions of the atmospherically important ClO free radical.

This thesis therefore describes two principal areas of research. In the first part, the design, construction, and testing of an experimental technique for the study of gas phase chemical reactions in a flow system are detailed. This apparatus consists of a conventional discharge flow tube in which reactions take place, coupled to a novel detection system. This detection, based upon chemical ionisation mass spectrometry (CIMS), uses a novel chemical ionisation scheme using proton transfer from H_3^+ ions. A high-pressure electrical discharge system using H_2 has been developed and used as the source of H_3^+. An electrostatic ion guide has also been designed and tested to transport ions efficiently from their region of interaction with the gas under study, to the detector. Experiments to characterise the detection efficiency and instrumental sensitivity have been carried out, along with studies of a variety of chemical systems.

In the second part of the thesis, a novel instrument has been applied to the study of gas phase free radical reactions. This instrument, employing flash photolysis with time resolved UV / visible absorption spectroscopy, is unique since charge-coupled device (CCD) monitoring of UV absorption is carried out, enabling unequivocal and

accurate monitoring of the free radicals in real time. A full investigation into the dimerisation of the chlorine monoxide (ClO) free radical has been carried out, providing kinetic information and thermodynamic characterisation of the atmospherically important ClO dimer, Cl_2O_2. In the concluding section of the thesis, the relative merits of the somewhat different experiments developed and applied in these studies are discussed, along with prospects for their further contribution towards understanding atmospheric trace gas chemistry and environmental consequences.

Acknowledgements

Firstly, I would like to thank my supervisors, David Rowley for his encouragement and enthusiasm, and Steve Price for his advice and support, over the past four years.

I would also like to thank my laboratory partners: Gavin Boakes, Kate Gawler and Daniel Stone for their friendship and advice in the laboratory and beyond. Similarly, all the members, past and present, of the extended 'PhysChem' group who've made the past few years so enjoyable.

Without the support work carried out by the technical staff in the chemistry department at UCL much of the work in this thesis would have been impossible. I am particularly grateful to Dick Waymark and Roy Northeast for their valuable help and advice, which has been sought on many occasions.

I am grateful to the NERC for the financial support that has made this research possible.

I would also like to thank my family for their support not only over the past four years but all those before. And finally I would like to thank Sean Dixie for his encouragement and consideration and most importantly, for keeping me smiling.

For mum

Instrumental Development for Understanding Atmospheric Chemistry and Kinetic Studies of Chlorine Monoxide Dimerisation

Contents

List of Figures

List of Tables

Chapter 1 Gas Phase Kinetics: Theory and Application

1.1 Introduction

The study of reaction kinetics - at its simplest level the rates of chemical reactions - is profoundly important both practically and fundamentally. Practically, knowledge of how fast a chemical reaction takes place gives an insight into how useful that reaction might be, for example, in an industrial synthesis. Fundamentally, the measurement of the rate of a chemical reaction can provide great insight into the very nature of the reaction - the reaction mechanism. In the gaseous phase, the kinetics of chemical reactions provide an insight into such important phenomena as combustion and the changing composition of Earth's atmosphere. This latter subject is of special interest, since many well publicised environmental problems, such as stratospheric ozone depletion, smog formation, and poor air quality result from changing trace gas composition in the atmosphere.

The challenge in understanding the gas phase kinetics that lies at the heart of such environmental problems is to measure reaction rates of gas phase species present at very small concentrations. Low concentrations of gas phase species often result from high reactivity and another goal is, therefore, to monitor species at extremely low concentrations on the timescales at which they react or to arrange for the reaction to occur under stable conditions so that a suitable detector can monitor reactants and products at a specific point in time. This thesis describes work carried out on separate apparatus operated under both regimes. In the main body of the work, a new mass spectrometric detection system incorporating chemical ionisation has been designed, constructed and tested. In the other part of this work, a flash photolysis with time-resolved UV spectroscopy study of the dimerisation of ClO free radicals has been carried out. All of this work is focussed towards laboratory studies of the kinetics of gas phase reactions of atmospheric importance. This chapter therefore begins with a

summary of some of the fundamental principles of reaction kinetics, with emphasis on the gas phase.

1.1.1 Reaction Rates

For a general chemical reaction in the gas phase:

$$aA + bB \quad = \quad cC + dD \qquad (1.1)$$

The extent of reaction, $\delta\xi$, is given by $\delta\xi = \delta n / \nu_Q$ where δn is the change in number of moles of species Q in any reaction and ν_Q is the stoichiometric number for any species in the reaction. The stoichiometric number is defined as negative for reactant and positive for product species. Hence:

$$\delta\xi = \frac{\delta n_a}{-a} = \frac{\delta n_B}{-b} = \frac{\delta n_C}{c} = \frac{\delta n_D}{d} \qquad (1.i)$$

The rate of reaction, $\tilde{r}$, for any species Q is defined as

$$\tilde{r} = \frac{d\xi}{dt} = \frac{1}{\nu_Q}\frac{dn_Q}{dt} \qquad (1.ii)$$

However, it is usually more convenient to express the rate of reaction in terms of the intensive quantity (rate / volume) and this is referred to as r:

$$r = \frac{1}{\nu_Q}\frac{d(n_Q/V)}{dt} = \frac{1}{\nu_Q}\frac{d[Q]}{dt} \qquad (1.iii)$$

where [Q] is the concentration of any species Q. In instances where product formation has no effect upon the rate of reaction, the experimentally observed rate of reaction is given by:

$$r = k_{obs}[A]^{\alpha}[B]^{\beta} \qquad (1.iv)$$

The observed rate constant, k_{obs}, the orders of reaction for each species A and B, α and β respectively, for the overall reaction are determined experimentally and cannot be predicted solely from the overall reaction.

This limitation of predictions of r can be overcome in certain cases. A predicted rate equation can be derived if the overall reaction proceeds *via* a series of known steps, or elementary reactions. An elementary reaction takes place in a single step, for example by collision, and the rate at which it proceeds is determined by the product of its rate constant, k, and the reactant concentrations raised to the power of their stoichiometric number, known as the molecularity. Hence, if reaction (1) is known to proceed *via* a mechanism comprising two elementary reactions - in this example (2) and (3), the rate equations (v) and (vi) may be developed for individual species. In cases where species appear in multiple elementary reactions, such as AB in this example, the rates of change of concentration are additive, giving (vii).

$$\mathrm{A + B} \rightarrow \mathrm{AB} \qquad (1.2)$$

$$\mathrm{AB} \rightarrow \mathrm{C + D} \qquad (1.3)$$

$$-\frac{d[A]}{dt} = -\frac{d[B]}{dt} = k_2[A][B] \qquad (1.v)$$

$$\frac{d[C]}{dt} = \frac{d[D]}{dt} = k_3[AB] \qquad (1.vi)$$

$$\frac{d[AB]}{dt} = k_2[A][B] - k_3[AB] \qquad (1.vii)$$

Solutions to these rate equations - if they exist - can then be used to predict the overall kinetic behaviour and compared with experiments. In some cases, approximations can be made (*e.g.* the steady-state approximation, described in section 1.3.3) or

numerical integration can be used to simulate temporal behaviour of species concentration. Mechanistic analysis techniques are summarised more completely in Section 1.3. Whilst such analyses allow for prediction of overall kinetics from known mechanisms, the reverse is not true. Fundamentally, reaction kinetics is an experimental discipline and general principles of experimental kinetics are given in the Chapter 2.

1.2 Kinetic Analyses

Laboratory measurements provide information on the rapidity and therefore usefulness of a reaction. Reaction kinetics also provides mechanistic insight into products formed. Fundamental theories of reaction rates have been developed but, as yet, the predictive capability of theoretical models in all but the simplest cases is limited. Good experimental data will often take precedence over theoretical estimates and hence experiments are carried out while theory is then used to understand the resulting data.

Experimentally, reaction *rates* are not normally measured directly; concentrations of reactants or products are measured as a function of time and reaction rates inferred from these data. The general procedure that is adopted by all kinetic experiments is outlined below in Figure 1.1.

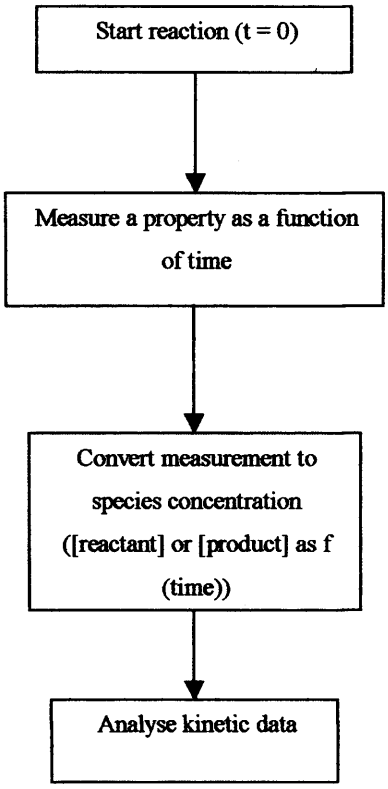

Figure 1.1: Flowchart indicating general procedure for kinetic experiments.

Since timescales involved in kinetic measurements can vary enormously, a wide range of experimental methods have been developed for kinetic studies and the details of some of these methods that are particularly relevant to this study are discussed in Chapter 2.

The last step of this flow chart determines order of reaction and rate constant for the reaction. A mechanism of elementary reactions may then be proposed and tested to attempt to reproduce experimental observations. A number of methods can be used to analyse the data, described here.

1.2.1 Initial Rates Method

For a general reaction

$$A + B = C + D \tag{1.4}$$

With a rate equation of the form

$$r_{obs} = \frac{-d[A]}{dt} = k_{obs}[A]^{\alpha}[B]^{\beta} \tag{1.viii}$$

In the initial stages of the reaction, when the concentrations of the products are very small and the concentrations of the reactants A and B are effectively constant:

$$r_0 = \frac{-d[A]_0}{dt} = k_{obs}[A]_0^{\alpha}[B]_0^{\beta} \approx constant \tag{1.ix}$$

and r_0 can be measured, simply from the initial gradient of [A] *versus* time. If the experiment is then repeated for a different known initial concentration of A, $[A]_0'$, and a second initial rate, r_0', is recorded, the ratio of these initial rates is given by:

$$\frac{r_0}{r_0'} = \frac{k_{obs}[A]_0^{\alpha}[B]^{\beta}}{k_{obs}[A]_0'^{\alpha}[B]^{\beta}} = \left(\frac{[A]_0}{[A]_0'}\right)^{\alpha} \tag{1.x}$$

Hence measurement of the two initial rates determines α. The order of reaction with respect to species B, β, may then be determined in comparable fashion, and k can then be determined from one of the values of r_0 using (viii) and the known values of [A] and [B].

1.2.2 Differential Method

In similar fashion to the initial rates method, a tangent drawn on a concentration *versus* time plot gives the rate of change of reactant or product concentration with time. Thus, if it is known that the reaction has a simple rate equation of the form:

$$r = \frac{-d[A]}{dt} = k[A]^{\alpha} \qquad (1.xi)$$

The value of r determined from the gradient is related to k, α and [A] *via*:

$$\log r = \log k + \alpha \log[A] \qquad (1.xii)$$

Repeated measurements of r at different concentrations of A then allow a plot of log r *versus* log [A] to be constructed, giving a straight line with intercept log k and gradient α.

This method is limited to situations in which the rate equation is known to be of a simple form. However, it is possible to use this method on reactions with more complex rate equations by imposing conditions in which the concentrations of other reactants are effectively kept constant. A practical way to achieve this is to have one or more reactants in great excess over the others. For example, a rate equation of the form

$$r = k[A]^{\alpha}[B]^{\beta} \qquad (1.xiii)$$

can be simplified to (xiv), where $k' = k[B]^{\beta}$, if [B] is in great excess of [A] and hence effectively constant.

$$r = k'[A]^{\alpha} \qquad (1.xiv)$$

Here, k' is termed a pseudo rate constant. For the case where $\alpha = 1$ and $\beta = 1$, the reaction is second order but k' is a pseudo first order rate constant. By reducing the rate equation to a simpler form, the differential method can be applied to determine the order with respect to $[A]$. This method of simplifying the rate equation is known as the *isolation method.*

1.2.3 Integration Methods

Kinetic parameters for simple reactions are more rigorously determined by solving the differential equations that define the reaction rates and plotting kinetic data in an appropriate form. However, since orders of reaction are unknown in the first instance, as discussed above, a trial and error method is employed, wherein the solutions to various possible rate equations are tested against experimental data. Solutions to the most simple kinetic schemes for a generic reaction A $\rightarrow$ Products are given in Table 1.1 below.

Reaction Order	Rate Equation	Solution
Zero	$-\frac{d[A]}{dt} = k$	$[A]_t = [A]_0 - kt$
First	$-\frac{d[A]}{dt} = k[A]$	$[A]_t = [A]_0 \exp(-kt)$
Second	$-\frac{d[A]}{dt} = k[A]^2$	$\frac{1}{[A]_t} = \frac{1}{[A]_0} + kt$

Table 1.1: Solutions to some simple kinetic schemes.

In all cases, a linear form of the solution may be produced and a plot of experimental data in this form will show which rate law, if any, holds. For example, if the reaction is second-order, a plot of $1/[A]_t$ *versus* time will exhibit linearity with a gradient defining k.

1.3 Mechanistic Analysis

Frequently chemical processes do not display simple orders of reaction and mechanisms may consist of multiple elementary reactions. In these cases, simplistic analysis methods such as those described in the previous section are not suitable. However, simple combinations of chemical reactions can be understood analytically once a rate equation is generated. These rate equations provide essential evidence for deducing the mechanisms of complex reactions. Although there are an infinite variety of mechanisms that can be encountered in reaction kinetics, there are a few fundamental types that can have a significant contribution to the understanding of considerable problems presented by complex reactions. The kinetic features of some of these fundamental mechanisms are discussed here.

1.3.1 Opposing Reactions (Equilibria)

Reactions always proceed to equilibrium, provided the standard Gibbs free energy for the reaction, $\Delta_r G^0$, is negative. For some reactions the equilibrium constant, defined simplistically as K = [*Products*]/[*Reactants*], is extremely large - *i.e.* the reaction goes to completion. However, in many cases the equilibrium concentrations are both finite and measurable. Many major kinetic features are illustrated with the simplest example of equilibrium – opposing unimolecular elementary reactions.

$$\mathrm{A} \rightarrow \mathrm{B} \qquad (1.5)$$

$$\mathrm{B} \rightarrow \mathrm{A} \qquad (1.\text{-}5)$$

where the rate equation is:

$$-\frac{d[A]}{dt} = k_5[A] - k_{-5}[B] \qquad (1.\mathrm{xv})$$

At equilibrium, the concentrations of A and B are constant and the overall rate of reaction is zero:

$$-\frac{d[A]}{dt} = k_5[A]_e - k_{-5}[B]_e = 0 \qquad \text{(1.xvi)}$$

where $[A]_e$ and $[B]_e$ are the equilibrium concentrations of A and B respectively. The equilibrium constant for this reaction is defined as:

$$K = \frac{[B]_e}{[A]_e} \qquad \text{(1.xvii)}$$

From expression (xvi), it can be seen that $[B]_e/[A]_e = k_5/k_{-5}$, therefore K can be written as:

$$K = \frac{k_5}{k_{-5}} \qquad \text{(1.xviii)}$$

The rate equation (xv) can be solved recognising that, at some point before equilibrium is reached, $[A] = [A]_e + x$ and $[B] = [B]_e - x$, where $[A]_e$ and $[B]_e$ are the equilibrium concentrations of A and B respectively. Thus, at this point:

$$\frac{-d[A]}{dt} = k_5([A]_e + x) - k_{-5}([B]_e - x) \qquad \text{(1.xix)}$$

Since, $k_5[A]_e - k_{-5}[B]_e = 0$, as given by expression (xvi), this becomes:

$$-\frac{d[A]}{dt} = \frac{-dx}{dt} = -(k_5 + k_{-5})x \qquad \text{(1.xx)}$$

Integrating this equation between the limits of t and 0 yields (xxi):

$$x = x_0 \exp -(k_5 + k_{-5})t \qquad \text{(1.xxi)}$$

Thus, the reactions approach equilibrium with first order kinetics with an observed rate coefficient, k_{obs}, of (k_5 + k_{-5}). Measurement of this rate coefficient, along with separate measurement of the equilibrium constant then gives two expressions combining k_5 and k_{-5} and the individual rate coefficients are readily determined.

1.3.2 Concurrent Reactions (Branching)

It is common for a reactant, A, to undergo competing reactions to form a variety of different products. The main kinetic features for this system may be illustrated for two competing first-order reactions:

$$\text{A} \rightarrow \text{B} \qquad \text{(1.6a)}$$

$$\text{A} \rightarrow \text{C} \qquad \text{(1.6b)}$$

The differential rate equation governing the behaviour of A is

$$\frac{-d[A]}{dt} = (k_{6a} + k_{6b})[A] \qquad \text{(1.xxii)}$$

hence

$$[A] = [A]_0 \{\exp -(k_{6a} + k_{6b})t\} \qquad \text{(1.xxiii)}$$

However, the products B and C appear at rates k_{6a}[A] and k_{6b}[A] respectively so, for product [B]:

$$\frac{d[B]}{dt} = k_{6a}[A] = k_{6a}[A]_0 \{\exp -(k_{6a} + k_{6b})t\} \qquad \text{(1.xxiv)}$$

Integrating between the limits of t and 0 gives

$$[B]_t = \frac{k_{6a}[A]_0}{(k_{6a}+k_{6b})}(1-\exp(-\{k_{6a}+k_{6b}\}t) \qquad \text{(1.xxv)}$$

Thus as time, t, tends to infinity (*i.e.* at the conclusion of the reaction) the fraction of a product formed is proportional to its rate of formation, k_{6a}, divided by the total rate coefficient for the loss of reactant A, (k_{6a} + k_{6b}), an intuitive result:

$$[B]_\infty = \frac{k_{6a}[A]_0}{(k_{6a}+k_{6b})} \qquad \text{(1.xxvi)}$$

The ratio $k_{6a}/(k_{6a}+k_{6b})$ is termed the *branching ratio* for formation of, in this case, product species B. The branching ratio in multi-channel reactions is an important parameter to determine, particularly in reactions of importance in the atmosphere, as one product channel may have drastic consequences, *e.g.* for the ozone budget, whilst the other channel may produce an inert product species.

1.3.3 Consecutive Reactions

An overall reaction often proceeds by a series of reactions involving the formation and subsequent reaction of an intermediate. Considering a reaction A $\rightarrow$ C comprising a mechanism of two elementary unimolecular reactions (7) and (8)

$$\text{A} \rightarrow \text{B} \qquad \text{(1.7)}$$

$$\text{B} \rightarrow \text{C} \qquad \text{(1.8)}$$

In this case $-d[A]/dt$ is not equal to $d[C]/dt$ since they are involved in separate reactions. Species A shows straightforward first-order kinetics as described above, hence $[A]_t = [A]_0 \exp(-k_7 t)$. Species B is more complex since $d[B]/dt = k_7[A] - k_8[B]$, thus

$$\frac{d[B]}{dt} + k_8[B] = k_7[A]_0 \exp(-k_7 t) \qquad \text{(1.xxvii)}$$

Integrating between the limits 0 and t yields

$$[B] = \frac{k_7[A]_0}{k_8 - k_7}\{\exp(-k_7 t) - \exp(-k_8 t)\} \qquad \text{(1.xxviii)}$$

Hence the time dependence of [B] may be plotted. Whilst [B] has a somewhat complex time dependence, the concentration of species C may be obtained using the principle of mass balance, *i.e.* if $[B]_0 = [C]_0 = 0$ then $[A] + [B] + [C] = [A]_0$. Thus,

$$[C] = [A]_0 - [A]_0 \exp(-k_7 t) - \frac{k_7[A]_0}{k_8 - k_7}\{\exp(-k_7 t) - \exp(-k_8 t)\} \qquad \text{(1.xxix)}$$

This simplifies to

$$[C] = [A]_0\left\{1 + \frac{k_7 \exp(-k_8 t) - k_8 \exp(-k_7 t)}{k_8 - k_7}\right\} \qquad \text{(1.xxx)}$$

Plots of [A], [B], and [C] *versus* time for two scenarios of $k_7 < k_8$ and $k_7 > k_8$ are shown below.

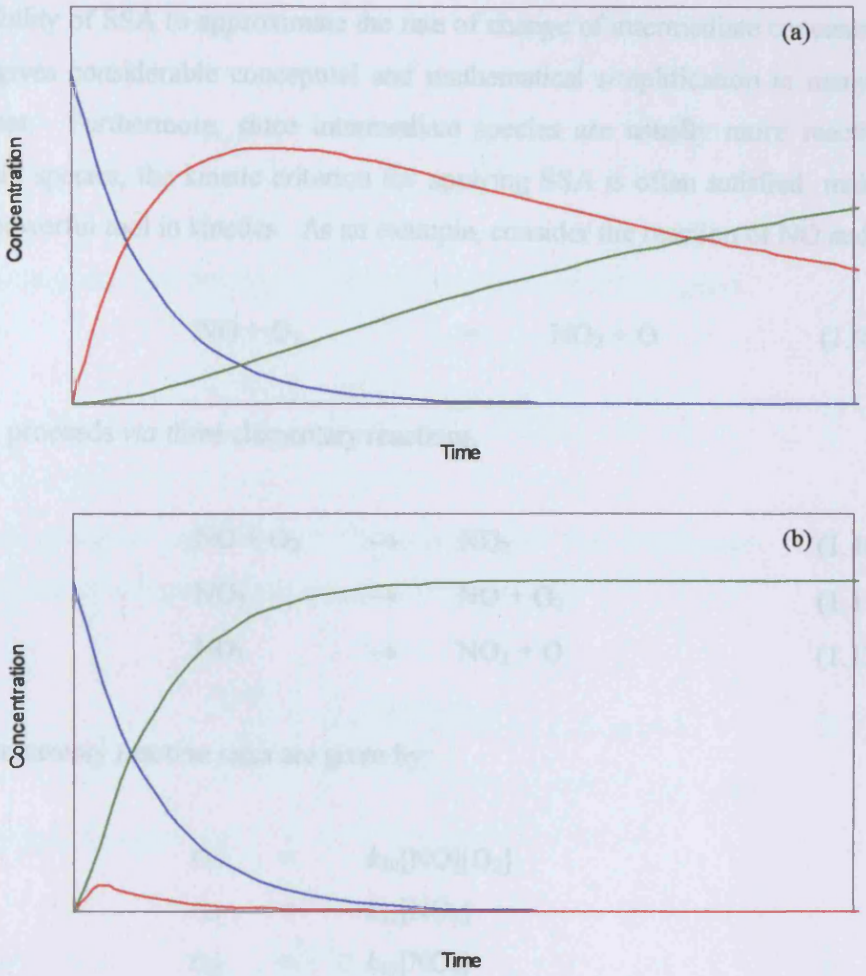

Figure 1.2: Plots of concentrations of A (blue), B (red) and C (green) with (a) $k_8 = 0.1k_7$ (b) $k_8 = 10k_7$.

It can be seen that if k_8 is much smaller than k_7 (Figure 1.2(a)), the concentration of species B becomes appreciable and there is a time lag between the decay of A and the appearance of product species C. However, if k_8 is much larger than k_7, (Figure 1.2(b)), the concentration of species B is always small. Moreover, after the initial period when [B] maximises, $d[B]/dt << d[A]/dt$ and we can make the approximation $d[B]/dt = 0$. This is known as the *steady state approximation* or the *stationary state approximation*, (SSA).

The ability of SSA to approximate the rate of change of intermediate concentration to zero gives considerable conceptual and mathematical simplification in many kinetic analyses. Furthermore, since intermediate species are usually more reactive than reactant species, the kinetic criterion for applying SSA is often satisfied, making it a very powerful tool in kinetics. As an example, consider the reaction of NO and O_2:

$$NO + O_2 \quad = \quad NO_2 + O \qquad (1.9)$$

which proceeds *via* three elementary reactions.

$$NO + O_2 \rightarrow NO_3 \qquad (1.10)$$

$$NO_3 \rightarrow NO + O_2 \qquad (1.11)$$

$$NO_3 \rightarrow NO_2 + O \qquad (1.12)$$

The elementary reaction rates are given by:

$$r_{10} = k_{10}[NO][O_2]$$

$$r_{11} = k_{11}[NO_3]$$

$$r_{12} = k_{12}[NO_3]$$

The rate equation for NO_2 formation is:

$$\frac{d[NO_2]}{dt} = r_{12} = k_{12}[NO_3] \qquad (1.xxxi)$$

Since NO_3 is a reactive intermediate in the mechanism, an expression for $d[NO_3]/dt$ can be developed and set to zero using SSA.

$$\frac{d[NO_3]}{dt} = k_{10}[NO][O_2] - k_{11}[NO_3] - k_{12}[NO_3] = 0 \qquad (1.xxxii)$$

Thus:

$$[NO_3] = \frac{k_{10}}{k_{11} + k_{12}}[NO][O_2] \qquad (1.xxxiii)$$

Substituting this into the expression for NO_2 formation, (xxxi), gives

$$\frac{d[NO_2]}{dt} = \frac{k_{10}k_{12}}{k_{11} + k_{12}}[NO][O_2] \qquad (1.xxxiv)$$

as the predicted rate of NO_2 formation from this mechanism. If now the experimentally determined rate equation is found to be

$$\frac{d[NO_2]}{dt} = k_{obs}[NO][O_2] \qquad (1.xxxv)$$

by comparison with (xxxiii)

$$k_{obs} = \frac{k_{10}k_{12}}{k_{11} + k_{12}} \qquad (1.xxxvi)$$

In this way application of SSA allows a check on the consistency of a proposed mechanism with experimental observations. Furthermore, SSA also allows expression of an experimentally obtained rate coefficient in terms of rate coefficients for the elementary steps in the mechanism.

1.3.4 More Complex Processes

Laboratory kinetics usually strives for a reductive approach whereby single reactions are isolated and studied individually. However, even apparently simple processes can have mechanisms that produce rate equations that are insoluble using classical techniques such as those described above. For these processes it becomes necessary

to carry out a simulation of the chemical system using numerical integration and fitting techniques in order to obtain kinetic information about the reaction in question. To illustrate the process of numerical integration, consider a simple first order reaction A → B. Setting [A] = y and time = t:

$$\frac{dy}{dt} = -ky \qquad \text{(1.xxxvii)}$$

Numerical methods of solving differential equations such as this approximate the classical solutions by employing increments, in this case

$$\frac{\Delta y}{\Delta t} \approx -ky \qquad \text{(1.xxxviii)}$$

A uniform time interval must be chosen, $\Delta t = h$. An estimate of k must then be made and an initial value stipulated (t_0, y_0). Points t_1 and y_1 are defined as the values describing the expression at the end of the first time increment:

$$\Delta t = h = t_1 - t_0 \qquad \text{(1.xxxix)}$$

$$\Delta y = y_1 - y_0 \qquad \text{(1.xl)}$$

The method approximates y_1 by using the estimate of $\Delta y/\Delta t$ over the time interval h. Thus

$$y_1 = y_0 + h\left(\frac{\Delta y}{\Delta t}\right) \qquad \text{(1.xli)}$$

Substituting from (xxxviii) gives:

$$y_1 = y_0 - hky_0 \qquad \text{(1.xlii)}$$

From this value of y_1, a new estimate of $\Delta y/\Delta t$ over the next time interval is used to generate a value of y_2, and so on. This method, known as the Euler method, forms the basis of many numerical integration features. The principal weakness of the method lies in the fact that $y = y_0$ only holds at the outset of the time increment, and therefore the approximation of $\Delta y/\Delta t$ is not a good representation of true $\Delta y/\Delta t$ throughout the time increment, as can be seen in Figure 1.3. Furthermore, since y_1 is used as the basis for y_2, *etc.* further error is potentially propagated into the simulation.

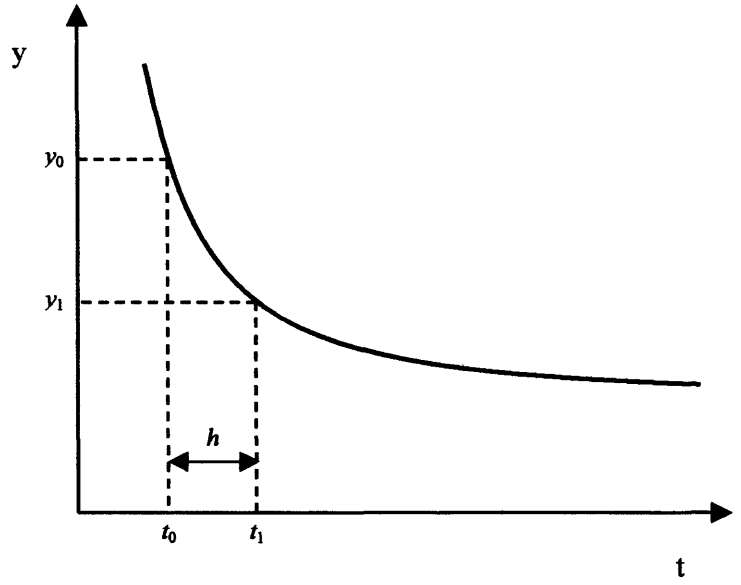

Figure 1.3: Typical decay curve ($y = f(t)$) illustrating the key parameters involved in numerical solution to a differential equation.

A practical way in which this method can be improved is by making the simulation time interval, h, very small indeed compared to the timescale of the (simulated) kinetics. However, this naturally implies that a very large number of calculations are required to produce a kinetic simulation over the timescale of interest, which for complex mechanisms, may become computationally intractable. An alternative to the Euler method is the Runge-Kutta method of numerical integration.[1] This method makes a better approximation of $\Delta y/\Delta t$ by using the mean value of $\Delta y/\Delta t$ at t_0 and t_1.

$$\left(\frac{\Delta y}{\Delta x}\right)_{avg} = \frac{-k(y_0 + y_1)}{2} \qquad \text{(1.xliii)}$$

However, since the quantity y_1 is unknown the estimation given by (xlii) is substituted into (xliii):

$$\left(\frac{\Delta y}{\Delta x}\right)_{avg} = -ky_0 + \frac{-hk^2 y_0}{2} \qquad \text{(1.xliv)}$$

Finally, substituting this expression into (xli) gives an equation in which all the parameters are known:

$$y_1 = y_0 - hky_0 + \left(h^2 k^2 y_0\right)/2 \qquad \text{(1.xlv)}$$

This final expression is now known as a *second order Runge-Kutta method*, as the average $\Delta y/\Delta t$ is calculated from two points in the time interval, the beginning and the end. Since there are an infinite number of points comprising the interval, this method could be expanded to use an infinite number of points from which to calculate the average. In practice kinetic problems are estimated adequately using a *fourth-order Runge-Kutta* process.

The successful simulation of a kinetic profile using methods of numerical integration described above is used to compare to experimental concentration *versus* time profiles to determine kinetic parameters. The basis of this comparison is a fitting wherein the root mean square residuals between simulated and experimental traces, defined by (xlvi) are minimised by allowing the kinetic parameters to vary freely.

$$\left\{(t_n,[X]_n)^2_{sim} - (t_n,[X]_n)^2_{\exp}\right\}^{0.5} \qquad \text{(1.xlvi)}$$

This optimisation algorithm is routinely available in many computer software packages, and will attempt to fit any experimental trace with any kinetic model.

Ideally, in such fitting, a single set of initial parameters and a single rate coefficient are varied to optimise fit. Necessarily, however, in complex models, several kinetic parameters are varied simultaneously in fitting to experimental traces. In such cases, it is very important to ensure that the best fit simulated traces exists uniquely for a single set of kinetic parameters (a 'global minimum' residual is obtained). In cases where equally good fits to experimental traces can be obtained using different sets of kinetic parameters, independent determination of one (or more) of these parameters must be sought. Lastly, in fitting experimental traces with complex kinetic models, the sensitivity of the fitted values of kinetic parameters obtained to uncertainties existing in the other kinetic parameters in the model must be minimised and quantified. As an example, in Chapter 5, the ClO + ClO dimerisation kinetics studies were naturally limited at high temperature due to just such a sensitivity issue.

1.4 Theories of Reaction Rates

The experiments and analyses discussed above provide a basis for understanding which elementary reactions comprise an overall reaction (the mechanism) and which are the key species participating in the overall chemistry observed. The fundamental chemical nature of reactivity - why some elementary reactions are fast and some slow - has also been the subject of much study. Following a discussion of the temperature dependence of reaction rates, this section summarises theories that have been developed to attempt to reconcile and ultimately predict the magnitude of temperature and pressure dependencies of reaction rate coefficients.

1.4.1 Temperature Dependence of Reaction Rates

It is well established that most rate coefficients vary greatly with temperature and hence kinetic experiments are carried out under constant temperature. Early kineticists found that this variation could often be fitted to a form $k = Ae^{-B/T}$ where A and B are constants.[2] Arrhenius and van't Hoff were the first to discover this and to

provide vital insight into the energetics of these reactions with the suggestion that activated molecules were formed in the system and it was the activated molecules that reacted.[3] They incorporated this idea into the empirical temperature equation by stating $B = E_{exp} / R$, where R is the gas constant and E_{exp} is the amount of energy required to form the activated species from reactants. This resulted in the Arrhenius expression, which satisfactorily describes many rate coefficients as a function of temperature:

$$k = A\exp(-E_a / RT) \qquad (1.xlvii)$$

Here E_a is the experimental activation energy and A is the pre-exponential factor. Thus, the temperature dependence of the rate coefficient is exponential and governed by the value of E_a. Now, most theories give expressions for the rate coefficient of a similar form to the Arrhenius expression.

1.4.2 Bimolecular Reaction Theories

The simplest approach to calculating rate constants for bimolecular reactions is using Simple Collision Theory (SCT). This associates the pre-exponential factor, A, with the frequency of collisions between the reactant molecules and E_a with an energy barrier to reaction. In SCT, the reactant molecules are treated as in kinetic theory, *i.e.* as incompressible spheres that only interact on collision. For the reaction

$$A + B \rightarrow \text{Products} \qquad (1.13)$$

the basic model for SCT can be expressed as

$$Rate = Z_{AB} \times F \qquad (1.xlviii)$$

where Z_{AB} is the collision frequency between A and B molecules and F is the fraction of collisions with sufficient energy for reaction. By consideration of kinetic theory, Z_{AB} can be expressed as

$$Z_{AB} = \sigma_{AB}\bar{\upsilon}_{AB}[A][B] \qquad (1.\text{xlix})$$

where σ_{AB} is the collisonal cross section (πd^2, where d is the sum of the reactant radii); $\bar{\upsilon}_{AB}$ is the relative mean speed of A and B molecules $(\{8k_BT/\pi\mu\}^{1/2}$, where k_B is the Boltzmann constant, T is the temperature and μ is the reduced mass of the reactants). The fraction of collisions that have sufficient energy to react is given by the Maxwell-Boltzmann distribution law:

$$F = \exp(-E_a/RT) \qquad (1.\text{l})$$

Thus, substituting for Z_{AB} and F in expression (xlviii) gives

$$Rate = \sigma_{AB}\bar{\upsilon}_{AB}\{\exp(-E_a/RT)\}\exp[A][B] \qquad (1.\text{li})$$

The experimental rate equation for an elementary process A + B $\rightarrow$ Products is $Rate = k[A][B]$. Thus comparing terms with expression (li) gives rise to an equation for the rate coefficient that closely resembles the experimental Arrhenius expression.

$$k_{bi} = \sigma_{AB}\bar{\upsilon}_{AB}\exp(-E_a/RT) \qquad (1.\text{lii})$$

SCT is a simple model that can be used to predict the broad features of observed rate coefficients. However, with the hard sphere approximation, this model fails to consider structures of molecules, hence ignoring the effects of steric factors on collisions. In addition, it does not account for the internal energy distribution within reactant and product species. Therefore, it has been found that this theory often

overestimates the experimentally determined reaction rate. A more realistic level of theory is hence required.

The basis for improving the theoretical treatment of an elementary reaction relies upon recognition that the total energy of the reactants and products is a function of all of the atomic co-ordinates in the reacting species. In the simplest case, for a co-linear A + BC → AB + C reaction, the total potential energy is a function of both the A....B and the B....C co-ordinates, which is therefore represented as a three dimensional potential energy surface (PES), shown in Figure 1.4, below. As reaction proceeds and the A...B separation decreases, potential energy goes up and the B.....C bond weakens and lengthens. This continues until the A...B and B...C separations are comparable, at the saddle point on the PES, where the {A...B...C} entity, known as the activated complex, is at the energy maximum along the reaction co-ordinate. This point on the reaction co-ordinate is known as the transition state, since subsequently the A...B separation shortens as the A-B bond is formed, lowering the energy whilst the B ...C separation increases as C leaves the system.

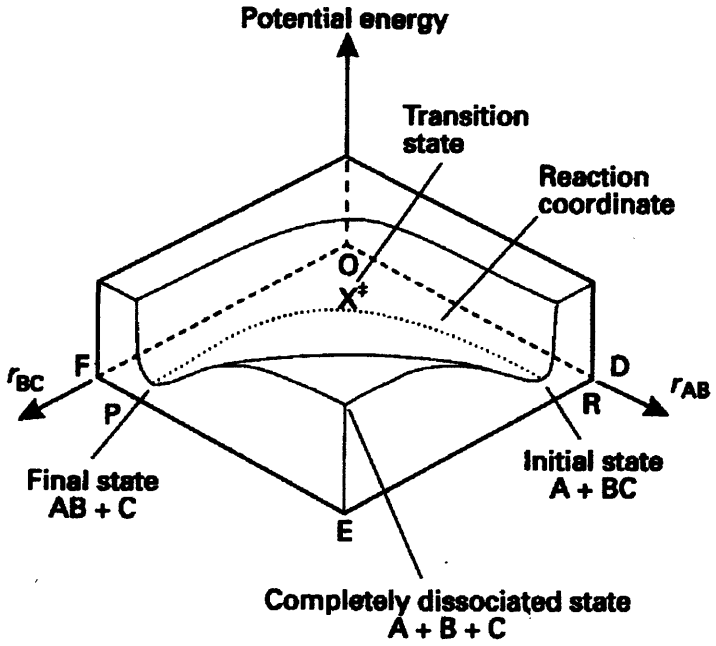

Figure 1.4: Potential energy surface for the reaction AB + C → A + BC.

Transition State Theory (TST, also known as Activated Complex Theory) interprets motion across the PES by postulating a state of equilibrium between the reactant molecules and the activated complex. Using this theory the overall rate of reaction is determined by the concentration of activated species and their rate of decomposition into product. Thus considering a reaction between A and BC, proceeding *via* the activated complex $ABC^{\ddagger}$:

$$A + BC \leftrightarrow ABC^{\ddagger} \quad (1.14)$$

$$ABC^{\ddagger} \rightarrow AB + C \quad (1.15)$$

The rate of product, AB, formation is given by:

$$\frac{d[AB]}{dt} = k[ABC^{\ddagger}] \quad (1.iii)$$

The concentration of the activated complex can be expressed in terms of the equilibrium constant between reactants and this complex:

$$K_{14} = \frac{[ABC^{\ddagger}]}{[A][BC]} \quad (1.iv)$$

The equilibrium constant, K_{14}, between the reactions and the transition state can be expressed in terms of the total partition functions, Q_n, for A, BC and $ABC^{\ddagger}$:

$$K_{14} = \left(\frac{Q_{ABC}}{Q_A Q_{BC}}\right)^{\ddagger} \exp\left(-\frac{\Delta\varepsilon_0}{k_B T}\right) \quad (1.lv)$$

where k_B is the Boltzmann constant and $\Delta\varepsilon_0$ is the difference between the lowest energy levels in the reactants and those in the activated complex. Thus combining equations (liii) – (lv) leads to an expression for the bimolecular rate constant k_{bi} of the form:

$$K_{bi} = k_7\left(\frac{Q_{ABC}^{\ddagger}}{Q_A Q_{BC}}\right)\exp\left(-\frac{\Delta\varepsilon_0}{k_B T}\right) \qquad (1.1vi)$$

The number of vibrational modes associated with the transition state lead to a more complex modification of expression (lvi) which gives rise to the following:

$$K_{bi} = \frac{\kappa k_B T}{h}\left(\frac{Q_{ABC}}{Q_A Q_{BC}}\right)^{\ddagger}\exp\left(-\frac{\Delta\varepsilon_0}{k_B T}\right) \qquad (1.1vii)$$

where Q_A and Q_{BC} represent the total partition functions for the reactant species A and BC respectively and $Q_{ABC}^{\ddagger}$ is the total partition function for the activated complex excluding the term that represents one dimensional motion along the reaction co-ordinate, which has already been accounted for. The fraction of activated complexes that lead to products instead of fragmenting back to reactant species is accounted for using the transmission coefficient, κ, and h is Planck's constant. The partition functions, Q_n, can be calculated *via* statistical mechanics with spectroscopically determined rotational and vibrational constants. However, it is often necessary to make assumptions for these parameters, as values are not available for many polyatomic activated complexes of interest since their lifetime is negligible.

For the most simple case where both reactants are monatomic and hence can be treated as hard spheres, SCT and TST treatments reduce to the same algebraic expression despite the differences in underlying theory which is of a similar form to the previously discussed Arrhenius expression, (xlvii). The exponential term generally dominates the temperature dependence of the measured rate coefficient, as predicted by the theories. However, in some cases the experimentally observed temperature dependence is found to deviate from the Arrhenius form. A modification to (xlvii) is gained if, using TST, the temperature dependence of each partition function is expressed as a power law:

$$k_{bi} = A' T^n \exp(-E_a/RT) \qquad (1.1viii)$$

This gives a more satisfactory parameterisation of the temperature dependent rate coefficients in cases where the pre-exponential factor displays a strong experimental temperature dependence or where large extrapolations are required.

1.4.3 Unimolecular and Termolecular Reactions

Many gas phase unimolecular reactions, such as dissociation or isomerization, appear to be elementary,and therefore first order, but are often found to have pressure dependent rate coefficients. Typically, as the initial reactant pressure decreases k_{exp} falls and at very low pressures these reactions display a change in kinetics from first order to second order. These features are indicative of a mechanism for dissociation that is not truly unimolecular. Lindemann first postulated an explanation for this behaviour when he proposed that the unimolecular reaction was not in fact a single elementary step but rather it proceeds *via* formation of an energised molecule:[4]

$$AB + M \rightarrow AB^* + M \qquad (1.16)$$

$$AB^* + M \rightarrow AB + M \qquad (1.-16)$$

$$AB^* \rightarrow A + B \qquad (1.17)$$

Here, M is any surrounding molecule and AB* is the energised molecule. The theory assumes that only the energised molecules undergo true elementary unimolecular reaction to give products. An expression for the rate of product formation is given by making the steady-state approximation for AB^* as shown below.

The rate of formation of dissociation products, A or B, is given by

$$\frac{d[A]}{dt} = \frac{d[B]}{dt} = k_{17}[AB^*] \qquad (1.lix)$$

Applying SSA to [AB^*]:gives

$$\frac{d[AB^*]}{dt} = k_{16}[AB][M] - k_{-16}[AB^*][M] - k_{17}[AB^*] = 0 \qquad (1.lx)$$

thus:

$$[AB^*] = \frac{k_{16}[AB][M]}{k_{-16}[M] + k_{17}} \qquad (1.lxi)$$

substituting for [AB*] in (lix)

$$\frac{d[A]}{dt} = \frac{d[B]}{dt} = \frac{k_{17}k_{16}[AB][M]}{k_{-16}[M] + k_{17}} \qquad (1.lxii)$$

This rate equation accounts for the observed change in reaction order. At low pressures, where $k_{17} >> k_{-16}$[M] and the denominator approximates to k_{17}, the rate of formation of A is second order and pressure dependent. At higher pressures, the opposite is true k_{-16}[M]<< k_{17}, hence the rate is first order and the rate coefficient tends to a limiting value of ($k_{17}k_{16}/k_{-16}$).

Similarly, the pressure dependence for termolecular association reactions can be explained using this method.

A + B	→	AB*	(1.18)
AB*	→	A + B	(1. -18)
AB* + M	→	AB + M	(1.19)

Using the steady-state approximation applied to AB* leads to the following expression for the rate of AB formation:

$$\frac{d[AB]}{dt} = \frac{k_{18}k_{19}[A][B][M]}{(k_{-18} + k_{19}[M])} \qquad (1.lxiii)$$

The rate of AB formation is pressure dependent and third order at low pressures (k_{19}[M]<<k_{-18}) and tends to a limiting second order value at higher pressures (k_{19}[M]>>k_{-18}), analogous to unimolecular dissociation.

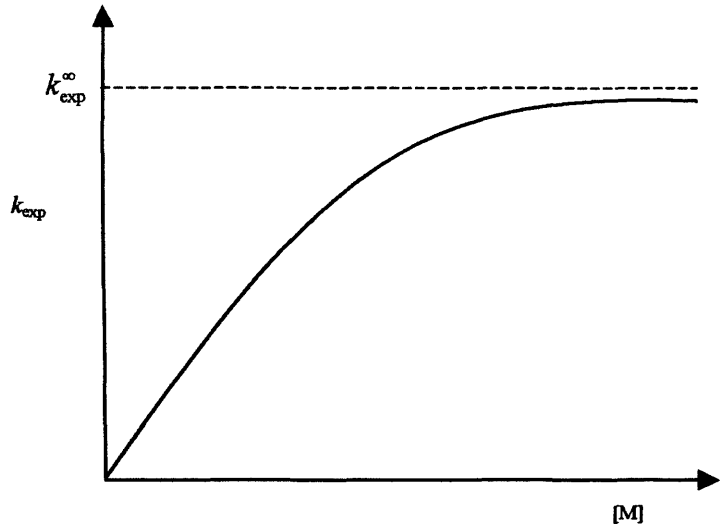

Figure 1.5: Schematic diagram of the apparent second-order rate constant, k, as a function of [M], showing that the rate constant is third order at low pressures and at high pressures tends to a limiting second order value.

The ability of Lindemann theory to quantitatively model unimolecular reactions is not perfect. Experimentally derived values of k are not exactly replicated. The theory neglects to account for the internal degrees of freedom of the molecule, particularly its vibrational modes. This has a large effect on the rates of activation and decomposition of the energised molecule AB^*. A rigorous determination should define rate coefficients for each vibrational and rotational level of the activated species and the overall rate constant derived from these coefficients, weighted according to population. This has led to many developments to Lindemann theory, the most recent of which is Rice–Ramsperger–Kassel–Marcus (RRKM) theory.[5-7] This does consider the internal energy distribution of the activated species and can often reproduce experimental data well.

1.5 Applications of Kinetics: Atmospheric Chemistry

An increasing demand for kinetic data in industrial and environmental applications has led to progress in experimental kinetics and technical innovation, which has been closely linked to advances in kinetic theory. The early impetus for applying kinetics to the understanding of elementary reactions was provided by high temperature processes involved in hydrocarbon pyrolysis combustion in the 1920s. This led to advances in theories of chain reactions in gases. The development of photochemistry, which provided a means of studying reactions involving atoms and radicals at low temperatures, followed soon after. This, coupled with the discovery of a series of controversies concerning atmospheric chemistry, such as the impact of halocarbons on the ozone layer and pollution of the troposphere, resulted in an added interest in kinetics. These atmospheric problems provided large injections of funds into chemical kinetic research and presented a focus for the development of a range of new techniques employed in the laboratory. More recently, the discovery of lasers has led to a new field of interest, that of state-resolved kinetics and reaction dynamics.

The work in this thesis is concerned with designing and employing instrumentation to collect data for use in atmospherically important reactions, thus this section discusses the application and importance of chemical kinetics to the field of atmospheric chemistry.

1.5.1 The Earth's Atmosphere

As discussed above, changes to the composition of the Earth's atmosphere have been recognised as environmentally important. The approach adopted to address such changes is based upon understanding the causes of such changes - especially the gas phase reactions - set against the physical conditions prevalent in the atmosphere. Conveniently, altitudes up to 50 km in the atmosphere (comprising more than 99% of the mass of the atmosphere) are split into two distinct vertical regions. The troposphere is the lowermost region, extending from the Earth's surface to 12-16 km

in altitude. The stratosphere, lying directly above this, extends up to *ca.* 50 km in altitude.

Throughout the atmosphere, the pressure decreases with increasing altitude. This decrease is exponential, and is defined by the hydrostatic equation, (lxiv).

$$p_z = p_0 \exp\left(\frac{-z}{H}\right) \qquad (1.\text{lxiv})$$

where pressure, p_z is given at an altitude z, relative to p_0, the pressure at zero altitude. H refers to the scale height, which in turn is defined as $H = RT/Mg$.

In contrast to the continuous fall in atmospheric pressure with increasing altitude, the vertical temperature profile of the atmosphere shows distinct non-uniformity as shown in Figure 1.6. In the troposphere, temperature decreases with increasing altitude (indeed the temperature profile defines the troposphere). However, at the junction of the troposphere and stratosphere (the tropopause) this decrease reverses and the temperature increases as altitude increases. This increase results from the presence of a very important trace gas in the atmosphere - ozone, O_3. The absorption of solar radiation by ozone, discussed in detail below, and the subsequent recombination of O atoms with O_2, releasing bond energy, provides the energy for this inversion, and also defines distinct dynamical conditions in this region compared to the troposphere.

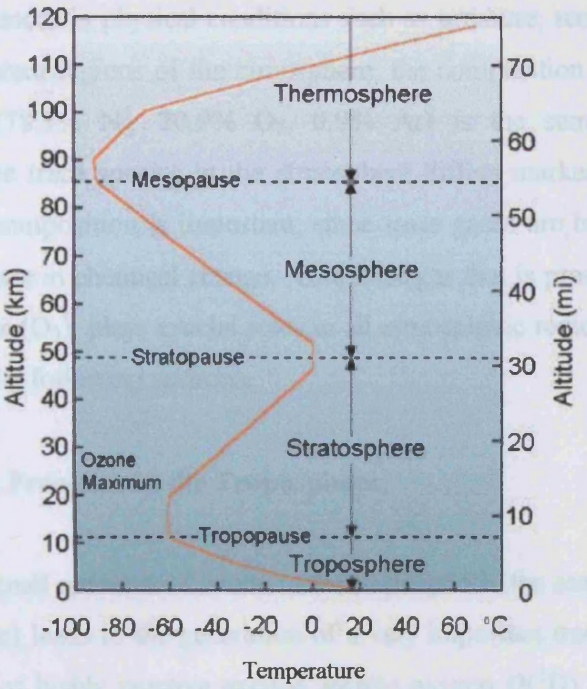

Figure 1.6: Typical temperature profile of the atmosphere.[8]

In comparing the dynamics of the troposphere and the stratosphere, it is convenient to consider the behaviour of a single, notionally isolated air parcel, and the response of this parcel to small perturbations in altitude. If any air parcel anywhere in the atmosphere is displaced vertically upwards, because of the decreasing pressure the parcel will expand. If this expansion takes place adiabatically - a reasonable approximation in the gas phase since thermal transfer is inefficient - the parcel must lose internal energy. Thus, the air parcel cools upon vertical displacement. In the troposphere, the surrounding atmosphere also cools with increasing altitude, and if this cooling exceeds that of the air parcel, after displacement the parcel will be warmer than it's surroundings, at the same pressure, and therefore will continue to rise. In stark contrast, in the stratosphere, whilst a vertically displaced air parcel will cool, the parcel will encounter a warmer surrounding atmosphere after displacement and will therefore experience a restoring force returning it to its original altitude. In this way the stratosphere is resistant to vertical transport (or 'stable') whereas in the troposphere vertical mixing (essentially convection) is readily set up.

Despite the differences in physical conditions such as pressure, temperature and ease of mixing in different regions of the atmosphere, the composition of the majority of the atmosphere (78.1% N_2, 20.9% O_2, 0.9% Ar) is the same. However the composition of the trace species in the atmosphere differs markedly. As discussed above, the trace composition is important, since trace gases are by their very nature those that participate in chemical change. One trace gas that is present throughout the atmosphere, ozone (O_3), plays crucial roles in all atmospheric regions, as is discussed in more detail in the following sections.

1.5.1.1 Chemical Processes in the Troposphere

The presence of small amounts of ozone in the troposphere (the majority of O_3 resides in the stratosphere) leads to the generation of a very important trace free radical OH. A small amount of highly reactive excited atomic oxygen $O(^1D)$ is produced in the troposphere by photolysing O_3 at wavelengths less than ~320 nm. At the high pressures found in the troposphere it is rapidly quenched *via* collision with other atmospheric constituents, typically N_2 or O_2, to ground state $O(^3P)$ which undergoes recombination with O_2 to reform O_3.

$$O_3 + h\upsilon \rightarrow O(^1D) + O_2(\,^1\Delta_g) \qquad (1.20)$$

$$O(^1D) + M \rightarrow O(^3P) + M \qquad (1.21)$$

However, the high mixing ratios of water vapour in this region facilitates effective competition with quenching to the ground state by reaction (22), to form hydroxyl radicals:

$$O(^1D) + H_2O \rightarrow 2OH \qquad (1.22)$$

This is fundamentally important, since reaction with the hydroxyl radical represents the primary mechanism of removal of many trace gases in the troposphere. Predominantly, OH reacts with CO in the atmosphere forming HO_2.

$$CO + OH \rightarrow H + CO_2 \quad (1.23)$$

$$H + O_2 + M \rightarrow HO_2 + M \quad (1.24)$$

HO_2 is reconverted to OH by reaction with ozone:

$$HO_2 + O_3 \rightarrow OH + 2O_2 \quad (1.25)$$

Owing to the rapid interconversion of OH and HO_2 set up in the atmosphere, they are conveniently referred to as the odd hydrogen (HO_x) family. Thus, HO_x is formed in the atmosphere following ozone photolysis, and removed from the atmosphere by reaction with other trace constituents, commonly to produce water-soluble products such as HNO_3 and H_2O_2, which can then be removed by precipitation. The HO_x present in the atmosphere is, as discussed below, responsible for the oxidation and atmospheric degradation of many pollutants.

In particular the oxidation of hydrocarbons and CO in the troposphere has important consequences for the ozone budget. As shown above, reaction of OH with CO initiates a complex series of reactions (23-25) that ultimately results in loss of ozone and regeneration of OH. Similarly, reaction of OH with methane produces the methylperoxy, CH_3O_2, radical.

$$OH + CH_4 \rightarrow H_2O + CO_2 \quad (1.26)$$

$$CH_3 + O_2 + M \rightarrow CH_3O_2 \quad (1.27)$$

The principal fate of CH_3O_2 in a 'clean' (low NO_2) environment is reaction with HO_2.

$$CH_3O_2 + HO_2 \rightarrow CH_3OOH + O_2 \quad (1.28)$$

CH_3OOH can then be rained or washed out of the troposphere. Thus in the unpolluted troposphere oxidation of hydrocarbons leads to a loss of both ozone and HO_x.

The composition of the local atmosphere can effect significant changes in these oxidation processes. In the polluted troposphere the presence of NO_x ($NO_x = NO + NO_2$) gives rise to a different chemical flux, resulting in ozone production. For example, the reaction of NO with peroxy radicals, such as CH_3O_2 formed in (27), leads to the formation of both NO_2 and CH_3O. This leads to further ozone formation *via* photolysis of NO_2, producing ground state oxygen atoms, which subsequently react with O_2. Reaction of CH_3O with O_2, (30), produces formaldehyde, HCHO, which can also be photolysed to liberate HO_x.

$$CH_3O_2 + NO \rightarrow CH_3O + NO_2 \qquad (1.29)$$

$$CH_3O + O_2 \rightarrow HCHO + HO_2 \qquad (1.30)$$

The balance between ozone production and destruction is largely controlled by the relative rates of reaction of peroxy radicals with ozone and NO. Mitigating factors include the reaction between O_3 and NO, which helps to maintain a photostationary state between NO, NO_2 and O_3. Numerical modelling has indicated that a tropospheric $[NO]/[O_3]$ ratio typically in excess of 2×10^{-4} is sufficient to ensure net ozone production.[9] In industrialised areas where NO_x emissions do exceed this critical value, the formation of low level ozone and "photochemical smog" has been observed.

1.5.2 The Stratosphere

Ozone is present in the stratosphere at higher mixing ratio than in the troposphere and is a species of major interest in this region. Ozone absorbs solar radiation in the ultraviolet region of the electromagnetic spectrum at wavelengths below 290 nm. It is this absorption that protects living organisms from the full extent of damaging solar radiation.

1.5.2.1 Stratospheric Ozone Chemistry

The explanation of ozone in the stratosphere is a conundrum that has been the focus of many studies. In 1930 Chapman[10] was the first to propose a theoretical explanation of the ozone layer. His mechanism was based on a static oxygen only photochemical steady-state model. The reactions in Chapman's scheme are:

$$O_2 + hv \rightarrow O + O \quad (1.31)$$

$$O + O_2 + M \rightarrow O_3 + M \quad (1.32)$$

$$O_3 + hv \rightarrow O + O_2 \quad (1.33)$$

$$O + O_3 \rightarrow 2O_2 \quad (1.34)$$

$$O + O + M \rightarrow O_2 + M \quad (1.35)$$

Reaction (35) is now known to be too slow to play a part in stratospheric ozone chemistry, given the abundance of O_2 and O_3 in the atmosphere, it cannot compete with reactions (32) and (34). Similarly, examination of the rates of reaction (32) and photolysis (33), which interconvert O and O_3, shows that they are much faster than the photolytic process (32) and reaction (34). Thus, in direct analogue to HO_x radicals in the troposphere the combined concentrations O and O_3 are known as 'odd-oxygen'. Reaction (31) creates odd oxygen and reaction (34) destroys it. Reactions (32) and (33) create no net effect on the odd-oxygen concentration but they determine the ratio [O] / [O_3]. Reactions (31) and (33) predominantly yield ground state O(^{3}P) atoms, although higher energy photons lead to production of some O(^{1}D) atoms. However, the principal fate of these is collisional deactivation, even at the low number densities and low water vapour mixing ratios present in the stratosphere. The vertical [O_3] profile observed in the atmosphere is a result of the variation in the balance of ozone production and destruction with altitude. As reaction (32) requires a third body, it becomes slower at lower pressures and, hence, at higher altitudes while reaction (33) becomes faster at higher altitudes due to increased intensity of solar radiation. Hence, atomic oxygen is favoured at high altitudes and ozone at lower ones, thus creating an

optimum altitude for ozone production, which occurs at 10-40 km. Given the vertical stability of the stratosphere this ozone is dynamically confined to a discrete layer.

The ozone layer is generally thinnest in the tropics[11] and here, is somewhat insensitive to seasonal variations. Ozone concentrations fluctuate most at high latitudes, with both annual and day-to-day changes. Concentrations of ozone are generally measured in Dobson Units (DU). Dobson Units are defined as the thickness in units of 0.01 mm that an ozone column would occupy at atmospheric pressure and 273 K. In absolute terms, 1 DU is equal to 2.7×10^{16} molecule cm^{-2}.

Whilst the Chapman mechanism gives a qualitative explanation for the existence of ozone in the stratosphere, atmospheric observations of ozone reveal that the ozone steady state concentration in the stratosphere is much lower than that predicted by the Chapman scheme alone. This implies that the scheme overestimates ozone production or underestimates its destruction. The source of odd-oxygen, and hence ozone, in the atmosphere is through reaction (31). The parameters that govern the rate of this reaction, the solar radiation profile, and the stratospheric oxygen abundance are well characterised and hence, overestimation of ozone production through this process is unlikely. However, reaction (34), which is the primary destruction process for odd oxygen in the Chapman cycle, has been found to have an unexpectedly high activation energy (E_a = 17 kJ mol^{-1})[12] and hence, is too slow at low temperatures to account for the lower than predicted ozone amounts. An additional or faster loss process for odd oxygen is needed to explain these observations.

The source of the discrepancy results from further chemistry. Since ozone is an intrinsically reactive molecule, it reacts with many trace species in the atmosphere, forming O_2. Rowland and Molina[13] suggested cyclic schemes in which the co-product of this reaction may then react further with atomic oxygen in the atmosphere to form another oxygen molecule and regenerate the original trace molecule. These cycles are catalytic, therefore, even small concentrations of trace species can still exert a considerable effect on ozone concentrations. The generalised form of such a cycle is

given below. It can be seen that the flux through the cycle conserves X and XO and that the overall effect of this cycle is identical to that of reaction (34).

	$X + O_3$	$\rightarrow$	$XO + O_2$	(1.36)
	$XO + O$	$\rightarrow$	$X + O_2$	(1.37)
Net:	$O + O_3$	$\rightarrow$	$2O_2$	

There are a number of candidates for X/XO in the atmosphere. The most important of these in the natural stratosphere are NO/NO_2, OH/HO_2, H/OH, Cl/ClO, Br/BrO and possibly I/IO. These species are present in much lower abundances than ozone, however, due to the catalytic nature of the loss cycles, they can exert profound influences on odd oxygen mixing ratios.

The continuing success of these odd-oxygen destroying cycles is dependent on any competing processes that can interrupt the cycle. For example, the NO/NO_2 cycle, which is responsible for around 50 % of odd oxygen destruction in the stratosphere:

	$NO + O_3$	$\rightarrow$	$NO_2 + O_2$	(1.38)
	$NO_2 + O$	$\rightarrow$	$NO + O_2$	(1.39)
Net:	$O + O_3$	$\rightarrow$	$2O_2$	

Competing chemistry results from NO and NO_2 interconversion. This interconversion in the presence of ozone results in a 'null cycle' that does not affect the overall concentration of odd-oxygen, rather just affecting the partitioning between O_3 and O.

	$NO + O_3$	$\rightarrow$	$NO_2 + O_2$	(1.38)
	$NO_2 + hv$	$\rightarrow$	$NO + O$	(1.40)
Net:	$O_3 + hv$	$\rightarrow$	$O_2 + O$	

Alternatively, active catalytic species can be converted into inactive species that are relatively unreactive towards odd-oxygen, thus breaking the catalytic ozone loss

cycle. Common examples of these species include $ClONO_2$ and HCl, which can be formed by the following reactions:

$$ClO + NO_2 + M \rightarrow ClONO_2 + M \quad (1.41)$$

$$Cl + CH_4 \rightarrow HCl + CH_3 \quad (1.42)$$

These species are known as "reservoirs" since they are sufficiently long-lived to allow them to be transported to other regions of the atmosphere where, subsequent photolytic release of active species might take place. Alternatively, these reservoirs lead to removal of the active species from the atmosphere through physical processes. Hence, the fate of these species plays an important role in stratospheric ozone chemistry. Heterogeneous processes involving these reservoir species have also been identified by recent studies that indicate that their role in the partitioning between active and reservoir forms can have a profound affect on the stratospheric ozone budget. For example, it is now recognised that reservoir species such as $ClONO_2$ and HCl can undergo reactions on condensed atmospheric matter, liberating molecular chlorine which results in the liberation of reactive chlorine atoms through photolysis in the sunlight.[14] This is especially important in polar regions where their effect is most pronounced, discussed in detail below.

$$ClONO_2 + HCl \rightarrow Cl_2 + HNO_3 \quad (1.43)$$

$$HOCl + HCl \rightarrow Cl_2 + H_2O \quad (1.44)$$

1.5.2.2 Stratospheric Ozone Trends

The British Antarctic Survey (BAS) has monitored ozone levels in the polar stratosphere for several decades. In the early 1980s, Farman *et al.* reported a decrease in springtime column ozone measurements relative to those taken prior to 1977.[15] Subsequent measurements have confirmed this observation and have shown that with each elapsing year, the severity of ozone destruction became more extreme. The loss of ozone was observed to be most severe in the Antarctic springtime when total

column ozone is typically depleted by up to 80%, whilst during the winter ozone levels recover, shown below in Figure 1.7.

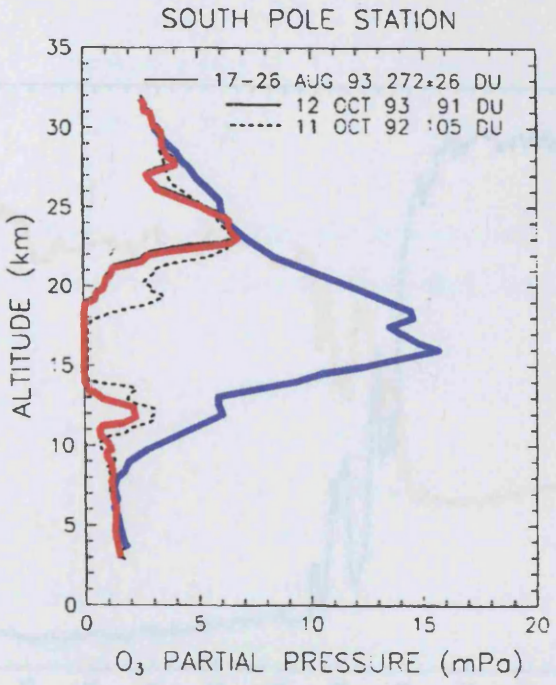

Figure 1.7: Vertical profile ozone abundances at the south pole in the winter of 1993 (blue) and the following springtime (red).[16]

The potential threat to ozone abundance in the stratosphere had, in fact, been identified many years before the discovery of the problem in the Antarctic. With the observation of accumulating halogenated hydrocarbons in the atmosphere, Molina and Rowland[13] recognised that chloroflurocarbons (CFCs), which were used as refrigerants and as aerosol propellants due to their inert nature, had such long atmospheric lifetimes that they could undergo transport to the stratosphere. Once there, chlorine atoms are liberated through short wavelength solar photolysis and initiate ozone depleting cycles such as those described above.

Aircraft measurements made during the spring of 1987 simultaneously monitored O_3 and ClO mixing ratios in the Antarctic Stratosphere (Figure 1.8).[17] The stark anticorrelation between these two species, shown below, confirmed the role of

chlorine atoms and ClO radicals in polar ozone depletion. These observations also demonstrated the catalytic nature of this chemistry, since ClO mixing ratios were much smaller than those of O_3.

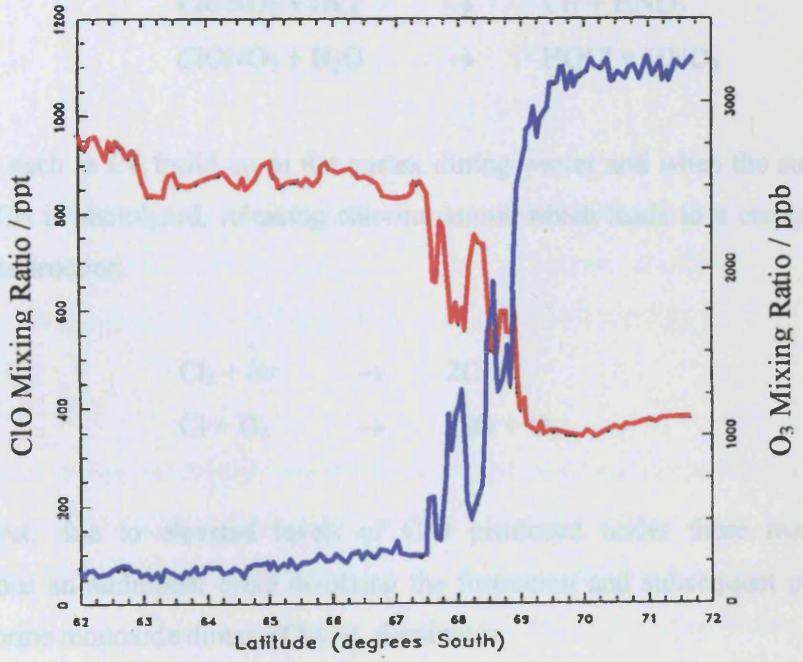

Figure 1.8: Simultaneous measurements of spatially resolved O_3 (red) and ClO (blue) abundances near the south pole during springtime.[17]

Whilst the work of Rowland and Molina predicted some stratospheric ozone loss, the extensive springtime depletion of ozone in the Antarctic was initially somewhat surprising. The explanation for this lies in a combination of meteorology and chemistry. During the Polar winter an isolated 'vortex' is formed as air cools and descends. At the core of the vortex, temperatures fall as low as 180 K, which facilitates the formation of polar stratospheric clouds (PSCs) thought to be composed of $HNO_3.3H_2O$ particles.[18] Temperatures below 188 K lead to rapid condensation of water upon these PSCs and particle growth occurs to the extent that denitrification (removal of nitrogen oxides) of the stratosphere occurs through gravitational separation.[19]

Under normal stratospheric conditions reactions involving chlorine reservoirs, such as $ClONO_2$ and HCl, occur slowly, but PSCs provide a site for heterogeneous reactions to occur, thus liberating more active chlorine containing species.

$$ClONO_2 + HCl \rightarrow Cl_2 + HNO_3 \quad (1.43)$$

$$ClONO_2 + H_2O \rightarrow HOCl + HNO_3 \quad (1.44)$$

Species such as Cl_2 build up in the vortex during winter and when the sun returns in spring Cl_2 is photolysed, releasing chlorine atoms which leads to a catalytic cycle of ozone destruction.

$$Cl_2 + h\nu \rightarrow 2Cl \quad (1.45)$$

$$Cl + O_3 \rightarrow ClO + O_2 \quad (1.46)$$

Moreover, due to elevated levels of ClO produced under these meteorological conditions an additional cycle involving the formation and subsequent photolysis of the chlorine monoxide dimer, (Cl_2O_2), dominates.

$$2(Cl + O_3 \rightarrow ClO + O_2) \quad (1.46)$$

$$ClO + ClO + M \leftrightarrow Cl_2O_2 + M \quad (1.47)$$

$$Cl_2O_2 + h\nu \rightarrow ClOO + Cl \quad (1.48)$$

$$ClOO + M \rightarrow Cl + O_2 + M \quad (1.49)$$

$$\text{Net } 2O_3 \rightarrow 3O_2$$

The efficiency of this cycle depends upon the thermal stability of the Cl_2O_2 molecules with respect to the ClO radicals (the subject of Chapter 5). Furthermore, if this is inefficient, and solar photolysis of Cl_2O_2 is rapid, the squared dependence of the rate of association of ClO, reaction (47), on ClO mixing ratios explains the severity of ozone loss.

Other catalytic cycles are thought to supplement that described above. For example, where bromine compounds are present in the stratosphere, a similar cycle involving the ClO + BrO reaction, (50), occurs.

$$ClO + BrO \rightarrow Cl + Br + O_2 \quad (1.50a)$$

$$\rightarrow Br + OClO \quad (1.50b)$$

$$\rightarrow BrCl + O_2 \quad (1.50c)$$

In contrast to the ClO self-reaction, the mixed ClO + BrO reaction does not involve the production of an adduct species. Hence a second photolytic process is not required in this cycle since halogen atoms are produced directly from channels (50a) and (50b).

The above processes responsible for the destruction of ozone have potentially great consequences to biological life on the surface. Loss of ozone causes increased UV-B radiation (280-315 nm). Increased UV-B radiation has been shown to induce skin cancer in humans[20] and can have a detrimental effect on crop yields, which also affects human welfare.

When the potential threat to ozone was highlighted in 1974, initial control measures were introduced by some countries to curb the production of non-essential CFCs. These restrictions were widened on discovery of the ozone hole[21] with the introduction of the Montreal Protocol and subsequent amendments.

1.5.2.3 Midlatitude Stratospheric Ozone

In the midlatitude region, ozone loss is less dramatic than observed in the polar regions. However, there is still reason to believe that erosion of stratospheric ozone does occur. The SAGE (Stratospheric Aerosol and Gas Experiment) campaign conducted over the period 1979-1996 provides evidence of erosion occurring at non-

polar latitudes (Figure 1.9).[22] Such ozone loss is potentially concerning since the majority of human population inhabits mid-latitudes.

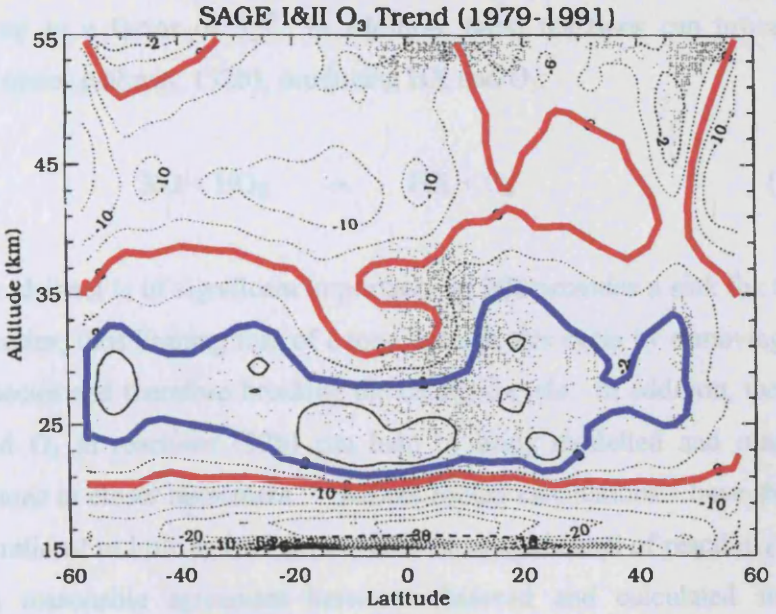

Figure 1.9: Spatial mapping of ozone trend (% loss per decade) at midlatitudes over the period 1979 – 1991. Highlighted are the areas with 6% loss (red) and 2% loss (blue).

Lower levels of stratospheric ozone in the midlatitudes have been attributed to out-mixing of ozone depleted polar air and to *in situ* free radical chemistry. Since conditions in the midlatitudes do not promote the formation of elevated levels of ClO and BrO radicals, cycles involving reactions (47) and (50a) do not play a large role. Instead, reactions *between* free radical families are the primary routes to chemical ozone loss in this region. For example, the reaction cycle shown below is of great importance to the ozone budget in midlatitudes:

$OH + O_3$	$\rightarrow$	$HO_2 + O_2$		(1.51)
$X + O_3$	$\rightarrow$	$XO + O_2$		(1.46)
$XO + HO_2$	$\rightarrow$	$HOX + O_2$		(1.52a)
$HOX + h\nu$	$\rightarrow$	$OH + X$	fast	(1.53)
Net: $2O_3$	$\rightarrow$	$3O_2$		

where X is Cl or Br. In each cycle the reaction XO + HO_2 (52a) is the rate limiting step in sunlight and despite extensive studies of gas phase halogen reactions that have been carried out in recent years the kinetics of these reactions still have uncertainty values of up to a factor of 3.[23] In addition, these reactions can proceed *via* an alternative minor pathway, (52b), producing HX and O_3:

$$XO + HO_2 \rightarrow HX + O_3 \qquad (1.52b)$$

This minor channel is of significant importance as HX provides a sink for free radical halogen species, thus limiting loss of ozone through this cycle by removing the active halogen species and therefore breaking the catalytic cycle. In addition, the formation of HX and O_3 in reactions (52b) can help to bring modelled and measured HX concentrations in closer agreement.[24] Recent model calculations[25] have shown that a branching ratio of as little as 0.01 for the HBr forming channel of reaction (52b) could lead to a reasonable agreement between observed and calculated stratospheric profiles. This demonstrates the need for accurate measurements of branching ratios for key atmospheric reactions, an instrumental challenge given that the primary products are themselves trace species.

1.6 Summary

This chapter has summarised the basic definitions used in kinetics and the analytical methods used to interpret kinetic data. An important application of gas phase chemical kinetics – understanding the chemistry of the Earth's atmosphere – has also been described. The methods for numerical integration of very complex kinetic schemes, described above in Section 1.3.4, are also applied to developing this understanding of atmospheric change. Numerical models of atmospheric composition aim to include all known gas phase (and heterogeneous) reactions in simulating past changes to atmospheric composition as measured in field campaigns. Ultimately, the goal of such models is to predict, and potentially to avert, damaging changes with

adverse environmental effects. The success of such predictions depends upon the provision of accurate kinetic and photochemical data for reactions of atmospheric trace species, which represents the principal challenge of laboratory studies. The next chapter illustrates the experimental principles behind the techniques developed to address such challenges.

1.7 References

(1) R. Jones "Specialist Periodical Report, Reaction Kinetics," The Chemical Society London, 1975.

(2) Hood J.J. *Phil. Mag* **1878**, *6*, 371.

(3) Arrhenius S. *Zeitschrift für Physikalische Chemie* **1889**, *4*, 226.

(4) Lindemann F.A. *Transactions of the Faraday Society* **1921**, *17*, 598.

(5) Rice O.K.; Ramsperger H.C. *Journal of the American Chemical Society* **1927**, *49*, 1617.

(6) Kassel L.S. *Journal of Physical Chemistry* **1928**, *32*, 225.

(7) Marcus R.A. *Journal of Chemical Physics* **1952**, *20*, 359.

(8) Adapted from: *Weather and Climate*; Idaho State University: http://www.physics.isu.edu/weather/kmdbbd/unit1_images.htm.

(9) Crutzen P.J.; Ed., B. C. *An overview of Atmospheric Chemistry, Topics in Atmospheric and Interstellar Physics and Chemistry*, Les editions de Physique, Les Ulis, 1994.

(10) Chapman S *Mem. Roy. Meterol. Soc.* **1930**, *3*.

(11) Rowland, F. S. *Annual Review of Physical Chemistry* **1991**, *42*, 731-768.

(12) Sander, S. P.; Friedl R.R.; Demore W.B.; Golden D.M.; Kurylo M.J.; Hampson R.F.; Huie R.E.; Moortgat G.K.; Ravishankara, A. R.; Kolb C.E.; Molina M.J. "Chemical Kinetics and Photochemical Data for use in Stratosphere Modeling - Evaluation No. 14," NASA JPL, Pasadena, CA, 2003.

(13) Molina MJ; Rowland FS *Nature* **1974**, *249*, 810.

(14) Hanson, D. R.; Ravishankara, A. R. *Journal of Geophysical Research-Atmospheres* **1993**, *98*, 22931-22936.

(15) Farman, J. C.; Gardiner, B. G.; Shanklin, J. D. *Nature* **1985**, *315*, 207-210.

(16) "Scientific Assessment of Ozone Depletion - Report no. 37," World Meteorolgical Association, 1994.

(17) Anderson, J. G.; Brune, W. H.; Proffitt, M. H. *Journal of Geophysical Research-Atmospheres* **1989**, *94*, 11465-11479.

(18) Crutzen, P. J.; Arnold, F. *Nature* **1986**, *324*, 651-655.

(19) Fahey, D. W.; Solomon, S.; Kawa, S. R.; Loewenstein, M.; Podolske, J. R.; Strahan, S. E.; Chan, K. R. *Nature* **1990**, *345*, 698-702.

(20) Tevini M (ED) *UV-B Radiation and Ozone Depletion*; Lewis Publishers, Boca Raton, 1993.

(21) Farman, J. C.; Gardiner, B. G.; Shanklin, J. D. *Nature* **1985**, *315*, 207.

(22) "Scientific Assessment of Ozone Depletion Report -no. 47," World Meterological Organisation, 2002.

(23) "Chemical Kinetics and Photochemical Data for use in Stratospheric Modelling, Evaluation No. 12," NASA JPL, Pasadena, U.S.A, 1997.

(24) Chance K; Traub WA; Johnson DG; Jucks KW; Ciarpallini P; Stachnik RA; Salawitch RJ; Michelsen HA *J. Geophys. Res* **1996**, *101*, 9031.

(25) Chartland DJ; McConnel JC *Geophysical Research Letters* **1998**, *25*, 55.

Chapter 2 Experimental Principles

2.1 Introduction

The underlying objective of these studies is the investigation of free radical reactions in the gas phase. The main body of this work has aimed to develop and construct apparatus that will provide sensitive, specific, accurate measurements of trace gas composition during a reaction using mass spectrometry with chemical ionisation. In a separate study an existing apparatus, with broadband time resolved UV spectroscopy, has been used to study the ClO + ClO association reaction in detail. The development and characterisation of the mass spectrometric apparatus are discussed in detail in Chapters 3 and 4. The ClO study is described in Chapter 5. In this chapter, the underlying experimental principles of how trace gas composition measurements are made, and how these measurements can give kinetically useful data, are discussed.

2.2 Strategies for Gas Kinetic Studies

Many important laboratory techniques are employed in gas kinetic studies. Fundamentally, these methods are concerned with measuring trace concentrations of transient reactants (or products) as a function of time. There are two main ways in which this may be achieved, namely real time monitoring or elapsed time monitoring. Both are considered in this section.

2.2.1 Real Time Monitoring

Real time monitoring methods are the most conceptually simple approach to recording concentration *versus* time data. Here, the reaction of interest is initiated and the progress observed and recorded as it happens, *i.e.* in real time. The fundamental requirement of real time monitoring is to be able to record species concentrations on the timescale of the reaction. In the case of radical reactions, where reactants are

short-lived species, a detection technique must therefore, have response times short enough to cope with rapid changes in concentration. Indeed, the response time of the detection system often proves to be the limiting factor when choosing an experimental timescale. Another preferred requirement is that the generation of the reactant radicals of interest takes place on a much shorter timescale than the subsequent reaction. Flash photolysis with time resolved spectroscopic monitoring is a particularly successful technique used for real time monitoring. The principles behind its operation are described in detail in Section 2.3.

2.2.2 Elapsed Time Monitoring

An alternative to the need for rapid initiation of reactant production followed by rapid real time monitoring of reactions is to set up a situation whereby a reaction is conducted continuously and observed at a fixed time following initiation. Varying the length of delay time before monitoring the reacting species may then be used to build up a concentration *versus* time profile, required for analysis by the methods described in Chapter 1.

Removal of the need for time resolution allows more general analytical detection techniques to be adopted. Other advantages of elapsed time monitoring include the ability to study reactions of chemically diverse species, due to the removal of the chemical constraints imposed by the need for rapid production of reacting species. Furthermore, in principle, the limitless signal integration time available for monitoring reacting species at a given time interval confers potential advantages in sensitivity. A convenient technique to study gas phase free radical reactions using elapsed time monitoring is the flow tube method, wherein radicals are generated in separate gas flows, mixing initiates reaction and downstream detection defines the elapsed time. This is discussed in detail in Section 2.4.

2.3 The Flash Photolysis Technique

In the flash photolysis technique a short, intense, pulse of light from a high voltage discharge lamp or a pulsed laser is used to initiate a reaction of interest. In the study of gas phase reactions, the light pulse photolyses components of a precursor mixture. This leads to generation of reactant species of interest, either by direct photodissociation or by further chemistry following the photochemical initiation. Either way, it is essential to produce the desired species on a timescale that is much shorter than the subsequent chemistry. This requirement essentially decouples the formation and decay kinetics of the reactive species of interest, allowing the unperturbed decay kinetics – the reaction of interest – to be investigated. Concentrations of both reactants and products are monitored directly as a function of time, commonly by UV-visible absorption spectroscopy, and analysed to determine kinetic data.

The real time nature of flash photolysis experiments for the study of highly reactive species requires detection techniques that are sufficiently fast to respond to rapidly changing concentrations. Typically, the speed of such detectors limits the timescales over which reactions can be studied *via* flash photolysis. Absorption spectroscopy permits the identification and absolute quantification of reacting species but problems can arise if detectors are not rapid enough to follow a particular reaction or if the wavelength coverage is not sufficient to distinguish between multiple absorbing species. The original flash photolysis experiments used absorption spectroscopy and modifications to this technique have concentrated on the detection systems. A brief history of the development of the technique follows.

2.3.1 History of Flash Photolysis

The flash photolysis technique was originally developed by Porter and co-workers in the 1950s to study reaction intermediates.[1,2] Reactions were initiated using flashlamp photolysis, and a second flashlamp was used as the source for absorption

measurements. In the original experiments, spectra were recorded on photographic plates. The photographic plate was aligned in the dispersive plane of a spectrograph and wavelength resolved light from the pulsed analysis lamp, transmitted through the reacting gas mixture, was recorded. The signals were converted manually into absorptions by measuring the degree of darkening across the plate relative to an exposure with no photolysis flash. Experiments were then repeated with different delay times to build up a temporal absorption profiles. Hence, experiments were wavelength resolved but not time resolved since successive experiments had to be carried out at different delay times between the photolysis and the analysis flash. An example of a set of flash photolysis spectra, reported for a study of CN radical kinetics by Dr David Husain (Cambridge),[3] is given in Figure 2.1.

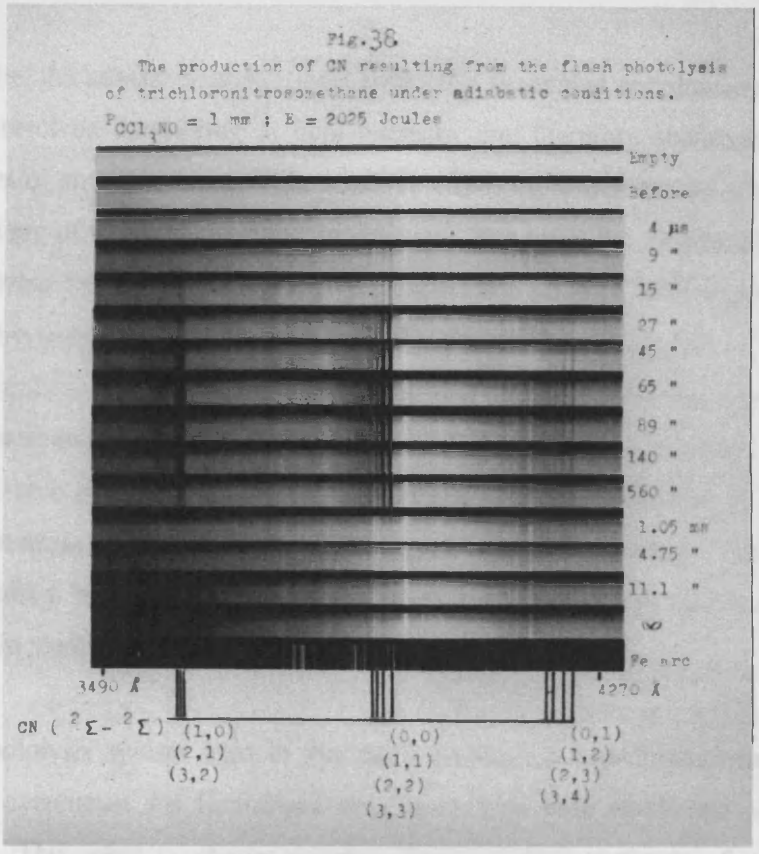

Figure 2.1: Photographic plate recorded transmission spectra of flash photolysed CCl_3NO (D. Husain)[3]

In the 1960s, the availability of electronic photodectors, photomultiplier tubes (PMTs), enabled the continuous real time monitoring of the absorption signal from a single flash photolysis experiment.[4] However, using PMTs, simultaneous wavelength resolved measurements were not possible, due to the inability of the PMT to distinguish between light falling on different parts of the detector window, coupled with its physical size compared to the dispersion of available spectrographs. Consequently, PMT experiments were limited to time resolved measurements of single wavelengths selected using a monochromator. The use of single wavelength absorption measurements restricted the ability to identify and discriminate between absorbing species, since multiple species can absorb at a single wavelength. However PMTs provide significant advantages over photographic plate methods and are still widely used in flash photolysis systems today.[5]

More recently, the advent of photodiode arrays has facilitated simultaneous time and wavelength resolved monitoring of light intensity, and therefore absorbance. These arrays consist of small, separate, light sensitive elements, which can be aligned in the dispersive plane of the spectrograph. In principle, this gives the best of both worlds. However, owing to the readout time (typically on the scale of milliseconds), which limits the time resolution, these are not suitable for fast kinetic studies. One way in which this limitation may be overcome is by fast gating of the array detection to record a transmission spectrum at a fixed time following reaction initiation. Here, as with photographic plate experiments, repeated experiments as a function of delay time between photolysis flash and detection are again required, however. Nevertheless, photodiode arrays have been successfully applied in studies of UV/ visible absorption spectra[6] and in studies of systems with intrinsically slow kinetics.[7]

The flash photolysis system used in this work employs a two-dimensional detector array which overcomes the limitations associated with both PMT and photodiode techniques.[8] This array, a charge coupled device (CCD), consists of a series of discrete pixels that can convert light to photocharge but also has the ability to rapidly and efficiently transfer this signal across the device. The rate of this charge transfer defines the time resolution of the CCD and is on the microsecond timescale, hence

enabling monitoring of fast kinetic reactions. Only a fraction of the array is illuminated by the wavelength resolved analysis light, and most pixels are optically masked in a storage region. Using charge transfer, the entire storage region is filled before the data is read out. Therefore, readout can take place on a slower timescale than data acquisition without compromising the efficiency of data collection.

2.3.2 Charge Coupled Devices

The CCD consists of a two-dimensional array of detector elements, or pixels. Each pixel, comprising a metal oxide semiconductor embedded in a silicon substrate, converts incident light to photocharge, which is stored in an electrically generated potential well within the pixel. The light to charge conversion efficiency of the CCD peaks at incident wavelengths near 700 nm, with a value of 60 %. For detection of wavelengths below 400 nm, the pixels are coated with a thin layer of phosphor that fluoresces on the nanosecond timescale at visible wavelengths. With such a coating, the light-to-charge efficiency is approximately 20 % between 180 nm and 400 nm.

The photocharge on the device can be moved from pixel to pixel along one axis of the array. This is induced by the application of a series of voltages on electrodes aligned perpendicular to the direction of charge transfer. This process is shown schematically in Figure 2.2. The efficiency of charge transfer is high, typically exceeding 99.9999 % per transfer. Transfer rates of up to 1 MHz (corresponding to 1μs time resolution) are readily attainable.

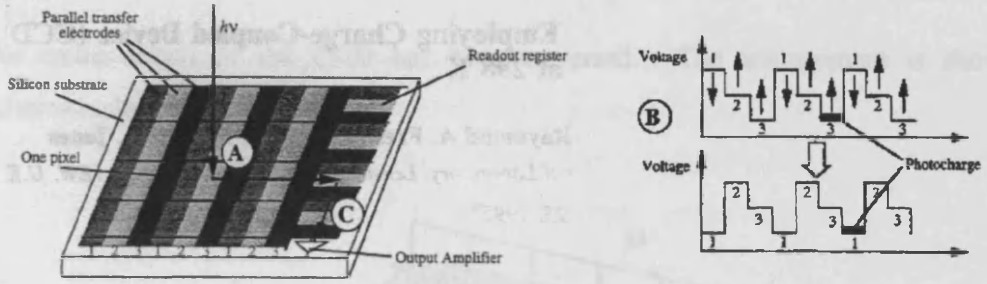

Figure 2.2: Principles of CCD operation and charge transfer. Incident light is converted to photocharge (A). Three sets of parallel transfer electrodes are charged cyclically to maintain a potential gradient across the device (B), moving charge. Finally, when the charge has traversed the entire device, the charge is read out *via* the output amplifier (C). Taken from Rowley *et al.*[8]

The main source of noise associated with the CCD is 'dark' current produced by the CCD. This dark current must be recorded for each pixel prior to exposure and subtracted from experimental intensities. Dark current is minimised by Peltier cooling the CCD to 200 K and enclosing it in a vacuum for thermal insulation. The other significant source of noise is photonic noise, inherent to the light incident upon the device. Since photon emission is a Poisson distribution, the photonic noise level is equivalent to the reciprocal of the square root of the number of photons detected at each pixel of the CCD, corresponding to ±0.07% for a typical full pixel capacity of 2×10^6 photoelectrons.

2.3.3 Application of CCD Detection to Flash Photolysis

In the flash photolysis experiment, output from a continuous UV/visible analysis lamp is directed through the reaction cell and into an astigmatic spectrograph. In this work, the CCD effectively replaces a photographic plate or diode array detector and is positioned with the axis of charge transfer perpendicular to the dispersive plane of the spectrograph. The top few rows of the CCD are illuminated by wavelength resolved transmitted analysis light, while the rest of the device is optically masked. The light to charge conversion takes place and the charge-transfer process rapidly moves the resulting rows of charge, representing transmission spectra, out of the illuminated region, permitting further continuous acquisition of spectral data. This continues until

the entire length of the CCD has been traversed. The arrangement is shown schematically in Figure 2.3.

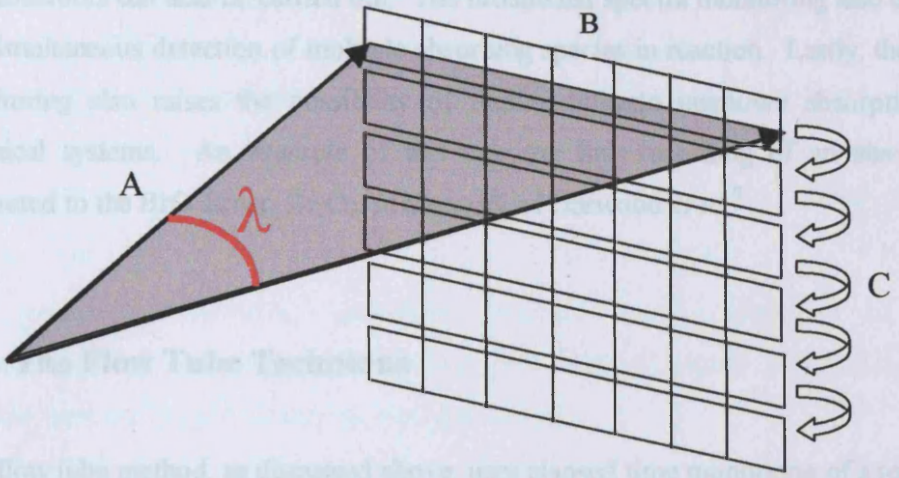

Figure 2.3: Application of the CCD in kinetic experiments. **A**: Wavelength resolved light from the spectrograph is imaged across the top of the CCD array axis; **B**: incident light generates photocharge at the device; **C**: rapid and efficient charge transfer allows recording of sequential spectra.

2.3.4 The Flash Photolysis Experiment

Apart from the unique CCD monitoring of time and wavelength resolved absorptions, the flash photolysis experiment used in this work is very similar to that originally developed by Porter. Thus, a gas handling system, using mass flow controllers is used to prepare suitable precursor gas mixtures. Reactions are initiated in a thermostatted quartz reaction cell by the output from a high voltage discharge lamp. The source for analysing UV absorption in this work is a continuous lamp, and the dispersing element, wavelength resolving the light transmitted through the reaction mixture, is a grating spectrograph. The full details of all of this apparatus are given in the flash photolysis study of ClO radical dimerisation in Chapter 5.

Use of the CCD detector enables entire sequential UV absorption spectra of a reacting gas mixture to be recorded on gas kinetic timescales. This confers many advantages

over previous flash photolysis systems, since definitive identification of the photolytically generated species present can be readily performed. Using spectral fitting techniques, detailed in Chapter 5, very accurate and specific quantification of UV absorbers can also be carried out. The broadband spectra monitoring also enables the simultaneous detection of multiple absorbing species in reaction. Lastly, the CCD monitoring also raises the possibility of finding hitherto unknown absorptions in chemical systems. An example of this was the first recording of an absorption attributed to the BrO dimer, Br_2O_2, in the work of Harwood *et al.*[9]

2.4 The Flow Tube Technique

The flow tube method, as discussed above, uses elapsed time monitoring of a reaction. Here, reactant radicals are created separately in gas flows, which are then mixed, defining the initiation of reaction. Downstream detection of reactants or products is then carried out, with the rate of gas flow and the distance to the detection defining the elapsed time. Variation of this time is used to build up the kinetic profile.

The flow tube kinetic method evolved from the early discharge tube studies of Wood[10,11] and Bonhoeffer.[12] These authors discovered that large concentrations of atoms and radicals could be generated in low-pressure discharges. Their work was primarily centred upon characterising sources of radiation emitted by discharged gases but the technique was quickly applied to kinetic measurements. The first flow tube kinetic measurements were made in the late 1920s. Smallwood[13] carried out experiments to measure the recombination of hydrogen atoms using a Wood-Bonhoeffer type discharge tube. The technique was also employed by Harteck and Kopsch[14] soon after in a study of the reactions of oxygen atoms with many other compounds.

The late 1950s and early 1960s provided many important discoveries that led to advances in the flow tube technique and instrumentation. Kaufman made two major

contributions to kinetics of flow tubes at this time. In his study of the air-afterglow reaction,[15] he showed that the intensity of the chemiluminescence from NO_2 is proportional to the concentrations of atomic oxygen and nitric oxide reacting to produce this NO_2:

$$O + NO \rightarrow NO_2 + hv \qquad (2.1)$$

$$I_{hv} \quad \propto \quad [O][NO] \qquad (2.i)$$

This provided a sensitive, quantitative method for the detection of small concentrations of oxygen atoms. Through this work, Kaufman also observed the reaction between oxygen atoms and nitrogen dioxide:

$$O + NO_2 \rightarrow \quad NO + O_2 \qquad (2.2)$$

He discovered that this reaction was extremely fast and hence could be used as a gas phase titration to measure atomic oxygen concentrations in a flow tube. The endpoint of the titration, in this case, indicated by the extinction of the airglow emission. Titration reactions are very important to flow tube kinetic measurements, as they are fast stoichiometric reactions that provide cleanly qualitative methods of monitoring or even preparing labile species. Kaufman[16] and Clyne[17,18] have extended the concept of gas phase titrations to many different atomic and simple radical species. The following section will describe the measurement and analysis procedures used in flow tubes to determine kinetic information.

2.4.1 General Considerations

A schematic diagram of a flow tube reactor is shown in Figure 2.4. The major component is the tube, typically constructed of Pyrex and in the range 2-5 cm internal diameter and 0.5-2 m in length. A carrier flow of inert gas is admitted to the flow tube at the far end from the detector. This gas is the major component in the tube and

hence defines the physical properties of the gas stream such as pressure, flow velocity, and temperature.

The first reactant species, Y, enters the flow through a side port downstream from the carrier gas entrance and the second reactant species, X, enters through an injector. At the point where the two flows meet, and the two radicals mix, the reaction is initiated and time = 0. The reaction zone is the distance, *z*, from this mixing to the detector, time = *t*. Flow tube kinetic measurements are made by varying the reaction zone length, *z*, which varies *t*. This is accomplished by either changing the position of the detector or the mixing point. Moveable detectors have been used in previous work,[13,16,19] but it is usually more convenient to change the position of the mixing point by moving the reactant inlet. For this purpose, most flow tube systems employ either a series of fixed valve ports along the flow tube or a moveable injector. As fixed inlets are short in length they present an advantage if the added reactant is very reactive, and can be destroyed by wall collisions or by gas phase recombination. However, the moveable inlet requires fewer connections through the flow tube and allows greater flexibility in varying the reaction zone length. For these reasons a moveable injector has been used in this work.

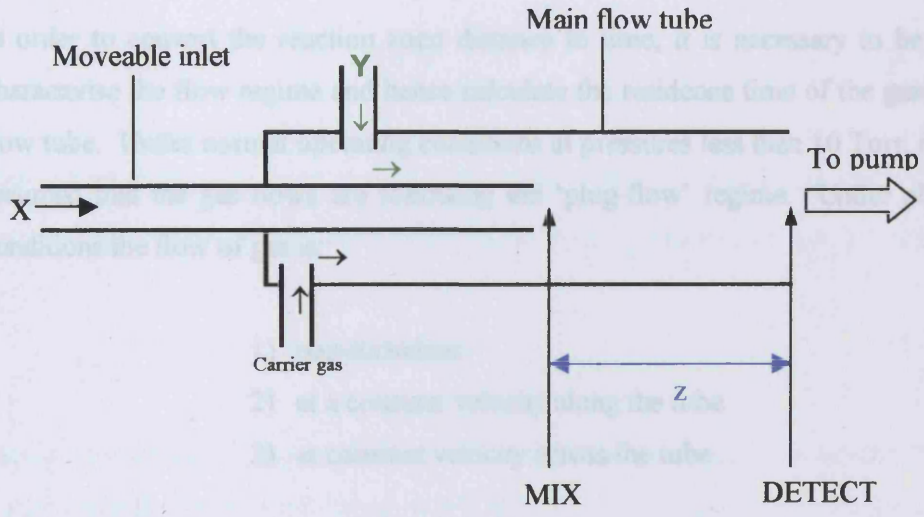

Figure 2.4: Schematic diagram of a flow tube reactor

In order to convert the reaction zone distance, z, to elapsed time, it is necessary to be able to calculate the residence time of the gases in the flow tube. Hence, the gas flow through the tube must be fully characterised.

2.4.2 Gas Flow Considerations

Depending on the physical conditions in the tube, fluid can flow through it in a variety of ways, some of which are illustrated in Figure 2.5.

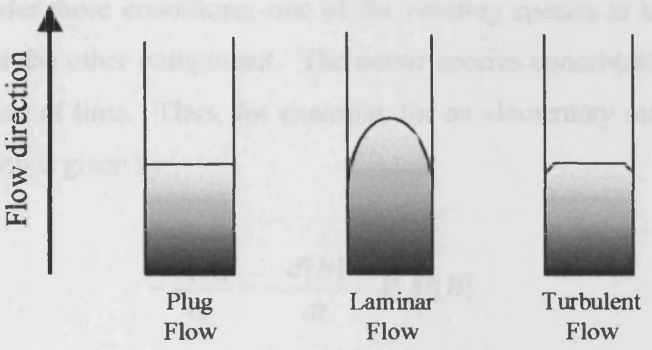

Figure 2.5: Types of fluid flow through a tube

In order to convert the reaction zone distance to time, it is necessary to be able to characterise the flow regime and hence calculate the residence time of the gases in the flow tube. Under normal operating conditions at pressures less than 10 Torr, it can be assumed that the gas flows are following the 'plug-flow' regime. Under plug-flow conditions the flow of gas is:

1) non-turbulent
2) at a constant velocity along the tube
3) at constant velocity across the tube

Hence, the basic assumption of the flow tube analysis is that the radical reactants are mixed homogeneously with the carrier gas and there are no concentration gradients. The carrier gas flow velocity, v, equals the transport velocity of the radicals, thus the

reaction time in the flow tube can be calculated simply as a function of the reaction zone, z, and the linear flow velocity, v.

2.4.3 Combining Flow Analysis and Kinetic Analysis

The majority of reactions studied using flow tubes are elementary bimolecular processes: *e.g.* radical-radical or radical-molecule reactions. The practical study of such processes, exhibiting second order kinetics, is often conveniently simplified by carrying out experiments under pseudo-first order conditions, as described in Section 1.2.2. Under these conditions, one of the reacting species is kept present in known excess over the other component. The minor species concentration is then monitored as a function of time. Thus, for example, for an elementary reaction A + B, the full rate equation is given by:

$$-\frac{d[A]}{dt} = -\frac{d[B]}{dt} = k[A][B] \qquad \text{(2.ii)}$$

If reactant B is in excess over reactant A, then the pseudo first order rate equation is given by:

$$-\frac{d[A]}{dt} = k'[A] \qquad \text{(2.iii)}$$

The psuedo-first order rate constant $k' = k[B]$, where k (cm^3 $molecule^{-1}$ s^{-1}) is the second-order rate constant. Integrating equation (iii) between time t and 0 gives:

$$[A]_t = [A]_0 \exp(-k't) \qquad \text{(2.iv)}$$

Hence, the decay of [A] with time is described by a simple exponential form. It should also be noted from equation (iv) that the kinetic information contained in k' can be obtained from the *relative* change of [A] with time. This means that [A] does not need to be measured absolutely, which is an enormous advantage experimentally. By contrast, the concentration of B must be known absolutely since kinetic analysis

determining k' is followed by use of $k' = k[B]$ to obtain k. Another important issue with radical-radical reactions, is that the species B does not undergo self-reaction at an appreciable rate, since, under conditions of excess B, this self-reaction would dominate the loss of B and lead to variation in the concentration of B along the flow tube.

Rate constant determinations are made in the flow tube by measuring the concentration of species A with the sliding injector at several different positions between mixing and detection, which gives several different values of z, and hence reaction time. The total reactant flow rate is held constant. The data obtained are then plotted in the form ln [A] *versus* z and the slope is used to obtain the pseudo first order rate constant, k'.

$$k' = -v\frac{d\ln([A]_t/[A]_0)}{dz} \qquad (2.v)$$

The concentration of species B in the flow reactor can be calculated from the total concentration of gas present, [Total], and the ratio of the flow rates of the individual component, f_b, to the total flow, Σf_i.

$$\frac{[B]}{[Total]} = \frac{f_b}{\Sigma f_i} \qquad (2.vi)$$

The total concentration of gas, [Total], can be calculated from the total pressure, p, and temperature, T, in the flow reactor and the Boltzmann constant k_B.

$$[Total] = \frac{p}{k_B T} \qquad (2.vii)$$

Conveniently, the pseudo-first order rate constant for loss of species A, measured for a variety of fixed co-reactant concentration, B, is then plotted against [B] to obtain the bimolecular rate constant, k, from the gradient. In principle, this 'bimolecular plot'

should pass through the origin, since $k' = k[B]$. However, as discussed below, some loss of A in the absence of B, attributed to loss of A on the walls of the flow tube or injector, manifests itself as a small y-axis intercept.

Alternatively, by combining equations (iv) to (vii) an expression for the second order rate constant can be derived.

$$k = \frac{(\Sigma f_i)^2}{f_b}\left(\frac{k_B T}{p}\right)^2 \frac{1}{\pi^2}\frac{d\ln[A]}{dt} \qquad \text{(2.viii)}$$

2.4.3.1 Pressure and Concentration Gradients

Analysis of flow tube kinetics relies upon the assumption that the flow through the tube follows plug flow conditions as described above. However, in practice deviations from plug flow do occur from pressure gradients. Consequently axial concentration gradients along the tube must be taken into consideration.

The flow through the reactor is fully developed viscous flow.[20] The forces moving the gas develop a pressure gradient along the tube. Under conditions of high flow velocities, this gradient can be significant in small diameter tubes. The pressure gradient can be described using the Poiseuille equation.

$$p_2^2 - p_1^2 = \frac{16\Sigma f x \eta R T}{r^4 \pi} \qquad \text{(2.ix)}$$

Where p_1 and p_2 are the pressures at each end of the flow tube, Σf is the total flow rate, x is the length of the reaction region, η is the gas viscosity, R is the universal gas constant, T is the temperature and r is the radius of the tube.

If $p_2 \approx p_1$, this expression can be simplified to equation (x), which involves a term for flow velocity rather than molecular flow rate.

$$\frac{\Delta p}{\Delta z} = 5.9 \times 10^{-3} \eta v / r^2 \qquad (2.x)$$

Hence, it would appear that slower flows are more desirable as the pressure drop along the tube would be smaller. However, this would lead to large axial concentration gradients and back diffusion.

It can be seen from expression (xi) that the assumption that there are no concentration gradients and that the flow velocity is the transport velocity of the reactants is violated whenever reaction occurs.

$$\frac{d[X]}{dz} = -k[X]/v \qquad (2.xi)$$

This axial concentration gradient will cause the radicals to be transported down the tube by an additional velocity component v_d given by Fick's first law:

$$J = -D\frac{d[A]}{dz} = v_d[A] \qquad (2.xii)$$

where J is the flux (molecules cm^{-2} s^{-1}) and D is the diffusion coefficient (cm^2 s^{-1}). Hence by combining expressions (xii) and (xiii), $v_d = Dk/v$, the correct transport velocity for the radicals is $v + v_d$. The correction for axial diffusion is then $(v + v_d)/v$ and the corrected rate constant, k'_{corr} is given by:

$$k'_{corr} = k'\left(\frac{1 + k'D}{v^2}\right) \qquad (2.xiii)$$

This result can also be obtained by integrating the one dimensional continuity equation, using the boundary conditions of [A] = $[A]_0$ at $x = 0$ and [A] = 0 at $x = \infty$ (x being the distance along the flow tube).[21]

2.4.4 Practical Considerations

2.4.4.1 Wall Losses

Since the fundamental transformation in flow tube kinetic analysis is the conversion of physical distance to elapsed time, the scale of the instrument and the rapidity of the reaction govern the gas flow conditions. For rapid bimolecular reactions with rate constants in the range 10^{-12} to 10^{-10} cm^3 $molecule^{-1}$ s^{-1}, given readily attainable pumping speeds, low pressures (1-10 Torr) are usually required to keep gas flows suitably fast. Under these conditions, inherent complications can arise from loss of radical species to the walls of the flow tube. Such wall losses can occur on both the central injector and the outer walls of the main flow tube, which must be taken into consideration.

Loss of a radical species from the main flow to the surfaces of the central injector wall can easily be measured and calibrated by monitoring the concentration of radical species A in the absence of any other species, while adjusting the injector position.[22] Typically a radical species A will undergo first-order heterogeneous recombination on the walls of the injector.

$$A \rightarrow \tfrac{1}{2} A_2 \qquad (2.3)$$

The concentration of A increases as the injector is pulled back from the detection area.

$$\frac{d[A]}{dz} = k'_{inj}[A] \qquad (2.xiv)$$

The central injector wall loss rate constant, k'_{inj}, can be calculated and, if added to the observed rate constant, k'_{obs}, will give the experimental rate constant, k'_{exp}.

$$k'_{exp} = k'_{obs} + k'_{inj} \qquad (2.xv)$$

Evidently, apart from losses of free radicals to the central injector, radicals can also be lost to the inside walls of the main flow tube. However, given that the time of exposure of free radicals passing outside the central injector to the walls of the tube is constant, this term does not affect measured rate coefficients. As shown originally by Clyne and Thrush,[23] the radical concentration, [A], at the detector at a fixed distance x from the radical source is given by:

$$[A] = [A]_0 \exp\left(\frac{-k'_{wall}x}{v}\right) \qquad \text{(2.xvi)}$$

where $[A]_0$ is the initial radical concentration at the source and k'_{wall} is the first order wall loss rate coefficient. When co-reactant B is added at a distance z from the detector, the detected concentration of radical A is:

$$[A] = [A]_0 \exp\left(\frac{-k'_{wall}x}{v}\right)\exp\left(\frac{-k'z}{v}\right) \qquad \text{(2.xvii)}$$

Taking logs and rearranging gives:

$$\ln\left(\frac{[A]}{[A]_0}\right) = \frac{-k'_{wall}x}{v} - \frac{k'z}{v} \qquad \text{(2.xviii)}$$

Thus, analysis of ln ($[A]/[A]_0$) as a function of contact distance (z) can be used to determine k', provided that the wall reaction term is constant along the length of the flow tube.

In practice, the problem of losses of free radicals to the walls of low pressure flow tubes is one that can be minimised by the application of various coatings to passivate the inside walls of the flow tube. For Pyrex tubes, such as that employed in this work, phosphoric acid (H_3PO_4) is commonly used. An alternative is coating the inside of the tube with halocarbon wax. PTFE liners have also been applied with some success,

although some evidence for reversible adsorption of trace species onto such inert coatings has been gathered.[24]

2.4.4.2 Mixing

Another practical problem with the application of discharge flow to the study of bimolecular reactions is the finite time over which the two gas streams mix and homogenise, which causes $t = 0$ to be poorly defined. Under most operating conditions, in the plug flow regime, this time has been reported to be of the order of 1-5 milliseconds, and reaction timescales are therefore chosen (by varying the concentration of the excess reagent) to be much longer than this time. Again, various practical modifications to the end of the sliding injector have been reported in the past, with the aims of promoting gas mixing. However, such arrangements, being more physically complex than a simple tube also run the risk of increasing the injector surface area for heterogeneous radical recombination. The efficacy of gas mixing can in practice be visualised by using a rapid reaction which produces chemiluminescence or even simply coloured gas products (such as O + NO). Usually, visual inspection of the gas flows at the mixing point can establish the interaction distance, and therefore an estimated time, over which the gas flows coalesce.

2.4.5 Recent Developments in the Flow Tube Method

The need for well established gas flow characteristics in discharge flow tubes, coupled with readily attainable pumping speeds in the laboratory, have typically restricted flow tubes to operation in the low pressure regime. However, in recent years, application of flow tubes at much higher gas pressures has been described. Pioneered by Seeley *et al.* in 1993[25], the operation of a flow tube at near atmospheric pressure, which requires very large pumping capacity to maintain rapidity of gas flow rates, has been described. Under such conditions, provided that the Reynolds number, R_e, of the flowing gas exceeds a value of 2000, the gas flow operates in the turbulent regime. The Reynolds number is given by:

$$R_e = \frac{2r\bar{u}\rho}{\eta} \qquad (2.xix)$$

where r is the radius of the flow tube, $\bar{u}$ is the average linear flow velocity, ρ is the density of the gas and η is the coefficient of viscosity.

Under these circumstances, a highly mixed core of gas flows along the tube with reasonably constant linear flow velocity, whilst gas very close to the edges of the tube moves rather slower (shown schematically in Figure 2.5). The effect of this slow moving layer of gas is to act as the effective wall of the flow tube, making free radical wall losses very small indeed. However, a corollary of this locally strong axial dependence of the linear flow rate is that detection must sample only the well-mixed central core of the flowing gas. Another practical consideration is the thermostatting of gas flows that effectively do not interact with the walls of the apparatus. Pre-cooling of the gas flows is needed in all low temperature applications, and owing to the massive amounts of cold gas required for such studies, most studies using this 'turbulent flow tube' technique have used nitrogen as the carrier gas, (generated from liquid nitrogen), which is at least appropriate for atmospheric studies.

2.5 Detection Systems for Flow Tubes

There are various techniques that can be applied to the measurement of concentrations of species found in discharge flow experiments. A review of these is given in this section.

2.5.1 Resonance Fluorescence

Resonance fluorescence (RF) is a versatile technique that is used for the detection of atoms in flow tubes. Resonance fluorescence is a process wherein the excitation and

subsequent fluorescence of a source species produces a resonant excitation, which is used to induce fluorescence in the species to be detected.

The initial source of excited atoms is provided by passing a suitable molecular precursor in a carrier flow, usually helium, through a microwave discharge. This causes some of the molecular species to dissociate. A fraction of the resulting atoms are collisionally excited to form electronically excited atoms. These excited atoms subsequently return to the ground state through fluorescence. The frequency of the fluorescing light is characteristic of the atoms produced by the discharge.

The light from this discharge lamp is then filtered and directed into the flow tube using appropriate optics. This causes resonant excitation and fluorescence by atoms of the same species in the flow tube. Importantly, the intensity of fluorescence emitted from the reaction cell is linearly proportional to the atom concentration in the cell, hence, monitoring the fluorescence using a photomultiplier tube provides a simple method of obtaining a relative measure of atom concentration. A schematic diagram of a typical resonance fluorescence arrangement is given in Figure 2.2.

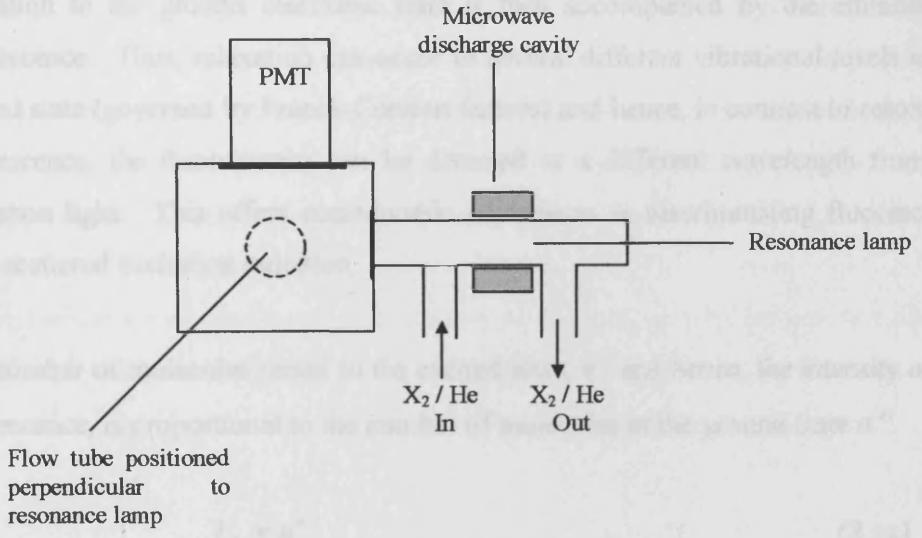

Figure 2.6: Schematic diagram of a typical resonance fluorescence apparatus.[26]

This technique is well suited to kinetic studies of reactions of atoms due to its simplicity, relatively low cost and very high specificity. Atomic lines are so sharp that it is highly unlikely that two atomic transitions of different species will coincide. Thus, for example, bromine atoms can be detected in the presence of chlorine atoms. Some small complications can occur in resonance fluorescence if the resonant emission from the atoms of interest in the reaction cell is subsequently reabsorbed by other atoms within the flow cell. This effect ('self-reversal') can however be minimised if atom concentrations are low, and the cell mixture is, therefore, optically thin.

2.5.2 Laser Induced Fluorescence

Laser induced fluorescence (LIF) works on a very similar principle to resonance fluorescence but can offer greater sensitivity and applicability, particularly for molecular radicals. In this case, the species to be detected is excited to an upper electronic state using a tuneable laser. Since laser output is intense, monochromatic and non divergent, such excitation can be very efficient, and optical pumping to excited states in a particular rovibronic level can be readily achieved. Subsequent relaxation to the ground electronic state is then accompanied by the emission of fluorescence. Thus, relaxation can occur to several different vibrational levels in the ground state (governed by Franck-Condon factors) and hence, in contrast to resonance fluorescence, the fluorescence can be detected at a different wavelength from the excitation light. This offers considerable advantages in discriminating fluorescence from scattered excitation radiation.

The number of molecules raised to the excited state, n', and hence, the intensity of the fluorescence, is proportional to the number of molecules in the ground state n'':

$$I_f \propto n'' \qquad (2.xx)$$

Therefore the fluorescence intensity rises linearly with the number of photons absorbed and hence with the excitation intensity. This leads to greater sensitivity than resonance fluorescence method because of the inherent high intensity of the laser source.

As with resonance fluorescence, laser induced fluorescence provides only a relative measure of concentration, which can be a disadvantage over less sensitive but absolute detection methods. As discussed above, however, if the species of interest reacts in a pseudo-first order fashion with another species in the gas phase, relative measurement of concentration of the minor species is suitable for extracting kinetic information. In addition, LIF is limited to species that have bound and accessible upper electronic states, which means that some important radical species *e.g.* (CH_3) cannot be detected using this method.

2.5.3 Laser Magnetic Resonance

Laser magnetic resonance (LMR) has been used for the detection of atmospherically important radicals, such as HO_2, ClO, NO_2 and NO in discharge flow systems.[27,28] A CO_2 laser is typically employed to probe radical concentrations. The laser produces a variety of lines in the infrared region of the spectrum. It is rare that these lines will coincide with a radical vibration-rotation absorption line but provided the radical has a magnetic moment it is possible to tune a radical's absorption to a laser frequency by applying a magnetic field.

Laser absorption can then be used to monitor the concentration of the radical using the simplified Beer-Lambert Law.

$$\frac{I_{abs}}{I_0} = \varepsilon c l \qquad \text{(2.xxi)}$$

where I_{abs} is the change in measured light intensity, I_0 the intensity before the photolysis pulse, ε is the absorption coefficient, c is the concentration and l is the path length of the absorption.

2.5.4 Mass Spectrometry

Mass spectrometry is a highly sensitive technique that can readily be employed with the discharge flow method. The flow tube is coupled to a high vacuum chamber that houses the mass spectrometric analyser. A sample of gas from the tube is taken, ionised, and these ions then travel through the high vacuum to the detector. A static or oscillating electromagnetic field is used to transport the ions through the vacuum region. Ions of different mass, velocity and charge move differently through this field. Hence, by taking account of charge and velocity effects, ions of specific masses can be separated and collected on a detector and their numbers precisely determined.

In contrast to optical techniques such as those described above, which often tune onto a specific resonant frequency of absorption or emission, mass spectrometry allows for the detection of many species simultaneously. This allows both reactants and products of a given reaction to be monitored in addition to potential side reactions.

The major drawback in using mass spectrometric techniques in kinetic studies is that the flow tube must be interfaced to a region of high vacuum and it must be ensured that the sample reaching the ion source and mass analyser is representative of the gas in the tube at the detection point. This is usually achieved by expanding the gas flow from the tube into high vacuum through a series of differentially pumped chambers. Mass spectrometry is used as the detection technique in this work and the underlying principles of the technique are discussed in detail in the next section.

2.6 Principles of Mass Spectrometry

2.6.1 Ion Sources

The region of the mass spectrometer where ions are generated is known as the ion source. There are a variety of techniques that may be applied to ionise molecules. This section discusses some of the more important methods that are particularly applicable to discharge-flow tube studies.

2.6.1.1 Electron Impact Ionisation

Traditionally, ions to be analysed in a mass spectrometer are produced from neutral molecules *via* electron impact ionisation, (EI). This technique was developed in the 1920s and can be used for the analysis of many gases, volatile compounds and metallic vapours. Sample molecules are passed through an inlet into an ionisation chamber, where they are bombarded by an orthogonal beam of electrons whose energy is greater than the ionisation energy of the sample gas molecules. The energy of the electron beam, which is usually produced from a hot metallic filament can be adjusted to maximise ionisation efficiency and is typically between 0 and 100 eV. Electron impact ionisation causes removal of an electron from the highest occupied molecular orbital of the sample molecule:

$$M + e \rightarrow \quad M^+ + 2e \qquad (2.4)$$

The energy given to the sample molecule by the electron beam is usually somewhat greater than the ionisation energy. Therefore, excess energy remains in the molecular ion, M^+, and this excess energy may be used to break one or more bonds causing the molecular ion to fragment. This fragmentation of the molecular ion is common when electron impact ionisation is used, in some cases it is not possible to detect an appreciable amount of the parent molecular ion and complex spectra often result. This may be advantageous for structural elucidations, *e.g.* of complex organic

molecules, but can prove to be a serious drawback when investigating the genuine products of a reaction.

Another potential drawback of EI ionisation is the possibility of multiple interfering signals contributing to the measured ion count recorded at a given mass to charge ratio. Such interference often results from the necessarily complex chemical scheme used to generate the free radicals of interest in the discharge flow tube. An example of this occurs in previous discharge flow / EI mass spectrometry studies of the atmospherically important HO_2 + ClO reaction.[29,30] In these previous studies, HO_2 radicals are generated following the reaction of chlorine atoms with CH_3OH, (5), and the subsequent reaction of CH_2OH with molecular oxygen, (6). Following ionisation, HO_2 radicals were detected at the parent ion (HO_2^+) mass to charge ratio, $m/z = 33$.

$$CH_3OH + Cl \rightarrow CH_2OH + HCl \qquad (2.5)$$

$$CH_2OH + O_2 \rightarrow HO_2 + HCHO \qquad (2.6)$$

In this work, interfering signals from the radical precursors were recorded at $m/z = 33$, and attributed to signals from $^{17}CH_3{}^{19}OH$ and from ^{17}OO isotopomers. The signal accountable to this pair was therefore determined using the signal recorded at $m/z = 33$, but with the discharge producing Cl atoms switched off, thereby producing no HO_2 radicals. An alternative chemical source of HO_2 radicals is the reaction of F atoms, generated in a discharge, with H_2O_2:

$$F + H_2O_2 \rightarrow HO_2 + HF \qquad (2.7)$$

Again, HO_2 radicals produced from this reaction are monitored at $m/z = 33$. In this case, however, direct ionisation and fragmentation of the parent H_2O_2 molecule can add a spurious signal to that recorded at this mass to charge ratio. This must be accounted for in experiments not producing HO_2, which essentially determine the fragmentation-to-parent ion ratio of the H_2O_2 signal, (*i.e.* the signal at $m/z = 33$:signal

at $m/z = 34$) and this ratio used to correct for the signal recorded at $m/z = 33$ with HO_2 present.

In similar fashion, experiments on the ClO + HO_2 reaction monitor the ClO signal at $m/z = 51$ and $m/z = 53$, attributed to the (different isotopomers of) ClO^+. The ClO is readily generated in discharge flow using the reaction of chlorine atoms with a variety of precursor molecules:

$$Cl + O_3 \rightarrow ClO + O_3 \qquad (2.8)$$

$$Cl + Cl_2O \rightarrow ClO + Cl_2 \qquad (2.9)$$

$$Cl + OClO \rightarrow ClO + ClO \qquad (2.10)$$

However, again when using EI in systems employing Cl_2O or OClO as the ClO radical source, electron impact ionisation of the Cl_2O or OClO parent molecule can lead to fragmentation to produce additional ClO^+, adding to the signals at $m/z = 51$ and 53, which must be accounted for.

2.6.1.2 Chemical Ionisation

As a consequence of the drawbacks associated with electron impact ionisation mass spectrometry when applied to discharge flow studies of free radical reactions, a more specific and selective ionisation scheme has been developed. Chemical ionisation, (CI), first developed in the 1960s for structural elucidation of molecules,[31] involves ionisation of molecules through gas phase ion-molecule reactions rather than electron bombardment. The ions required for this process – so called reagent ions – are produced from a high pressure ion source region, and mixed with the gas under study, producing a parent ion from the molecule or radical of interest. The internal energy content of this parent ion produced by chemical ionisation is generally much less than in the case of electron impact ionisation. Consequently, a smaller amount of fragmentation is observed in CI and hence there is a much greater possibility of detecting the species of interest without interfering signals from other sources.

The specificity of chemical ionisation is particularly useful in discharge flow studies of reactions between radicals, where the reactant and product molecules are present in a complex gas mixture on reaching the detector. Furthermore, there is an enormous variety of CI reagents ions that can be utilised, hence it is invariably possible to find a reagent ion that will selectively ionise a target molecule in a given gas mixture.

CI has been used to detect many important atmospheric species in the laboratory, (the gas phase chemistry of free radicals including ClO, BrO, HO_2 and OH have all been investigated using this method).[32-34] Similarly, the heterogeneous chemical interactions of stable molecular species including HNO_3, N_2O_5 and HOCl have also been studied.[35-38] Commonly, selective ionisation of gas phase molecules has been accomplished using SF_6^- or I^- as the reagent ion. SF_6^- is a particularly useful ion source, since it is readily generated and readily transfers an electron, in a typically very fast reaction, onto many gas phase molecules, leaving the rather inert SF_6 molecule.[39] For example:

$$NO_2 + SF_6^- \rightarrow NO_2^- + SF_6 \qquad (2.11)$$

$$Cl_2 + SF_6^- \rightarrow Cl_2^- + SF_6 \qquad (2.12)$$

CI studies using SF_6^- have successfully been used in the laboratory to determine kinetic data for atmospherically important gas phase reactions. An example is the reaction between BrO and HO_2 free radicals.[40] This reaction is known to produce HOBr in a principal reaction channel, with a possible minor, but highly significant, contribution from $HBr + O_3$.

$$HO_2 + BrO \rightarrow HOBr + O_2 \qquad (2.13a)$$

$$\rightarrow HBr + O_3 \qquad (2.13b)$$

The detection of BrO radicals was then readily achieved by formation of BrO^- by electron transfer from SF_6^-:

$$SF_6^- + BrO \rightarrow SF_6 + BrO^- \quad (2.14)$$

By contrast, HO_2 radicals were detected as $SF_4O_2^-$ produced *via* multistep pathways. The presence of such multichannel reactions complicated the ionisation chemistry somewhat. Thus, HOBr was detected as the SF_5O^- ion, and HBr was tentatively detected as the $HBrF^-$ ion, produced by fluoride ion transfer from SF_6^-. Consequently, attempts to assess the branching ratio for the BrO + HO_2 reaction focussed on the detection of the small quantity of the ozone co-product of HBr. Ozone is known to undergo fast electron transfer from SF_6^-:

$$O_3 + SF_6^- \rightarrow O_3^- + SF_6 \quad (2.15)$$

However, this route to the branching ratio was also complicated, since the relatively large concentrations of oxygen used in the experiments to produce HO_2 radicals also underwent electron transfer from SF_6^-, and participated in subsequent chemistry providing another source of O_3^-:

$$O_2 + SF_6^- \rightarrow O_2^- + SF_6 \quad (2.16)$$

$$O_2^- + O_2 \rightarrow O_3^- + O \quad (2.17)$$

In conclusion, for this example reaction, CI has been successfully applied to investigate the reaction kinetics, but progress on the branching ratio remains limited.

An alternative general strategy for CI studies of atmospherically important reactions may be adopted using a more specific ion molecule reaction for the chosen product, and using a reagent ion that possesses fewer chemical possibilities of product species. One such ion, which is known to undergo rapid proton transfer to a variety of gas phase chemical species is the H_3^+ ion, and in this work, a CI instrument has been developed and constructed and details of this proton transfer investigated. This instrument, and the characterisation studies carried out, are described in Chapters 3 and 4.

2.6.1.3 Proton Transfer

A common ionisation reaction used in chemical ionisation mass spectrometry of organic molecules is the proton transfer from gaseous Bronsted acids to neutral molecules:[41]

$$XH^+ + M \rightarrow MH^+ + X \qquad (2.18)$$

The efficiency of reaction (18) is governed by the thermodynamics of the reaction. Exothermic proton transfer reactions are highly efficient, with the reaction occurring on essentially every collision. The high efficiency of exothermic proton transfer reactions has been established in studies using a variety of Bronsted acids.[42,43] However, as the proton transfer reaction becomes thermoneutral, the reaction efficiency drops and becomes very low for endothermic reactions.[44] Thus, using proton transfer it is possible to selectively ionise a species present in a gas mixture by examination of the thermodynamics of the reaction and careful choice of a suitable Bronsted acid that will undergo fast reaction with the species of interest.

The standard enthalpy of reaction, $\Delta_r H^0$, of reaction (18) can be calculated by examination of the proton affinities of both species X and M. The proton affinity of a species B is defined as the standard enthalpy of the reaction:

$$B + H^+ \rightarrow BH^+ \qquad (2.19)$$

Numerous studies have provided extensive data on the proton affinities of many molecules.[42,45,46] Table 2.1 lists the proton affinities of some atmospherically relevant species.

Species	Proton Affinity / kJ mol^{-1}
Argon (Ar)	369.2
Oxygen (O_2)	421.0
Hydrogen (H_2)	422.3
Nitrogen (N_2)	493.8
Nitrogen monoxide (NO)	531.8
Carbon dioxide (CO_2)	540.5
Methane (CH_4)	543.5
Hydrogen chloride (HCl)	556.9
Nitrogen dioxide (NO_2)	591.0
Ozone (O_3)	625.5
Water (H_2O)	691.0

Table 2.1: Proton affinities for some atmospherically important species.

The proton transfer method developed in this work uses H_3^+ as the Bronsted acid. Thus, for example, the detection of O_3 in the presence of O_2 is possible since the reaction of O_3 with H_3^+ is exothermic, and therefore rapid, while the reaction of H_3^+ with O_2 is endothermic, and therefore does not readily occur. This is in contrast to other mass spectroscopic methods, as discussed above.

The method of production of H_3^+ ions in this work uses an electrical discharge in H_2 gas. The design and construction of this discharge is described in detail in Chapter 3. The discharge produces H_2^+ ions that react with the neutral H_2 present:

$$H_2^+ + H_2 \rightarrow H_3^+ + H \qquad (2.20)$$

Self protonation reactions, such as (20), are ubiquitous for many molecules and occur on rapid timescales.

2.7 Summary

This chapter has described the underlying principles behind two important techniques used for the measurement of trace gas composition, which have both been employed in this work. Kinetic measurements of the ClO dimerisation have been made using the flash photolysis technique and these are described fully in Chapter 5. The development of a discharge flow chemical ionisation mass spectrometer, employing a novel chemical ionisation scheme is described fully in the following chapter.

2.8 References

(1) Porter G. *Proceedings of the Royal Society of London: Series A* **1950**, *200*, 284.

(2) Norrish R.G.W.; Porter G. *Nature* **1949**, *164*, 658.

(3) Husain D., University of Cambridge, 1962.

(4) Porter G.; West P. *Proceedings of the Royal Society of London: Series A* **1964**, *279*, 302.

(5) Lightfoot P.D.; Lesclaux R.; Veyret B. *Journal of Physical Chemistry* **1999**, *100*, 3020.

(6) Harwood, M. H.; Jones R.L. *Journal of Geophysical Research* **1994**, *99*, 22955.

(7) Rattigan O.V.; Rowley, D. M.; Wild O.; Jones R.; Cox R.A. *Journal of the Chemical Society; Faraday Transactions* **1994**, *90*, 819.

(8) Rowley, D. M.; Harwood, M. H.; Freshwater, R. A.; Jones, R. L. *Journal of Physical Chemistry* **1996**, *100*, 3020-3029.

(9) Harwood, M. H.; Rowley, D. M.; Cox R.A.; R.L., J. *Journal of Physical Chemistry A* **1998**, *102*, 1790.

(10) Wood R.W *Phil. Mag* **1905**, *6*, 513.

(11) Wood R.W; F.L, M. *Physics Review* **1918**, *11*, 70.

(12) Bonhoeffer K.F *Zeitschrift für Physikalische Chemie* **1924**, *113*, 199.

(13) Smallwood H.M. *Journal of the American Chemical Society* **1929**, *51*, 1985.

(14) Harteck P.; Kopsch U. *Z. Phys. Chem* **1931**, *B12*, 327.

(15) Kaufman F. *Proceedings of the Royal Society of London: Series A* **1958**, *247*, 123.

(16) Kaufman F.; Del Greco F.P. *Discussions of the Faraday Society* **1962**, *33*, 128.

(17) Clyne M.A.A. *Physical Chemistry of Fast Reactions*; Plenum Press, New York, 1973.

(18) Clyne M.A.A.; Nip W.S. *Reactive Intermediates in the Gas Phase*; Academic Press Inc.,, 1979.

(19) Trainor D.W.; Ham D.O.; Kaufman F. *Journal of Chemical Physics* **1973**, *58*, 4599.

(20) Dushman S.; Lafferty. *Scientific Foundations of Vacuum Technique*; Wiley: New York, 1962.

(21) Jost W. *Diffusion in Solids, Liquids and Gases*; Academic Press: New York, 1952.

(22) Howard C.J. *Journal of Physical Chemistry* **1979**, *83*, 3.

(23) Clyne M.A.A.; Thrush B.A. *Proceedings of the Royal Society of London: Series A* **1962**, *269*, 404.

(24) Rattigan O.V.; Jones R.L; R.A., C. *Chemical Physics Letters* **1994**, *230*, 121.

(25) Seeley, J. V.; Jayne, J. T.; Molina, M. J. *International Journal of Chemical Kinetics* **1993**, *25*, 571-594.

(26) Pilling M.J.; Seakins P.W. *Reaction Kinetics*; Oxford University Press: Oxford, 1995.

(27) Jemi-Alade A.A.; Thrush B.A. *Journal of the Chemical Society; Faraday Transactions* **1990**, *86*, 3355.

(28) Lee Y.P.; Stimpfle R.M.; Perry R.A.; Mucha J.A.; Evenson K.M.; Jennings D.A.; Howard C.J. *International Journal of Chemical Kinetics* **1982**, *14*, 711.

(29) Knight G.P.; Beiderhase T.; Helleis F.; Moortgat G.K.; Crowley J.N. *Journal of Physical Chemistry A* **2000**, *104*, 1674 - 1685.

(30) Leck T.J.; Cook J.L.; Birks J.W. *Journal of Chemical Physics* **1980**, *72*, 2364.

(31) Munson M.S.B.; Field F.H. *Journal of the American Chemical Society* **1966**, *88*, 2621.

(32) Viggano A.A; Davidson J.A; Fehsenfeld F.C; Ferguson E.E *Journal of Chemical Physics* **1981**, *74*, 6113.

(33) Lovejoy E.R; Murrells T.P; Ravishankara, A. R.; Howard C.J *Journal of Physical Chemistry* **1990**, *94*, 2386.

(34) Gleason J.F.; Howard C.J *Journal of Physical Chemistry* **1988**, *92*, 3314.

(35) Hanson D.R.; Ravishankara, A. R. *Geophysical Research Letters* **1991**, *18*, 1699.

(36) Hanson D.R.; Ravishankara, A. R. *Journal of Physical Chemistry* **1992**, *96*, 2682.

(37) Hanson D.R.; Ravishankara, A. R. *Journal of Geophysical Research* **1991**, *96*, 17307.

(38) Hanson D.R. *Geophysical Research Letters* **1992**, *19*, 2063.

(39) Huey L.G.; Hanson DR; Howard C.J *Journal of Physical Chemistry* **1995**, *99*, 5001 - 5008.

(40) Elrod M.J.; Meads R.F.; Lipson J.B.; Seeley J.V.; Molina M.J. *Journal of Physical Chemistry* **1996**, *100*, 5808 - 5812.

(41) Harrison A.G. *Cemical Ionization Mass Spectrometry*; CRC Press Inc.: Boca Raton, Florida, 1983.

(42) Bohme D.K. In *Interactions between ions and molecules*; Ausloos P., Ed.; Plenum Press: New York, 1975.

(43) Hemsworth R.S.; Payzant J.D.; Schiff H.I.; Bohme D.K. *Chemical Physics Letters* **1974**, *26*, 417.

(44) Bohme D.K.; Mackay G.I.; Schiff H.I. *Journal of Chemical Physics* **1980**, *73*, 4976.

(45) Taft R.W. In *Proton Transfer Reactions*; Caldin E.F., Gold V., Eds.; Chapman and Hall: London, 1975.

(46) Aue D.H.; Bowers M.T. In *Gas Phase Ion Chemistry*; M.T, B., Ed.; Academic press: New York, 1979.

Chapter 3 Chemical Ionisation Mass Spectrometer Development: Design and Construction

3.1 Introduction

The previous chapter has described the underlying principles of the techniques used in this work. This chapter describes the design and construction of the chemical ionisation mass spectrometer and flow tube apparatus developed in the course of this work. The principal objective was the development of a highly specific, sensitive mass spectrometer for use with a discharge flow system.

3.2 Outline of the Experiment

The components of the experiment are described in detail in this chapter. A brief outline of the experiment is given here.

1. Separate reagent gases are introduced to a carrier flow in the flow tube *via* side arms and a sliding injector. Reactive species (*i.e.* free radicals or atoms) are generated in the side arm by microwave discharge.

2. Reaction is initiated at the point of mixing of the reagent gases in the flow tube.

3. H_3^+ reagent ions are generated in a separate cell using an electrical discharge in H_2 gas.

4. The H_3^+ flow and a sample of the reacting gas flow are mixed in a low pressure chamber at the end of the flow tube and the reacted gas mixture is ionised *via* proton transfer.

5. A small fraction of the reacted and ionised flow is skimmed into a differentially pumped chamber. Ions, produced from proton transfer, are guided through this chamber *via* an electrostatic ion guide into the detection chamber.

6. Product ions are mass / charge filtered using a quadrupole and are passed to a channeltron electron multiplier detector.

7. Pulses from the channeltron resulting from ion impact are counted and recorded using custom developed software.

3.3 The Flow Tube

The prototype discharge flow tube designed for use in this work consists of a simple main Pyrex tube, 1 metre long and internal diameter 30 mm. The tube is fitted with two side arms and a centrally mounted sliding injector of outside diameter 10 mm. The sliding injector is coupled to the main flow tube *via* a large O-ring seal that allows movement to vary the injector position, whilst maintaining a vacuum tight seal for work at low pressures. Reagent and carrier gases are supplied to the tube *via* teflon tubing coupled to the Pyrex tube using compression fittings. The gases are dried using P_2O_5 traps before entering the flow tube. Gas flows are controlled by mass flow controllers (MFCs) of various flow capacities (1000 sccm (standard centimetres cubed per minute), 100 sccm, 50 sccm). The MFCs were calibrated by the supplier using the specific heat capacity of the respective gas passing through them. This calibration was checked by recording the time taken to sweep out a given volume of a burette over a series of flow rates. In this way, the expected flow rate was compared to the observed flow rate and hence actual flow rates and therefore experimental concentrations could be accurately calculated. An example calibration graph for the 100 sccm mass flow controller is shown in Figure 3.1.

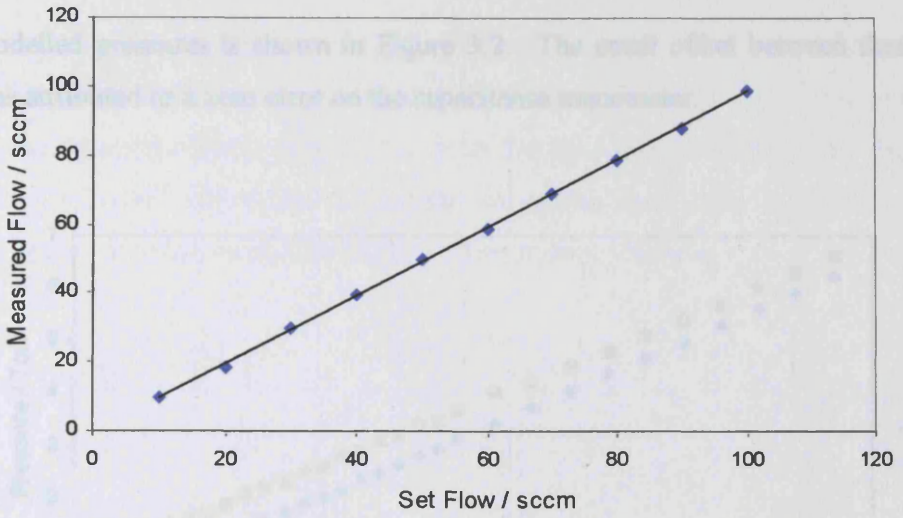

Figure 3.1: Calibration of 100 sccm mass flow controller.

To aid the design of the flow tube, a model that simulates the flow rates and kinetics in the tube was created. This was initially used to calculate pressure and flow rate regimes and hence ultimately the range of k that could be measured. As discussed in Chapter 2, experiments carried out in a flow tube must be under laminar flow conditions in order to be able to accurately determine the characteristics of the gas flow using the plug-flow approximation. This requires that the flow tube must be kept at low pressures, typically 2 - 10 Torr. To maintain these pressures, pumping was carried out with a rotary pump (16 m^3 hr^{-1}, Edwards) and the effective pumping speed was controlled by a large gas tap used as a throttle. To carry out kinetic experiments, linear flow velocities of typically hundreds of centimetres per second are required, and gases must be well diluted in the carrier flow. Thus, typically, total mass flow rates of thousands of sccm (standard centimetres cubed per minute) are required. Hence pumping of the tube must be able to maintain low pressures whilst these flows are in use. Simple numerical modelling of the gas flow characteristics under these conditions (assuming ideality and using $p\{dV/dt\} = \{dn/dt\}RT$) showed that the 16 m^3 hr^{-1} pump should be sufficient at these flow rates. Indeed, the pressure in the flow tube was measured at different flow rates using a capacitance manometer and was found to be in good agreement with this model. A plot of the measured and

modelled pressures is shown in Figure 3.2. The small offset between these curves was attributed to a zero error on the capacitance manometer.

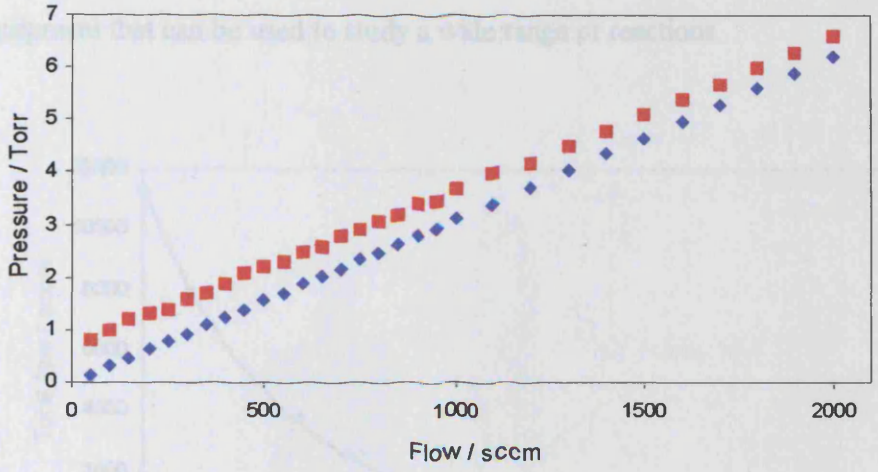

Figure 3.2: Plot of simulated (blue) and measured pressures (red) in the flow tube as a function of total flow rate.

Having characterised the pressure regime in the tube, simulation of a kinetic profile for a pseudo-first order reaction X + Y(excess) was carried out to ascertain the rate constant range that could, in principle, be determined. The criterion used to determine whether a rate coefficient could be measured was a simulated decay profile of minor species, X, spanning over three half lives along the total contact time afforded by the flow tube. The total contact time, and hence the extent of reaction that can occur in the tube can be controlled by changing the linear flow velocity of the gas through the tube, since time is equivalent to distance multiplied by velocity in the flow tube. Hence, for the maximum contact distance of 80 cm and a large rate coefficient, decreasing the flow velocity of the gas will increase the extent of reaction that occurs before the end of the flow tube is reached. In addition, if the flow rates of the reagents are fixed and the carrier flow is varied, this will have the added effect of changing the concentration of the excess reagent and will also change the extent of reaction that occurs. A plot of total flow rate required for three half lives of decay to be monitored *versus k* is shown below in Figure 3.3, where the X precursor gas flow

is 10 sccm (0.5 % of which is species X) and Y flow is 50 sccm and the pressure in the flow tube is 6 Torr. It can be seen that for a total flow of up to 10000 sccm, it is, in principle, possible to measure reactions that have rate coefficients of between 10^{-10} and 10^{-14} cm^3 $molecules^{-1}$ s^{-1} which makes the flow tube a versatile piece of equipment that can be used to study a wide range of reactions.

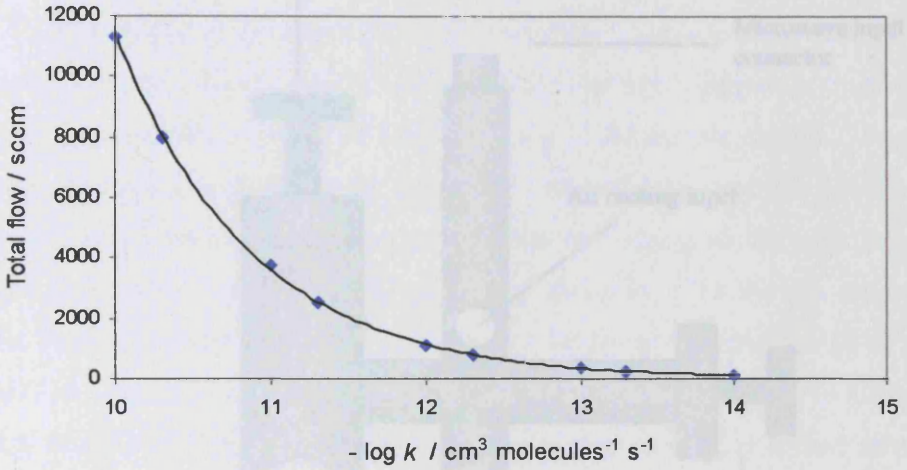

Figure 3.3: Plot showing required total flow rate for monitoring three half lives of a simulated decay profile as a function of rate coefficient (P = 6 Torr).

3.4 Generation of Reactive Species

For the study of reactive species (atoms and radicals) in the gas phase, their generation in the gas flow is achieved through microwave dissociation of suitable precursors producing atoms. Atoms that are produced in this way can then be used directly as a reactant or can undergo further reaction to produce radical species. For example, methyl radicals can be produced by microwave dissociation of Cl_2 in the presence of excess methane as described by:

$$Cl_2 \xrightarrow{\mu wave} 2Cl \qquad (3.1)$$

$$Cl + \underset{excess}{CH_4} \rightarrow HCl + CH_3 \qquad (3.2)$$

The microwave excitation used to dissociative gases provides a convenient, non invasive and non thermal excitation. The effectiveness of such radiation in exciting and dissociating the gas phase molecules depends on the coupling of the gas, as a reactive load, into the microwave cavity. This work uses an Evenson cavity[1] for this purpose, shown schematically in Figure 3.4.

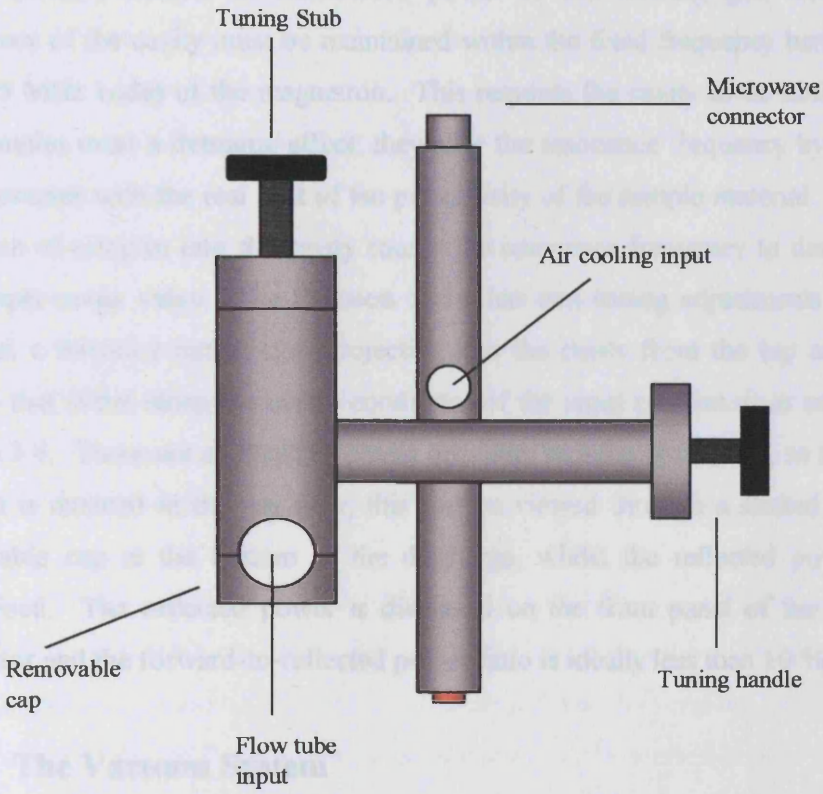

Figure 3.4: Schematic diagram of the Evenson cavity.

The Evenson cavity is a quarter-wave coaxial cavity that can excite discharges in flowing gases at pressures ranging from a few milli-Torr to several hundred Torr. The device is made from brass with a silver coating, which increases surface conductivity. The body of the cavity is 28 mm in diameter and 126 mm in length. The Evenson cavity is put around the side arm of the flow tube *via* a removable cap at the bottom of the cavity, which allows for it to be used with tubes up to 14 mm outer diameter. The cavity is air cooled to prevent overheating the flow tube.

Microwave radiation of frequency 2450 MHz is supplied to the cavity from a 0 - 300 W microwave generator using a 1m coaxial cable with N-type BNC connectors. The discharge in the flowing gas is initiated by a brief spark from a high frequency coil and, typically, microwave power of 30 W is used.

For maximum transfer of microwave power to the flowing gas, the resonance frequency of the cavity must be maintained within the fixed frequency band (typically 5 to 15 MHz wide) of the magnetron. This requires the cavity to be tuned since the gas samples exert a detuning effect: they alter the resonance frequency by an amount that increases with the real part of the permittivity of the sample material. In general, insertion of samples into the cavity causes the resonance frequency to decrease from the empty-cavity value. The Evenson cavity has two tuning adjustments to account for this, a threaded tuning stub projecting into the cavity from the top and a tuning handle that slides along the centre conductor of the input connector, as an be seen in Figure 3.4. These are adjusted to obtain optimum running conditions, so that a stable plasma is attained in the gas flow, this can be viewed through a slotted hole in the removable cap at the bottom of the discharge, whilst the reflected power is also minimised. The reflected power is displayed on the front panel of the microwave generator and the forward-to-reflected power ratio is ideally less than 10 %.

3.5 The Vacuum System

As discussed above, the flow tube operates at pressures in the region of 10 Torr. However, once the reacting gases have been ionised, it is necessary to ensure that ions travelling through the instrument do not suffer any collisions with other gas molecules that will cause them to be scattered, lose energy, react or fragment before they reach the detection point. This requires the mean free path of the ions at the pressure within the vacuum system to be long compared to the physical dimensions of the instrument chamber.

From kinetic theory of gases, the mean free path, l, of a gas at any pressure, p, is given by:

$$l = \frac{RT}{n\sqrt{2}\pi d^2 p} \tag{3.i}$$

where n is the number density of the gas particles, d is their diameter, R is the gas constant and T is the temperature. Thus for a given type of gas at a fixed temperature, and number density this relationship reduces to:

$$l = \frac{k}{p} \tag{3.ii}$$

where k is a constant which can be readily calculated. Given that the mean free path in any gas increases as the pressure is reduced, vacuum pressure of 10^{-6} Torr or less is required for unimpeded ion transport and detection.

Hence, two vastly different pressure regions are required in the CIMS system, 2- 10 Torr in the flow tube and 10^{-6} Torr in the detection region. This is achieved by coupling the flow tube to a differentially pumped vacuum system. The design and construction of the gas handling and pumping system is described in the next section.

3.5.1 Pumping Systems

Vacuum technology[2] categorises different vacuum pressures into one of four broad groups, as shown in Table 3.1.

Vacuum type	Pressure regime	Particles m^{-3} at 295K
Low	Atmosphere – 1 Torr	2.5×10^{25} - 3.2×10^{22}
Medium	1 Torr – 1×10^{-3} Torr	3.2×10^{22} - 3.2×10^{19}
High	1×10^{-3} Torr - 1×10^{-8} Torr	3.2×10^{19} - 3.2×10^{14}
Ultra-High	1×10^{-8} Torr - 1×10^{-11} Torr	3.2×10^{14} - 3.2×10^{11}

Table 3.1: Vacuum categories and their associated pressures.

Under high and ultra-high vacuum conditions, gas particles behave differently to low or medium pressure conditions. This change in behaviour occurs at around 1×10^{-3} Torr and can be explained in terms of the mean free path of the gas, (i). At pressures above 1×10^{-3} Torr, the number density of the gas is sufficiently high that the mean free path of the gas is short enough for many collisions to occur between the gas particles. The motion of the gas has fluid-like properties and is well described as viscous flow. Gas particles under these conditions can readily be pumped by a displacement pump such as a rotary pump.

Below 1×10^{-3} Torr, the number density of the gas particles is such that their mean free path becomes very large and the particles become more likely to have collisions with the walls of the chambers containing them than with each other. The gas is now said to be under molecular flow conditions. Gas particles under molecular flow conditions can no longer be pushed along by each other, as there is little interaction between them. Thus, in this case, a molecular drag pump such as a vapour diffusion pump or turbo-molecular pump is needed. A typical vapour diffusion pump operates using oil that has a vapour pressure of as low as 10^{-8} Torr at room temperature. This oil is contained in a reservoir at the base of the pump, where it is boiled during operation. The vapour from the oil passes up a chimney and strikes deflecting vanes that cause it to flow back down towards the reservoir. Gas particles become trapped in this vapour stream and are then compressed and delivered to the discharge outlet where they are pumped away by a rotary pump. The oil vapour recondenses on the water-cooled walls and returns to the reservoir. Several deflectors can be fitted to improve the pumping efficiency which maximises at low pressures. Indeed a

diffusion pump will not operate at pressures above 10^{-1} to 10^{-2} Torr due to back-streaming of the gas and so a backing pump must always be used in conjunction with the diffusion pump to bring the system down to this initial pressure.

3.5.2 Vacuum Chambers

The vacuum system consists of three stainless steel chambers sealed with conflat flanges, as shown in Figure 3.5.

The flow tube is coupled to the first of these chambers, referred to as the ionisation chamber, using a custom-built flange and O-ring seal. The discharge cell that produces H_3^+ ions is also coupled to this chamber through a side port. It is here that reacting gas from the flow tube is ionised. This chamber is pumped using a pair of rotary pumps with pumping speeds of $16 m^3 hr^{-1}$. Pressures are monitored in the ionisation chamber using a capacitance manometer.

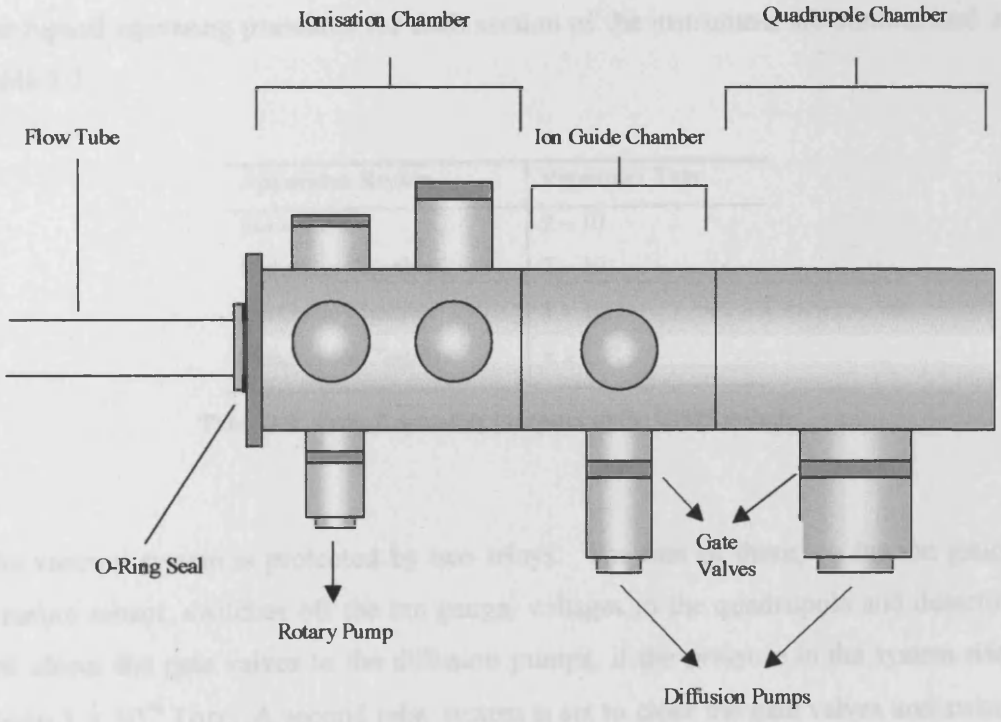

Figure 3.5: Schematic diagram of the vacuum system.

The second chamber houses the ion guide (described fully in Section 3.7) and is referred to as the ion guide chamber. The ionisation chamber and the ion guide chamber are linked *via* a small diameter skimmer, which forms the entrance of the ion guide. This means that only a small portion of the ionised gas from the flow tube is admitted into the ion guide chamber, which allows for a significant reduction in pressure. The ion guide chamber is differentially pumped, as it serves to connect the relatively high pressure region of the flow tube to the high vacuum conditions required in the final, detection, chamber. An 800 Ls^{-1} two-stage diffusion pump is used for this purpose.

The final chamber houses the quadrupole mass filter and the channeltron detector. Again, a small aperture links this to the ion guide chamber. As discussed above, the detection chamber is operated under high vacuum conditions, of the order of 10^{-6} Torr, and is pumped using a 300 Ls^{-1} two-stage diffusion pump. Pressures in both the ion guide and detection chambers are monitored using hot filament ion gauges.

The typical operating pressures for each section of the instrument are summarised in Table 3.2.

Apparatus Region	Pressure / Torr
Flow Tube	2 – 10
Ionisation Chamber	2 – 10
Ion Guide Chamber	1×10^{-4}
Quadrupole Chamber	8×10^{-6}

Table 3.2: Typical operating pressures in the CIMS system.

The vacuum system is protected by two relays. The first of these, on the ion gauge pressure sensor, switches off the ion gauge, voltages to the quadrupole and detector, and closes the gate valves to the diffusion pumps, if the pressure in the system rises above 1×10^{-4} Torr. A second relay system is set to close the gate valves and switch off the diffusion pumps if the backing pressure or temperature of the diffusion pumps

gets too high. When this second relay system is triggered, the first is also automatically activated.

3.6 Ionisation

The first stage of the mass spectrometer is the ionisation of the sample gas under study, which was carried out in this work using both electron impact and chemical ionisation as discussed in Chapter 2.

3.6.1 Electron Impact Ion Source

In the initial developmental stages of this work, an electron impact ion source was utilised to produce ions. This allowed initial testing of the quadrupole mass spectrometer and ion guide while the chemical ionisation source (discussed in Section 3.6.2) was developed.

A standard ionisation source was used, a schematic diagram of which is shown in Figure 3.6. This ionisation source was positioned in the ionisation chamber. The flow tube was not coupled to the vacuum system while this ion source was in use.

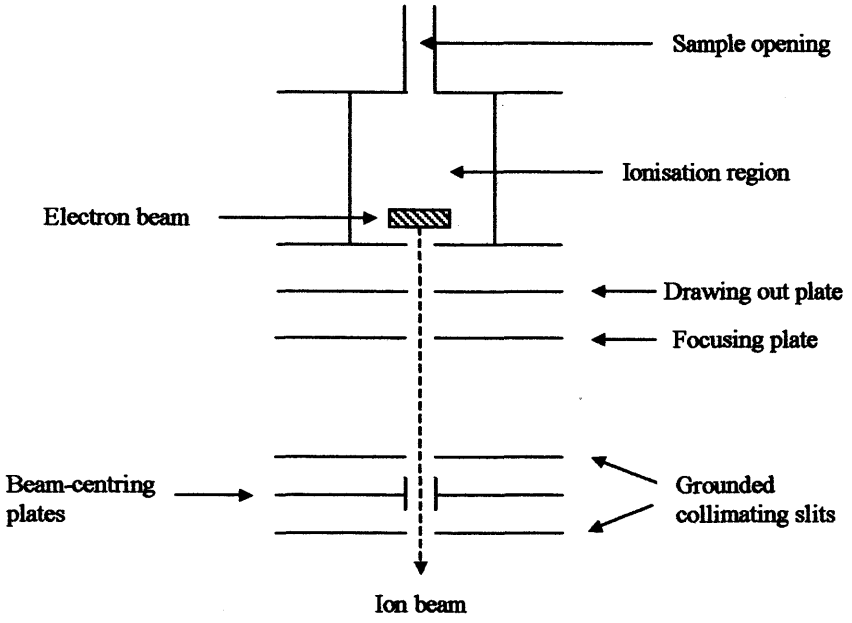

Figure 3.6: Schematic diagram of the electron impact ion source.

The sample, in the form of either gas or vapour from a condensed phase sample, passes through the opening to the ionisation chamber where it is bombarded by a beam of electrons, which are produced and accelerated from a hot filament. By varying the filament current, the energy of the electron beam can be varied from 0 – 100 eV to maximise the ionisation efficiency. For most singly charged ions the ionisation cross section maximises in the region of 70 – 90 eV.

The ions formed are urged downward by a drawing out field created by an electrode just outside the ionisation region. They are then focused and accelerated by a strong field that is created between the focusing plate and the grounded collimating slit. The beam is then centred and collimated by the final electrodes before entering the ion transport and analysing regions.

3.6.2 Chemical Ionisation

As discussed in Chapter 2, chemical ionisation provides in theory a much more specific and selective way of producing ions from individual components of the sample gas under study. In this work chemical ionisation from reactions of H_3^+ ions has been developed.

3.6.2.1 Corona Discharge Ionisation

A convenient way in which to produce ions in the gas phase at relatively high pressures (> 10 Torr) is by using a corona discharge. Such a discharge occurs due to ionisation of the gas surrounding an electrical conductor, when the potential on that conductor causes the voltage gradients around it to exceed a certain critical value, but not sufficient to cause complete electrical breakdown. This situation arises when the characteristic size of the electrode is much smaller than the interelectrode distance, such as a point to plane geometry. The mechanism of corona discharge also depends upon the polarity of the electrode surface.[3,4] In practice, a corona discharge is conveniently set up using a needle electrode near to an accompanying earthed plane. When hydrogen is passed through a corona discharge, ionisation occurs producing H_2^+ ions. These H_2^+ ions then undergo reaction with H_2 producing H_3^+. Several designs of the discharge used to produce H_3^+ ions were developed in the course of this work. These are described below.

3.6.2.2 Low Pressure H_2 Discharge

The initial design for the hydrogen discharge was based on a set up used in the work of Seeley *et al.*[5] which was employed to produce SF_6^- ions. This consists of a simple design of a steel needle held at a high electric potential and a grounded 6 mm stainless-steel tubular counter electrode. The body of the needle is electrically isolated from the steel tube using Pyrex tubing so that just the tip of the needle is exposed to the counter electrode, shown schematically in Figure 3.7. A 100 sccm flow of hydrogen was passed through the tube and a voltages of up to 1000 V applied

to the needle. It was found that if the entire outer tube was steel then the discharge would occur before the end of the needle, despite the Pyrex insulator. To overcome this problem, stainless steel was used only for the end 10 cm of the tube, which was inside the ionisation chamber, and glass tube was used for the rest.

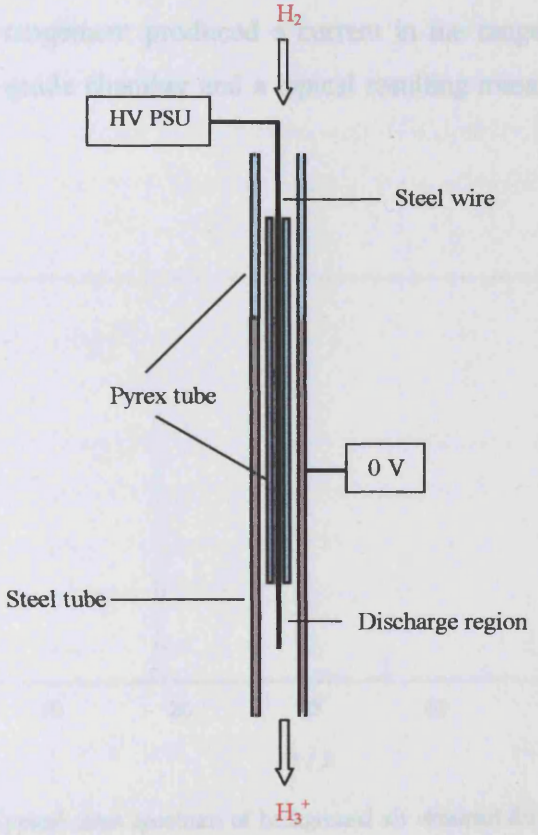

Figure 3.7: Schematic diagram of low pressure discharge.

This discharge cell was directed into the centre of the ionisation chamber, perpendicular to the flow of gas from the main flow tube. Hence, the flow of ions from the discharge streamed into the centre of the gas mixture exiting the flow tube, allowing good mixing of the ions and molecules, facilitating proton transfer.

Several variations on the above design were employed to ascertain the most stable arrangement for the discharge to occur. The length of wire exposed to the counter

electrode was varied and the distance from the end of the needle to the end of the counter electrode was varied. The stability of the discharge and the number of ions produced were examined by monitoring the current on the entrance to the ion guide chamber, held at –30 V. The optimal arrangement was found to be with 10 mm of the needle exposed to the counter electrode. If more than 10 mm of the needle was exposed to the counter electrode, this caused electrical breakdown and arcing in the discharge. This arrangement produced a current in the range of 7 – 8 μA on the entrance to the ion guide chamber and a typical resulting mass spectrum is shown in Figure 3.8.

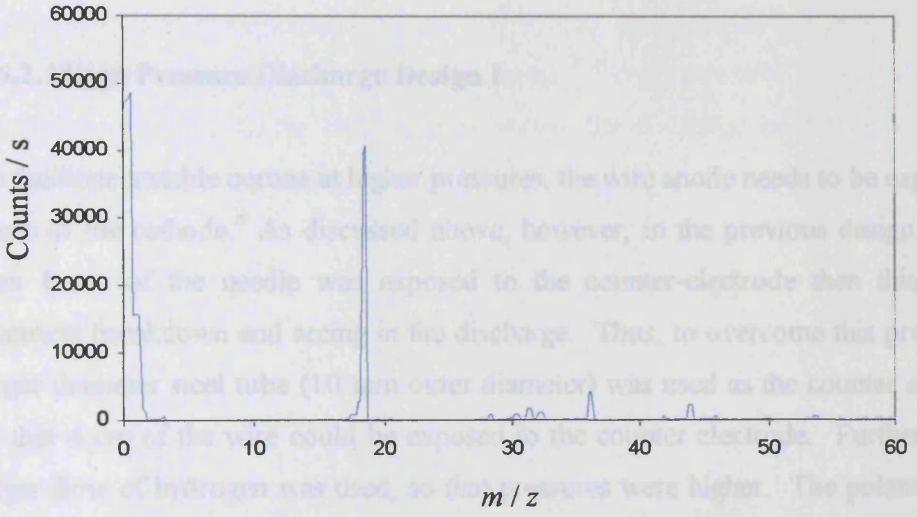

Figure 3.8: Typical mass spectrum of background air obtained from low pressure H_2 discharge.

The mass spectrum of the ions produced from the hydrogen discharge did not initially show a peak at $m/z = 3$ (possibly due to a leak in the hydrogen line), as would be expected for H_3^+ but did show peaks that are characteristic with proton transfer to components of the background air present, *i.e.* peaks at m/z 19, 29, and 45 attributed to H_3O^+, HN_2^+, and HCO_2^+ respectively. Significantly, no peaks were observed attributable to O_2^+ or HO_2^+. These species would be expected if background air drawn into the flow tube had been directly ionised, but because of the difference in

proton transfer affinities between H_2 and O_2, would not be expected to form from proton transfer reactions, as described in Section 2.6.1.3. Thus, this non-observation of peaks of O_2^+ or HO_2^+ provides (negative) evidence that the ionisation of the air in this initial mass spectrum did indeed result from H_3^+ reactions.

Whilst this initial design did prove successful in producing H_3^+ ions and in facilitating proton transfer, it was found that the discharge would only run reliably at pressures below 1 Torr, making it very limiting for the mixing in of ions to the discharge flow tube gases. Furthermore, this arrangement was found to be extremely sensitive to even tiny changes in the total pressure, and further modifications were therefore carried out.

3.6.2.3 High Pressure Discharge Design I

To facilitate a stable corona at higher pressures, the wire anode needs to be exposed to more of the cathode.[6] As discussed above, however, in the previous design if more than 1 cm of the needle was exposed to the counter-electrode then this caused electrical breakdown and arcing in the discharge. Thus, to overcome this problem, a larger diameter steel tube (10 mm outer diameter) was used as the counter electrode so that 4 cm of the wire could be exposed to the counter electrode. Furthermore, a larger flow of hydrogen was used, so that pressures were higher. The polarity of the voltage on the needle was also changed as it was thought that this may encourage a more stable discharge.[4] Using this arrangement, with negative voltages of up to 1000 V on the needle, and with a typical flow of 300 sccm hydrogen, produced a stable discharge, at pressures of 5 - 10 Torr in the ionisation chamber. Unfortunately, however, the current observed on the front plate of the ion guide was very small (1-2 nA), and represented too few ions to direct through the ion guide to the detector. A target, electrically biased at -30 V, was thus mounted directly opposite the discharge cell. The current observed on this target was in the range 3 – 4 μA. This, therefore, demonstrates that the discharge was producing ions but they were not reaching the entrance to the ionisation chamber. Given that the pressure and flow rate of the hydrogen was higher in this case, this was tentatively attributed to ions crossing the

ionisation chamber rapidly and being lost to the walls, rather than being drawn into the ion guide chamber.

To overcome this problem, a piece of Pyrex tubing was used to direct the ions towards the ion guide chamber. However, transport of ions along this tube reduced their number significantly, this was attributed to quenching of ions through collisions with the tubing walls. Therefore, in a further modification, a bend was put into the glass tube before the start of the discharge cell so that the flow of ions was directed straight towards the ion guide chamber. This produced a further problem in that instead of producing a discharge between the needle and the steel tube, a discharge was being generated between the needle and the entrance plate of the ion transport chamber. In this arrangement the entrance plate, at -30 V, was acting as the counter electrode to the needle generating a point to plane discharge.[7] To prevent this, a cap with a 2 mm aperture was added to the steel tube to contain the discharge inside the tube. This design is illustrated schematically in Figure 3.9.

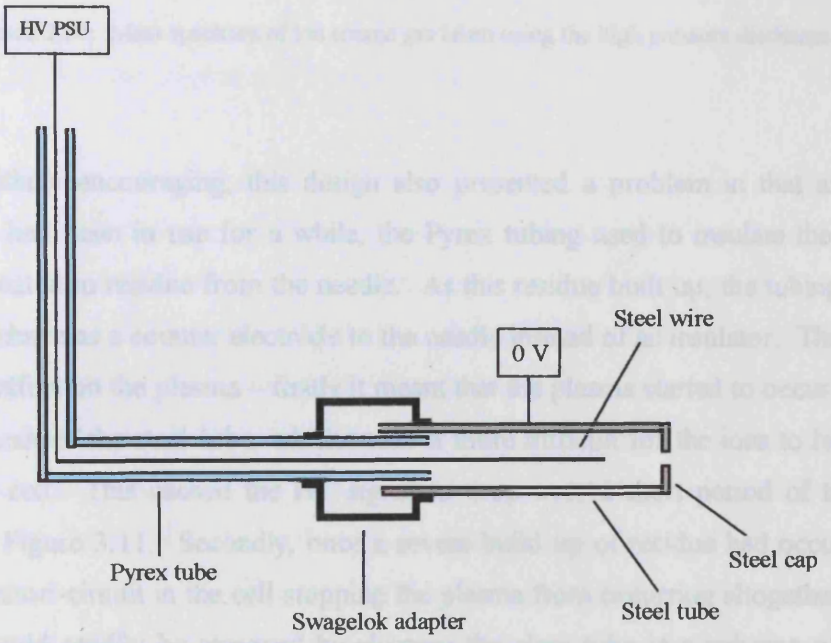

Figure 3.9: Schematic diagram of high pressure discharge design I.

This arrangement provided a stable plasma and generated 3 μA on the entrance plate. A mass spectrum of the background gas present in the ion source chamber taken using this design at a chamber pressure of 10 Torr is shown in Figure 3.10. This spectrum clearly shows the peak at $m/z = 3$, attributed to H_3^+.

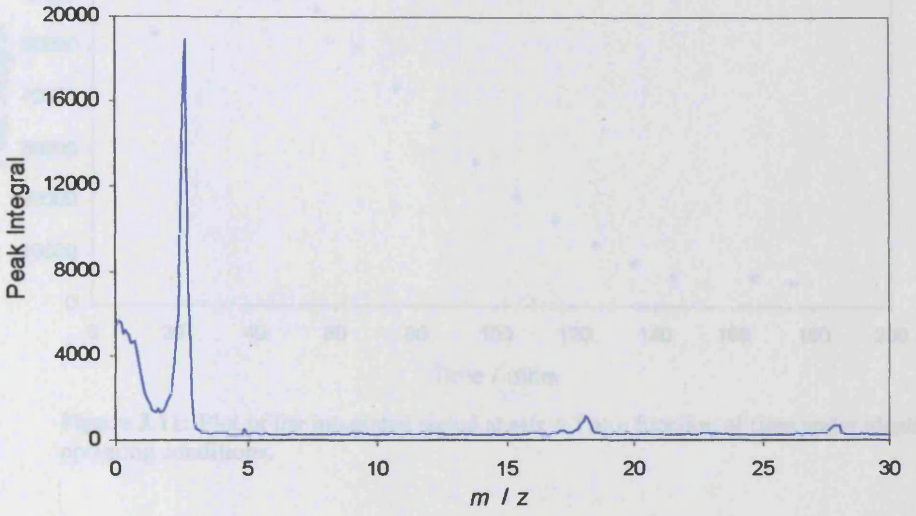

Figure 3.10: Mass spectrum of ion source gas taken using the high pressure discharge.

Whilst initially encouraging, this design also presented a problem in that after the discharge had been in use for a while, the Pyrex tubing used to insulate the needle became coated in residue from the needle. As this residue built up, the tubing began itself to behave as a counter electrode to the needle instead of an insulator. This had a two-fold effect on the plasma – firstly it meant that the plasma started to occur further from the exit of the steel tube, which made it more difficult for the ions to leave the discharge cell. This caused the H_3^+ signal to drop over a short period of time, as shown in Figure 3.11. Secondly, once a severe build up of residue had occurred, it caused a short-circuit in the cell stopping the plasma from occurring altogether. This residue could readily be removed by cleaning the glass tube in a solution of aqua-regia (HNO_3 / HCl mixture) but this had to be done frequently and involved venting

the chambers to atmosphere and hence did not constitute a practical solution. This led to a further design for the discharge cell described below.

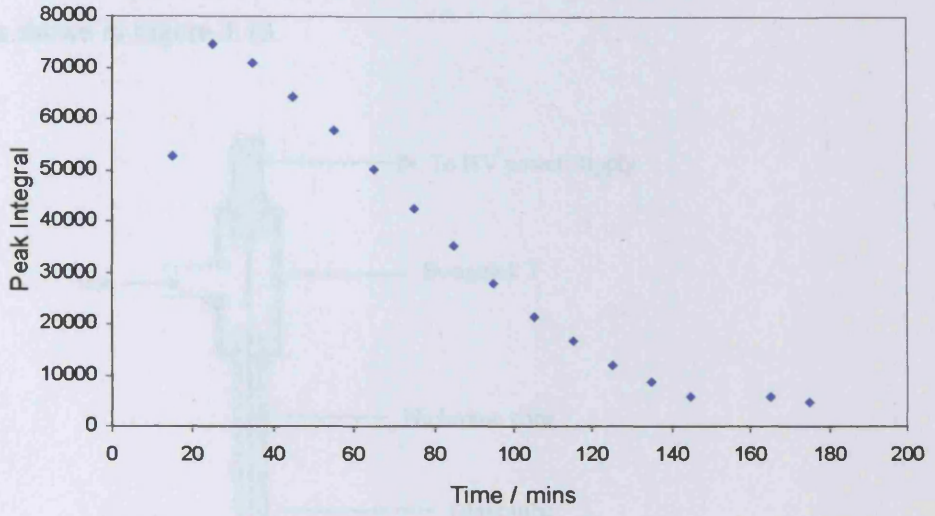

Figure 3.11: Plot of the integrated signal at $m/z = 3$ as a function of time under identical operating conditions.

3.6.2.4 High Pressure Hydrogen Discharge II

The final design for the hydrogen discharge cell used in this work is described here. As above, the discharge is created by flowing hydrogen gas over a needle held at high electrical potential relative to a target electrode. In this design, the discharge cell consists of a 1 mm diameter steel needle mounted in the centre of a stainless steel tube, 10 mm diameter and 4 cm length. The steel tube has a cap with a 2 mm hole in the centre through which the ions emerge. This is mounted onto a 6 mm glass tube *via* a metal to glass seal. A second, smaller glass tube (outer diameter 4 mm) is held in the centre of the 6 mm glass tube *via* an internal glass seal and extends to the beginning of the steel tube. This smaller glass tube is used to support the needle so that it lies in the centre of the steel tube. The needle (length 6 cm) is placed such that 3 cm of it is exposed to the grounded tube. This was found sufficient to keep the needle in the centre of the steel tube, thus preventing short-circuiting by the needle

coming into contact with the walls. Crucially, in this design, none of the glass insulator extended into the discharge region of the cell, thereby precluding problems from the gradual coating of the glass insulator during operation. A schematic diagram of this design is shown in Figure 3.12 and a photograph of the (dismantled) discharge is shown in Figure 3.13.

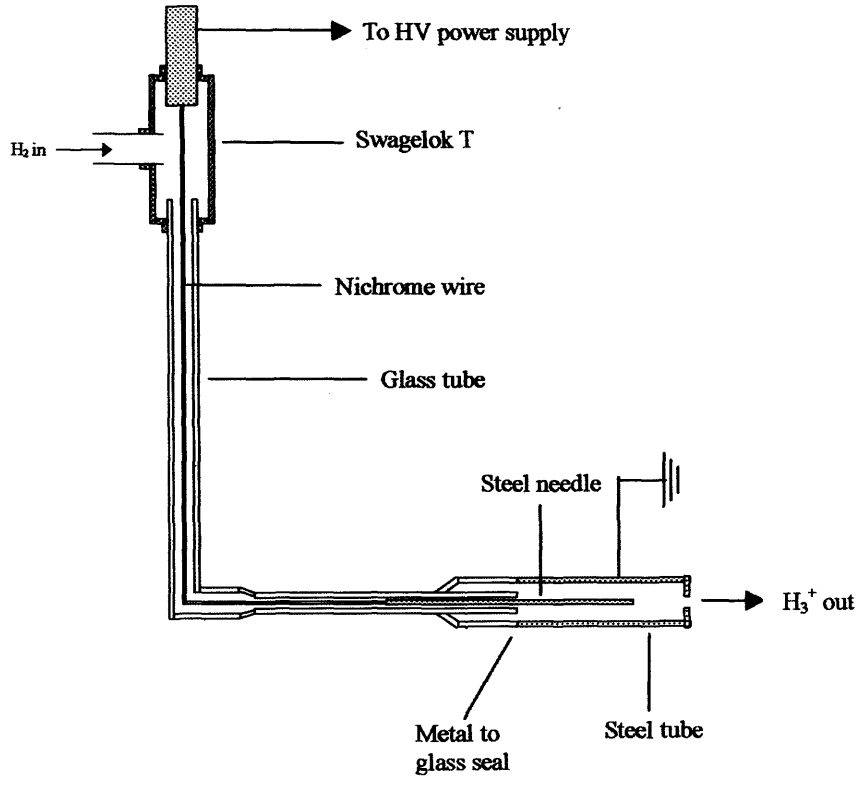

Figure 3.12: Schematic diagram of the high pressure discharge design II.

Figure 3.13: Photograph of the final design for the hydrogen discharge (dismantled).

The outer, 6 mm, glass tube carries the hydrogen from the gas manifold into the ionisation chamber *via* a high vacuum feedthrough and is positioned such that the steel discharge cell is in the centre of the ionisation chamber, 3 cm from the entrance to the ion guide chamber. A schematic diagram of the arrangement in the ion source chamber is shown in Figure 3.14.

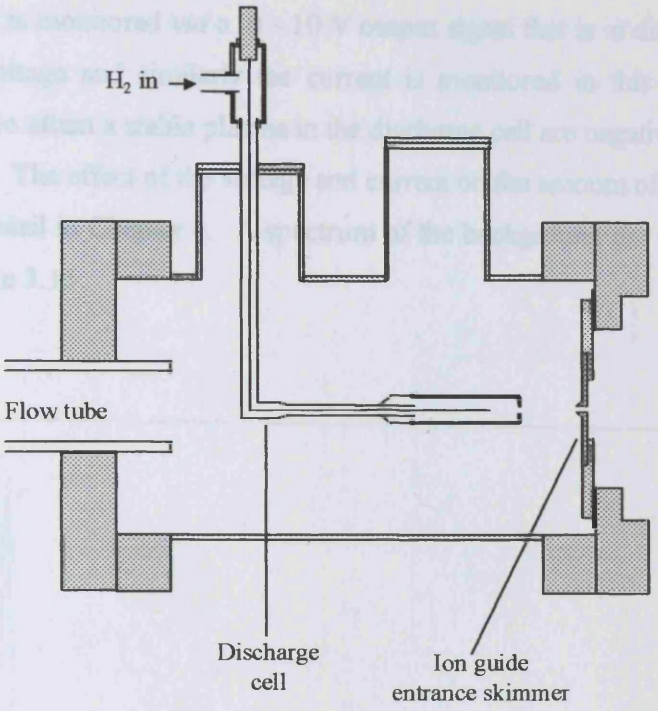

Figure 3.14: Schematic diagram illustrating the final arrangement in the ion source chamber.

Outside the chamber, the glass tube is connected to a t-piece compression fitting. One part of this t–piece connects to the gas line, allowing hydrogen to flow through and the other connects to a steel rod. The steel rod is connected to the power supply for the discharge. A nichrome wire (0.5 mm diameter) passed down the centre of the glass tube connects the steel rod on the outside of the chamber to the needle inside the chamber, thus carrying the high voltage required to produce the potential difference for the corona discharge. Thin nichrome wire is used for this purpose because it is suitably low resistance whilst flexible enough to be pushed round the bend in the glass tube.

The power for the corona discharge is provided by a high voltage power supply unit. This provides a maximum (negative) voltage of 1000 Volts and up to 75 mA current. The voltage is supplied to the discharge from this unit and the current is limited by use of a 10 KΩ potentiometer. The output voltage supplied from the unit to the

discharge needle is monitored *via* a 0 - 10 V output signal that is in direct proportion to the output voltage and similarly the current is monitored in this way. Typical conditions used to attain a stable plasma in the discharge cell are negative 600 - 650 V and 15 - 20 mA. The effect of the voltage and current on the amount of ions produced is discussed in detail in Chapter 4. A spectrum of the background gas in the chamber is shown in Figure 3.15.

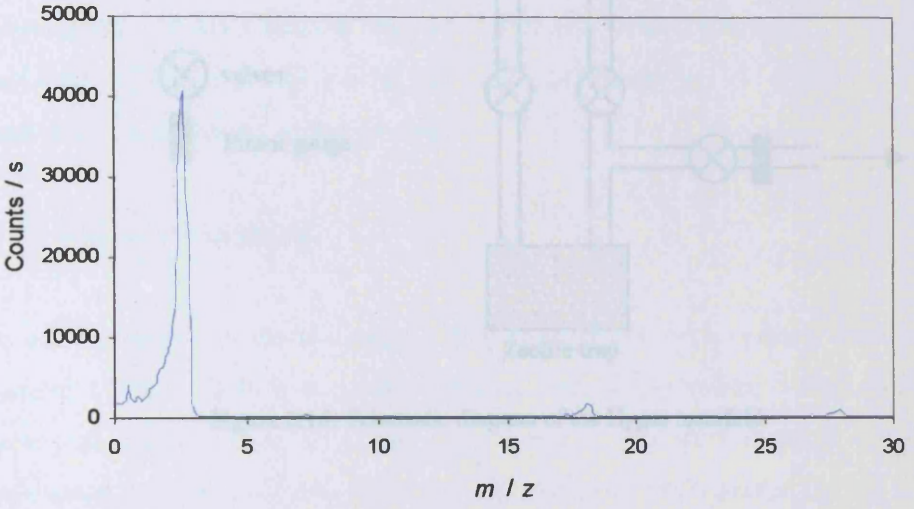

Figure 3.15: Mass spectrum of background gas in ion source chamber using high pressure discharge design II.

As discussed further in Chapter 4, this arrangement did produce a stable, reproducible source of H_3^+ ions, which could be used as a chemical ionisation source to detect neutral species of interest.

3.6.2.5. H_2 Gas Manifold

Molecular hydrogen (99.999% purity) is supplied to the discharge cell through a simple gas manifold, as shown in Figure 3.16. The hydrogen is passed from the cylinder through copper tubing into a zeolite trap, which is held at liquid nitrogen temperatures to remove any impurities from the gas. The flow of gas into the

discharge is controlled by a needle valve that is connected to the discharge cell with PTFE tubing. The flow of hydrogen allowed into the cell is monitored by measuring the pressure in the ion source chamber using a pirani gauge.

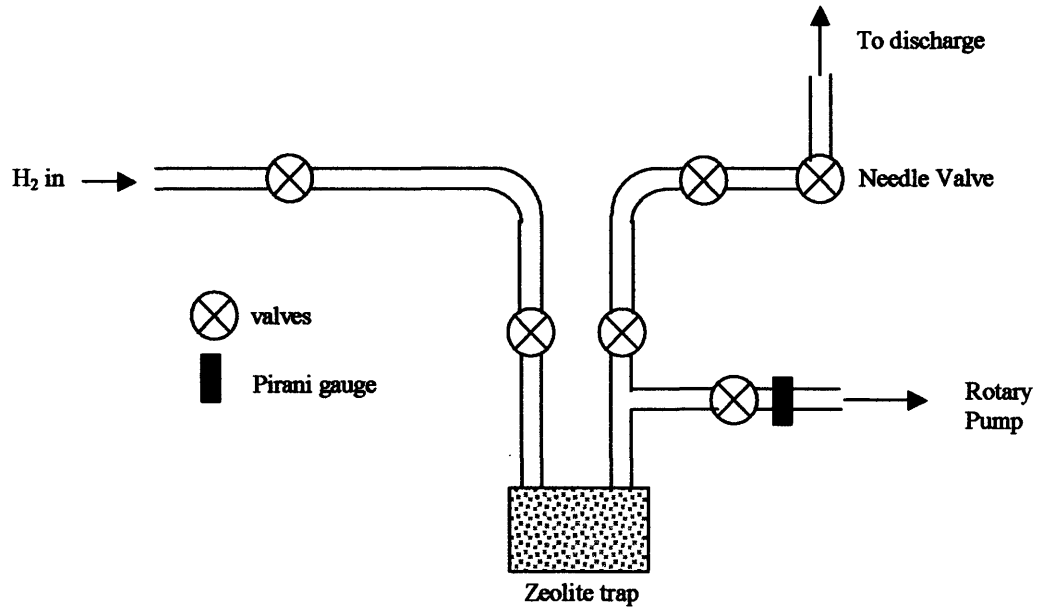

Figure 3.16: Schematic diagram of the H_2 gas manifold.

3.7 Ion Transport

Following ionisation of the gases from the flow tube, it is necessary to extract and transport ionic species from a relatively high pressure source (typically up to 10 Torr) into a mass analyser operating in a low pressure regime, typically of the order of 10^{-6} Torr. Since this necessarily leads to a reduction in number density, the efficient transmission of these ions into the analyser region is imperative to maintaining the high detection sensitivity of the apparatus. Several techniques have been developed for this purpose, for example employing electrostatic lenses and supersonic jet expansions to constrain ions in a beam focused along the central axis.[8] More recently, an electrostatic ion guide has been successfully used for this purpose. Ion guides have previously been used in many different applications. The electrostatic ion guide was first used to increase the mean free path of electrons in an orbitron ionisation

gauge.[9,10] In 1967, Oakey and MacFarlane described the principles of operation behind an electrostatic ion guide designed to transport charged products of nuclear decay over several metres from the reactor to the detector.[11] The electrostatic ion guide has long been a useful tool in time-of flight mass spectrometry[12-16] and more recently electrospray ionisation time-of-flight mass spectrometry. Zhang *et al.* have recently developed an electrostatic ion guide for use in chemical ionisation mass spectrometry.[17] Unlike previous studies mentioned above where the ion guide has been used exclusively as a transport device for charged particles the potential use of the ion guide for ion/molecule separation has also been explored.[18] The ion guide developed in this work is based the work of Zhang *et al.* and its design and construction is described in this section.

3.7.1 Design of ion guide

The basic principle of the ion guide is that an electric field is created between a wire mounted in the centre of a cylinder held at suitable potentials. This electric field causes ions to travel in a spiral motion round the wire through the cylinder, preferentially transmitting ions whilst neutral molecules are removed by pumping.

Ion trajectory simulations were performed for the experimental conditions with various parameters for the injected ions and the guide using SIMION.[19] The purpose of these simulations was to determine the array of voltages that provided the most efficient ion transmission. An example of such a simulation is shown in Figure 3.17.

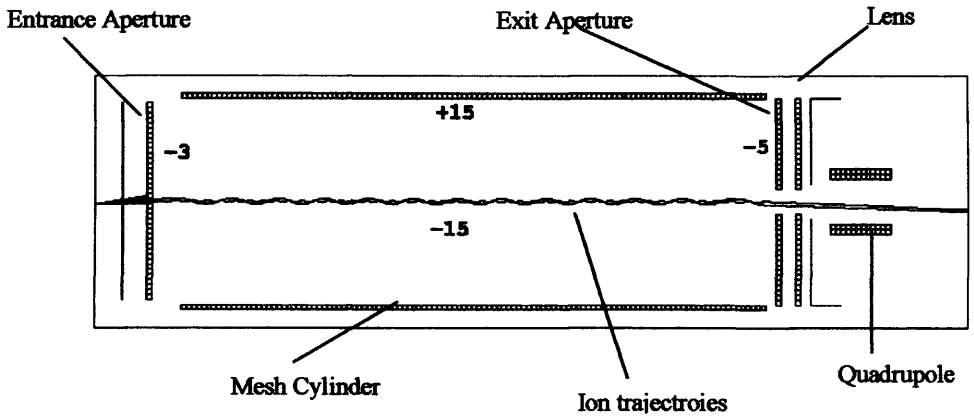

Figure 3.17: Theoretical ion trajectory simulation for an ion guide.

As can be seen from Figure 3.17 the SIMION calculations indicate that with appropriate potentials on each component of the ion guide, the ions can be transmitted through the differentially pumped chamber and into the quadrupole mass filter.

3.7.2 Construction of Ion Guide

The ion guide was designed to fit into the middle chamber of the vacuum system shown in Figure 3.5. The entrance aperture from the ionisation chamber, which forms the entrance to the ion guide, is a brass plate, 60 mm diameter, 2 mm thickness, with a small diameter nozzle. This was mounted onto a flange that linked the ion source and differential chambers, shown schematically in Figure 3.18. The nozzle of this entrance aperture was designed so that it could be changed easily without removing the ion guide from the flange. Several nozzles with diameters ranging from 0.5 mm to 2 mm were made and different diameter apertures were put in place and the pressure regime in the chambers optimised. The small opening allows only a fraction of the gases from the ionisation chamber to be drawn into the ion guide chamber. A cylindrical aluminium frame, (128 mm long, 38 mm outer diameter), was mounted on the other side of the conflat flange. This provided a frame on which copper wire was wound to make a cylindrical electrode, which was still sufficiently open to allow for removal of neutral species through pumping of the chamber. At the end of the

aluminium cylinder, brass plates with apertures of 4 mm were mounted, using ceramic spacers and nylon screws to keep them electrically isolated. These plates form the ion guide exit aperture and a lens to focus the ions into the centre of the quadrupole rods. The central wire (0.01 mm diameter nichrome) was mounted in the centre of the cylinder using kevlar thread. The ion guide is installed such that the central wire, all orifices of the ion guide and the entrance aperture into the quadrupole are on the same axis.

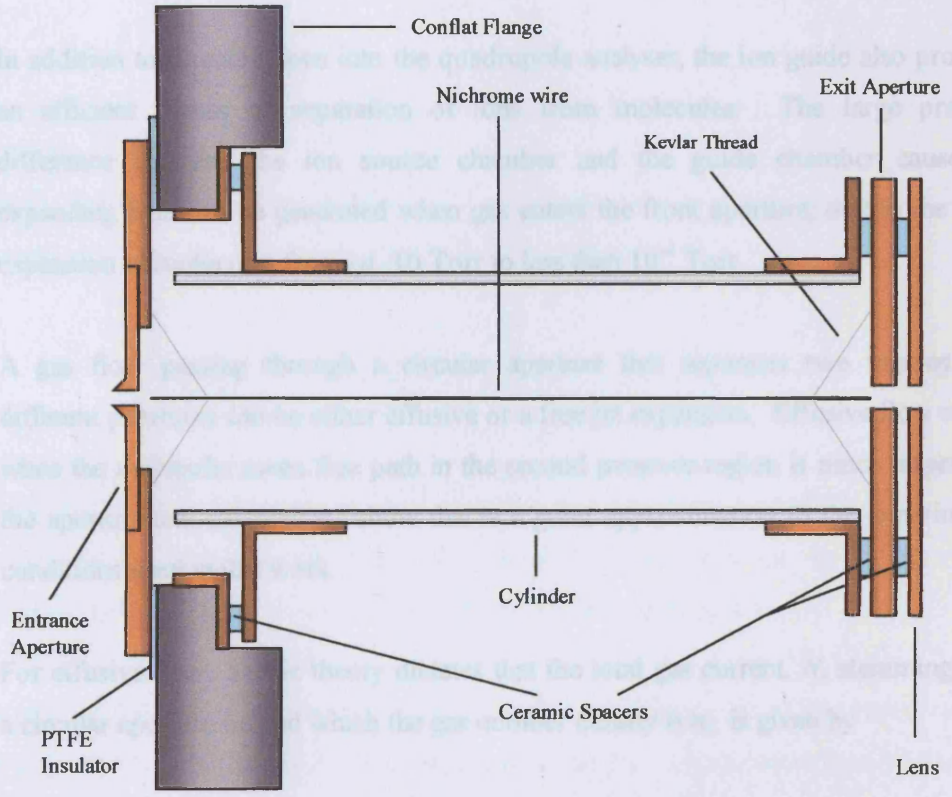

Figure 3.18: Schematic diagram of the electrostatic ion guide

A 30 V Power supply is used to supply the potentials for the ion guide; this gives two outputs: + 30 V and – 30 V with current 2 mA. These outputs are each split into four separate outputs *via* a distribution box. Each output from the distribution box is controlled by a 100 kΩ potentiometer which allows the output voltages to be varied from 0 to (±) 30 V. The required voltages are then applied to each component of the

ion guide *via* a ceramic feedthrough into the ionisation chamber. Using potentiometers to control the output voltage to the ion guide component provides an easy and efficient means of tuning the ion beam through the guide. The current generated from ions hitting the electrodes is monitored using a floating picoammeter. Thus the ion transmission through the ion guide can be monitored and maximised by varying the applied voltages.

3.7.3 Ion – Molecule Separation

In addition to directing ions into the quadrupole analyser, the ion guide also provides an efficient means of separation of ions from molecules. The large pressure difference between the ion source chamber and the guide chamber causes an expanding beam to be generated when gas enters the front aperture, due to the rapid expansion of molecules from *ca.* 10 Torr to less than 10^{-4} Torr.

A gas flow passing through a circular aperture that separates two regions with different pressures can be either effusive or a free jet expansion. Effusive flow occurs when the molecular mean free path in the second pressure region is much larger than the aperture and calculations show this is a good approximation to the experimental conditions used in this work.

For effusive flow, kinetic theory dictates that the total gas current, N, stemming from a circular aperture behind which the gas number density is n_s, is given by

$$N = \frac{n_s v \pi D^2}{16} \qquad \text{(3.iii)}$$

where the mean molecular thermal velocity $v = (8kT/\pi m)^{1/2}$, k is the Boltzmann constant, T is the temperature, m the molecular weight, and D the diameter of the aperture.

The molecular flux density, J, is related to the angle θ, measured between the direction normal to the plane of the aperture and the direction of observation, by:

$$J = \frac{N \cos\theta}{\pi L^2} \qquad \text{(3.iv)}$$

where L is the distance between the source and the point of detection of the molecules. Substituting for N in expression (iv) gives

$$J = \frac{n_s v D^2 \cos\theta}{16 L^2} \qquad \text{(3.v)}$$

With conservation of molecules, $J = nv$, hence the number density of beam molecules, n, at any observation point, L, is expressed by

$$n = \frac{n_s D^2 \cos\theta}{16 L^2} \qquad \text{(3.vi)}$$

Thus n maximises when $\cos\theta = 1$ or $\theta = 0$ *i.e.* the maximum concentration occurs on axis. In addition, expression (vi) illustrates that the molecular density decreases rapidly as the point of observation moves further from the source.

Using the laboratory conditions, where D = 1 mm, simulations of the kinetic theory explained above show that a decrease of molecular flux density more than two orders of magnitude is expected over the distance from the entrance to the exit end of the ion guide. This is illustrated in Figure 3.19.

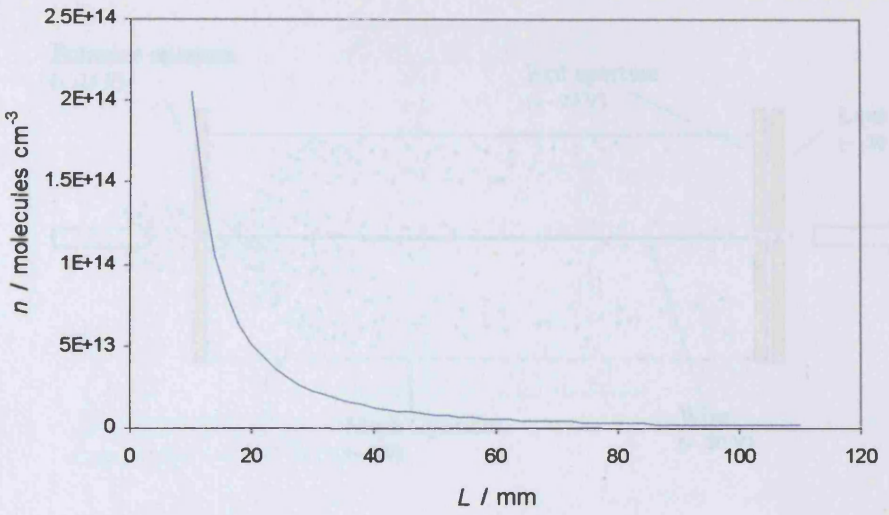

Figure 3.19: Number density of molecules, n, on axis of aperture vs. distance from aperture, L. Calculated using $D = 1$ mm and $\theta = 0$.

The generation of this expanding beam allows for efficient ion-molecule separation, as only neutral molecules will be removed in this way. Figure 3.20 illustrates that since the maximum concentration of species occurs on axis at the entrance of the ion guide, charged species are captured and transported through the ion guide while neutral species travel through the mesh cylinder and are removed by differential pumping.

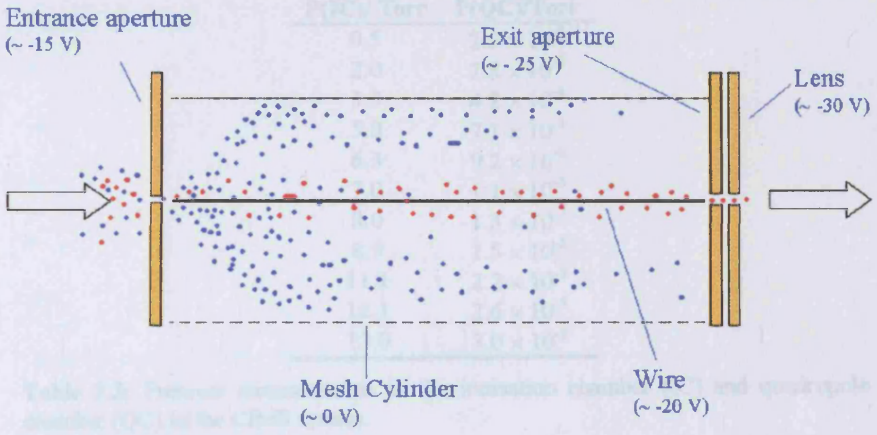

Figure 3.20: Schematic diagram of species flowing through the ion guide. Charged species (red) are transported through the guide while neutral molecules (blue) are removed.

3.7.4 Ion Guide Testing

Table 3.3 lists the pressures monitored in the ionisation chamber and the quadrupole chamber. Using a 1 mm diameter aperture at the entrance of the ion guide and a 5 mm aperture between the ion guide chamber and the quadrupole chamber, it can been seen that the system allows for efficient removal of neutral species. For example, increasing the pressure in the flow tube chamber by a factor of 25 leads to only a 10-fold increase in pressure in the quadrupole chamber. Hence, the system permits efficient removal of species as described in Section 3.7.3. With a smaller aperture between the chambers, the pumping efficiency would increase although this would be accompanied by a reduction in species and hence ions transferred to the detector.

P(IC)/ Torr	P(QC)/Torr
0.5	2.5×10^{-6}
2.0	2.8×10^{-6}
3.3	4.2×10^{-6}
5.0	7.1×10^{-6}
6.3	9.2×10^{-6}
7.0	1.1×10^{-5}
8.0	1.3×10^{-5}
8.9	1.5×10^{-5}
11.1	2.2×10^{-5}
12.1	2.6×10^{-5}
13.0	3.0×10^{-5}

Table 3.3: Pressure measurements in the ionisation chamber (IC) and quadrupole chamber (QC) in the CIMS system.

Initial experiments to test that the ion guide facilitated transmission of ions into the quadrupole were carried out using an electron impact ion source (described in Section 3.6.1) to produce ions. Perfluorotributylamine, $(CF_3(CF_2)_3)_3N$), which is commonly used as a calibrant in electron impact mass spectrometry, was used for this purpose. This calibrant is particularly useful since it shows an intense peak at $m/z = 69$ due to the CF_3^+ fragment. A small amount of perfluorotributylamine vapour was introduced to the ion source chamber *via* a needle valve and spectra were recorded over the *m/z* range 50 – 80. With voltages applied to the ion guide components a signal was observed at $m/z = 69$, which was maximised by varying the applied voltages from the values calculated in SIMION to give the maximum signal, shown in Figure 3.21. Peaks were not observed when the voltages to the ion guide were removed.

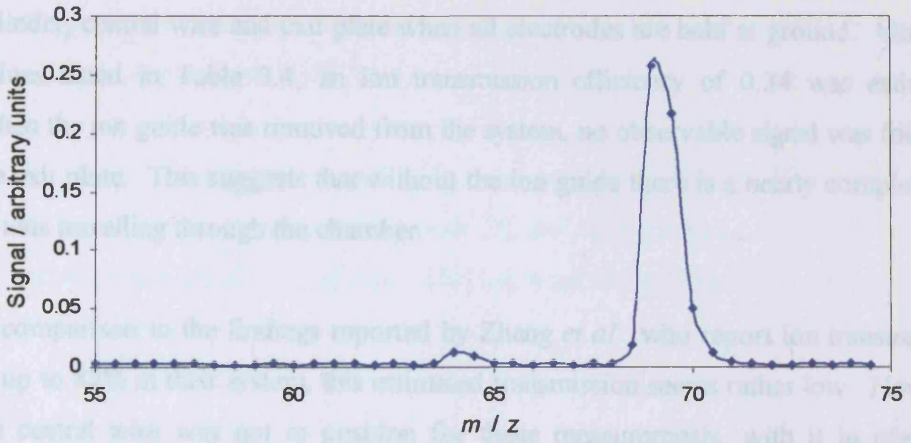

Figure 3.21: Mass spectrum of perfluorotributylamine.

In addition to maximising the mass spectrometric ion counts, measurements were also carried out to determine the ion transmission efficiency through the ion guide. Here, the ion current at each electrode in the ion guide was measured using a floating picoammeter. H_3^+ ions made by a corona discharge of H_2 gas, (described in Section 3.6.2), were used for these measurements.

Electrode	Current (nA)	Conditions
Front aperture	1.3×10^3	
Outer cylinder	12.2	$V_o = V_e = 0$
Exit Aperture	0.4	$V_o = V_e = 0$
	4.3	$V_o = -20$, $V_e = -30$

Table 3.4: Current measurements on ion guide electrodes. V_o and V_e are the voltages applied to the outer cylinder and the exit aperture respectively. The front aperture is held at –30 V.

It can be seen from these results that the ion current transmitted through the guide increases significantly when appropriate voltages are applied to the electrodes. The ion transmission efficiency was estimated from the ratio of the ion current at the exit of the ion guide to the total current entering the ion guide. The total current that enters the ion guide can be estimated by the sum of the currents measured on the outer

cylinder, central wire and exit plate when all electrodes are held at ground. Using the values listed in Table 3.4, an ion transmission efficiency of 0.34 was estimated. When the ion guide was removed from the system, no observable signal was found on the exit plate. This suggests that without the ion guide there is a nearly complete loss of ions travelling through the chamber.

In comparison to the findings reported by Zhang *et al.*, who report ion transmissions of up to 82% in their system, this estimated transmission seems rather low. However, the central wire was not in position for these measurements, with it in place the transmission efficiency is expected to rise markedly. By comparison, reported transmission efficiencies for using three equally spaced electrostatic lenses in place of the ion guide are in the order of 10 - 15%, hence, even without the central wire, the ion guide used in this system leads to a better transmission efficiency than a simple arrangement of lenses.

3.8 Mass Separating and Detecting Ions

Once ions have been separated from neutral molecules through the ion guide, the final stage in the mass spectrometer concerns their identification and detection. The process for doing this is described in this section. Briefly, a quadrupole analyser is used to filter ions of a specific mass, these then hit a channeltron electron multiplier, which generates an electric pulse for each impact. These pulses are then amplified and counted using a PC with custom developed software.

3.8.1 Quadrupole Analyser

The quadrupole filter, first introduced by Paul *et al.* in the late 1950s has become a very useful tool in mass spectrometry.[20,21] Quadrupole instruments offer a variety of advantages over other types of mass spectrometers. They are relatively simple to construct; the spectrometers do not require accurate magnetic fields, they have no

moving parts and are compact in size. Furthermore, quadrupoles can be operated to (relatively) high pressures (10^{-4} Torr).

For this work, a commercial quadrupole mass analyser was used. It consists of four parallel, equally spaced rods carrying both DC and RF potentials. This is mounted in the centre of the detection chamber. The ion beam is focused down the axis of this structure.

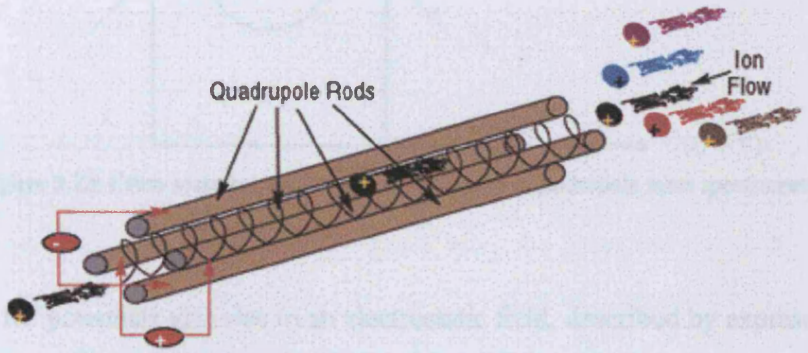

Figure 3.22: Schematic diagram of a quadrupole mass spectrometer.

For a particular set of RF and DC potentials, ions of a single mass/charge (*m/z*) ratio have a stable path, oscillating closely around the axis and striking the detector at the far end. Ions of different *m/z* ratios follow trajectories that do not strike the detector. Changing the DC and RF potentials changes the mass of the ions collected.

3.8.1.1 Underlying Principles

The governing principle of the quadrupole as described by Paul and Steinwedel[22] is based on an alternating electric charge applied to four hyperbolic electrodes in a square array, as illustrated in Figure 3.23. Practically, cylindrical rods are used as a good approximation to the hyperbolic field. A combination of radio frequency (RF) and DC potentials is applied to each set of diagonally opposed rods.

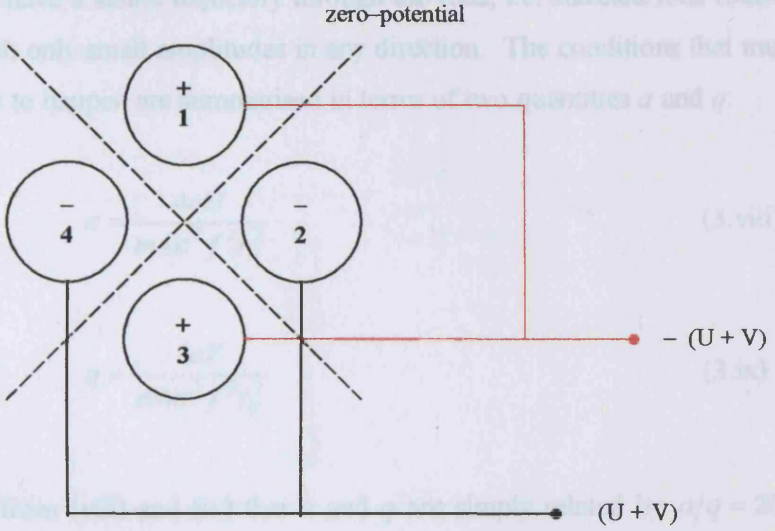

Figure 3.23: Cross sectional view through the rods of a quadrupole mass spectrometer.

The two RF potentials give rise to an electrostatic field, described by expression (vii), that gives bounded oscillations to an ion of the selected *m/z* ratio and unbounded oscillations to all ions of different *m/z* ratios.

$$\Phi = (U + V\cos\omega t)\frac{(x^2 - y^2)}{2r_0^2} \qquad (3.\text{vii})$$

where x and y are the co-ordinates of an ion in the field, $2r_0$ is the distance between the electrodes, U is the DC potential, V is the RF potential and ω is the angular frequency of the RF component.

The trajectory of an ion passing along the rods is complicated and can only be described in terms of complex differential equations, which are beyond the scope of this work. However, these equations show that the amplitudes of the motion of any ion away from the central path depends on the relative magnitudes of U and V and on the mass, m, of the ions. Ions of most masses follow trajectories of rapidly increasing amplitudes and are lost either by striking the rods or by passing through the spaces between them. It is possible, however, to choose values of U and V such that ions of a

particular mass have a stable trajectory through the rods, *i.e.* selected ions follow the path closely with only small amplitudes in any direction. The conditions that must be satisfied for this to happen are summarised in terms of two quantities a and q:

$$a = \frac{4eU}{m4\pi^2 f^2 r_0^2} \qquad \text{(3.viii)}$$

$$q = \frac{2eV}{m4\pi^2 f^2 r_0^2} \qquad \text{(3.ix)}$$

It can be seen from (viii) and (ix) that a and q are simply related by $a/q = 2U/V$. Furthermore, for fixed values of U and V, the frequency, f, bears a simple relationship to the mass, m, of the ion transmitted. Thus, masses transmitted can be controlled by varying f and in this way, mass selection can be obtained. Alternatively, U and V can be varied together at a fixed frequency to obtain mass selection.

3.8.2 Electron Multiplier

The ion detector is a single channel electron multiplier (CEM) mounted off-axis behind the quadrupole. This consists of a small curved tube, inner diameter 1 mm, outer diameter 4 mm and length 22 mm made from lead silicate glass. A potential difference is created through the tube by applying a voltage of (-1700) – (-2000) V to the front of the multiplier, while the back is held at ground. Voltages are supplied by a negative high voltage power supply.

The inside wall of the electron multiplier has a high surface resistance. When a potential is applied between the ends of the tube, the resistive surface becomes a continuous dynode. Thus, an ion striking the input face of the device produces 2-3 secondary electrons that are accelerated down the channel by the positive bias. These electrons hit the channel walls, producing additional secondary electrons. This process continues until, at the output end, a pulse of up to $10^7 - 10^8$ electrons emerges,

shown schematically in Figure 3.24. The ratio of the output current to the input current is defined as the *gain* of the electron multiplier.

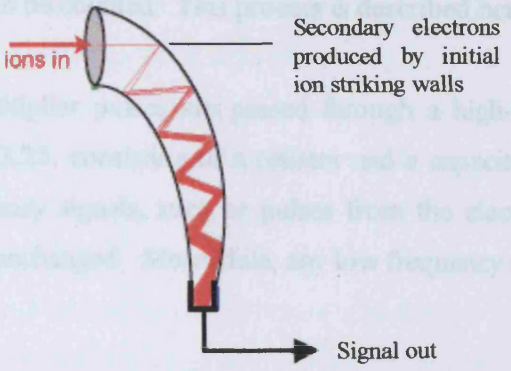

Figure 3.24: Schematic diagram showing signal accumulation in an electron multiplier.

Electron multipliers can operate in two modes: analog or pulse counting. The primary difference between these two modes is that pulse counting CEMs produce output pulses with a characteristic amplitude whereas analog CEMs have a very wide distribution of output pulse amplitudes. This is because pulse counting CEMs operate in space charge saturation. This occurs when the total amount of charge in the electron cloud in a CEM reaches 10^9 electrons and the gain cannot increase any further. At this point, the space-charge repels the emitted secondary electrons so that they strike the wall before acquiring sufficient energy from the field to make useful multiplying collisions. Thus, the multiplier has a narrow pulse-height distribution. In this mode the multiplier is analogous to a Geiger counter, in that a pulse of given amplitude is produced irrespective of the manner of its excitation.

A pulse counting electron multiplier was used in this work. This was chosen because the high, saturated gain allows a discriminator level to be set that will reject low-level noise while passing all the signal pulses. This results in very good signal-noise performance.

3.8.3 Signal Processing

The electron pulses that come from the electron multiplier must be amplified and smoothed before they can be counted. This process is described here.

Firstly, the electron multiplier pulses are passed through a high-pass filter, shown schematically in Figure 3.25, consisting of a resistor and a capacitor. The high pass filter allows high frequency signals, such as pulses from the electron multiplier, to pass through the circuit unchanged. Meanwhile, any low frequency noise is blocked.

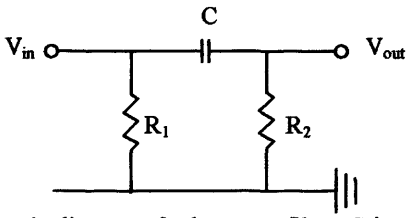

Figure 3.25: Schematic diagram of a low pass filter. C is a capacitor (710 PF, 4kV) and R_1 and R_2 are resistors, (51 K and 390 K respectively)

A fast preamplifier and a fast amplifier are used to boost the intensity of the signal. From the amplifier, the signal is passed to a constant fraction discriminator (CFD). The CFD discriminates noise from signals according to the threshold level, which is set manually. Typically, the threshold level is set to 500 mV. The CFD produces an output transistor-transistor logic (TTL) pulse for each input pulse from the amplifier that is above the threshold level. The TTL pulses are counted using a PC as described in the next section.

3.8.4 Event Counting

A 16 bit data acquisition (DAQ) card in a PC is used to control the mass range swept by the quadrupole and to count the signal pulses in order to obtain a mass spectrum. A computer programme developed in the course of this work is used to control the DAQ card and to gather data.

The DAQ card has two analogue output channels that give outputs of -10 to +10 volts. One of these channels is connected to the quadrupole electronics module and is used to sweep the masses filtered through the quadrupole. An output of negative 0.1 V corresponds to ions of $m/z = 10$ to travel through the quadrupole. A 16 bit DAQ card was used as this allowed the mass to be swept in steps of as small as $m/z = 0.03$. The DAQ card is also equipped with a counting input, which is used to count the TTL pulses from the CFD.

Typically, a mass spectrum is recorded by sweeping the desired m/z range in steps of $m/z = 0.1$ and recording the number of pulses counted by the DAQ card over a period of 1 second at each point. These data are then plotted in the form of a mass spectrum.

3.9 Summary

This chapter has described the full design and construction of the discharge-flow chemical ionisation apparatus that has taken place in the course of this work. A schematic diagram of the full apparatus is shown in Figure 3.26 and photographs of the apparatus in the laboratory are shown in Figures 3.27 and 3.28. The characterisation of the H_3^+ ionisation source is described in the following chapter.

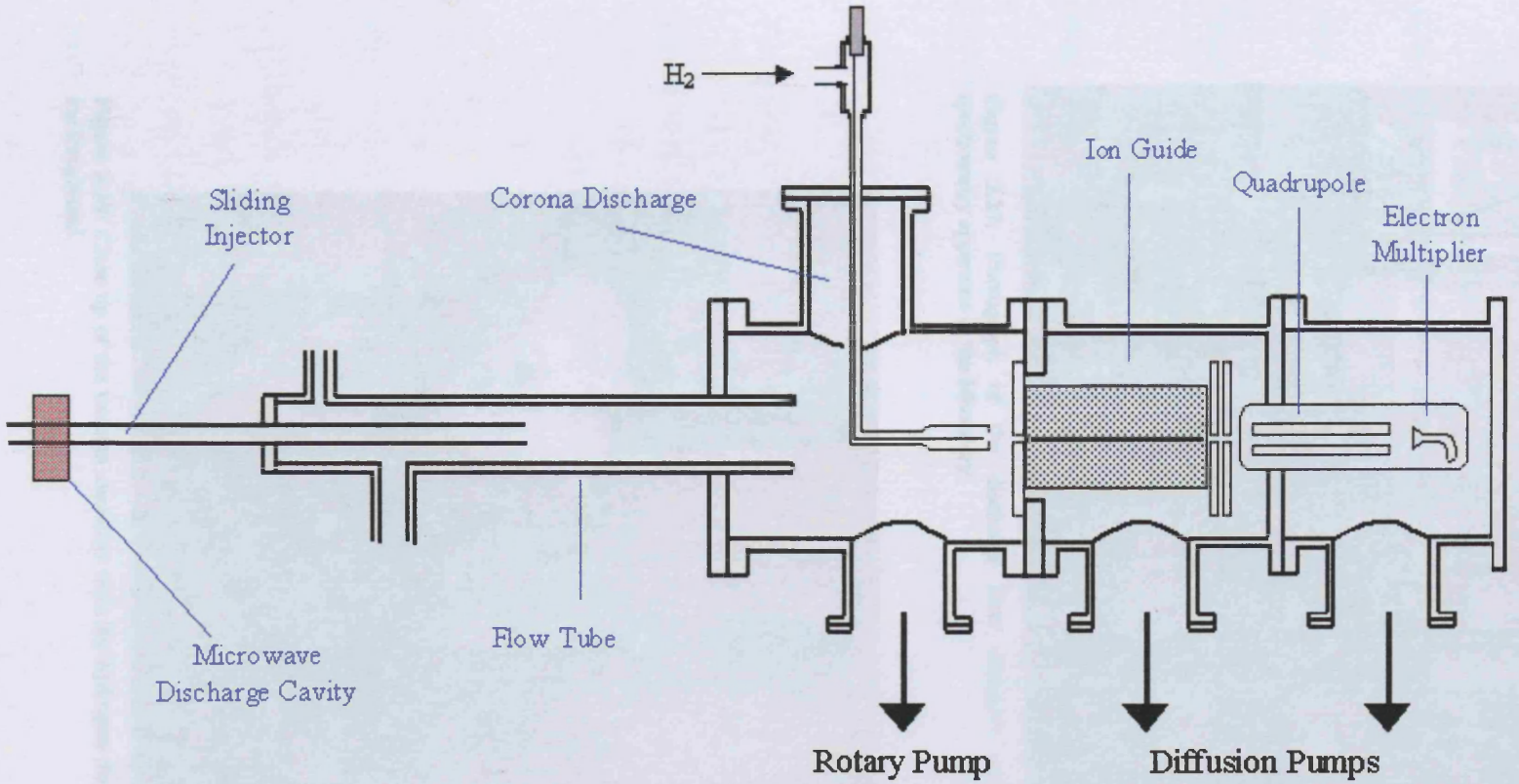

Figure 3.26: Schematic diagram of the discharge flow chemical ionisation mass spectrometer apparatus

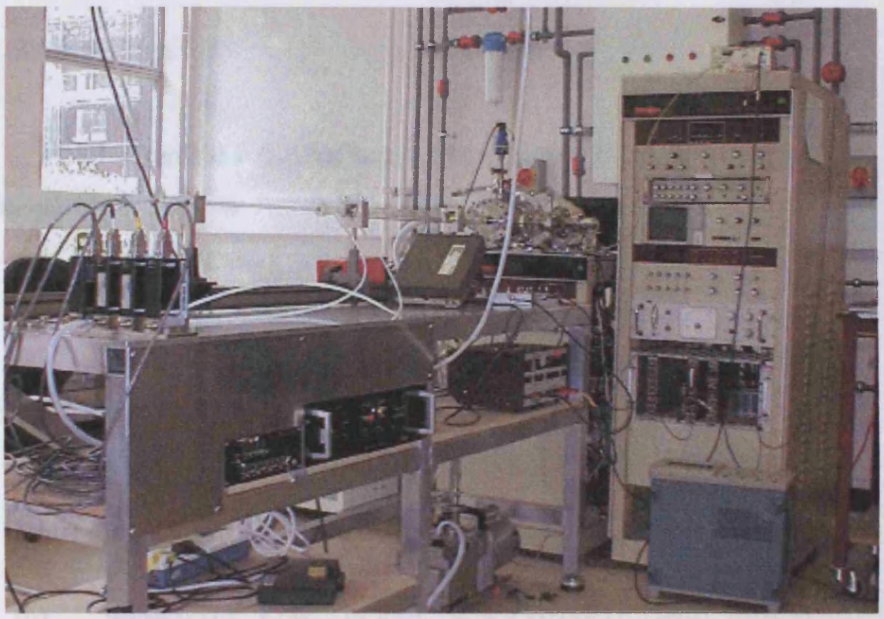

Figure 3.27: Photograph of the discharge flow chemical ionisation mass spectrometry apparatus in the laboratory.

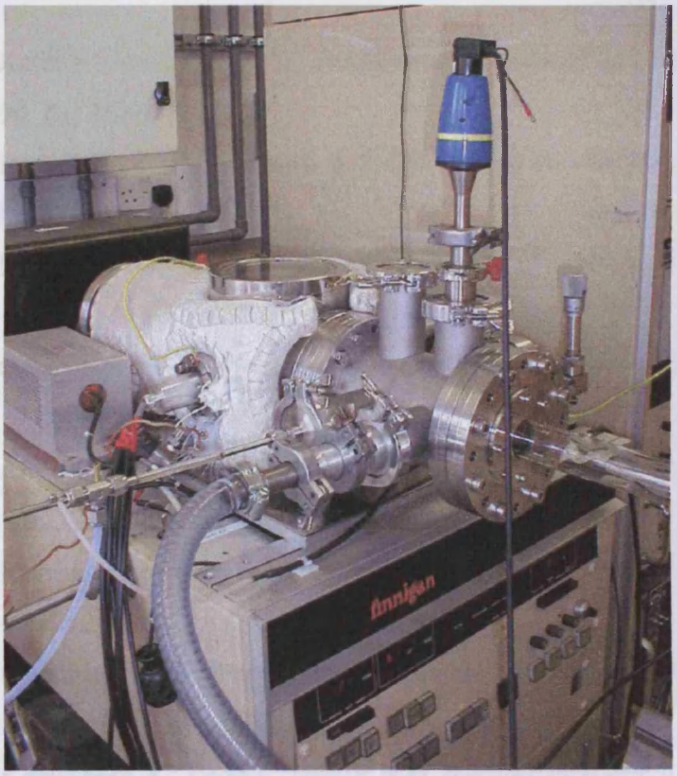

Figure 3.28: Close up of the vacuum chambers with the hydrogen discharge cell in the foreground.

3.10 References

(1) Fehsenfeld F.C; Evenson K.M.; Broida H.P. *Review of Scientific Instruments* **1965**, *36*, 294.

(2) Chambers A.; Fitch R.K.; Halliday B.S *Basic Vacuum Technology*, 1991.

(3) Meek M.D.; Craggs J.D. *Electrical Breakdown of Gases*; Wiley: Chichester, 1978.

(4) Raizer Y.P. *Gas Discharge Physics*; Springer: Berlin, 1991.

(5) Seeley, J. V.; Jayne, J. T.; Molina, M. J. *Journal of Physical Chemistry* **1996**, *100*, 4019.

(6) Weston G.F. *Cold Cathode Glow Discharge Tubes*; Iliffe & sons Ltd: London, 1968.

(7) Tabrizchi M.; Khayamian T.; Taj N. *Review of Scientific Instruments* **2000**, *71*, 2321.

(8) Kofel S.; Anderson M.A.; Smalley R.E. *Review of Scientific Instruments* **1990**, *61*, 3686.

(9) Herb R.G.; Pauly T.; Fisher K.J. *Bulletins of the American Physical Society* **1963**, *8*, 336.

(10) Mourad W.G.; Pauly T.; Herb R.G. *Review of Scientific Instruments* **1964**, *35*, 661.

(11) Oakey N.S.; Macfarlene R.D. *Nuclear Instrument and Methods* **1967**, *49*, 220.

(12) Abbe J.C.; Amiel S.; Macfarlene R.D. *Nuclear Instrument and Methods* **1972**, *102*, 73.

(13) Igersheim R.; Abbe J.C.; Paulus A.M.; Amiel S. *Nuclear Instrument and Methods* **1973**, *109*, 301.

(14) Macfarlene R.D.; Torgerson D.F. *International Journal of Mass Spectrometry and Ion Processes* **1976**, *21*, 81.

(15) Kenigsberg A.; Leon J.; Shafrir N.H. *Nuclear Instrument and Methods* **1978**, *148*, 605.

(16) Geno P.W.; Macfarlene R.D. *International Journal of Mass Spectrometry and Ion Processes* **1986**, *74*, 43.

(17) Zhang R.; Molina L.T.; Molina M.J. *Review of Scientific Instruments* **1998**, *69*, 4002.

(18) Zhang R.; Wenfang L.; Molina L.T.; Molina M.J. *International Journal of Mass Spectrometry* **2000**, *194*, 41.

(19) Dahl D.A. SIMION 3D Version 6.0; Idaho National Engineering Laboratory, 1995.

(20) Paul W.; Reinhard H.P.; von Zahn U. *Zeitschrift für Physik* **1958**, *152*, 143.

(21) Dawson P.H.; Whetten N.R. *Advances in Electronics and Electron Physics* **1969**, *27*, 60.

(22) Paul W.; Steinwedel H. *Zeitschrift für Naturforschung* **1953**, *8a*, 448.

Chapter 4 Chemical Ionisation Mass Spectrometer Development: Testing

4.1 Introduction

This chapter presents the first chemical results obtained from the CIMS experiment following design and construction of the equipment as described in the previous chapter. The aim of these initial experiments was to demonstrate that the equipment is suitable for generating H_3^+ ions, carrying out proton transfer and therefore detecting small concentrations of gas phase species. Measurements of detection efficiencies of NO_2 and O_3 are presented.

4.2 H_3^+ Ion Source

The H_3^+ ion source was constructed and attached to the ionisation chamber as discussed in Chapter 3. As discussed previously, the discharge cell consists of a stainless steel tube, through which a flow of H_2 is passed, with a steel needle mounted along the central axis of this tube. A large potential difference is created between needle and the tube by applying a negative voltage to the needle while holding the tube at ground. This potential difference creates a plasma (a corona discharge) in the hydrogen gas which leads to ionisation to H_2^+. These H_2^+ ions then undergo rapid reaction with unionised H_2 producing H_3^+ ions:

$$H_2^+ + H_2 \rightarrow H_3^+ + H \qquad (4.1)$$

The ionisation source was first investigated by monitoring the electrical current passing through the needle. Typically, a hydrogen flow rate of 300 sccm was passed through the source. These measurements showed that as the negative potential of the needle was increased, typically to a value near –500 V, a current of the order of a few μA was observed on the electrode that provided the entrance to the ion guide

chamber. The cut-off between the condition of current and no current was sharp, indicative of the onset and quenching of a discharge. Typically, the voltage cut-off from current flowing to current not flowing (*i.e.* the cut off observed when lowering the magnitude of the applied potential) occurred at a smaller (negative) potential than the cut-off observed when increasing the magnitude of the potential. Again, this is consistent with a gas discharge being struck and quenched, since the voltage required to sustain a pre-running discharge is typically lower than that required to initiate a discharge in flowing neutral gas.[1]

Further evidence for the operation of a corona discharge in the flowing hydrogen gas was obtained by investigating the current as a function of applied voltage. For low current, self sustaining discharges, such as corona discharges, Townsend's formula[2] relates the discharge current, I, to the applied voltage, V and to the excess voltage over the ignition potential, V_0, according to:

$$I \propto V(V - V_0) \qquad (4.i)$$

A plot of I / V versus V from the current and voltage measurements made in this work is shown in Figure 4.1, below. As can be seen, for (negative) voltages up to 620 V, the Townsend plot shows excellent linearity indicative of a stable corona discharge. Above these applied voltages a degree of deviation from linearity was observed, and the current fluctuations became significant. As discussed below, at high applied voltages, other evidence for an inefficient and unstable discharge was also observed.

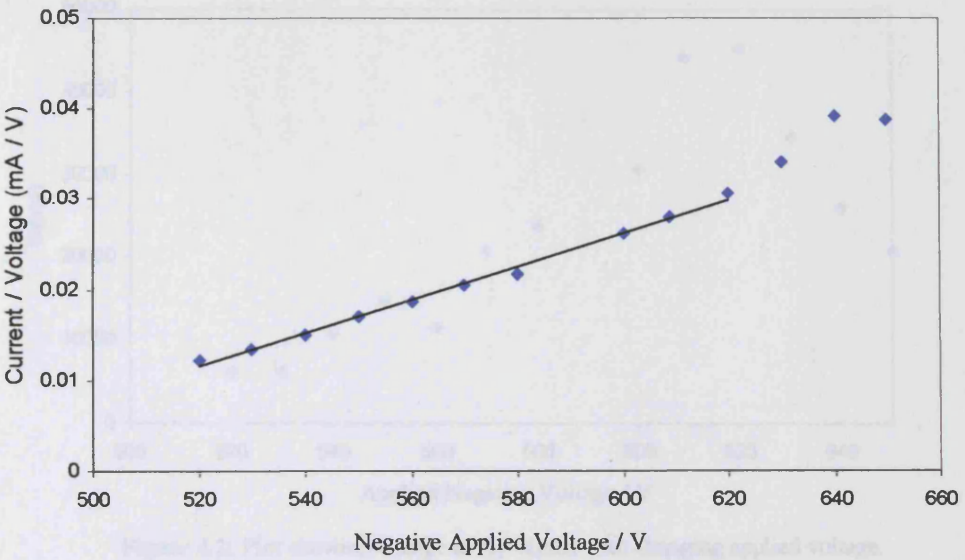

Figure 4.1: Plot of observed I / V *versus* applied negative needle voltage.

The clearest evidence for the successful operation of a discharge ionising H_2 and producing H_3^+ through reaction (1) was provided by the significant signal observed in the mass spectra at $m/z = 3$. This signal was not present in the absence of an applied potential on the corona discharge, and the magnitude of this signal when voltage was applied, was used to optimise discharge conditions. The voltage (and therefore current) applied to the discharge needle was adjusted to provide a stable discharge environment with maximum signal. Figure 4.2 shows the effect of changing the applied voltage to the discharge on the integrated H_3^+ signal at $m/z = 3$.

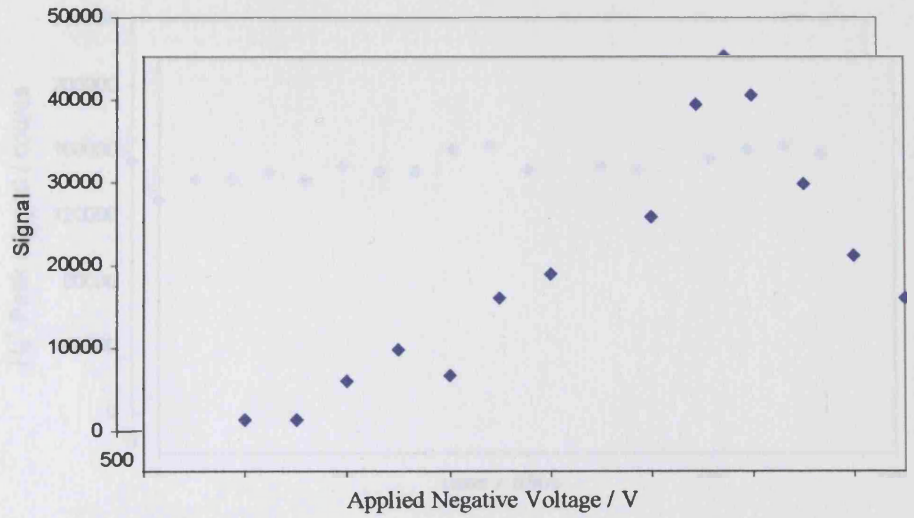

Figure 4.2: Plot showing change in H_3^+ signal with changing applied voltage.

As discussed above, an applied negative voltage of 500 V was required to ignite the plasma and increasing the magnitude of this voltage produced more ions as shown in Figure 4.2. This trend continues until the negative applied voltage exceeds 620 V when the recorded signal at $m/z = 3$ starts decreasing. This decrease in the ion signal at $m/z = 3$, attributed to H_3^+, was accompanied by a reduction in stability of the discharge (as evidenced by significant fluctuations in the current flowing through the discharge) and presumably therefore, a decrease in the degree of ionisation. Therefore the optimum voltage to run the discharge at was chosen to be 620 V.

The stability of the discharge with time was investigated, since it is important to have a consistent number of ions produced over the course of an experiment. A plot of the H_3^+ peak integral *versus* time through the course of a typical experiment is shown in Figure 4.3. This plot shows excellent stability of the H_3^+ signal over the course of a three hour run under constant conditions.

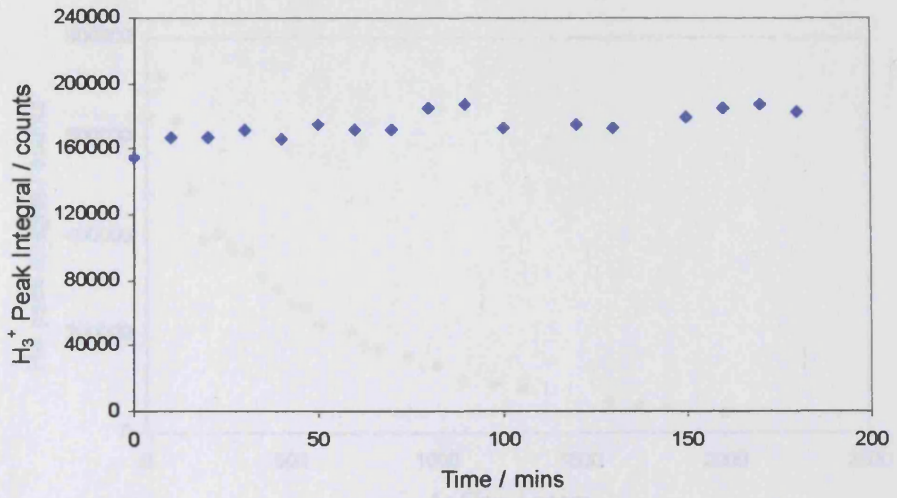

Figure 4.3: Plot of H_3^+ peak integral as a function of time.

The characterisation of the H_3^+ signal described above was carried out with the hydrogen required for the corona discharge being the only gas entering the chamber. Naturally, other gases would also be present during experiments, and the effect of gases from the flow tube entering the ionisation chamber was also characterised. Initially, a flow of argon was passed through the flow tube at varying flow rates and the H_3^+ signal monitored, as shown in Figure 4.4. The proton affinity of argon is 369.2 kJ mol^{-1} and therefore, proton transfer reaction with H_3^+ is not expected to occur. Indeed, for this reason argon is a good candidate for use as a carrier gas in future flow tube experiments.

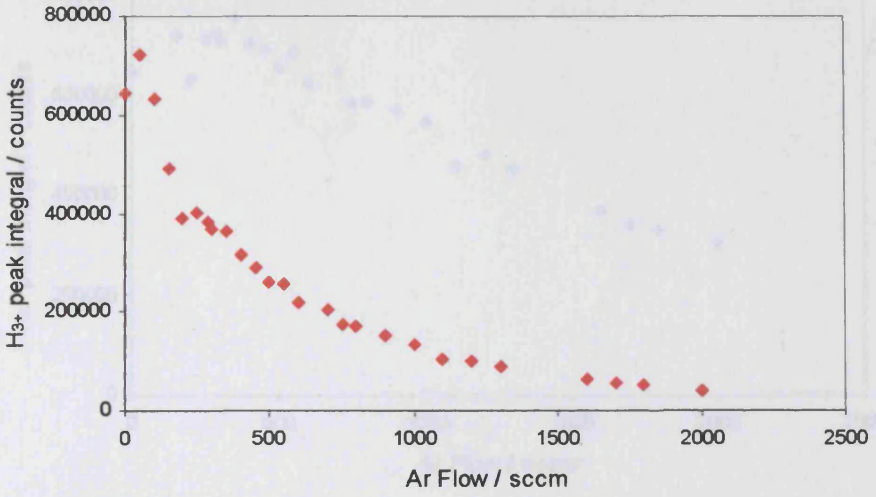

Figure 4.4: Plot of H_3^+ peak integral as a function of argon flow rate.

Figure 4.4 shows that the observed H_3^+ peak integral decreases at constant H_2 flow, but with increasing argon flow rates. Whilst this decrease in signal appears profound, potentially compromising the efficiency of the experiment, the change in the actual production efficiency of H_3^+ ions in the hydrogen discharge is, in fact, less significant. This is because some of the drop in H_3^+ signal shown in Figure 4.4 is simply a manifestation of the higher total gas pressures and therefore higher dilution of the H_3^+ ions in the ionisation chamber, when large flow rates of argon were used. Taking the pressure measurements accompanying the argon flow rates, and accounting for the dilution of the H_3^+ shows that the production efficiency of H_3^+ is much less affected by ionisation chamber pressure, as shown in Figure 4.5 below.

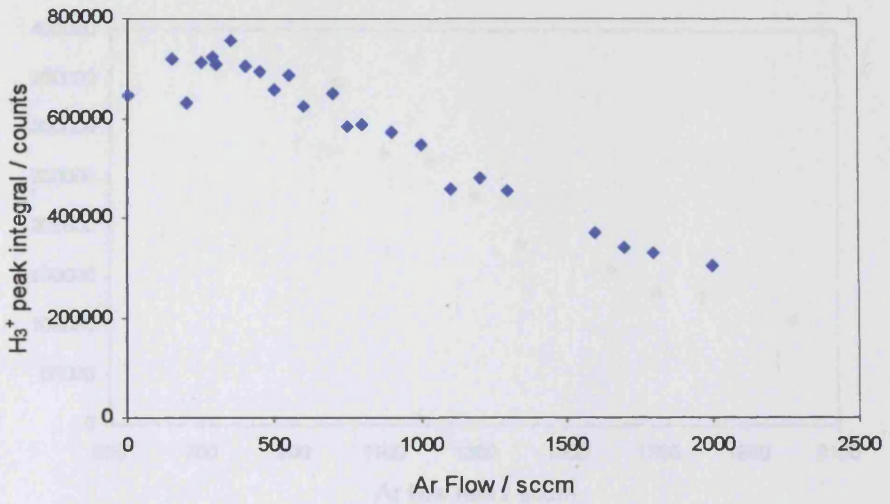

Figure 4.5: Plot of H_3^+ peak integral, corrected for number density, as a function of argon flow rate.

Importantly, even at flow rates of 2000 sccm, typical flow rates that might be used in a discharge flow experiment, the (diluted) H_3^+ signal was still significant. Furthermore, the H_3^+ signal at high dilutions could be optimised by increasing the detector (channeltron) voltage. This procedure could not be carried out using hydrogen alone, since very large numbers of ions were produced, which led to saturation of the detector. Results from further experiments carried out with the detector voltage increased from -1850 V to -1900 V are displayed in Figure 4.6.

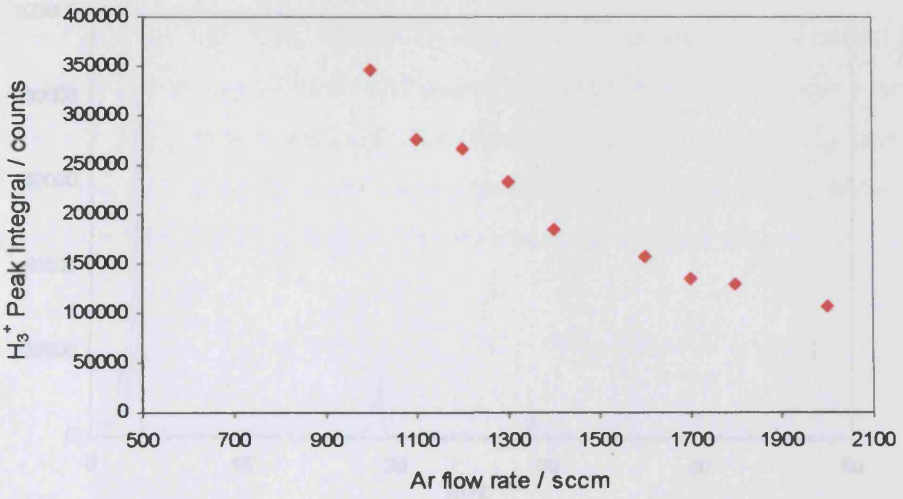

Figure 4.6: Plot of H_3^+ peak integral as a function of Ar flow rate with increased detector voltage.

4.3 Evidence for Proton Transfer

Figure 4.7 shows a typical mass spectrum of a small leak of air into the ionisation chamber mixed with the output from the hydrogen discharge. The principal peak occurs at $m/z = 3$ and is attributable to production of H_3^+ by the discharge. However, in addition to this, there are smaller peaks at $m/z = 19$, 29, and 45. These peaks are attributed to proton transfer reactions to the components of the small amount of air present in the ionisation chamber and therefore result from H_3O^+, HN_2^+, and HCO_2^+ respectively. Since the air in the chamber evidently includes O_2, the absence of a peak at $m/z = 33$ (attributable to HO_2^+) or indeed $m/z = 32$ (attributable to O_2^+) indicates that the process forming the additional ions is proton transfer from the H_3^+ produced by the corona discharge, rather than direct ionisation of the air. This lack of HO_2^+ signal is expected from the relative proton affinities of molecular oxygen and hydrogen, as discussed in Section 2.6.1.3. Furthermore, addition of small concentrations of O_2 *via* the flow tube also did not result in observation of a peak attributable to either O_2^+ or HO_2^+. Thus it is confident that the process occurring in the chamber producing the additional ions is proton transfer from the H_3^+ produced by the corona discharge and further experiments to use this H_3^+ were carried out.

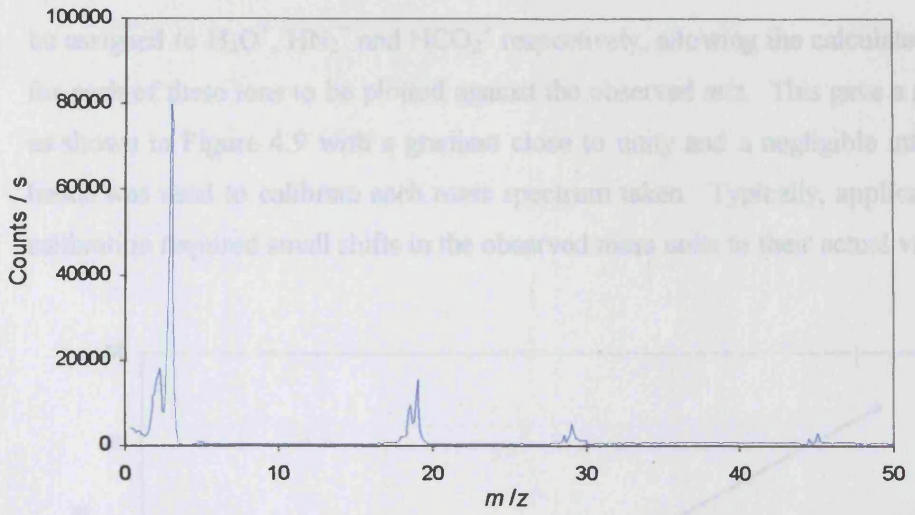

Figure 4.7::Mass Spectrum of background air in ionisation chamber over the range m/z =0 – 50.

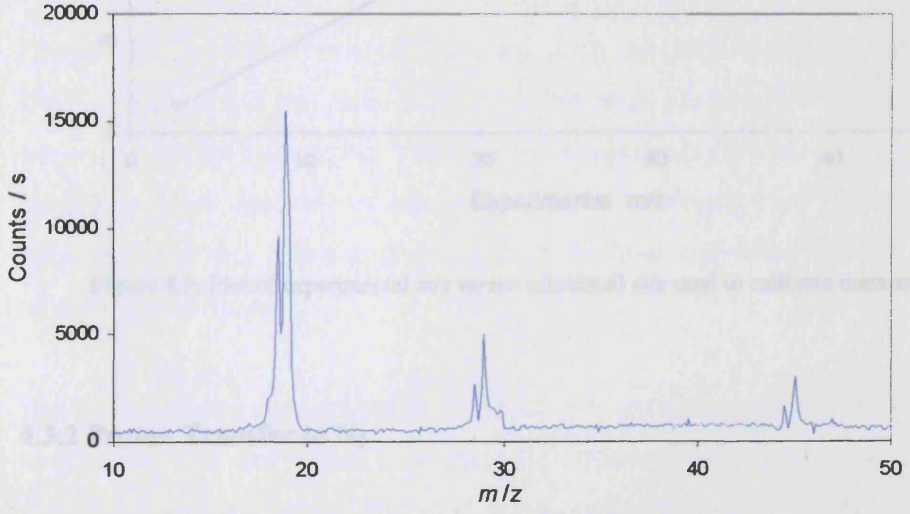

Figure 4.8: Expanded view of Figure 4.7 showing peaks due to H_3O^+, HN_2^+ and HCO_2^+.

4.3.1 Mass Calibration

The mass spectrum produced by proton transfer to the small amounts of air let into the chamber provided a convenient means to fine calibrate the m/z scale over this mass range. Since the peaks present were near m/z = 19, 29 and 45, they could confidently

be assigned to H_3O^+, HN_2^+ and HCO_2^+ respectively, allowing the calculated exact *m/z* for each of these ions to be plotted against the observed *m/z*. This gave a straight line as shown in Figure 4.9 with a gradient close to unity and a negligible intercept, and hence was used to calibrate each mass spectrum taken. Typically, application of this calibration required small shifts in the observed mass units to their actual values.

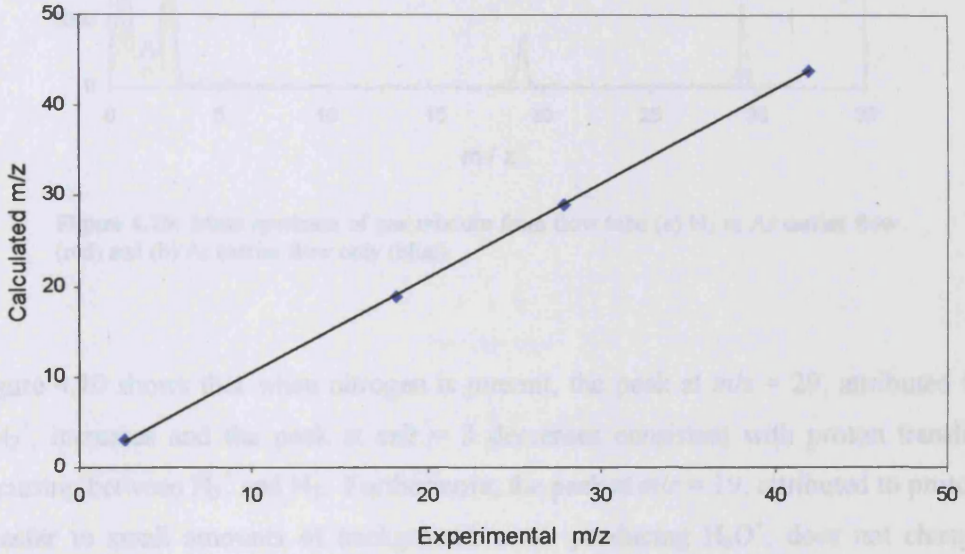

Figure 4.9: Plot of experimental *m/z versus* calculated *m/z* used to calibrate mass spectra.

4.3.2 Proton Transfer to N_2

Since a peak at *m/z* =29 attributed to HN_2^+ formed by reaction of H_3^+ with N_2 had already been observed using a small leak of laboratory air into the system, further addition of N_2 *via* the flow tube was carried out to affirm that this observed peak was indeed attributable to HN_2^+ and to determine the concentrations of species that could be detected using this chemical ionisation scheme. A small flow of nitrogen in a carrier flow of argon was therefore passed into the side arm of the flow tube. Figure 4.10 shows mass spectra obtained in the presence and absence of N_2.

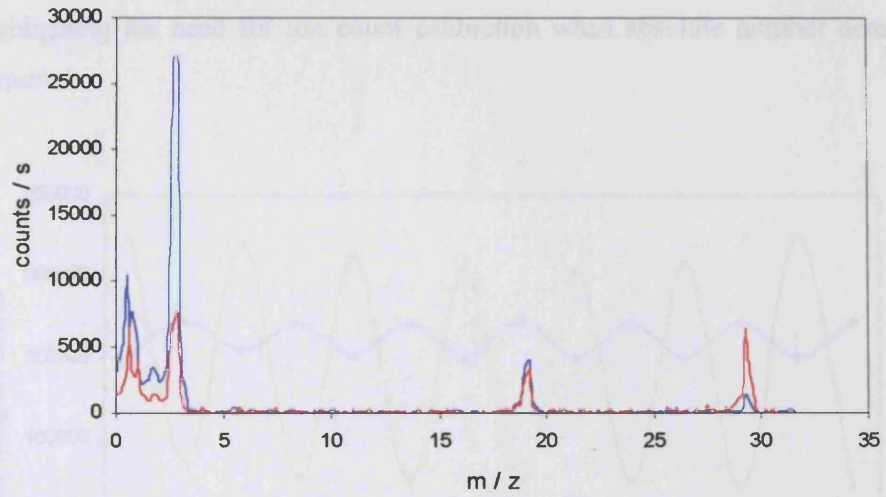

Figure 4.10: Mass spectrum of gas mixture from flow tube (a) N_2 in Ar carrier flow (red) and (b) Ar carrier flow only (blue).

Figure 4.10 shows that when nitrogen is present, the peak at $m/z = 29$, attributed to HN_2^+, increases and the peak at $m/z = 3$ decreases consistent with proton transfer occurring between H_3^+ and N_2. Furthermore, the peak at $m/z = 19$, attributed to proton transfer to small amounts of background water producing H_3O^+, does not change significantly by this addition of nitrogen to the flow, indicating that the spectra are otherwise unaffected.

Having established the qualitative detection of a gas phase species ionised by proton transfer, the next step was to investigate the reproducibility of the detection. Thus, a flow of molecular nitrogen, diluted in argon, was passed into the flow tube as above, and the integrated signals at $m/z = 3$ and $m/z = 29$ were monitored while the nitrogen flow was switched on and off in succession. As shown in Figure 4.11, below, both signals consistently returned to stable levels both in the presence and absence of nitrogen. This experiment also demonstrates that the absolute change in the number of ion counts at the two different mass/charge peaks differed somewhat (when, in principle, the change in ion counts should be equal due to stoichiometry). This is an indication of the gain of the mass spectrometer differing at the two masses,

highlighting the need for ion count calibration when absolute number densities are required.

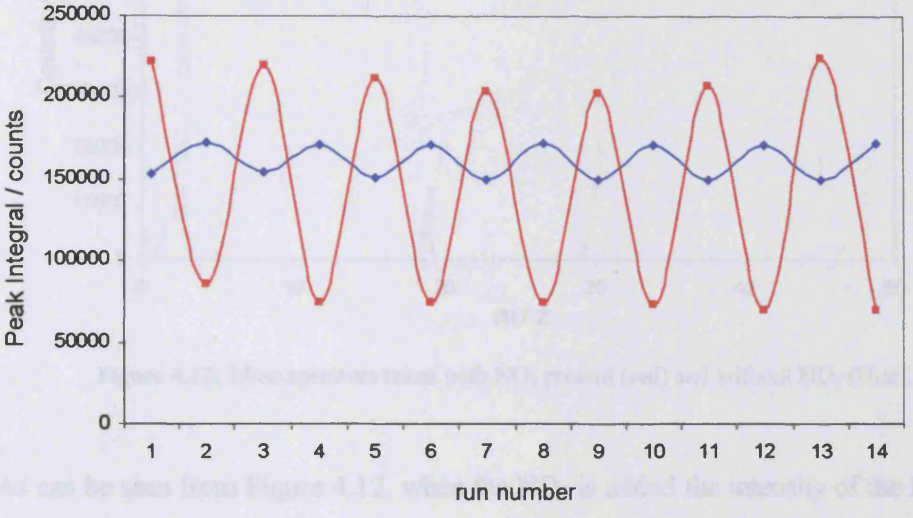

Figure 4.11: Plot of H_3^+ peak integral (red) and the HN_2^+ peak integral (blue) as a function of run number. N_2 flow was off in run number 1 and then alternately switched on and off in subsequent runs.

4.4 Proton Transfer to NO_2

A further series of experiments was undertaken to determine the efficiency of detection of even smaller concentrations. Thus, a 1 % NO_2 / He gas mixture was flowed into the side arm of the flow tube *via* a mass flow controller and diluted in a carrier flow of argon. The flow rates of the NO_2 / He mixture and the argon carrier flow were adjusted to change the concentration of the NO_2 in the flow tube whilst maintaining a constant total flow rate, and hence a constant pressure, in the flow tube. Figure 4.12 shows mass spectra taken in the presence and absence of a flow of NO_2.

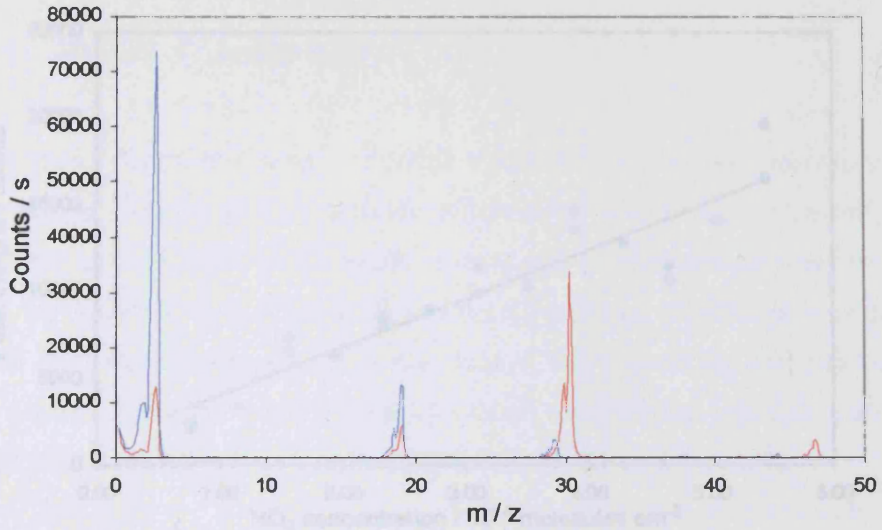

Figure 4.12: Mass spectrum taken with NO_2 present (red) and without NO_2 (blue).

As can be seen from Figure 4.12, when the NO_2 is added the intensity of the H_3^+ peak falls and new peaks are present at $m/z = 30$ and $m/z = 47$. The peak at $m/z = 47$ is readily attributed to HNO_2^+ ion – formed by the proton transfer of H_3^+ with NO_2. The second new peak, at $m/z = 30$ is thought to indicate NO^+. The presence of NO^+ can be tentatively explained by the fact that the proton transfer reaction from H_3^+ to NO_2 is exothermic, as can be calculated from the proton affinities listed in Table 2.1. Furthermore, in this case, the reaction is sufficiently exothermic so that dissociative proton transfer occurs:

$$H_3^+ + NO_2 \rightarrow HNO_2^+ \quad (4.2)$$

$$HNO_2^+ + M \rightarrow HNO_2^+ \quad (4.3a)$$

$$\rightarrow NO^+ + OH \quad (4.3b)$$

Such dissociative proton transfer reactions involving NO_2 have been evidenced in previous studies.[3] Experiments were carried out as a function of NO_2 concentration to determine whether the NO^+ and HNO_2^+ peaks changed linearly with concentration. Plots of the peak integrals attributed to HNO_2^+ and NO^+ as a function of NO_2 concentration are shown in Figures 4.13 and 4.14.

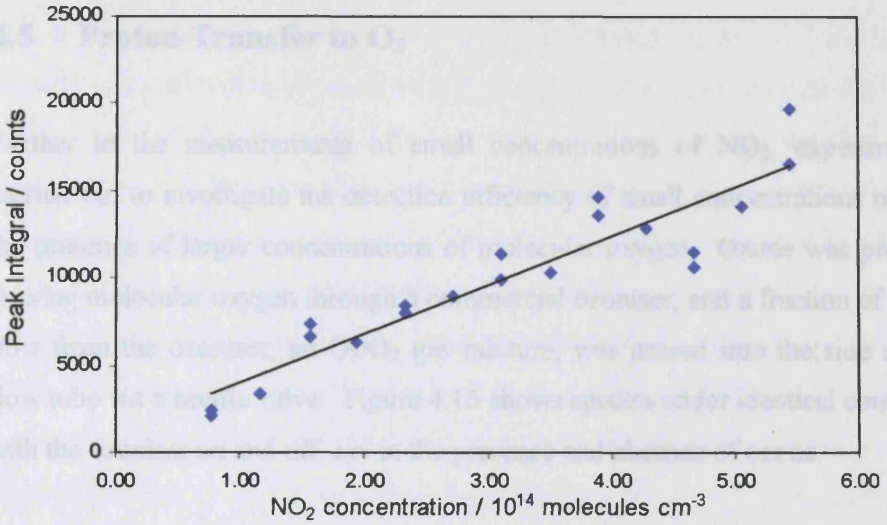

Figure 4.13 Plot of HNO_2^+ peak integral *versus* NO_2 concentration.

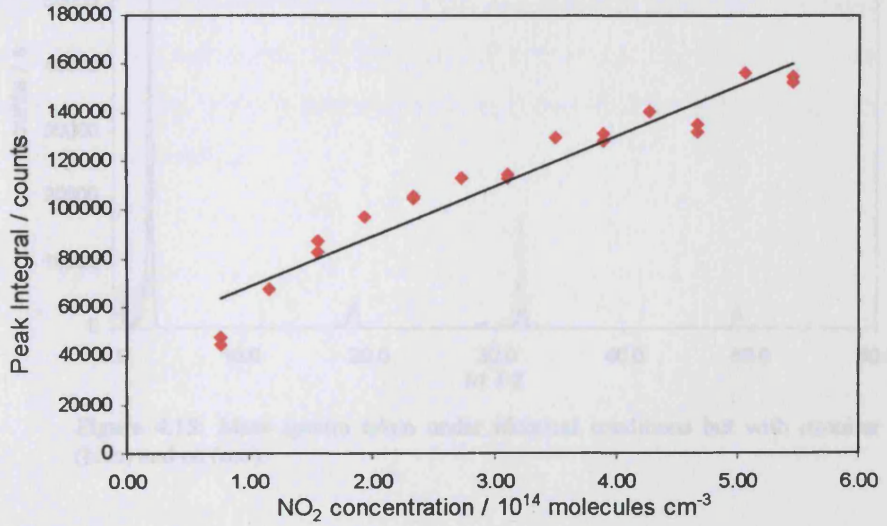

Figure 4.14: Plot of NO^+ peak integral *versus* NO_2 concentration.

4.5 Proton Transfer to O_3

Further to the measurements of small concentrations of NO_2, experiments were carried out to investigate the detection efficiency of small concentrations of ozone in the presence of larger concentrations of molecular oxygen. Ozone was produced by flowing molecular oxygen through a commercial ozoniser, and a fraction of the output flow from the ozoniser, an O_3/O_2 gas mixture, was passed into the side arm of the flow tube *via* a needle valve. Figure 4.15 shows spectra under identical conditions but with the ozoniser on and off, *i.e.* in the presence and absence of ozone.

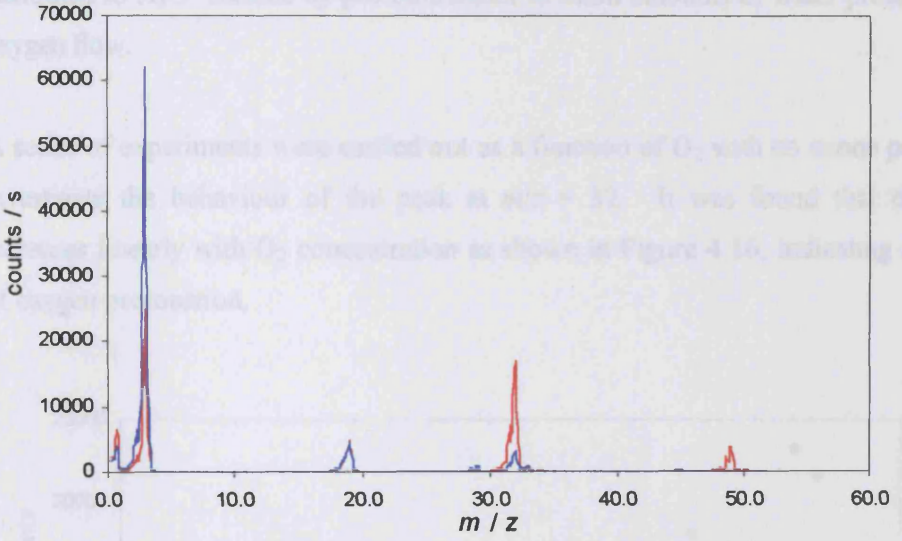

Figure 4.15: Mass spectra taken under identical conditions but with ozoniser off (blue) and on (red).

As can be seen from Figure 4.15, when the ozoniser is switched on, and hence O_3 is added to the flow, the intensity of the H_3^+ peak falls and a new peak is present at m/z = 49 and the peak at m/z = 32 increases. The peak at m/z = 49 is readily attributed to the HO_3^+ ion – formed by the proton transfer of H_3^+ with O_3. The second peak, at m/z = 30 is thought to indicate O_2^+. Analogously to the protonation of NO_2 described above, the presence of O_2^+ can be also be tentatively explained by the fact that the proton transfer reaction from H_3^+ to O_3 is sufficiently exothermic so that dissociative

proton transfer occurs. However, it is also notable that Figure 4.15 also shows that with the ozoniser off and hence, with just a flow of oxygen entering the flow tube, there is still a small peak at *m/z* 32. The presence of this peak is somewhat surprising, since proton transfer from H_3^+ to O_2 is not expected to occur because the proton affinity of H_2 is larger than that of O_2. However, the difference is small (1.3 kJ mol^{-1}), and considering the large concentrations of O_2 used in these experiments, it is possible that some O_2 will undergo proton transfer forming HO_2^+. Analysis of the energetics of the HO_2^+ ion with respect to O_2^+ and H shows that any HO_2^+ formed is likely to break down into O_2^+ and H. Hence the observed peak at $m/z = 32$ is attributed to O_2^+. The peak at $m/z = 19$ is present and the same intensity in both spectra, hence this is attributed to H_3O^+ formed by proton transfer to small amounts of water present in the oxygen flow.

A series of experiments were carried out as a function of O_2 with no ozone present to investigate the behaviour of the peak at $m/z = 32$. It was found that this peak increases linearly with O_2 concentration as shown in Figure 4.16, indicating a degree of oxygen protonation.

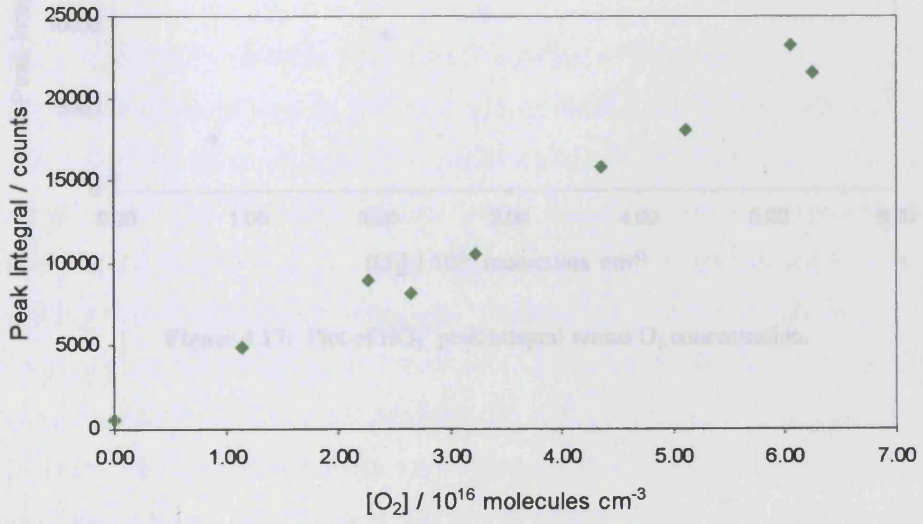

Figure 4.16: Plot of O_2^+ peak integral as a function of O_2 concentration.

This linearity of the peak intensity at $m/z = 32$ allows for a straightforward correction to be applied to the peak intensity when O_3 is present. It should be noted that the intensity of the peak at $m/z = 32$, is much more sensitive to O_3 concentration than O_2 concentration. For example in spectra shown in Figure 4.15, the peak at $m/z = 32$ where only oxygen is present has an integral of 15778 counts and the concentration of oxygen is 4.3×10^{16} molecules cm^{-3}, whilst in contrast when ozone is present the peak integral is 82317 with an ozone concentration of only 4.3×10^{14} molecules cm^{-3}.

Experiments were carried out as a function of O_3 concentration to determine whether the HO_3^+ and O_2^+ peaks varied linearly with concentration. Plots of the peak integrals attributed to HO_3^+ and O_2^+ as a function of O_3 concentration are shown in Figures 4.17 and 4.18.

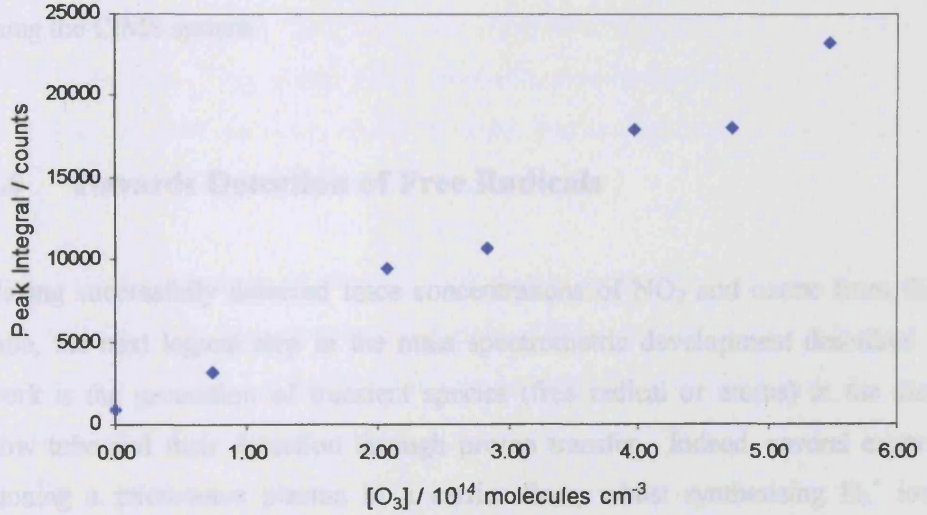

Figure 4.17: Plot of HO_3^+ peak integral *versus* O_3 concentration.

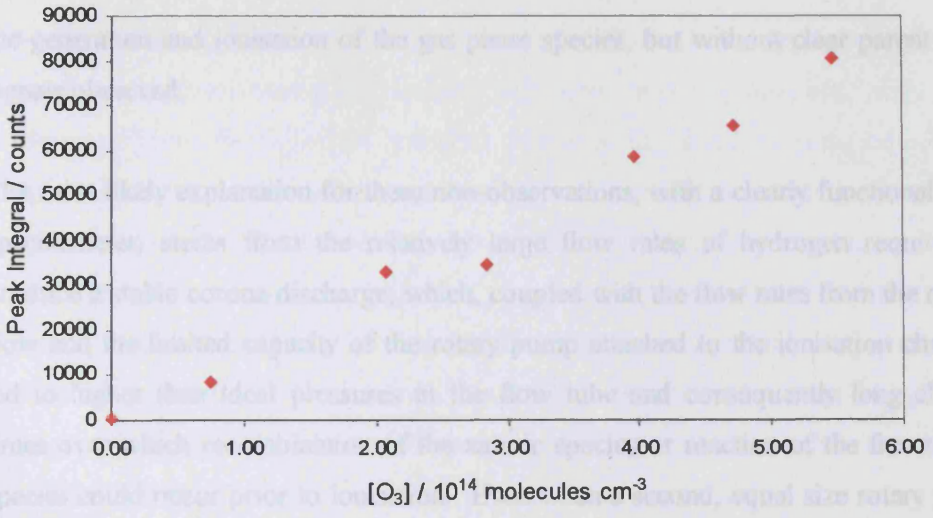

Figure 4.18: Plot of O_2^+ peak integral *versus* O_3 concentration.

These figures show that it is possible to detect these small concentrations of ozone using the CIMS system.

4.6 Towards Detection of Free Radicals

Having successfully detected trace concentrations of NO_2 and ozone from the flow tube, the next logical step in the mass spectrometric development described in this work is the generation of transient species (free radical or atoms) in the discharge flow tube and their detection through proton transfer. Indeed, several experiments running a microwave plasma in a carrier flow, whilst synthesising H_3^+ ions and recording mass spectra were attempted. Unfortunately, such experiments, in plasmas containing O atoms, N atoms and even more complex species such as vinyl bromide did not conclusively demonstrate atom or radical detection . (Although signals attributable to free radicals from vinyl bromide fragmentation were observed, these were also observed in the absence of microwave power to the Evenson cavity and therefore attributed to fragmentation of the ionised species.) Several arrangements of the microwave discharge were adopted, changing the effective elapsed time between

the generation and ionisation of the gas phase species, but without clear parent atom signals observed.

The most likely explanation for these non-observations, with a clearly functional mass spectrometer, stems from the relatively large flow rates of hydrogen required to produce a stable corona discharge, which, coupled with the flow rates from the carrier flow and the limited capacity of the rotary pump attached to the ionisation chamber led to higher than ideal pressures in the flow tube and consequently long elapsed times over which recombination of the atomic species or reaction of the free radical species could occur prior to ionisation. Even when a second, equal size rotary pump was connected to pump the ionisation chamber and flow tube in parallel, this problem persisted, and clearly a larger capacity rotary pump is needed to attain the requisite linear flow velocities in the flow tube when larger flows of the H_2 / H_3^+ ionisation gas are also in use. An alternative solution, which is now being considered, is the use of separate pumps for the flow tube and ionisation chamber, with a skimmer cone between the two. This would allow only a fraction of the flow tube gas to enter the ionisation chamber, at much lower pressure, and ionisation of a fraction of this gas followed by ion transport and detection.

With these improved flow velocities, a detection sensitivity of 10^8 molecules cm^{-3} is estimated for this experimental arrangement. This is perfectly adequate since radical concentrations of 10^{11} molecules cm^{-3} are envisaged and is in keeping with previous similar experimental arrangements.[4]

4.7 Summary

Notwithstanding this lack of success in developing the flow tube / CIMS instrument in detecting transient species in the gas phase, the work described in this and the preceding chapters has successfully led to the full development and characterisation of a powerful mass spectrometer for gas phase species. The ionisation source involving proton transfer has been idealised, and the electrostatic ion guiding system has been

fully designed tested and optimised, providing excellent ion – neutral separation. A channeltron electron multiplier detector has also been implemented, with pulse counting software developed in house to maximise the signal to noise ratio of the mass spectrometry. Such instrument development is a central part of improving the technology available for laboratory studies of atmospheric gas phase processes. In the next chapter of this thesis, a pre-existent set up for monitoring gaseous free radicals accurately and unequivocally has been applied in an extensive study of an important atmospheric reaction. The use of this unique experimental capability perhaps illustrates the huge potential of new instrument development described in this and the preceding chapter.

4.8 References

(1) Raizer Y.P. *Gas Discharge Physics*; Springer: Berlin, 1991.
(2) Meek M.D.; Craggs J.D. *Electrical Breakdown of Gases*; Wiley: Chichester, 1978.
(3) Smith D.; Spanel P.; Mayhew C.A. *International Journal of Mass Spectrometry and Ion Processes* **1992**, *117*, 457.
(4) Seeley, J. V.; Jayne, J. T.; Molina, M. J. *International Journal of Chemical Kinetics* **1993**, *25*, 571-594.

Chapter 5 Laboratory Study of the ClO + ClO Dimerisation using Flash Photolysis

This chapter presents the results of a flash photolysis study of the dimerisation of ClO free radicals. The principles behind the flash photolysis technique are discussed in Chapter 2. This chapter contains a full description of the flash photolysis apparatus, together with kinetic and thermodynamic analyses of data obtained. The atmospheric implications of these findings are briefly discussed.

5.1 Introduction

The ClO radical is well known to play a pivotal role in human-induced polar ozone depletion.[1] As discussed in Chapter 1, ClO radicals are formed in the atmosphere following reaction of chlorine atoms, liberated from solar photolysis of chlorine containing pollutants, with ozone. Subsequent reactions of ClO to return chlorine atoms complete a catalytic cycle for ozone loss. This ozone loss has been shown to be most dramatic over Polar regions in local springtime. As discussed in Chapter 1, this massive ozone loss follows 'activation' of chlorine to photolabile forms involving heterogeneous reactions during wintertime. When sunlight returns, in spring, elevated chlorine atom and hence ClO radical concentrations occur, and the catalytic ozone destruction cycle involving the ClO self reaction and dimer photolysis, first proposed by Molina and Molina in 1987, is thought to be the principal route to ozone loss under such circumstances.[2] This cycle is described by reactions (5.1) to (5.4).

$2(Cl + O_3$		$\rightarrow$	$ClO + O_2)$	(5.1)
$ClO + ClO + M$		$\leftrightarrow$	$Cl_2O_2 + M$	(5.2a)
$Cl_2O_2 + h\nu$		$\rightarrow$	$ClOO + Cl$	(5.3)
$ClOO + M$		$\rightarrow$	$Cl + O_2 + M$	(5.4)
Net:	$2O_3$	$\rightarrow$	$3O_2$	

In the sunlit stratosphere, the rate of Cl_2O_2 photolysis is rapid. Furthermore, reaction (4) is rapid even under stratospheric conditions, since ClOO is estimated to be only 20 kJ mol^{-1} bound with respect to Cl + O_2.[3,4] Thus the rate determining step of the cycle is reaction (2a), which produces the ClO dimer. Consequently, it is important to gain an accurate knowledge of the rate coefficient for this process in order to accurately simulate and quantify the extent of polar ozone loss. As indicated in the reaction sequence, the association of ClO radicals is in fact reversible. However, the Δ_rH^0 for this process is estimated to be of the order of -80 kJ mol^{-1}, according to the current NASA recommendations,[5] and at stratospheric temperatures, the back dissociation of Cl_2O_2 is likely to be unimportant. During the day, the prime fate of stratospheric ClOOCl is photolysis through reaction (3). At night, however, slow removal of ClOOCl is dominated by thermal decomposition. Quantification of the ClO association channel under stratospheric conditions has recently been undertaken in our laboratory.[6] The stability of the ClO dimer is another important parameter – both in the nighttime stratosphere and indirectly in laboratory studies of ClO chemistry, and forms the focus of this chapter.

Apart from the reversible termolecular dimerisation of ClO radicals, three bimolecular channels of the ClO self-reaction are also known to exist.

ClO + ClO	→	$Cl_2 + O_2$	(5.2b)
	→	ClOO + Cl	(5.2c)
	→	OClO + Cl	(5.2d)

Under ambient conditions, these bimolecular channels make a minor contribution to the overall decay of ClO radicals ($k_{2b+2c+2d} = 0.03k_{2a}$ at 298 K and 760 Torr).[5] Furthermore, all three channels show positive temperature dependencies[7] implying that their contribution to ClO loss at stratospheric temperatures is likely to be negligible. As discussed below, however, when studying the ClO dimerisation at higher temperatures these channels must be considered.

5.2 The Flash Photolysis Apparatus

The flash photolysis apparatus used to conduct the experiments described in this chapter is that described in detail by Rowley *et al.*[8] A general description of the system (shown schematically in Figure 5.1) and its operation follows.

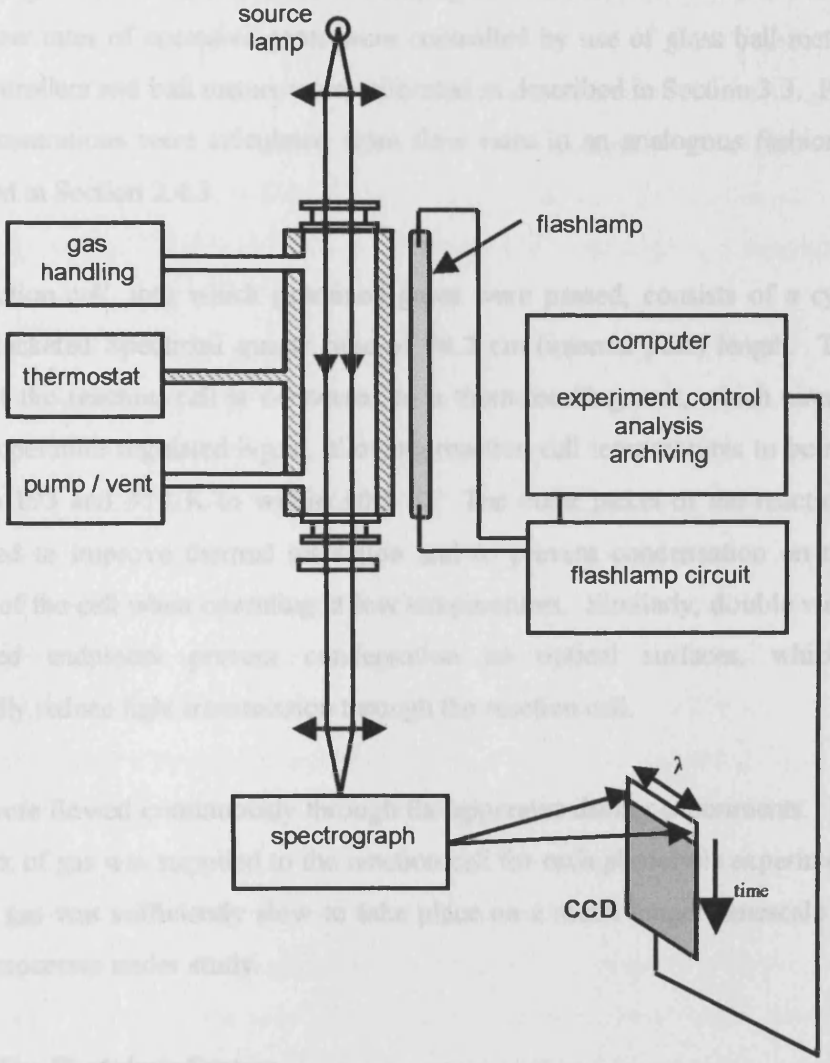

Figure 5.1: Schematic diagram of the flash photolysis apparatus

5.2.1 Gas Handling

Precursor gases were mixed in a carrier gas flow in a standard Pyrex mixing line equipped with Teflon taps. The gas mixing line consists of a carrier gas flow tube and five gas injectors aligned against the carrier flow to promote efficient mixing. Non-corrosive gases were introduced to the mixing line *via* mass flow controllers (MFCs) while flow rates of corrosive gases were controlled by use of glass ball-meters. All flow controllers and ball meters were calibrated as described in Section 3.3. Precursor gas concentrations were calculated from flow rates in an analogous fashion to that described in Section 2.4.3.

The reaction cell, into which premixed gases were passed, consists of a cylindrical double-jacketed Spectrosil quartz tube of 98.2 cm (internal path) length. The inner jacket of the reaction cell is connected to a thermostatting unit, which circulates an inert temperature regulated liquid, allowing reaction cell temperatures to be regulated between 193 and 373 K to within ±0.5 K. The outer jacket of the reaction cell is evacuated to improve thermal insulation and to prevent condensation on the outer surface of the cell when operating at low temperatures. Similarly, double windowed, evacuated endpieces prevent condensation on optical surfaces, which could potentially reduce light transmission through the reaction cell.

Gases were flowed continuously through the apparatus during experiments. Hence, a fresh mix of gas was supplied to the reaction cell for each photolysis experiment. The flow of gas was sufficiently slow to take place on a much longer timescale than the kinetic processes under study.

5.2.2 The Photolysis System

Free radicals and atoms were generated in the reaction cell using flashlamp photolysis. The photolysis source used is a 1 m long xenon arc lamp filled to a pressure of 50 Torr. The lamp is situated adjacent and parallel to the reaction cell and is powered from a 25 kV, 2.6 μF rapid discharge capacitor. The capacitor was

typically charged to 20 kV using a high-voltage power supply. This high voltage causes spontaneous breakdown in the lamp thereby causing it to flash. Thus to prevent uncontrolled firing, a spark gap isolated the flashlamp from the capacitor until triggering was required. The spark gap was initiated by a trigger module which itself was initiated by a TTL (+5 V) pulse from the control computer. The pulse energy of the flashlamp, approximately 500 J, was completely discharged in 20 μs.

The reaction cell and flashlamp are housed in a light-tight metal box to minimise the escape of light. The box is earthed to minimise radiofrequency interference from the flashlamp. Similarly, the flashlamp circuit is enclosed in a Faraday cage, earthed to the same point. All electrical leads are screened and mains power is supplied from a filtered unit.

5.2.3 Species Monitoring

Radicals and molecules in the reaction cell were identified and monitored before, during, and after photolysis by time-resolved UV/visible absorption spectroscopy. The light source used in these experiments was a 70 W continuous xenon arc lamp. The lamp output was collimated along the length of the reaction cell and focused, using a pair of Spectrosil quartz lenses, onto the entrance slit of a 250 mm focal length astigmatic Czerny-Turner spectrograph, which images the dispersed light onto the charge coupled device (CCD) detector array.

The spectrograph was fitted with three interchangeable diffraction gratings (150, 300 and 600 grooves / mm) corresponding to wavelength coverage of 130, 60 and 30 nm respectively. Increasing the spectral coverage compromised resolution, hence limiting resolutions of the spectra associated with the respective gratings were approximately 0.11, 0.22 and 0.45 nm / CCD pixel. In practice, the spectrograph entrance slit width determines resolution. In each experiment, the diffraction grating in use was both dispersion and wavelength calibrated relative to the known spectral lines of a mercury pen-ray lamp, as described in Section 5.3.3.1.

The principle of operation of the CCD has been described in Section 2.3.2. The CCD consists of an array of 298 (columns) × 1152 (rows) of light sensitive pixels mounted in a Peltier cooled camera head. The short axis of the array is aligned in the dispersive plane of the spectrograph, representing the wavelength-resolved axis. 31 rows of the CCD are simultaneously exposed to light, while the others are optically masked. The camera head is coupled to the spectrograph *via* a micrometer adjustable flange to permit precise and repeatable alignment of the CCD. A mechanical shutter is integrated into the optical line to prevent the accumulation of signal (photocharge) between experiments.

5.2.4 Operating Procedure

The CCD, spectrograph, and flashlamp trigger were controlled from a personal computer. The procedure for a typical photolysis experiment is outlined in the flow chart in Figure 5.2. To improve the signal to noise ratio, experiments typically incorporate 5 – 100 co-added photolysis runs. The experimental repetition rate was limited by the cell flow out time (dependent on total flow rate and pressure) and the high voltage capacitor recharge time (15 s). Following co-addition, data files of light intensity *versus* wavelength *versus* time were transferred to a separate PC for analysis.

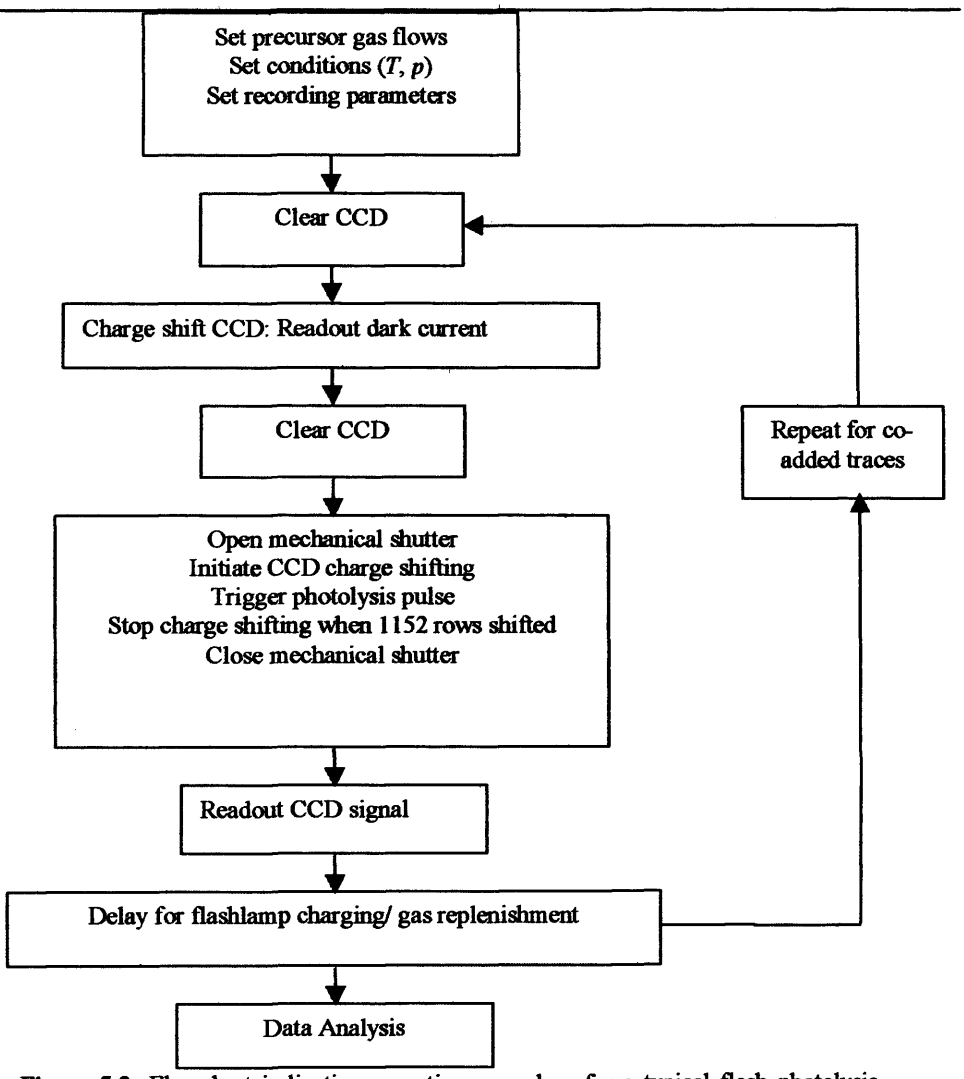

Figure 5.2: Flowchart indicating operation procedure for a typical flash photolysis experiment.

5.2.5 Analytical Procedure

For each kinetic experiment, a wavelength resolved transmission spectrum was recorded on every row on the CCD before, during, and after photolysis. Absorbances were calculated for each row relative to the time averaged light intensities recorded during the pre-flash period by applying Beer's law:

$$A_{\lambda,t} = \ln\left(\frac{< I_{0,(\lambda,t)} >}{I_{t,(\lambda,t)}}\right) \qquad (5.i)$$

where $A_{\lambda,t}$ is the absorbance within the reaction cell at a given wavelength, λ, and time, *t*. $\langle I_{0,(\lambda,t)} \rangle$ is the *average* intensity at a given wavelength in the preflash region and $I_{t,(\lambda,t)}$ is the intensity at a given wavelength and time after the flash. Thus, the absorption spectrum generated for any row on the CCD represents the change in absorbance resulting from the photolysis pulse and subsequent chemistry. Sequential spectra prepared in this way show time evolution of these absorbance changes.

In practice a small complication arises from the charge shifting routine executed by the CCD. As a row of signal is shifted down the CCD, a small amount of additional charge, termed 'dark current', is acquired. This effect is cumulative so that data acquired at earlier times in a given run, in which charge has traversed down the entire length of the CCD, accumulates more of this charge than data acquired later in the run, which is shifted down fewer rows. This phenomenon was corrected for by running a non-flashed experiment for each flashed experiment under identical conditions and subtracting the absorptive contribution for this accumulating charge by modifying (i):

$$A_{\lambda,t} = \ln\left(\frac{\langle I_{0,(\lambda,t)} \rangle}{I_{t,(\lambda,t)}}\right)_{flashed} - \ln\left(\frac{\langle I_{0,(\lambda,t)} \rangle}{I_{t,(\lambda,t)}}\right)_{non-flashed} \qquad (5.ii)$$

Typically, the correction imposed by the non-flashed run was small, of the order of 1×10^{-4} absorbance units.

A second, rather more significant, correction required during analysis of the time-resolved spectra recorded from the CCD was the effect resulting from the simultaneous illumination of 31 CCD rows by the spectrograph. The result of this was essentially to impose a 'sliding average' on the time-resolved spectra, which had to be accounted for in the kinetic analysis. This effect was more pronounced during rapid changes in UV/visible absorption recorded by the CCD - typically during build-up of photolytically produced free radical concentrations, and is demonstrated for a simulated absorbance *versus* time trace in Figure 5.3 below.

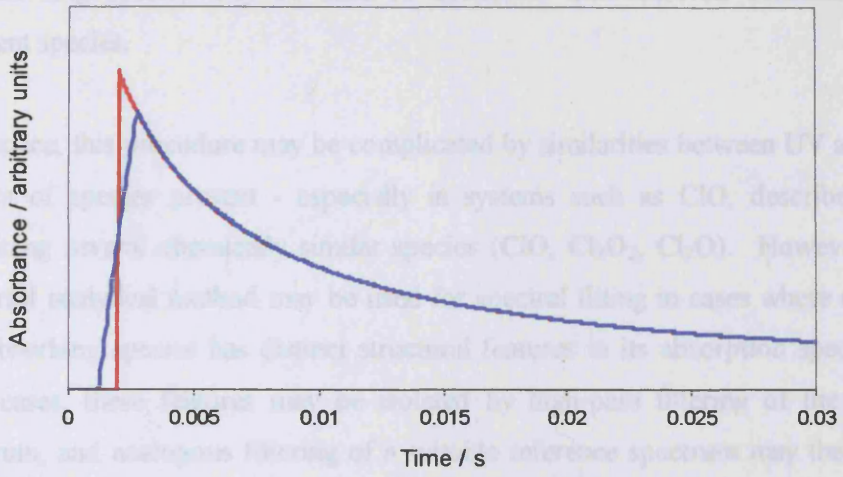

Figure 5.3: Effect of 31 row sampling at the CCD. The red curve is a simulated absorbance *versus* time trace. The blue curve illustrates the temporal distortion to this, imparted by temporal averaging from simultaneous illumination.

In kinetic analyses of concentrations derived from absorbances, the classical or analytical solution of controlling rate equations was readily averaged in an identical fashion to account for this artefact – which is unique to the CCD recording of time resolved absorption.

5.2.6 Determination of Species Concentration

In UV-visible spectrometry, the absorbance of a fluid mixture is related to the concentration of its components by the Beer-Lambert law:

$$A_\lambda = \sum_i \sigma_i(\lambda)[i]l \qquad (5.iii)$$

where, $\sigma_i(\lambda)$ is the absorption cross-section of species i at a given wavelength (typically reported in cm^2 $molecule^{-1}$) $[i]$ is the concentration of species i (typically in molecules cm^{-3}) and l is the optical path length (typically in cm). Using the CCD, entire sequential absorbance spectra of a reacting gas mixture are recorded. Thus,

since the path length, l, is known, fitting reference absorption cross-sections (spectra) of absorbing species may be used to determine time-resolved concentrations of transient species.

In practice, this procedure may be complicated by similarities between UV absorption spectra of species present - especially in systems such as ClO, described below, containing several chemically similar species (ClO, Cl_2O_2, Cl_2O). However, a very powerful analytical method may be used for spectral fitting in cases where one of the UV absorbing species has distinct structural features in its absorption spectrum. In such cases, these features may be isolated by high-pass filtering of the observed spectrum, and analogous filtering of a suitable reference spectrum may then be used to produce 'fingerprint' spectra solely due to species exhibiting structured absorption features. So-called 'differential' fitting of the (high-pass filtered) reference cross-sections to the filtered observed spectra then yields a multiplier (concentration × path length) defining uniquely the concentration of the spectrally structured absorber. This process is shown diagrammatically in Figure 5.4 below, and for the ClO radical in Section 5.3.2.

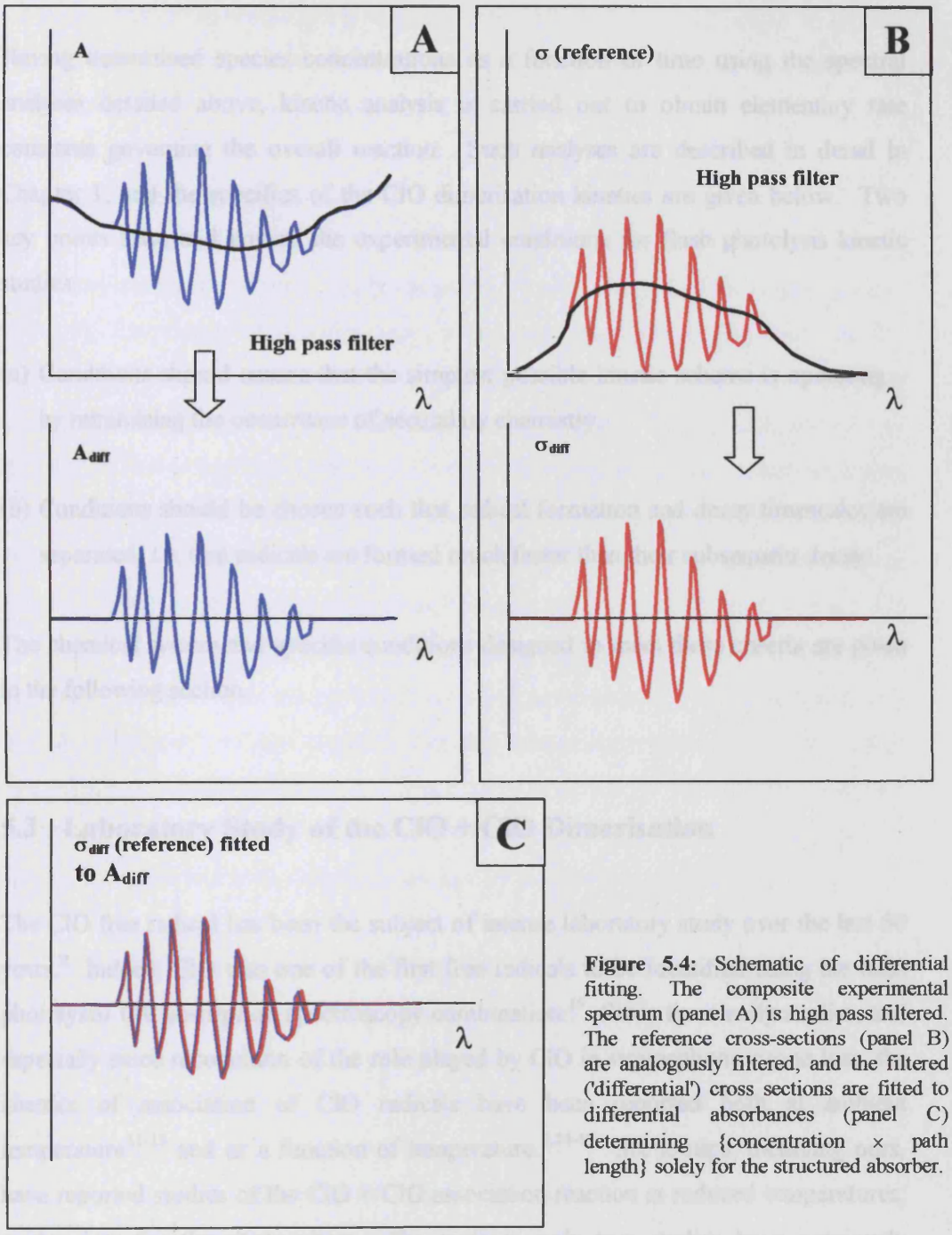

Figure 5.4: Schematic of differential fitting. The composite experimental spectrum (panel A) is high pass filtered. The reference cross-sections (panel B) are analogously filtered, and the filtered ('differential') cross sections are fitted to differential absorbances (panel C) determining {concentration × path length} solely for the structured absorber.

5.2.7 Kinetic Analyses

Having determined species concentrations as a function of time using the spectral analyses detailed above, kinetic analysis is carried out to obtain elementary rate constants governing the overall reaction. Such analyses are described in detail in Chapter 1, and the specifics of the ClO dimerisation kinetics are given below. Two key points arise and govern the experimental conditions for flash photolysis kinetic studies:

(a) Conditions should ensure that the simplest possible kinetic scheme is operating – by minimising the occurrence of secondary chemistry.

(b) Conditions should be chosen such that radical formation and decay timescales are separated, *i.e.* that radicals are formed much faster than their subsequent decay.

The chemical system and specific conditions designed to meet these criteria are given in the following section.

5.3 Laboratory Study of the ClO + ClO Dimerisation

The ClO free radical has been the subject of intense laboratory study over the last 50 years.[9] Indeed, ClO was one of the first free radicals to be identified using the flash photolysis/ UV absorption spectroscopy combination.[10] Since these early studies, and especially since recognition of the role played by ClO in stratospheric ozone loss, the kinetics of association of ClO radicals have been reported both at ambient temperature[11-13] and as a function of temperature.[7,14-17] Six groups, including ours, have reported studies of the ClO + ClO association reaction at reduced temperatures, appropriate for the stratosphere. By contrast, only two studies have previously reported the equilibrium constant for ClO dimerisation, from which the thermal stability of the ClO dimer has been inferred.[7,18] This section details a comprehensive

study of the equilibrium constant for ClO association, over the temperature range 280 – 310 K. Whilst this temperature range appears limited, it is argued below, in Section 5.4.2.1, that it is appropriate owing to different limitations of the chemical sensitivity at the extremes of temperature used.

5.3.1 ClO Radical Generation

Numerous candidate reactions for the photolytic generation of ClO free radicals exist. Evidently, the reaction of chlorine atoms with ozone - the reaction that produces ClO in the stratosphere - is one possibility. However, since the peak of the ClO absorption spectrum occurs near 250 nm, and since ozone is a very strong absorber of UV radiation at this wavelength, this reaction is far from ideal in experiments employing UV spectroscopy to monitor ClO. An alternative reaction to generate ClO is that of oxygen atoms with molecular chlorine. This reaction is, however, rather slower than the reaction of oxygen atoms with other halogen molecules (k(298 K) = 3 × 10^{-14} molecules^{-1} cm^3 s^{-1}),[19] and would consequently require a considerable excess of molecular chlorine to ensure rapid and exclusive conversion of oxygen atoms to ClO radicals. Another, practical, problem with this scheme is the photolytic production of oxygen atoms using the flashlamp. This can be achieved by photolysing molecular oxygen at wavelengths near and below 200 nm, but even using the quartz reaction vessel, only small yields of oxygen atoms may be produced in this fashion.

A much more convenient source of ClO radicals is available following the preparation of chlorine oxides. In particular, dichlorine monoxide, Cl_2O, is a source of ClO through both its direct photolysis and through rapid reactions abstracting a chlorine atom from Cl_2O. Both chlorine and bromine atoms are readily generated using flashlamp photolysis of the halogen precursor, and since bromine in particular is rather more photolabile than chlorine, the reaction of bromine atoms with Cl_2O was used in this study. Hence, flash photolysis of $Br_2/Cl_2O/N_2$ gas mixtures was used to produce ClO free radicals in this work.

The Cl_2O in these experiments was produced *in situ*, in a trap upstream from the gas mixing line by the method originally described by Hinshelwood and Pritchard.[20] Chlorine (5% in N_2, purity >99.9%) was passed through a trap containing dried mercuric (II) oxide (purity >99%) interspersed with glass beads to allow a flow of gas through.

$$2Cl_2(g) + nHgO(s) \rightarrow Cl_2O + HgCl_2.(n\text{-}1)HgO(s) \quad (5.5)$$

The yield of Cl_2O produced by this method has been investigated previously[6] and has been found to be typically 70 %, using fresh HgO.

Bromine was introduced to the gas mixing line by continuous bubbling of a small flow of nitrogen (>99.98% purity) through liquid bromine (>99.8 % purity). The bubbler was held at 273 K to ensure that a constant and known vapour pressure of Br_2 was incorporated into the N_2 carrier flow.

Photolytic generation of bromine atoms and their subsequent reaction with excess Cl_2O represented the dominant source of ClO in the reaction vessel:

$$Br_2 + h\nu \rightarrow 2Br \quad (5.6)$$

$$Br + Cl_2O \rightarrow ClO + BrCl \quad (5.7)$$

In addition, some photolysis of residual, unconverted Cl_2 gave rise to ClO production *via*:

$$Cl_2 + h\nu \rightarrow 2Cl \quad (5.8)$$

$$Cl + Br_2 \rightarrow Br + BrCl \quad (5.9)$$

$$Br + Cl_2O \rightarrow ClO + BrCl \quad (5.7)$$

$$Cl + Cl_2O \rightarrow ClO + Cl_2 \quad (5.10)$$

Typical precursor species concentrations are given in Table 5.1.

Precursor Species	Pre-flash Concentration
Br_2	$(0.5\text{-}2.5) \times 10^{16}$
Cl_2O	$(2\text{-}7) \times 10^{15}$
Cl_2	1.90×10^{16}
N_2	Balance to atmosphere

Table 5.1: Typical precursor concentrations in molecules cm^{-3} at 298 K, 760 Torr.

Under these conditions, as shown below, flash photolysis of the precursor gas mixture led to rapid generation of ClO radicals in comparison to the timescale of their subsequent decay.

5.3.2 ClO Spectroscopy

Figure 5.5 shows a time averaged absorption spectrum recorded following the photolysis of a $Br_2/Cl_2O/N_2$ gas mixture. As discussed in Section 5.2.6, above, absorbance is calculated relative to pre-photolysis transmitted light intensities, and the spectrum consequently shows changes in absorbance bought about by the photolysing flash and subsequent chemistry. Evident in the spectrum are well–defined absorption bands, which coincide with those from the vibronic ($A^2\Pi \leftarrow X^2\Pi$) transition of ClO radicals. Also present in the spectrum is a continuum absorption, resulting from the loss of the Cl_2O parent molecule and the formation of the ClO dimer, Cl_2O_2, both of which absorb in the spectral window selected.

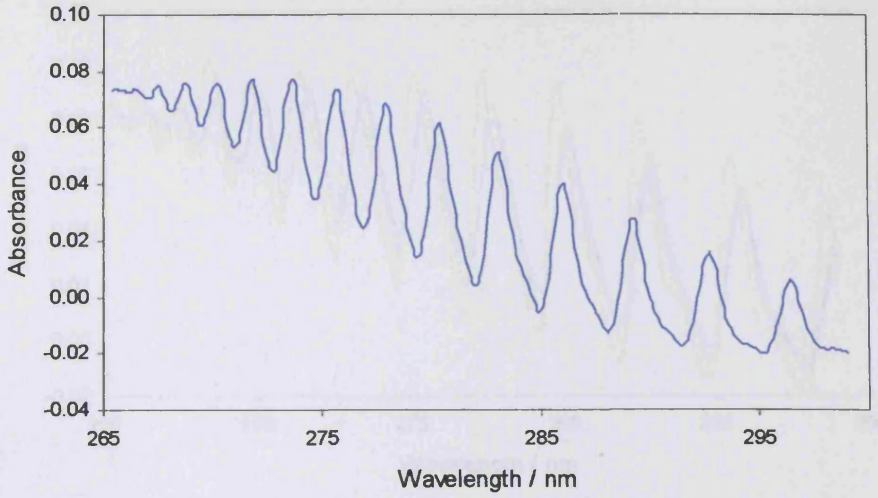

Figure 5.5: Typical post-flash absorption spectrum of Br_2 / Cl_2O / Cl_2 / N_2 gas mixture.

As discussed in Section 5.2.7, above, the presence of well-defined absorption bands enables the unequivocal and accurate monitoring of ClO radicals using the technique of differential spectroscopy. However, in order to carry out this procedure, a calibrated reference spectrum of ClO radicals is required. The procedure used to calibrate the ClO absorption cross sections is described in the following section, although the spectrum ultimately adopted in this analysis was normalised to the recent, more extensive study of ClO cross-sections reported by Boakes *et al.* from this laboratory.[6] Care was taken to ensure that the instrumental resolution used in this study was identical to that employed by Boakes *et al.*, since it is well established that the effective absorption cross-section for structured absorbers is directly dependent upon resolution. This is illustrated in Figure 5.6, which shows ClO spectra taken under identical experimental conditions but with different spectral resolutions. It is clear that the spectrum taken at the highest resolution is sharper and shows a larger ClO cross section than those taken at lower resolutions.

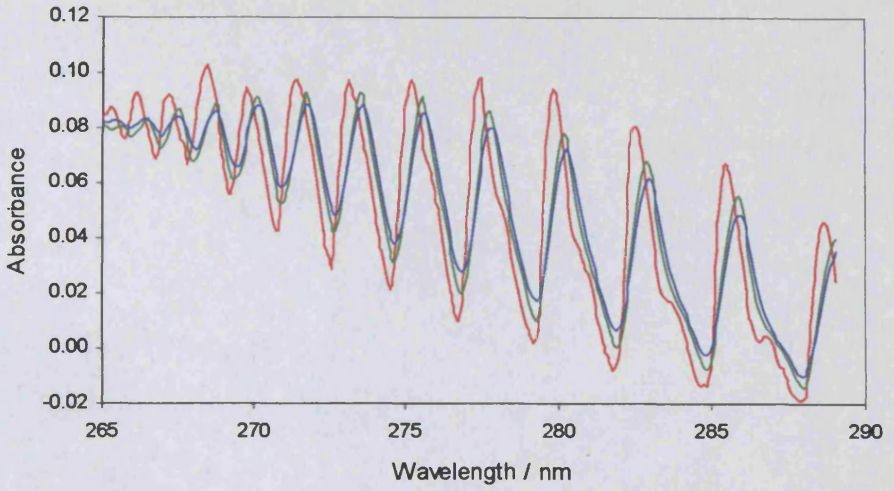

Figure 5.6: ClO spectra recorded under identical conditions but at different spectral resolutions: red – 0.3 nm (FWHM), green – 0.5 nm (FWHM), blue – 0.8 nm (FWHM)

An example of the differential fit of a calibrated ClO reference spectrum to a time averaged experimental spectrum is shown in Figure 5.7, below. This fitting, carried out for each individual row of absorbance produced from the CCD readout, was used to determine time-resolved ClO concentrations for kinetic analysis.

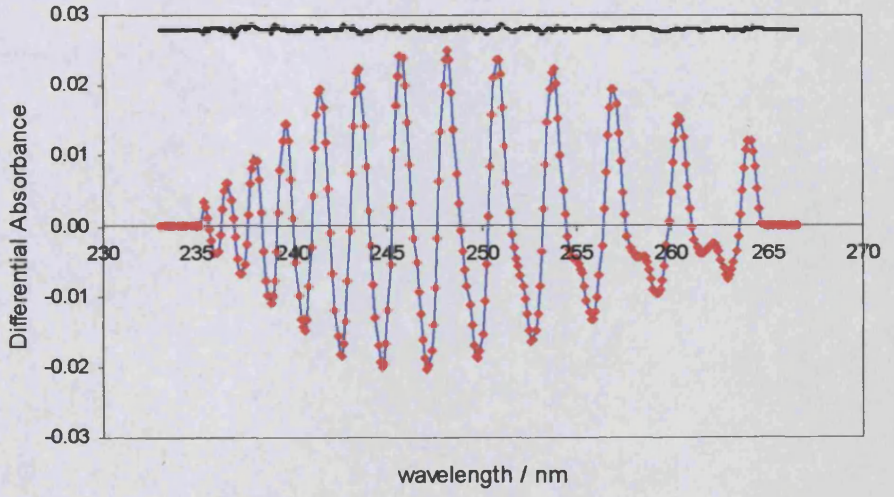

Figure 5.7: Differential fit of the ClO cross section (red) to the experimental ClO absorption cross section (blue). The residual to the fit, offset by 0.028 absorbance units, is shown in black.

5.3.3 Calibration of ClO absorption cross sections.

In the kinetic analysis of ClO temporal profiles, which show non-first order kinetic decay, knowledge of the absolute time resolved ClO concentration is essential. Thus, whilst absorption cross sections for the structured part of the ClO spectrum were taken from the extensive study of Boakes *et al.*,[6] an internal calibration of the cross sections was also carried out to check consistency with the reference cross-sections used. Further, it has also been reported that the differential absorption cross-sections of ClO are temperature dependent, albeit showing a very weak dependence over the comparatively narrow temperature range used in this study. Initially, as discussed below, all of the ClO temporal traces were analysed using 298 K absorption cross sections reported by Boakes *et al.* However, in refining the analysis, an investigation of the temperature dependence of the ClO absorption cross-sections was also carried out, encompassing the temperature range over which the ClO dimerisation was studied. The cross section determinations all adopted the same procedure, which is summarised here.

The absorption cross section of the vibronic bands in the ClO reference spectrum are known to be instrument resolution and temperature dependent as discussed in the previous section. However, since the ClO absorption band results in a predissociative transition, the spectrum at shorter wavelengths is smooth and unstructured. For this part of the spectrum, the resolution and temperature dependence of the absorption cross-sections are zero, and literature values of absorption cross sections for ClO (and for other absorbing species) in this region can be used to calibrate the structured region. A post flash spectrum recorded at a shorter wavelength setting is shown in Figure 5.8, below.

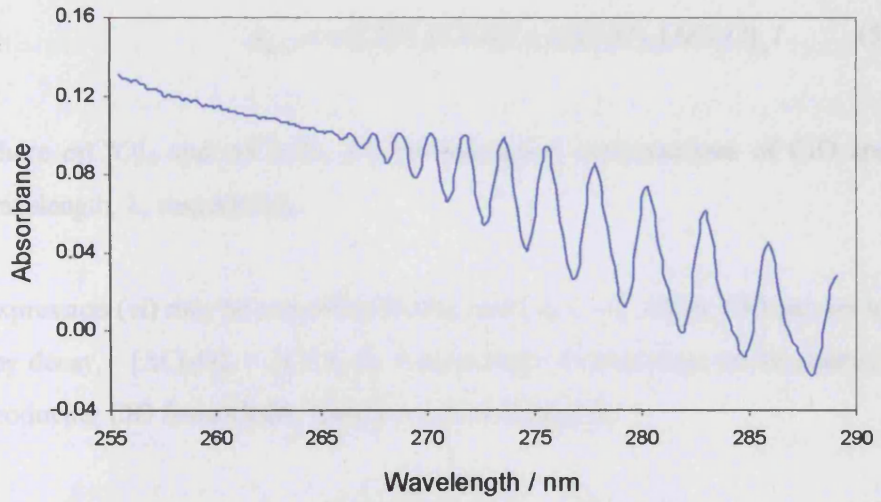

Figure 5.8: Typical post-flash spectrum of Br_2 / Cl_2O / Cl_2 / N_2 gas mixture recorded over wavelengths 255 – 290 nm

In the continuum region of the post-flash spectra (λ < 265 nm) the absorbance calculated relative to the preflash intensities consist of three contributions from ClO, Cl_2O_2, and the change in Cl_2O parent molecule. At any wavelength λ in this continuum, the time resolved evolution of this absorbance may therefore be expressed as:

$$A_{\lambda,t} = A(ClO)_{\lambda,t} + A(Cl_2O_2)_{\lambda,t} + A(\Delta Cl_2O)_{\lambda,t} \qquad (5.iv)$$

where ΔCl_2O represents the change in Cl_2O relative to the preflash spectrum. Immediately after photolysis, referred to as time t_0, ClO radicals have been produced but have not yet reacted and hence no Cl_2O_2 is present. Thus, expression (iv) simplifies to a two absorber system:

$$A_{\lambda,t_0} = A(ClO)_{\lambda,t_0} + A(\Delta Cl_2O)_{\lambda,t_0} \qquad (5.v)$$

Using the Beer-Lambert law, (v) becomes

$$A_{\lambda,t_0} = \sigma(ClO)_\lambda [ClO]_0 l + \sigma(Cl_2O)_\lambda [\Delta Cl_2O]_{t_0} l \qquad (5.vi)$$

where $\sigma(ClO)_\lambda$ and $\sigma(Cl_2O)_\lambda$ are the absorption cross-sections of ClO and Cl_2O at wavelength, λ, respectively.

Expression (vi) may be simplified further since at $t = 0$, where ClO has yet to undergo any decay, $[\Delta Cl_2O]_0 = [ClO]_0$ by stoichiometry (irrespective of the chemical scheme producing ClO from Cl_2O), therefore (vi) simplifies to:

$$A_{\lambda,t_0} = [ClO]_0 l \{\sigma(ClO)_\lambda - \sigma(Cl_2O)_\lambda\} \qquad (5.vii)$$

Hence the initially generated ClO concentration, $[ClO]_0$ can be expressed in terms of the t_0 absorbance in the continuum region at wavelength λ, the optical path length and the ClO and Cl_2O continuum cross-sections at λ:

$$[ClO]_o = \frac{A_{\lambda,0}}{\{\sigma(ClO)_\lambda - \sigma(Cl_2O)_\lambda\} l} \qquad (5.viii)$$

At higher wavelengths, where ClO absorption exhibits characteristic vibronic structure, the *differential* time zero ClO absorbance at any wavelength λ_2 results solely from the ClO radicals and may be expressed as:

$$A_{diff,\lambda_2} = \sigma(ClO)_{diff,\lambda_2} [ClO]_0 l \qquad (5.ix)$$

Rearranging (ix) to another expression for $[ClO]_0$ and combining with (viii) then yields a relationship of differential time zero absorbance at λ_2, and continuum time zero absorbance at λ, showing an expected proportionality:

$$A_{diff,\lambda_2,0} = \frac{\sigma(ClO)_{diff,\lambda_2}}{\{\sigma(ClO)_\lambda - \sigma(Cl_2O)_\lambda\}} \times A_{\lambda,0} \qquad (5.x)$$

Thus provided $A_{diff,\lambda_2,0}$ and $A_{\lambda,0}$ can be measured, a plot of $A_{diff,\lambda_2,0}$ *versus* $A_{\lambda,0}$ from a set of experiments with differing $[ClO]_0$ should be linear with a gradient determining $\{\sigma(ClO)_{diff,\lambda_2}/\{\sigma(ClO)_\lambda - \sigma(Cl_2O)_\lambda\}$.

In order to determine $A_{diff,\lambda_2,0}$, experiments were performed generating and monitoring ClO, with the sequential spectra fitted to an uncalibrated ClO spectrum. The resulting trace was then fitted to a realistic model of ClO dimerisation kinetics, albeit using arbitrary kinetic parameters. The purpose of this fitting was simply to enable the short back extrapolation of the trace to true t_0, which was required owing to the sliding averaging function imparted to the data from the CCD. Knowledge of the differential absorbance in the uncalibrated spectrum used to generate this trace and the amount of this spectrum fitted to the temporal trace at t_0 readily determined $A_{diff,\lambda_2,0}$. An example of the trace, fit and back extrapolation is given in Figure 5.9.

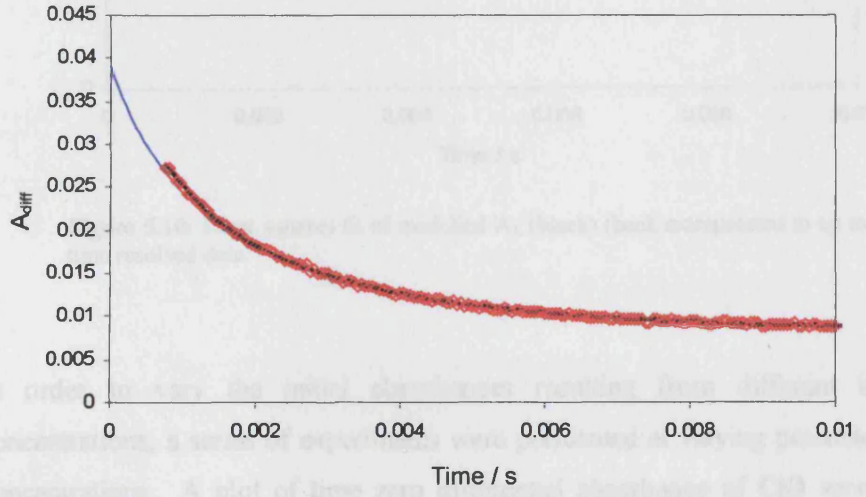

Figure 5.9: Least squares fit of modelled A_{diff} (black) to the time resolved data (red). The back extrapolation is indicated in blue.

In similar fashion, traces of absorbance *versus* time were produced from the CCD output and fitted, again using a model of ClO dimerisation, to a model of time

resolved absorbance in the spectral continuum. In this case, the model of absorbance contained contributions from all three absorbing species, and an example of this fit and back-extrapolation is given in Figure 5.10, below. In this case, the trace (recorded at 257.5 nm) is seen to show much less of a decay with time than the differential (ClO only) trace shown in Figure 5.9. This reflects the increasing contribution to the absorbance made by the Cl_2O_2 compensating for the loss in ClO absorbance as time elapses. Again, the short back extrapolation was required to account for the sliding averaging.

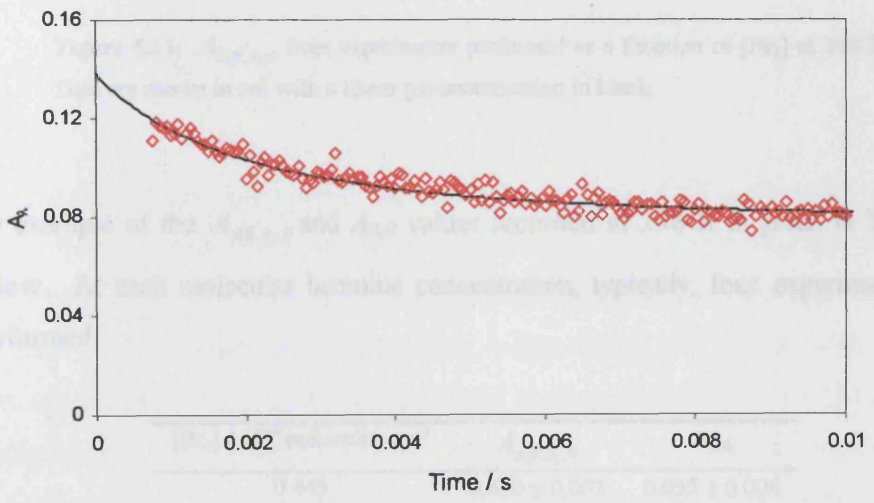

Figure 5.10: Least squares fit of modelled A_λ (black) (back extrapolated to t_0) to the time resolved data.

In order to vary the initial absorbances resulting from different initial ClO concentrations, a series of experiments were performed at varying precursor bromine concentrations. A plot of time zero differential absorbance of ClO *versus* $[Br_2]$ is given in Figure 5.11, below. As can be seen from the figure, and as designed in experimental conditions, the principal source of ClO in these experiments was bromine photolysis, with a small contribution - manifested as a small positive y-axis intercept from Cl_2 and Cl_2O photolysis.

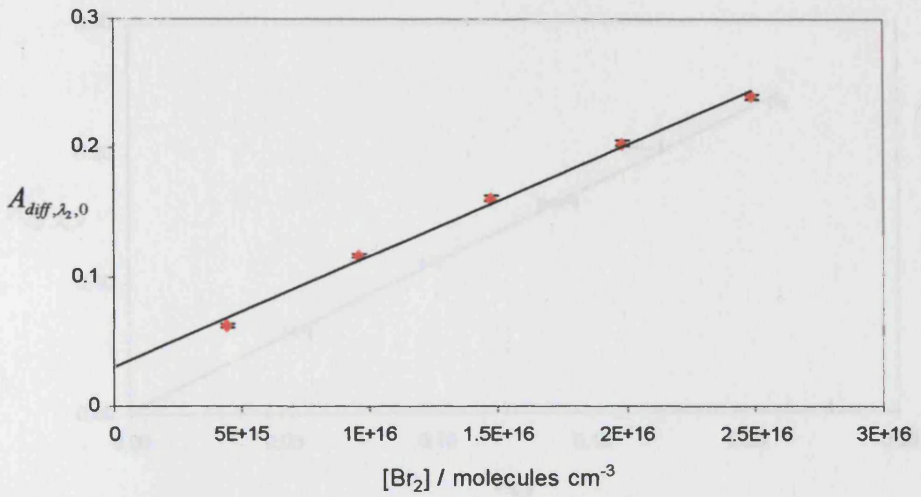

Figure 5.11: $A_{diff,\lambda_2,0}$ from experiments performed as a function of $[Br_2]$ at 298 K. Data are shown in red with a linear parameterisation in black.

An example of the $A_{diff,\lambda_2,0}$ and $A_{\lambda,0}$ values recorded at 298 K is given in Table 5.2 below. At each molecular bromine concentration, typically, four experiments were performed.

$[Br_2]$ / 10^{16} molecules cm^{-3}	$A_{diff,\lambda_2,0}$	$A_{\lambda,0}$
0.445	0.630 ± 0.002	0.055 ± 0.004
0.956	1.166 ± 0.001	0.098 ± 0.003
1.47	1.614 ± 0.002	0.140 ± 0.006
1.98	2.040 ± 0.002	0.167 ± 0.006
2.49	2.398 ± 0.002	0.211 ± 0.002

Table 5.2: Experimentally determined values of $A_{diff,\lambda_2,0}$ and $A_{\lambda,0}$ at 298K. Errors are 2σ, statistical only.

The resulting calibration plot for these data is shown in Figure 5.12. As can be seen, the calibration satisfies equation (x) well, showing excellent linearity and a zero intercept.

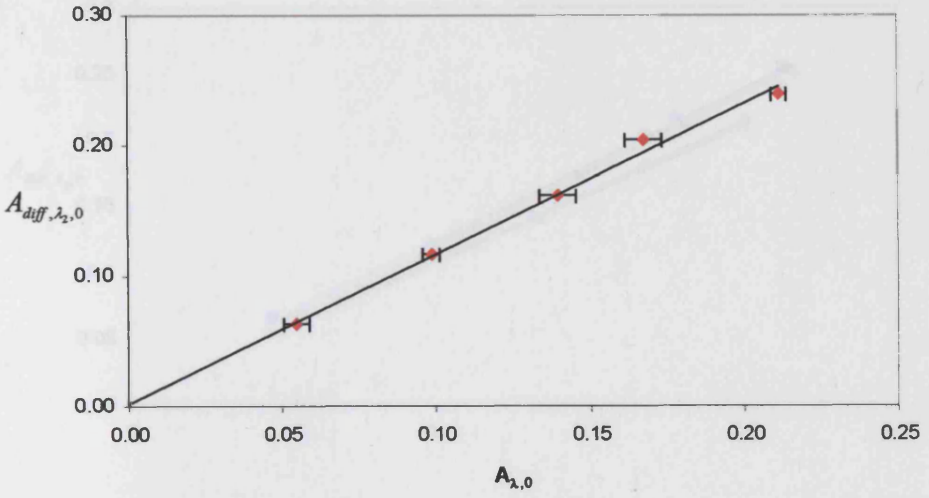

Figure 5.12: Calibration plot to determine $\sigma(ClO)_{diff}$ at 298 K.

As discussed above, the temperature dependence of the ClO differential absorption cross-sections has been reported to be very weak over the limited temperature range 280-310 K, and in the preliminary analysis of kinetic data, all traces were fitted using the 298 K ClO cross-sections. However, partly due to the stronger than expected gradient of initial ClO concentrations as a function of temperature (discussed in Section 5.4.1, below), but also in order to confirm or deny the existence of even a small temperature dependence of $\sigma(ClO)_{diff}$, further calibrations were performed. The ClO absorption cross-section calibration plots at five temperatures covering the total range of temperature used in the dimerisation kinetics studies are show in Figure 5.13. As can be seen, all of the plots show excellent linearity, and similar gradients, implying that $\sigma(ClO)_{diff}$ is indeed a weak function of temperature over this temperature range.

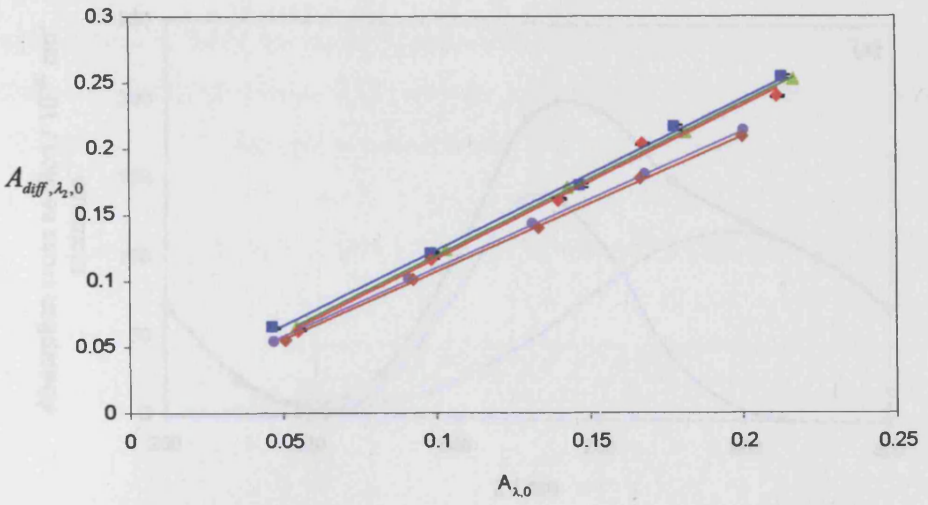

Figure 5.13: Calibration plots to determine $\sigma(ClO)_{diff}$ at 5 different temperatures. Data shown for 280 K (green), 288 K (blue), 298 K (red), 303 K, (purple), 310 K (brown).

Having determined the gradients of the calibration plots, equivalent to $\{\sigma(ClO)_{diff,\lambda_2}/\{\sigma(ClO)_\lambda - \sigma(Cl_2O)_\lambda\}$, literature values for the calibrating absorption cross-sections of ClO and Cl_2O in the spectral continuum were used to obtain absolute values of the ClO differential cross section. This analysis naturally required that the ClO spectra were adequately wavelength and dispersion calibrated, which is described in Section 5.3.3.1. The analysis also required a degree of interpolation of the ClO and Cl_2O cross-sections, which are typically reported at 10 nm intervals. The ClO and Cl_2O reference spectra were taken from the latest NASA JPL evaluation of photochemical data for atmospheric purposes. Previous determinations of the Cl_2O cross section are in good agreement,[21-24] the determination by Knauth[21] has been used in this study in accordance of the recommendation by the NASA publication.[5] Similarly, the reported unstructured ClO cross sections show good agreement. The mean determinations of Sander and Friedl,[15] Simon *et al.*,[24] Mandelman and Nicholls[25] and Trolier *et al.*[16] were used in this work. Single and multiple semilogarithmic Gaussian fitting was used to parameterise these reference cross sections, as shown in Figure 5.14. The temperature dependencies of the calibrating continua cross-sections have both been reported to be zero,[16] hence these 298 K calibrating cross-sections were used for the analysis of all of the data.

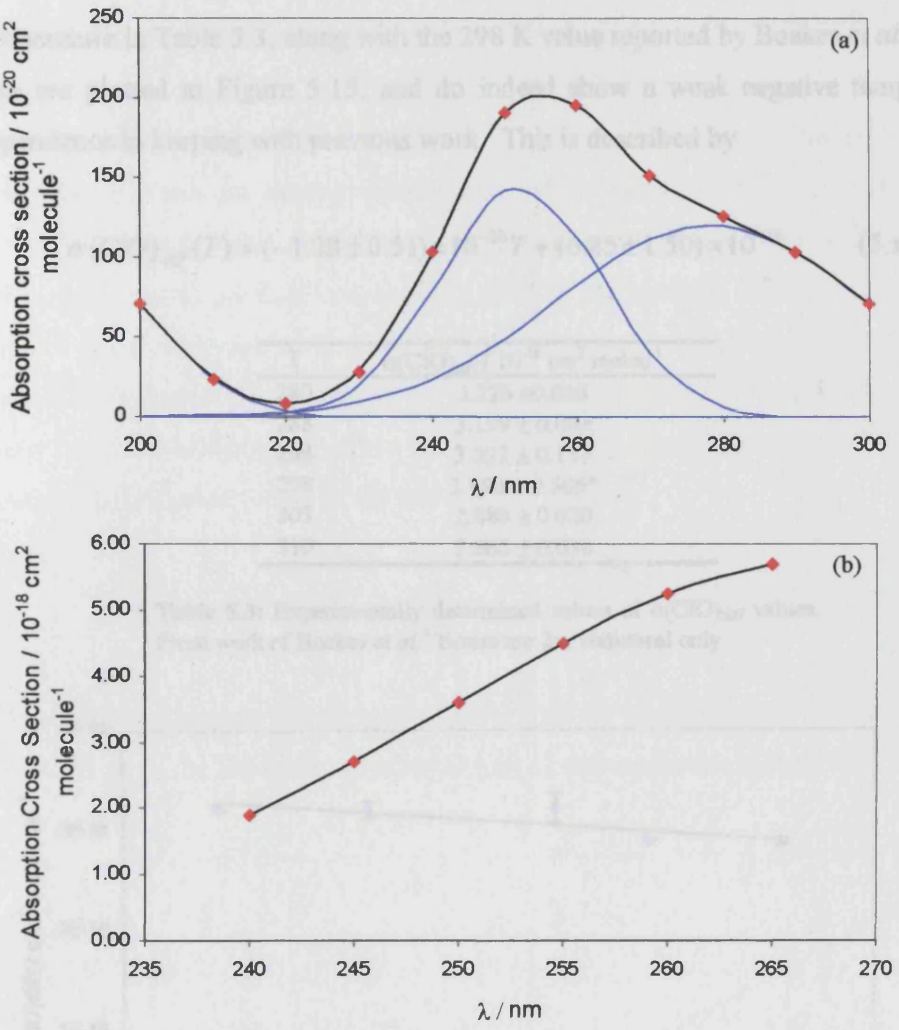

Figure 5.14: Gaussian fits to literature absorption cross sections (a) Cl_2O– NASA values (red), 3 Gaussians used to fit (blue) and fit (black), (b) ClO – NASA values (red) and Gaussian fit (black).

The single continuum wavelength chosen for calibration of the ClO cross sections was 257.5 nm. This wavelength was chosen to maximise the amount of ClO vibronic structure recorded by the CCD, but also following the recommendations of Boakes *et al.*, who report some minor inconsistencies with the ClO differential absorption cross-section as a function of calibrating wavelength.[6]

The absolute differential cross sections of ClO, reported between the (12, 0) peak at 275.2 nm and the trough at higher wavelengths are given below as a function of

temperature in Table 5.3, along with the 298 K value reported by Boakes *et al.* These data are plotted in Figure 5.15, and do indeed show a weak negative temperature dependence in keeping with previous work. This is described by

$$\sigma(ClO)_{diff}(T) = (-1.28 \pm 0.51) \times 10^{-20} T + (6.85 \pm 1.50) \times 10^{-18} \quad \text{(5.xi)}$$

T	$\sigma(ClO)_{diff}$ / 10^{-18} cm^2 molec^{-1}
280	3.225 ±0.038
288	3.189 ± 0.084
298	3.222 ± 0.147
298	3.890 ± 0.505*
303	2.886 ± 0.020
310	2.866 ± 0.038

Table 5.3: Experimentally determined values of $\sigma(ClO)_{diff}$ values. From work of Boakes *et al.*[6] Errors are 2σ, statistical only

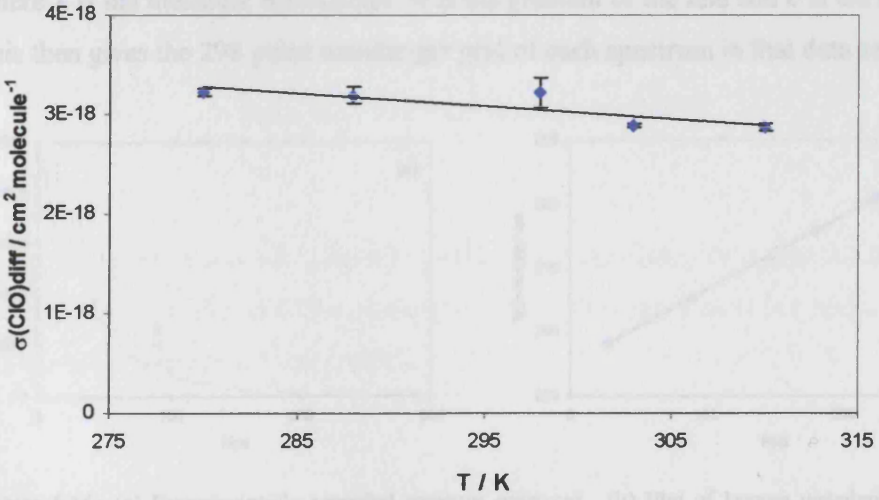

Figure 5.15: Measured temperature dependence of $\sigma(ClO)_{diff}$ (blue) and linear parameterisation (black).

It should be stressed that whilst differential cross-sections are reported for a single peak and the adjacent trough, the entire ClO differential spectrum is calibrated in this way, and used to fit to the ClO temporal traces at the appropriate temperature, for kinetic analysis.

5.3.3.1 Wavelength Calibration

For each set of data recorded, a spectrum of a low-pressure mercury pen ray lamp was also taken to calibrate the wavelength scale of the recorded spectra, an example is shown in Figure 5.16(a). This is necessary because even small irreproducibility in the diffraction grating position can cause a shift in the spectral coverage. The sharp distinct peaks observed in the mercury spectrum can be inspected in comparison to equivalent literature wavelength values. The exact pixel numbers at which the peaks occur are noted and plotted against the corresponding literature wavelengths to gain a straight line, Figure 5.16(b), of the form:

$$\lambda = (m \times pixel) + c \qquad (5.xii)$$

where λ is the literature wavelength, m is the gradient of the line and c is the intercept. This then gives the 298 point wavelength grid of each spectrum in that data set.

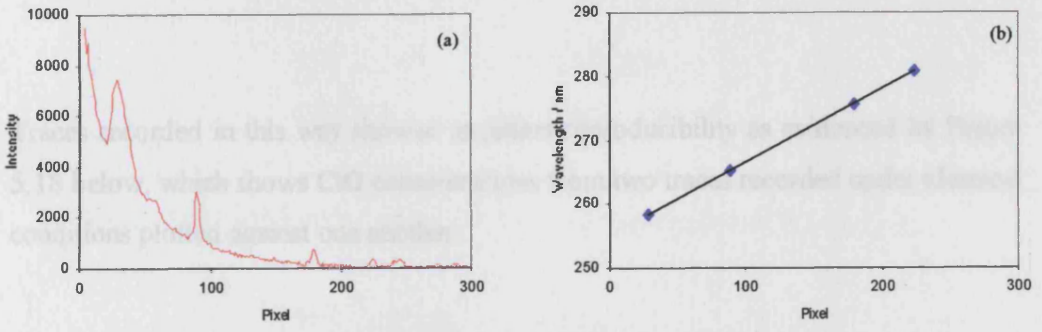

Figure 5.16: (a) Experimentally recorded mercury spectrum. (b) Plot of known wavelengths of Hg peaks *versus* CCD pixel number (blue) and linear parameterisation (black) used to calibrate wavelength of experimental spectra.

5.3.4 Kinetics of the ClO + ClO dimerisation

ClO dimerisation kinetics were investigated at atmospheric pressure and as a function of temperature at 13 temperatures over the range 280 - 310 K. ClO traces were initially analysed using 298 K absorption cross sections, and a typical ClO temporal

trace is shown in Figure 5.17. As can be seen from this trace ClO radical concentrations decay to a nonzero equilibrium value, consistent with equilibration between ClO and the Cl_2O_2 dimer:

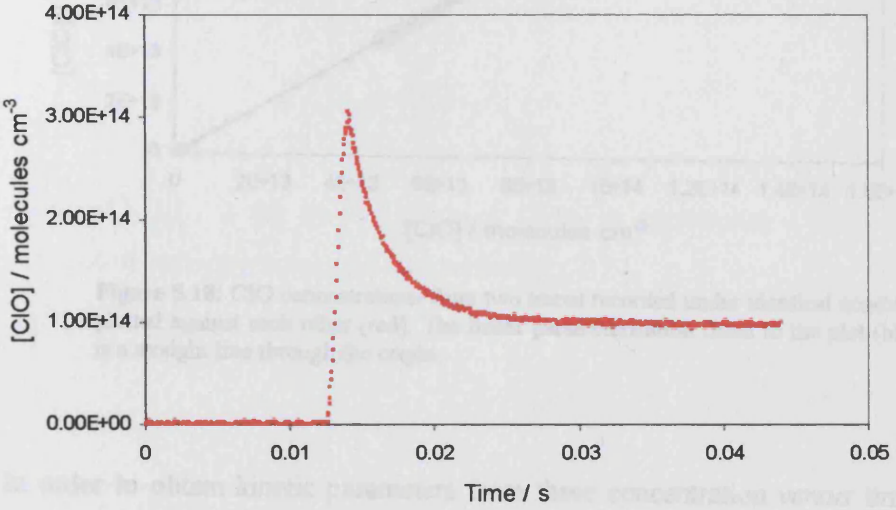

Figure 5.17: Typical $[ClO]_t$ decay trace at 298 K

Traces recorded in this way showed excellent reproducibility as evidenced by Figure 5.18 below, which shows ClO concentrations from two traces recorded under identical conditions plotted against one another.

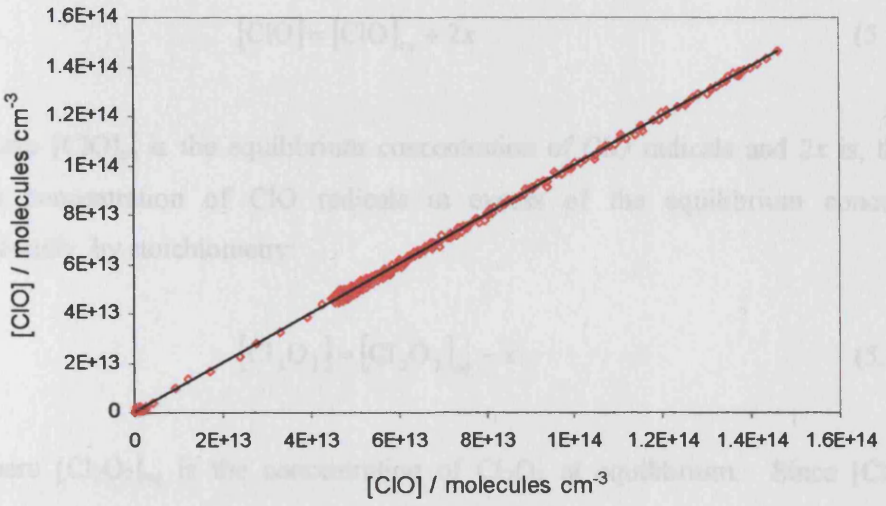

Figure 5.18: ClO concentrations from two traces recorded under identical conditions plotted against each other (red). The linear parameterisation fitted to the plot (black) is a straight line through the origin

In order to obtain kinetic parameters from these concentration *versus* time traces, a kinetic model is fitted to the data. The reactions of interest in the model are:

$$ClO + ClO \rightarrow ClOOCl \qquad (5.2a)$$

$$ClOOCl \rightarrow ClO + ClO \qquad (5.\text{-}2a)$$

The differential equation describing the temporal behaviour of ClO decay is:

$$-\frac{1}{2}\frac{d[ClO]}{dt} = \frac{d[Cl_2O_2]}{dt} = k_{2a}[ClO]^2 - k_{-2a}[Cl_2O_2] \qquad (5.\text{xiii})$$

The solution to this differential equation is complex and as a result most studies have focussed on low temperature studies ($T < 250$ K) where k_{-2a} becomes negligible, and the dimer is effectively stable. At such low temperatures, the kinetics can be adequately described by a simple second order solution. However, an exact solution to the differential equation needed for higher temperature analysis *can* be evaluated by making the substitution:

$$[ClO] = [ClO]_{eq} + 2x \qquad (5.xiv)$$

where $[ClO]_{eq}$ is the equilibrium concentration of ClO radicals and $2x$ is, therefore, the concentration of ClO radicals in excess of the equilibrium concentration. Secondly, by stoichiometry:

$$[Cl_2O_2] = [Cl_2O_2]_{eq} - x \qquad (5.xv)$$

where $[Cl_2O_2]_{eq}$ is the concentration of Cl_2O_2 at equilibrium. Since $[Cl_2O_2]_{eq}$ is constant the rate equation can be simplified to:

$$\frac{d[Cl_2O_2]}{dt} = -\frac{dx}{dt} = k_{2a}[ClO]^2 - k_{-2a}[Cl_2O_2] \qquad (5.xvi)$$

Substituting (xiv) and (xv) into (xvi) yields:

$$-\frac{dx}{dt} = k_{2a}([ClO]_{eq} + 2x)^2 - k_{-2a}([Cl_2O_2]_{eq} - x) \qquad (5.xvii)$$

Furthermore, by definition, the equilibrium constant is given by the following expression:

$$K_{2a} = \frac{k_{2a}}{k_{-2a}} = \frac{[Cl_2O_2]_{eq}}{[ClO]_{eq}^2} \qquad (5.xviii)$$

This can be conveniently rearranged to:

$$k_{2a}[ClO]_{eq}^2 = k_{-2a}[Cl_2O_2]_{eq} \qquad (5.xix)$$

Expanding (xvii) and substituting (xix) into the resulting expression gives:

$$-\frac{dx}{dt} = 4k_{2a}[\mathrm{ClO}]_{eq}x + 4k_{2a}x^2 + k_{-2a}x \qquad (5.xx)$$

Hence,

$$\frac{dx}{x\left(4k_{2a}[\mathrm{ClO}]_{eq} + 4k_{2a}x + k_{-2a}\right)} = -dt \qquad (5.xxi)$$

This is a differential equation of the form:

$$\frac{dx}{x(a+bx)} = -dt$$

where constants a and b are defined as:

$$a = 4k_{2a}[ClO]_e + k_{-2a} \quad \text{and} \quad b = 4k_{2a}$$

Integrating gives:

$$\int_{x_0}^{x_t} \frac{dx}{x(a+bx)} = -\int_0^t dt$$

$$-\frac{1}{a}\ln\left(\frac{a+bx_t}{x_t}\right) + \frac{1}{a}\ln\left(\frac{a+bx_0}{x_0}\right) = -t$$

$$\ln\left(\frac{a+bx_0}{x_0}\cdot\frac{x_t}{a+bx_t}\right) = -at$$

Thus:

$$x_t = \frac{ax_0 \exp(-at)}{a + bx_0 - bx_0 \exp(-at)} \qquad (5.xxii)$$

and (xiv) converts x_t to the experimental quantity, $[ClO]_t$.

$$[ClO]_t = [ClO]_{eq} + 2x_t \qquad (5.xiv)$$

This is the exact solution to the rate equation and was used to simulate ClO decay. Least squares fitting was employed to minimise the residuals between the experimental and simulated ClO traces by allowing the kinetic parameters ($[ClO]_0$, k_{2a}, and k_{-2a}) to vary. A typical fit is shown in Figure 5.19.

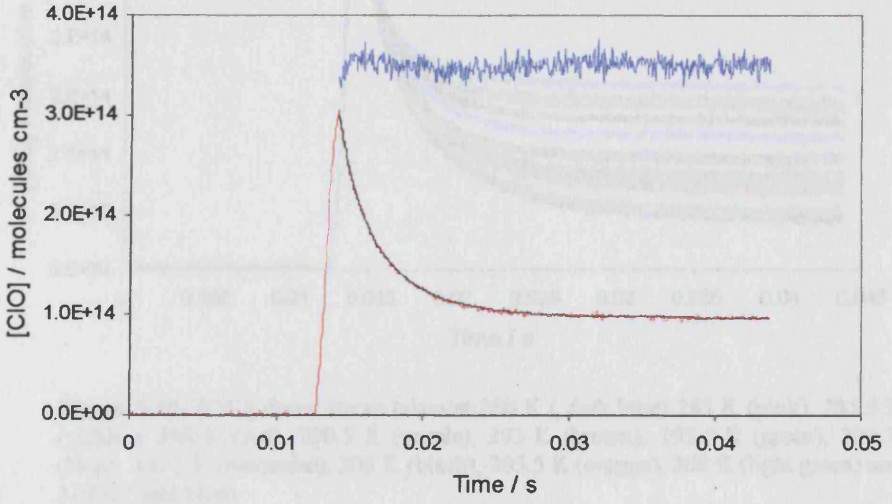

Figure 5.19: Typical [ClO] *versus* time decay trace (red) and classical fit (black). The residual of the fit is also shown (blue) offset by 3.5×10^{14} and multiplied by 5, for clarity.

As can be seen from Figure 5.19, the quality of the fit between the model and the data was very good. The model yielded values of k_{2a}, k_{-2a}, and $[ClO]_0$. From these parameters the equilibrium constant K_c was evaluated according to

$$K_c = \frac{k_{2a}}{k_{-2a}} \qquad \text{(5.xxiii)}$$

ClO traces were recorded and analysed at thirteen temperatures in the range 280 – 310 K. A collection of traces recorded at different temperatures but under identical conditions is shown in Figure 5.20, below. Clearly, the equilibrium concentration of ClO is a strong function of temperature, allowing investigation of the equilibrium constant for ClO dimerisation, discussed below.

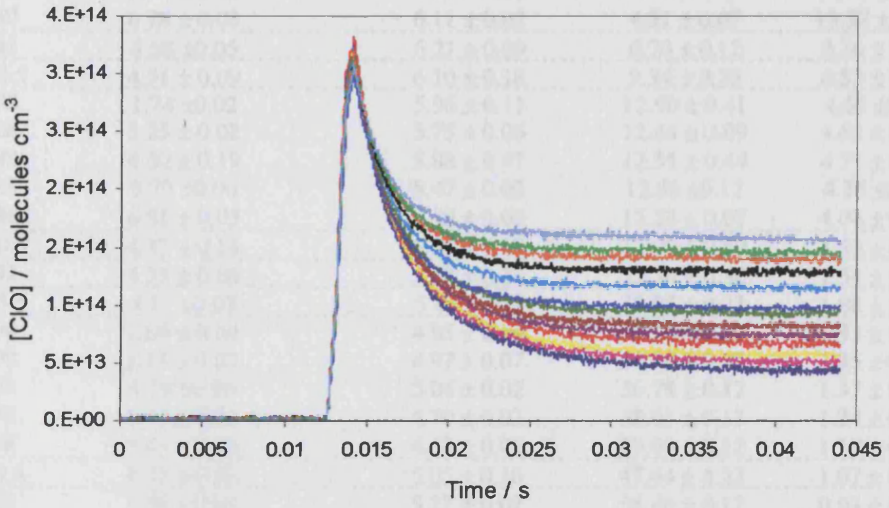

Figure 5.20: [ClO] decay traces taken at 280 K (dark blue) 283 K (pink), 285.5 K (yellow), 288 K (red), 290.5 K (purple), 293 K (brown), 295.5 K (green), 298 K (blue), 300.5 K (turquoise), 303 K (black), 305.5 K (orange), 308 K (light green) and 310 K (light blue).

5.4 Results

5.4.1 Preliminary Analysis

Results from a simple kinetic analysis of ClO decays, fitted to equation (xxii) are summarised in Table 5.4 below. The full list of results is in Appendix 1. Kinetic parameters were recorded as a function of temperature (280 – 310 K) at thirteen temperatures and as a function of molecular bromine concentration ($0.5 - 2.5 \times 10^{16}$ molecules cm^{-3}) at five temperatures encompassing the total experimental temperature range. All traces were recorded at atmospheric pressure.

T / K	$[ClO]_o$ / 10^{14} molecules cm^3	k_{2a} / 10^{13} $molec^{-1}$ cm^3 s^{-1}	k_{-2a} / s^{-1}	K_c / 10^{-14} cm^3 $molec^{-1}$
280	1.74 ± 0.06	6.65 ±0.02	3.48 ±0.16	19.09 ± 0.86
280	3.33 ± 0.06	6.46 ± 0.04	3.97 ± 0.15	16.30 ± 0.55
280	4.65 ± 0.19	6.36 ± 0.29	4.32 ± 0.26	14.73 ± 0.78
280	5.70 ± 0.03	6.18 ± 0.01	4.46 ± 0.07	13.87 ± 0.24
280	6.78 ± 0.03	6.11 ± 0.02	4.51 ± 0.07	13.57 ± 0.23
283	4.58 ±0.05	6.21 ± 0.09	6.70 ± 0.12	9.26 ± 0.14
285.5	4.51 ± 0.09	6.10 ± 0.18	9.34 ± 0.26	6.53 ± 0.29
288	1.74 ±0.02	5.96 ± 0.11	12.90 ± 0.41	4.62 ±0.09
288	3.25 ± 0.02	5.75 ± 0.06	12.44 ± 0.09	4.62 ± 0.06
288	4.50 ± 0.19	5.88 ± 0.47	12.51 ± 0.44	4.71 ± 0.50
288	5.79 ±0.06	5.47 ± 0.02	12.85 ±0.12	4.26 ±0.05
288	6.81 ± 0.03	5.39 ± 0.03	13.23 ± 0.07	4.08 ± 0.04
290.5	4.37 ± 0.14	5.80 ± 0.12	17.09 ± 0.50	3.39 ± 0.08
293	4.25 ± 0.06	5.68 ± 0.21	22.36 ± 0.36	2.54 ± 0.11
295.5	4.17 ±0.03	5.47 ±0.07	29.05 ± 0.23	1.88 ± 0.04
298	1.69 ± 0.04	4.93 ± 0.49	37.26 ± 1.81	1.33 ± 0.18
298	3.13 ± 0.02	4.97 ± 0.07	36.88 ± 0.35	1.35 ± 0.02
298	4.19 ±0.06	5.04 ± 0.02	36.78 ± 0.12	1.37 ± 0.05
298	5.47 ± 0.06	4.70 ± 0.02	38.01 ± 0.12	1.24 ± 0.05
298	6.43 ± 0.06	4.62 ± 0.02	39.00 ± 0.12	1.19 ± 0.05
300.5	4.03 ± 0.10	5.05 ± 0.16	47.44 ± 4.22	1.07 ± 0.09
303	1.46 ± 0.06	5.27 ± 0.02	56.40 ± 0.12	0.93 ± 0.05
303	2.73 ±0.02	5.10 ± 0.06	56.21 ± 0.71	0.91 ± 0.01
303	3.89 ± 0.06	4.87 ± 0.02	58.39 ± 0.12	0.84 ± 0.05
303	4.84 ± 0.06	4.73 ± 0.02	58.22 ±0.12	0.81 ± 0.05
303	5.72 ± 0.06	4.54 ± 0.02	59.78 ± 0.12	0.76 ± 0.05
305.5	3.88 ± 0.08	4.53 ± 0.15	71.73 ± 2.69	0.632 ± 0.02
308	3.79 ± 0.07	4.49 ± 0.39	87.63 ± 2.97	0.512 ± 0.04
310	1.51 ± 0.05	4.33 ± 0.19	100.43 ±3.32	0.43 ± 0.01
310	2.72 ± 0.04	4.15 ± 0.10	100.41 ± 1.10	0.41 ± 0.01
310	3.71 ± 0.13	4.12 ± 0.22	103.33 ± 7.22	0.40 ± 0.04
310	4.76 ± 0.05	3.82 ± 0.06	104.08 ± 0.33	0.37 ± 0.01
310	5.61 ± 0.03	3.80 ± 0.03	106.77 ± 0.81	0.36 ± 0.00

Table 5.4: Determinations of k_{2a}, k_{-2a} and $K_{2a,c}$ using classical analysis. Errors are quoted as 2σ, statistical only.

As can be seen from Table 5.4, no significant systematic variation of k_{2a}, k_{-2a} or $K_{2a,c}$ could be seen with molecular bromine concentration over the range adopted. By contrast, the initial ClO radical concentration, which showed proportionality with bromine concentration, as shown above (Figure 5.11), did exhibit an apparent temperature dependence at a fixed flow of bromine, shown in Figure 5.21.

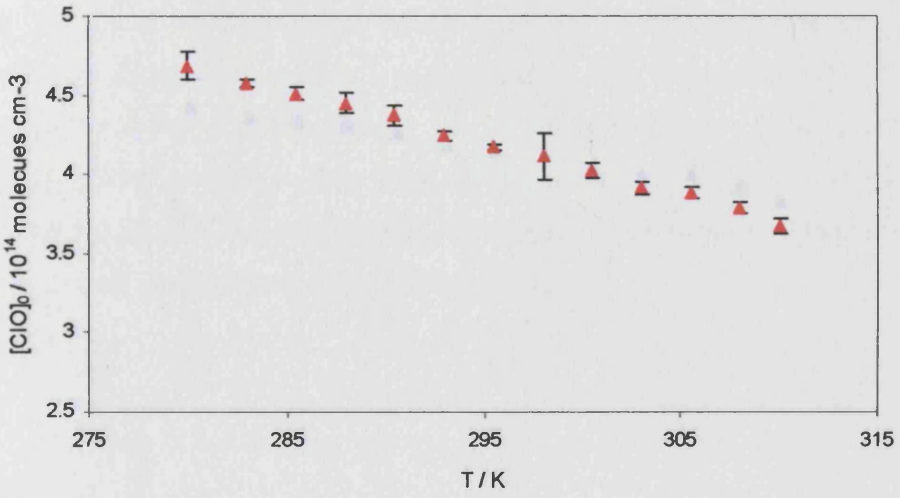

Figure 5.21: Plot of average initial ClO concentration as a function of temperature

This dependence was initially rationalised by considering the simple change in absolute number densities of precursor gases (N / V) as a function of temperature at a fixed pressure. Hence, it should be possible to correct for this by multiplying [ClO] concentrations by a factor of 298/T:

$$[ClO]c = [ClO](T)\frac{298}{T} \qquad \text{(5.xxiv)}$$

However, as can be seen from Figure 5.22, even after this normalisation had been applied, there is still a significant dependence of $[ClO]_0$ on temperature. This gradient was attributed to the temperature dependence of the ClO cross-section, since, in this preliminary analysis, all of the ClO temporal traces were analysed using 298 K

absorption cross sections reported by Boakes *et al.* However, as discussed above in Section 5.3.3, the ClO cross-sections are reported to have weak temperature dependence over this narrow temperature range. Therefore, a second, refined analysis was carried out which took into consideration the temperature dependence of the ClO cross section. This is described in the next section.

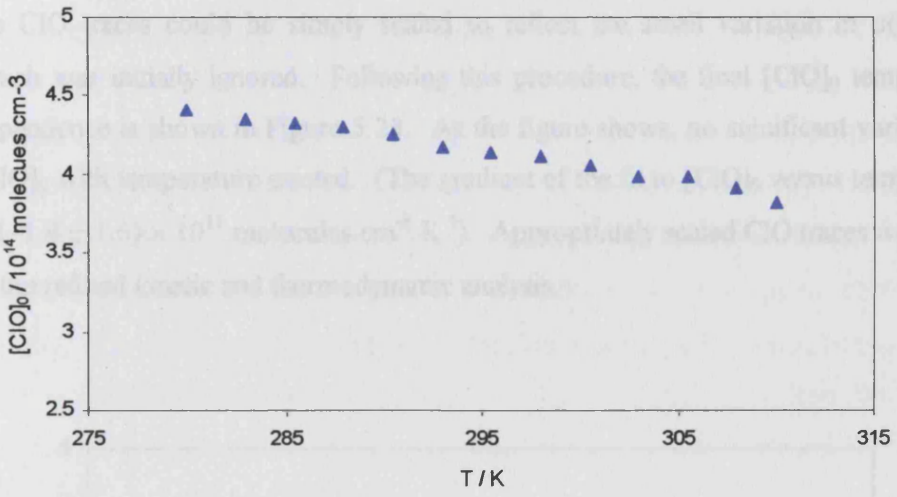

Figure 5.22: Plot of average $[ClO]_0$ concentration corrected for N/V as a function of temperature.

5.4.2 Refined Analysis

As discussed above, even after having accounted for some of the variation in the initial ClO concentration with temperature by considering absolute number densities (equivalent to correcting for the same absolute number density of molecular bromine), Figure 5.22, above, shows that $[ClO]_0$ still exhibits a small negative temperature dependence. This initially surprising result was the motivation for investigating the temperature dependence of the ClO absorption cross sections despite the very narrow temperature range over which the experiments were performed. In keeping with the work of Boakes *et al.*,[6] and other authors including Bloss *et al.*,[17] the ClO absorption cross sections do show a weak negative temperature dependence, (Figure 5.15, above)

which must also be accounted for. Conversely, without accounting for this temperature dependence, as in the initial analysis of data, the existence of larger ClO cross-sections than used at lower than ambient temperatures, and *vice versa* at higher temperatures would indeed impart a negative temperature dependence to the apparent ClO concentrations as was observed. A full reanalysis of the temperature dependent ClO traces, using temperature dependent cross sections normalised to the dependence of these cross sections, as shown in Figure 5.15, was not required, however. Rather, the ClO traces could be simply scaled to reflect the small variation in $\sigma(ClO)_{diff}$, which was initially ignored. Following this procedure, the final $[ClO]_0$ temperature dependence is shown in Figure 5.23. As the figure shows, no significant variation of $[ClO]_0$ with temperature existed. (The gradient of the fit to $[ClO]_0$ *versus* temperature is $(-1.4 \pm 1.6) \times 10^{11}$ molecules cm^{-3} K^{-1}). Appropriately scaled ClO traces were used in the refined kinetic and thermodynamic analysis.

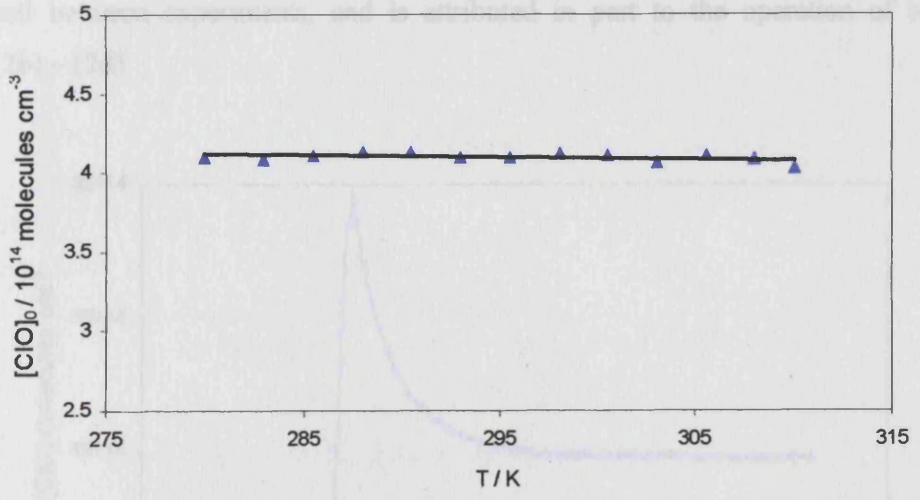

Figure 5.23: Plot of average $[ClO]_0$ concentration (corrected for number density and ClO cross section dependence on temperature) as a function of temperature

As discussed in Section 5.4.2.1, below, this study of the dimerisation of ClO radicals was naturally temperature limited at low temperatures due to sensitivity to k_{-2a}, and at

high temperatures due to the existence of additional bimolecular channels of the ClO self-reaction:

$$ClO + ClO \rightarrow Cl_2 + O_2 \quad (5.2b)$$

$$\rightarrow ClOO + Cl \quad (5.2c)$$

$$\rightarrow OClO + Cl \quad (5.2d)$$

Whilst these channels are very slow at ambient temperature ($k_{2b+2c+2d} = 0.03k_{2a}$ at 298 K and 760 Torr), they are all known to possess positive activation energies and hence their small contribution to the ClO decay will increase as temperature increases. As an illustration of the effect of the bimolecular channels of ClO decay, Figures 5.24 – 5.30 show experimental ClO decay traces recorded on progressively longer timescales – by changing the shift time of the CCD over the range of 50 μs to 2000 μs – at 298 K. The clear non-zero gradient of the 'equilibrium' ClO concentration at long times is greater than can be accounted for by the flowout of gases from the reaction cell between experiments, and is attributed in part to the operation of reactions (2b) – (2d)

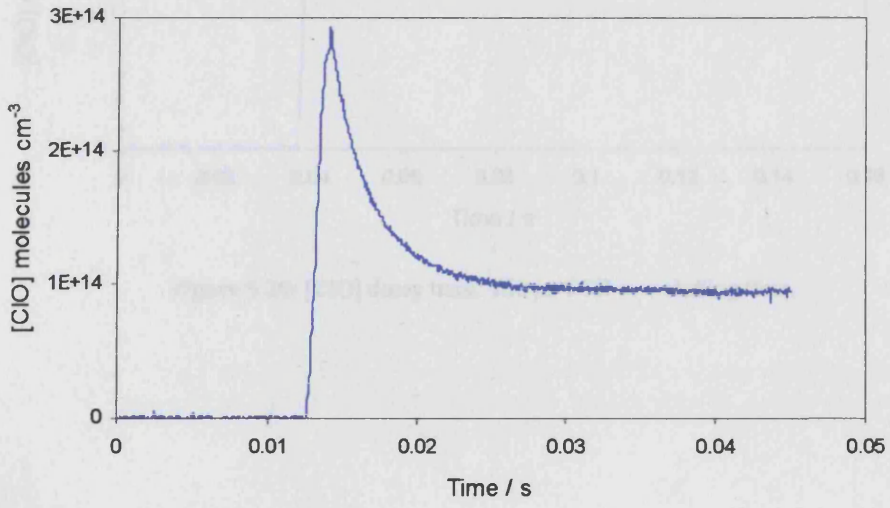

Figure 5.24: [ClO] decay trace: 50 μs CCD row shifting time.

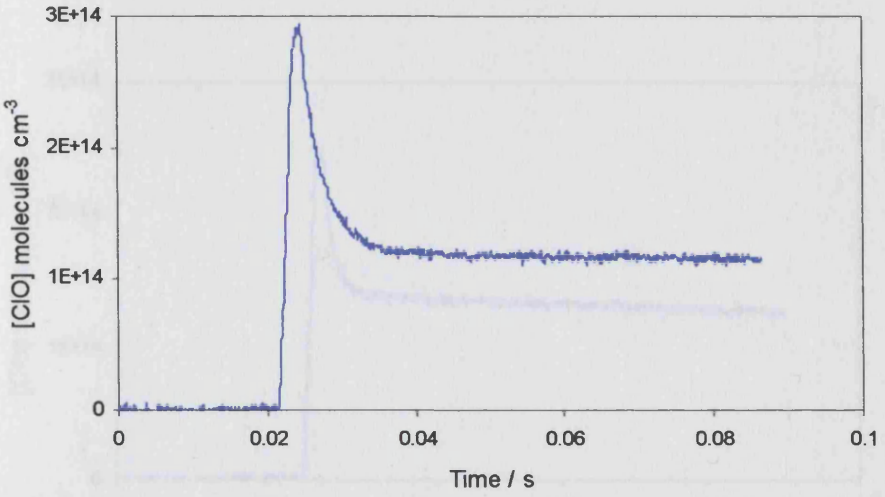

Figure 5.25: [ClO] decay trace: 100 μs CCD row shifting time.

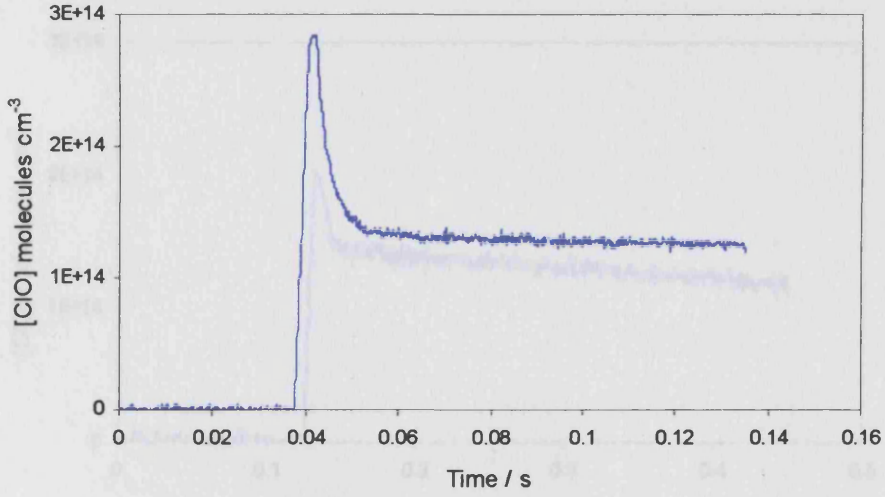

Figure 5.26: [ClO] decay trace: 150 μs CCD row shifting time.

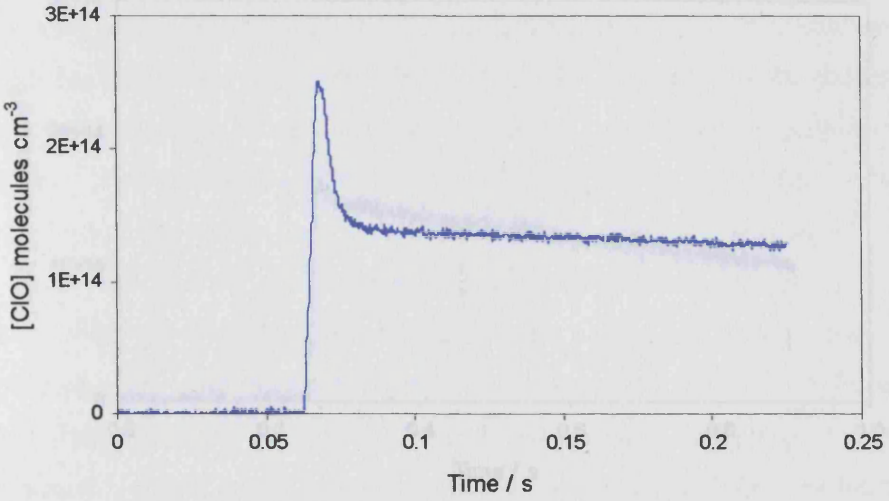

Figure 5.27: [ClO] decay trace: 250 μs CCD row shifting time.

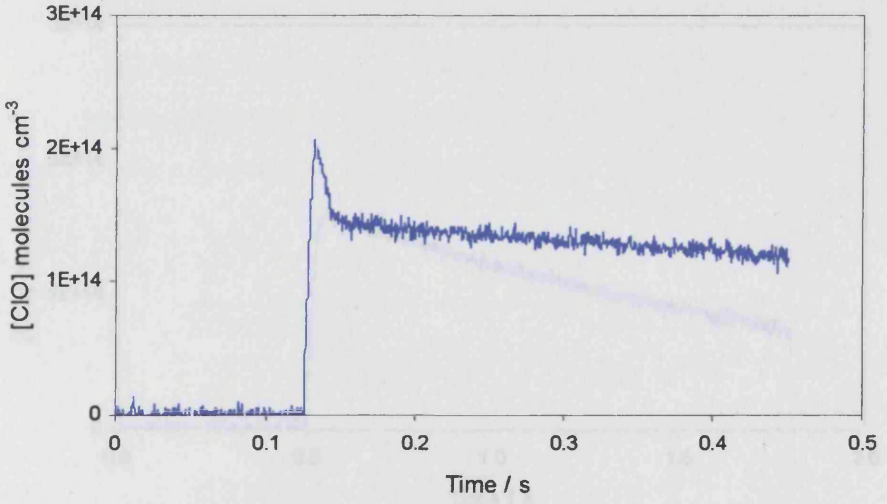

Figure 5.28: [ClO] decay trace: 500 μs CCD row shifting time. (Note: signal to noise ratio decreased as light levels were decreased to prevent detector saturation. This effect is also apparent in Figures 5.29 and 5.30.)

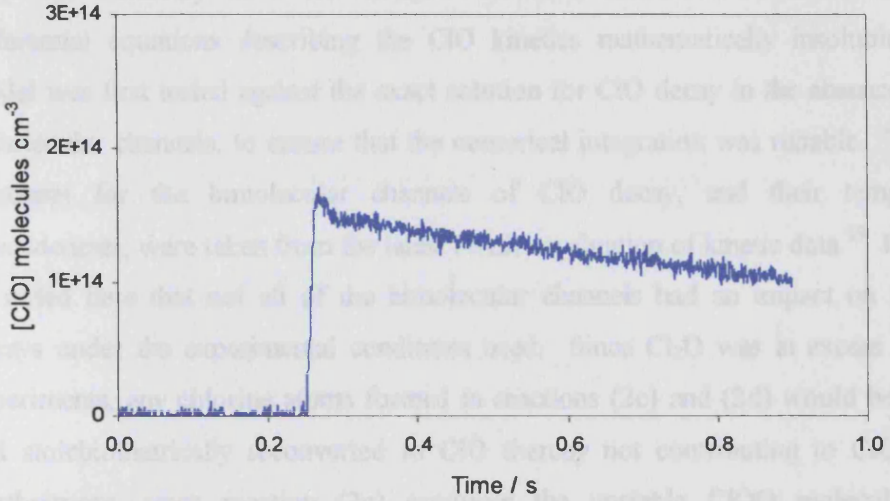

Figure 5.29: [ClO] decay trace: 1000 μs CCD row shifting time.

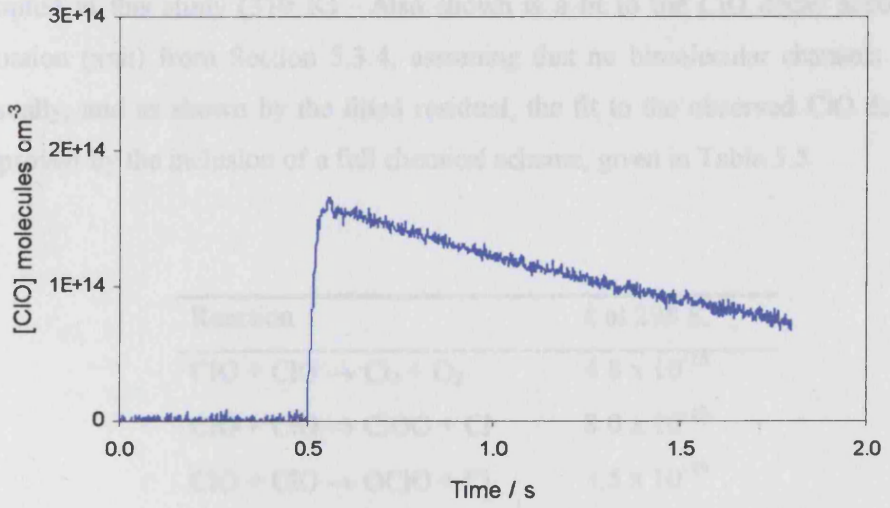

Figure 5.30: [ClO] decay trace: 2000 μs CCD row shifting time.

To account for the small contribution to the ClO decay from reactions (2b) – (2d), a full model of ClO formation and decay was constructed using numerical integration.

This was necessary since the existence of these additional reactions made the differential equations describing the ClO kinetics mathematically insoluble. The model was first tested against the exact solution for ClO decay in the absence of any bimolecular channels, to ensure that the numerical integration was reliable. The rate constants for the bimolecular channels of ClO decay, and their temperature dependencies, were taken from the latest NASA evaluation of kinetic data.[19] It should be noted here that not all of the bimolecular channels had an impact on the ClO decays under the experimental conditions used. Since Cl_2O was in excess in these experiments, any chlorine atoms formed in reactions (2c) and (2d) would be rapidly and stoichiometrically reconverted to ClO thereby not contributing to ClO decay. Furthermore, since reaction (2c) produces the unstable ClOO molecule, itself decomposing to Cl + O_2, this reaction channel effectively disappeared from the observed ClO decay kinetics, along with half of the reaction channel producing OClO. Figure 5.31 shows a fit to a ClO decay trace recorded at the highest temperature adopted in this study (310 K). Also shown is a fit to the ClO decay according to equation (xxii) from Section 5.3.4, assuming that no bimolecular channels operate. Visually, and as shown by the fitted residual, the fit to the observed ClO decay was improved by the inclusion of a full chemical scheme, given in Table 5.5.

Reaction	k at 298 K
$ClO + ClO \rightarrow Cl_2 + O_2$	4.8×10^{-15}
$ClO + ClO \rightarrow ClOO + Cl$	8.0×10^{-15}
$ClO + ClO \rightarrow OClO + Cl$	3.5×10^{-15}
$ClO + ClO \rightarrow ClOOCl$	Optimised

Table 5.5: Chemical reactions coded into the bimolecular model for ClO formation data,. All units are $cm^3 molecule^{-1} s^{-1}$. All rate constants taken from the latest NASA evaluation of kinetic data.[19]

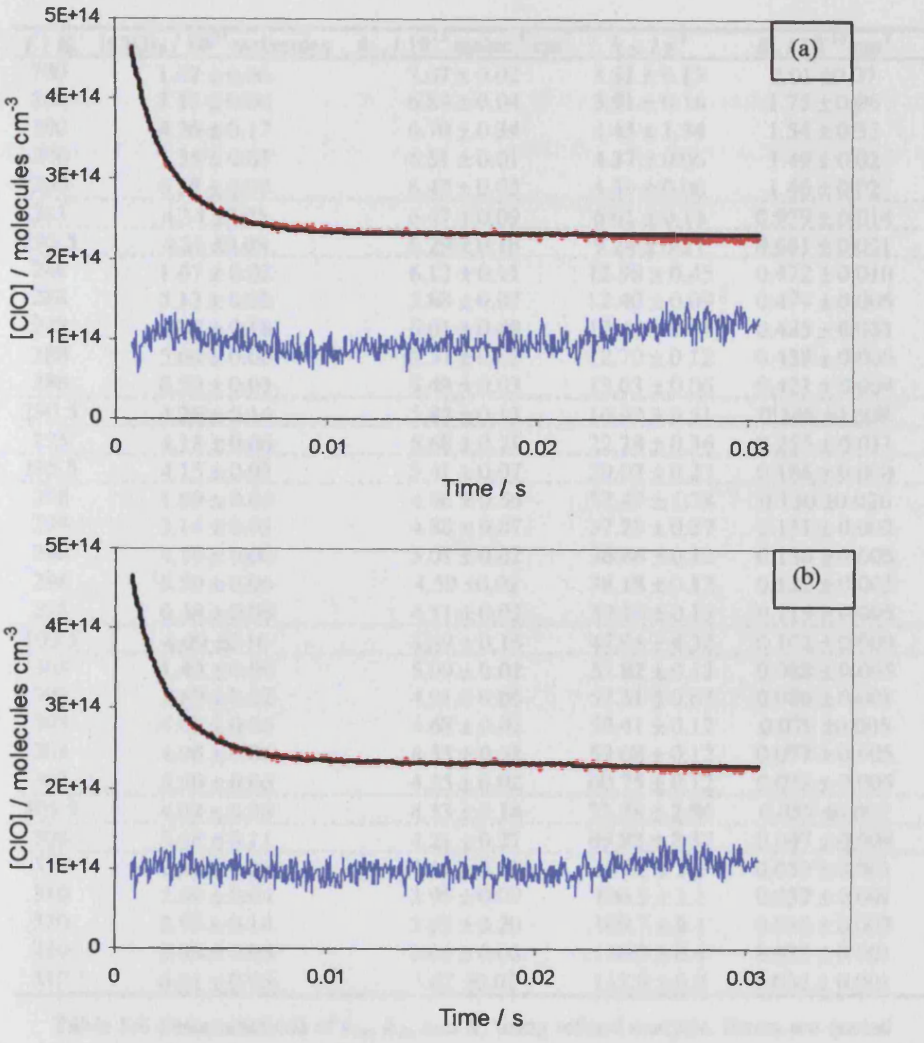

Figure 5.31: [ClO] decay traces (red) and modelled fits (black) at 310 K (a) classical model – neglecting bimolecular channels and (b) model including bimolecular channels. The residuals to the fits, multiplied by 5 and offset by 1×10^{14} molecules cm^{-3} are also shown (blue).

The kinetic parameters for ClO dimerisation obtained from a fit to traces using temperature dependent cross-sections and employing a full chemical model are listed in Appendix 2 and are summarised in Table 5.6, below.

T / K	$[ClO]_0$ / 10^{14} molecules	k_{2a} / 10^{13} molec^{-1} cm^3	k_{-2a} / s^{-1}	K_c / 10^{-13} cm^3
280	1.62 ± 0.06	7.07 ± 0.02	3.52 ± 0.13	2.01 ±0.07
280	3.11 ± 0.06	6.84 ± 0.04	3.91 ± 0.16	1.75 ± 0.06
280	4.36 ± 0.17	6.70 ± 0.34	4.43 ± 1.34	1.54 ± 0.35
280	5.35 ± 0.03	6.51 ± 0.01	4.37 ± 0.06	1.49 ± 0.02
280	6.38 ± 0.03	6.43 ± 0.03	4.39 ± 0.06	1.46 ± 0.02
283	4.34 ±0.05	6.47 ± 0.09	6.61 ± 0.13	0.979 ± 0.014
285.5	4.31 ±0.08	6.29 ± 0.18	9.24 ± 0.27	0.681 ± 0.031
288	1.67 ± 0.02	6.12 ± 0.11	12.98 ± 0.45	0.472 ± 0.010
288	3.13 ± 0.02	5.88 ± 0.07	12.40 ± 0.09	0.474 ± 0.006
288	4.35 ± 0.18	6.01 ± 0.49	12.40 ± 0.44	0.485 ± 0.053
288	5.60 ± 0.06	5.57 ± 0.02	12.70 ± 0.12	0.439 ± 0.005
288	6.59 ± 0.03	5.48 ± 0.03	13.03 ± 0.06	0.421 ± 0.004
290.5	4.26 ± 0.14	5.85 ± 0.13	16.99 ± 0.51	0.345 ±0.008
293	4.18 ± 0.06	5.68 ± 0.21	22.28 ± 0.36	0.255 ± 0.011
295.5	4.15 ± 0.03	5.41 ± 0.07	29.07 ± 0.23	0.186 ± 0.004
298	1.69 ± 0.04	4.86 ± 0.56	37.47 ± 1.78	0.130 ±0.020
298	3.14 ± 0.03	4.88 ± 0.07	37.28 ± 0.37	0.131 ± 0.002
298	4.19 ± 0.06	5.01 ± 0.02	36.86 ± 0.12	0.136 ± 0.005
298	5.50 ± 0.06	4.59 ±0.02	38.18 ± 0.12	0.120 ± 0.005
298	6.48 ± 0.06	4.51 ± 0.02	39.10 ± 0.12	0.115 ± 0.005
300.5	4.09 ±0.10	4.89 ± 0.16	47.94 ± 4.32	0.102 ± 0.009
303	1.49 ± 0.06	5.09 ± 0.02	57.82 ± 0.12	0.088 ± 0.005
303	2.80 ± 0.02	4.91 ± 0.06	57.31 ± 0.67	0.086 ± 0.001
303	4.00 ± 0.06	4.68 ± 0.02	59.41 ± 0.12	0.079 ±0.005
303	4.98 ± 0.06	4.53 ± 0.02	59.08 ± 0.12	0.077 ± 0.005
303	5.90 ± 0.06	4.35 ± 0.02	60.75 ± 0.12	0.072 ± 0.005
305.5	4.03 ± 0.08	4.33 ± 0.14	73.78 ± 2.80	0.059 ±0.002
308	3.98 ± 0.11	4.21 ± 0.27	89.88 ± 2.37	0.047 ± 0.004
310	1.60 ± 0.06	4.14 ± 0.19	107.1 ± 3.5	0.039 ± 0.001
310	2.89 ± 0.04	3.96 ± 0.09	106.5 ± 1.1	0.037 ± 0.001
310	3.95 ± 0.14	3.92 ± 0.20	109.7 ± 8.1	0.036 ± 0.003
310	5.08 ± 0.05	3.64 ± 0.06	110.3 ± 0.4	0.033 ± 0.001
310	6.01 ± 0.03	3.62 ±0.03	112.9 ± 0.9	0.032 ± 0.001

Table 5.6 Determinations of k_{2a}, k_{-2a} and K_c using refined analysis. Errors are quoted as 2σ statistical only.

5.4.2.1 Temperature Limits

As discussed above in refining the analysis of ClO traces, the temperature range of the present study (280 – 310 K) is somewhat limited. This is argued to be quite appropriate, however, for the following reasons.

At low temperatures, the reverse reaction of ClO association, which is the thermal decomposition of Cl_2O_2 (-2a) becomes increasingly slow. The effect of this is for the ClO decay traces to appear increasingly irreversible and to show increasingly pure

second order character as the temperature is lowered. This is shown in Figure 5.32, and, on shorter timescales Figure 5.33 which shows second order (1/[ClO]) *versus* time plots for ClO decay as a function of temperature. As the temperature is lowered, the initial parts of these traces become more linear, showing the tendency towards pure second order kinetics.

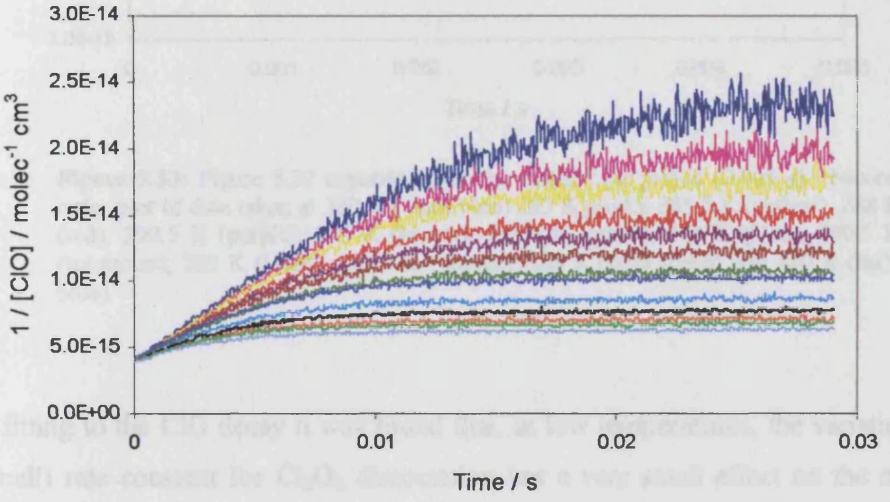

Figure 5.32: Second order plot of data taken at 280 K (dark blue) 283 K (pink), 285.5 K (yellow), 288 K (red), 290.5 K (purple), 293 K (brown), 295.5 K (green), 298 K (blue), 300.5 K (turquoise), 303 K (black), 305.5 K (orange), 308 K (light green) and 310 K (light blue)

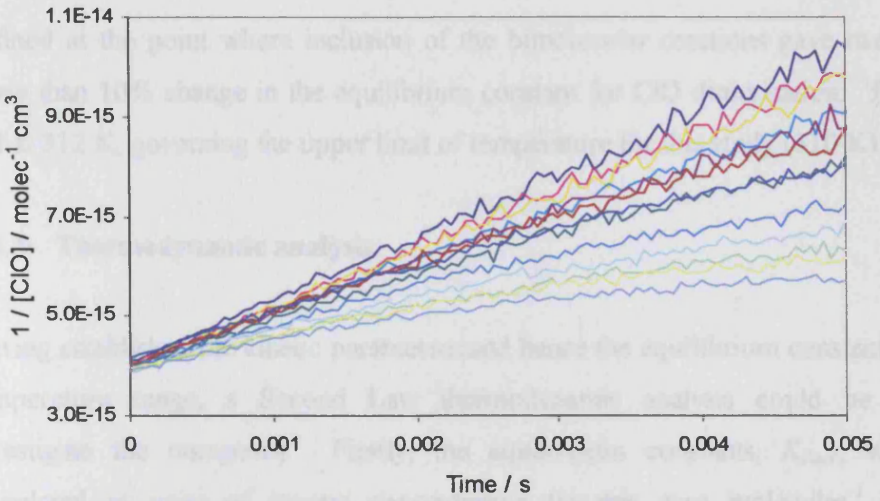

Figure 5.33: Figure 5.32 expanded over the initial time period (0.005 s). Second order plot of data taken at 280 K (dark blue) 283 K (pink), 285.5 K (yellow), 288 K (red), 290.5 K (purple), 293 K (brown), 295.5 K (green), 298 K (blue), 300.5 K (turquoise), 303 K (black), 305.5 K (orange), 308 K (light green) and 310 K (light blue)

In fitting to the ClO decay it was found that, at low temperatures, the variation in the (small) rate constant for Cl_2O_2 dissociation has a very small effect on the modelled traces – in other words the model loses sensitivity to this parameter at low temperatures. This sensitivity, and therefore the threshold lowest temperature adopted, was chosen by examining the variation of the residual between two modelled traces with the same input kinetic parameters apart from the value of k_{-2a}, which was varied by a factor of two. When this effective difference between the traces was comparable or smaller than a typical experimental residual, it was decided that the model could no longer determine k_{-2a} (and therefore $K_{2a,c}$) with suitable accuracy, and lower temperature experiments were not undertaken.

At high temperatures, as discussed above, the bimolecular channels of the ClO self-reaction contribute to the decay of ClO. The rate constants for these channels are in principle well-established.[5] However, the effect of uncertainty in these literature rate constants, coupled with the possibility of products of these reactions (such as OClO) participating in secondary chemistry involving ClO complicated the ClO decay analysis. As a safeguard against this, the high temperature limit of these studies was

defined at the point where inclusion of the bimolecular reactions gave rise to a no more than 10% change in the equilibrium constant for ClO dimerisation. This point fell at 312 K, governing the upper limit of temperature for this study (310 K).

5.4.3 Thermodynamic analysis

Having established the kinetic parameters and hence the equilibrium constant over the temperature range, a Second Law thermodynamic analysis could be used to investigate the energetics. Firstly, the equilibrium constants, $K_{2a,c}$, which are calculated in units of inverse concentration (in this case molecules^{-1} cm^3) are converted into equilibrium constants K_p, for standard states of one atmosphere and ideal gas. To achieve this, for a stoichiometric reaction of the form:

$$aA + bB + \ldots \leftrightarrow \quad xX + yY + \ldots$$

The relationship between K_c and K_p is given by

$$K_p = K_c(RT)^{\Delta n} \qquad \text{(5.xxv)}$$

where Δn is the mole change in the reaction given by (xxvi) and in this case is –1.

$$\Delta n = (x + y + \ldots) - (a + b + \ldots) \qquad \text{(5.xxvi)}$$

The calculated values of $K_{2a,p}$, suitably converted to units of reciprocal atmospheres are given in Table 5.6, below.

T / K	$K_{2a,p}$ / atm^{-1}
280	$(4.24 \pm 1.14) \times 10^6$
283	$(2.54 \pm 0.04) \times 10^6$
285.5	$(1.75 \pm 0.04) \times 10^6$
288	$(1.19 \pm 0.08) \times 10^6$
290.5	$(8.71 \pm 0.20) \times 10^5$
293	$(6.38 \pm 0.27) \times 10^5$
295.5	$(4.62 \pm 0.09) \times 10^5$
298	$(3.20 \pm 0.49) \times 10^5$
300.5	$(2.50 \pm 0.22) \times 10^5$
303	$(1.93 \pm 0.27) \times 10^5$
305.5	$(1.41 \pm 0.06) \times 10^5$
308	$(1.12 \pm 0.09) \times 10^5$
310	$(8.40 \pm 1.16) \times 10^4$

Table 5.7 Averaged values of $K_{2a,p}$. Errors are 2σ statistical only.

These values of K_p are directly related to the standard Gibbs free energy change for the reaction:

$$\Delta_r G^0 = -RT \ln K_p \qquad \text{(5.xxvii)}$$

In turn, $\Delta_r G^0$ is related to the standard reaction enthalpy, $\Delta_r H^0$, and the standard reaction entropy, $\Delta_r S^0$ through:

$$\Delta_r G^0 = \Delta_r H^0 - T\Delta_r S^0 \qquad \text{(5.xxviii)}$$

Combining (xxvii) and (xxviii) gives the van't Hoff equation (or van't Hoff isochore):

$$\ln K_p = -\frac{\Delta_r H}{R}.\frac{1}{T} + \frac{\Delta_r S}{R} \qquad \text{(5.xxix)}$$

This shows that a graph of ln K_p *versus* reciprocal temperature should exhibit linearity. A van't Hoff plot for the data in Table 5.6 is shown in Figure 5.34 below.

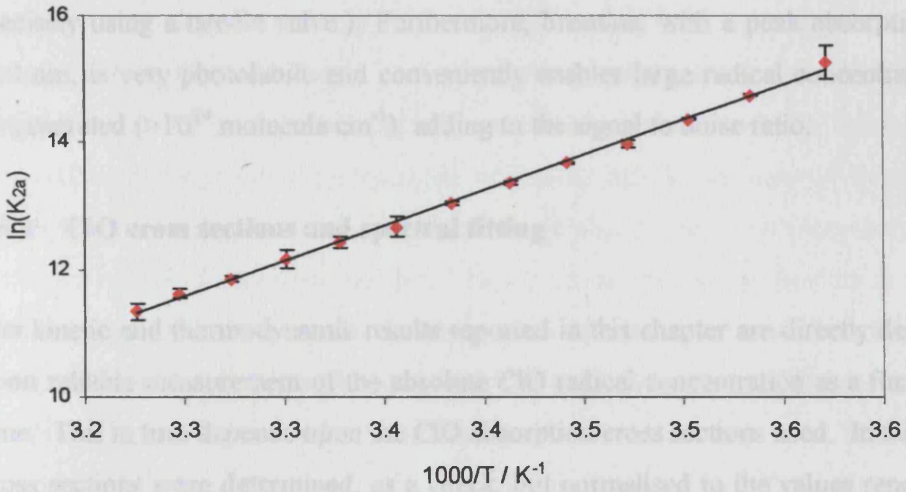

Figure 5.34: Van't Hoff plot of experimental data (red) and linear parameterisation (black)

As can be seen from Figure 5.34, the plot shows excellent linearity. A linear parameterisation fitted to the data yields a value of $\Delta_r H^0 = -(92.15 \pm 1.19)$ kJ mol^{-1} and $\Delta_r S^0 = -(203.2 \pm 4.04)$ J K^{-1} mol^{-1}, where errors are 2σ statistical only. These findings are discussed in the context of other studies in the next section.

5.5 Discussion

This study of the equilibration of ClO radicals as a function of temperature is the most extensive reported to date, and the first to employ broadband (wide spectral range) monitoring of the entire ClO vibronic absorption spectrum in order to quantify ClO. This results in the excellent signal to noise ratio of the ClO decay traces, and - using the differential spectroscopy technique - the recording of direct ClO concentrations which are fitted to the solution to the kinetic equations governing ClO decay. This study is also the first to use bromine as a source of ClO radicals. This has practical advantages in that a steady flow of bromine is readily maintained by bubbling nitrogen from a flow controller through liquid bromine, (whereas chlorine mixtures cannot be passed through a mass flow controller and are therefore controlled less

precisely using a needle valve.) Furthermore, bromine, with a peak absorption near 410 nm, is very photolabile and conveniently enables large radical concentrations to be generated (>10^{14} molecule cm^{-3}), adding to the signal to noise ratio.

5.5.1 ClO cross sections and spectral fitting

The kinetic and thermodynamic results reported in this chapter are directly dependent upon reliable measurement of the absolute ClO radical concentration as a function of time. This in turn depends upon the ClO absorption cross sections used. In this study, cross sections were determined, as a check, but normalised to the values reported by Boakes *et al.*, from a very extensive study of ClO association over a wide range of conditions.[6] The method for determining the ClO absorption cross sections in this work is advantageous, since the simultaneous recording of spectral structure and spectral continuum using the CCD detector precludes the need for additional experiments. The short back extrapolations of the differential and continuum traces were reliable, and the calibration plots obtained using this analysis were also consistently linear with zero intercept, as predicted by equation (x) used to calibrate $\sigma(ClO)_{diff}$. The value of this ClO differential cross section obtained is evidently directly dependent upon the (difference between) the continuum cross sections of ClO and Cl_2O taken from the literature, at 257.5 nm. Agreement between the various studies of these cross sections is very good indeed,[5] and the most recent recommendation from NASA was used as the basis for these literature cross-sections. The parameterisation of these cross sections, using semilogarithmic Gaussian functions was successful (as shown in Figure 5.14), and an improvement on some previous studies which have taken the value of these cross sections linearly interpolated between the nearest wavelengths reported. The final differential cross sections of ClO will potentially contain systematic error resulting from potential error in the calibrating continua cross sections, estimated by NASA to be ± 10% on each. Hence, since the difference in literature values is used, the final differential ClO absorption cross section will contain a potential systematic error of approximately 14%.

The cross sections reported here for the (12, 0) band at 275.2 nm and the trough to higher wavelengths were found to lie near the lower limit of error of the values reported by Boakes *et al.*[6] Since, as discussed above and as shown in Figure 5.6, the cross-sections for spectrally structured absorbers are a function of instrumental resolution, it is not possible to directly compare absorption cross sections from this work with those from other studies. However, as shown by Boakes *et al.*, the instrumental resolution-dependent cross sections recorded in this laboratory, extrapolated to the high resolution adopted by the recent study of Bloss *et al.*[17] are consistent.

In similar fashion, the temperature dependence of the ClO absorption cross sections was measured in this work, and normalised to the ambient temperature cross section reported by Boakes *et al.* Here, the cross sections do show a weak negative temperature dependence, in keeping with Boakes *et al.* and with previous work, which is illustrated in Figure 5.35 below. It should be noted that neither of the calibrating continua cross sections show significant temperature dependence[16] and the 298 K values of these parameters were therefore used without correction.

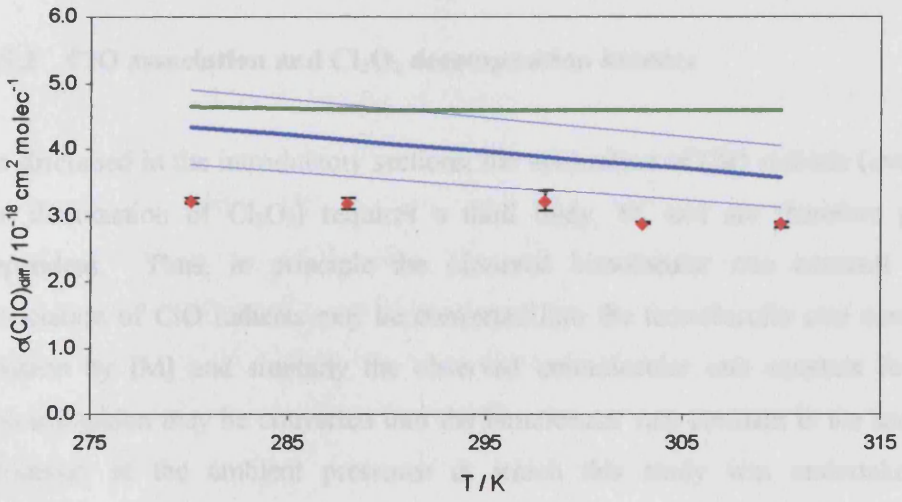

Figure 5.35: Measured temperature dependence of the ClO cross section (red). Also shown are the parameterisations reported by Bloss *et al.*[17] (green).and Boakes *et al.*[6] (bold blue line), the upper and lower uncertainty limits of Boakes *et al.* are also indicated in blue.

The spectral fitting routine used in this work to fit ClO cross sections to sequential spectra (shown in Figure 5.7, above) ensured that ClO concentrations were determined completely unequivocally. This represents a considerable advantage over previous studies, which have commonly used single wavelength monitoring (at a peak of the ClO absorption spectrum) or dual wavelength monitoring at a ClO peak and at the adjacent trough at higher wavelengths.[17] In all of these cases, the monitoring will record the composite time resolved absorption signal at the chosen wavelengths, containing contributions from all UV absorbing species present. This has to be accounted for in analysis of temporal traces. One final point concerning spectral fitting concerns wavelength calibration. In this, and in other studies, spectra are routinely wavelength calibrated using the well-known peaks from a mercury lamp. However, it was found during spectral fitting that very small shifts in wavelength were required (always < 0.1 nm) to optimise the fit of the ClO reference to experimental spectra. This correction was attributed to small shifts in the wavelength calibration of the spectrometer over the course of a series of experiments. This shift may be unique to this apparatus, but if similar shifting were to occur in single or even dual wavelength monitoring, it would be very difficult to account for and could profoundly affect apparent ClO absorption cross sections.

5.5.2 ClO association and Cl_2O_2 decomposition kinetics

As discussed in the introductory sections, the association of ClO radicals (and indeed the dissociation of Cl_2O_2) requires a third body, M, and are therefore pressure dependent. Thus, in principle the observed bimolecular rate constant for the association of ClO radicals may be converted into the termolecular rate constant by division by [M] and similarly the observed unimolecular rate constant for Cl_2O_2 decomposition may be converted into the bimolecular rate constant in the same way. However, at the ambient pressures at which this study was undertaken, ClO dimerisation is known to be in the 'fall off' region, where the kinetics of association are in between third and second order. The pressure dependent rate constants for the ClO association may, under these circumstances, be described by the simple Lindemann model as described in Chapter 1. However a more accurate representation

of the experimental rate constants as a function of temperature and [M], and that adopted for atmospheric model studies,[5] is that provided by Troe.[26] This expression defines the rate constant at a given temperature and [M] as:

$$k_{ter}(M,T) = \frac{k_0(T)[M]}{1+(k_0(T)[M]/k_\infty(T))} \times F \qquad (5.xxx)$$

where k_0 and k_∞ are the limiting low pressure (third order) and high pressure (second order) rate coefficients and F is a broadening factor given by:

$$F = F_c^{\{1+[\log(k_0(T)[M]/k_\infty(T))]^2\}^{-1}} \qquad (5.xxxi)$$

The value that F_c takes is specific to the particular reaction under consideration but in practice a value of 0.6 provides a satisfactory description of termolecular rate coefficients for atmospherically relevant processes.[5] The temperature dependencies of k_0 and k_∞ are described in the form:

$$k(T) = k^{300}(T/300)^{-n} \qquad (5.xxxii)$$

A full study of the pressure and temperature dependence of the ClO association kinetics is required to determine k_0, k_∞ and their temperature dependence, and to characterise the ClO + ClO reaction under all atmospheric conditions. This has recently been carried out by Boakes *et al.*[6] in this laboratory. In the present study, the focus was on studying the equilibrium constant, which is pressure independent. Intercomparison of the k_{2a} and k_{-2a} values obtained can be carried out, however, using the parameterisations provided by Boakes *et al.* (for k_{2a}) and the latest NASA evaluation (for k_{2a} and k_{-2a}),[5] this is shown in Figure 5.36, below.

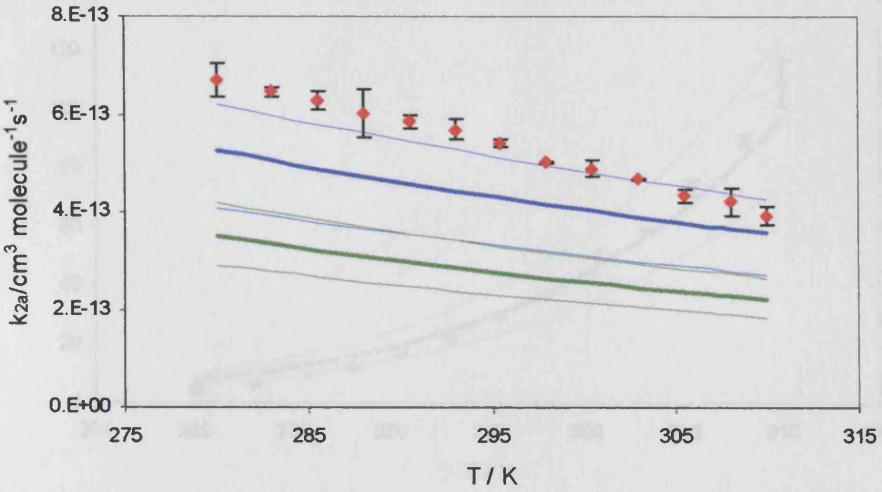

Figure 5.36: Experimental values of k_{2a} reported in this work (red) and the parameterisations from Boakes *et al.* (blue) and the latest NASA evaluation (green) – parameterisations are indicated in bold lines with their respective upper and lower limits of uncertainty indicated in lighter lines.

As can clearly be seen, the k_{2a} values reported here are somewhat greater than those reported by Boakes *et al.* These higher values are attributed directly to the upward normalisation of the ClO absorption cross sections adopted in this study.

Figure 5.37, below, compares the experimental k_{-2a} values from this study together with the latest NASA evaluation (calculated from the NASA recommended k_{2a} and K_{2a}). In this case, the kinetic parameters show excellent agreement.

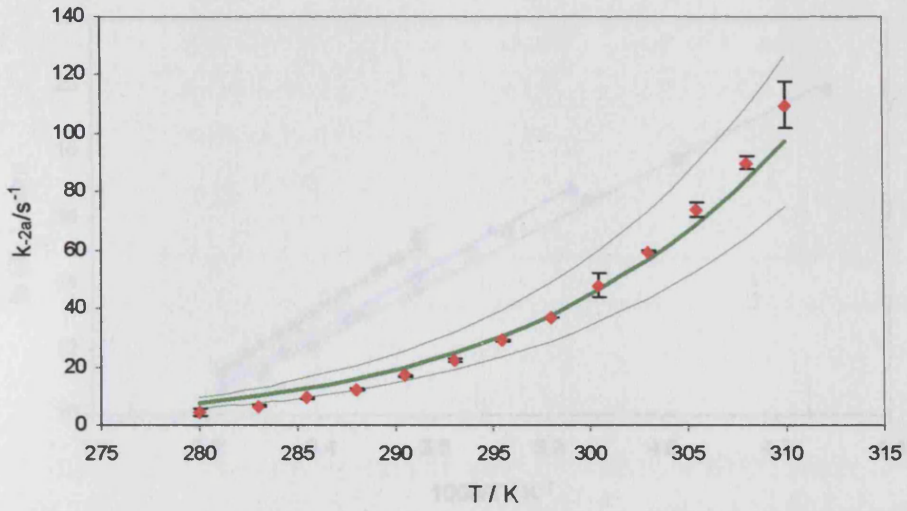

Figure 5.37: Experimental values of k_{-2a} reported in this work (red) and the parameterisation from the latest NASA evaluation (green) – (Parameterisation indicated by bold line and upper and lower limits in lighter lines.)

Given that k_{2a} reported here is significantly greater than the recent previous studies of k_{2a}, whereas k_{-2a} is in keeping with previous work, equilibrium constants, K_{2a}, will also be greater than those reported previously. However, given that the increase in k_{2a} appears to reflect the scaled up absorption cross-sections, and that the form of the temperature dependence of k_{2a} is similar to that of recent studies, this increase will exist as a multiplicative factor on k_{2a} and K, and should not therefore affect the gradient of the van't Hoff plot (and consequently $\Delta_r H^0$) greatly. By contrast, the intercept of the van't Hoff plot will be affected by such an increase, affecting $\Delta_r S^0$. However, the large back extrapolation of the van't Hoff plot required to obtain $\Delta_r S^0$, means that $\Delta_r S^0$ is not very well constrained by these and others' data.

5.5.3 Equilibrium constant and Thermochemistry

The temperature dependent ClO association equilibrium constant is plotted in van't Hoff form along with the previous studies of Nickolaisen *et al.*[7] and Cox *et al.*[18] in Figure 5.38 (over the full temperature range) and Figure 5.39 (over the narrower temperature range of this study) below

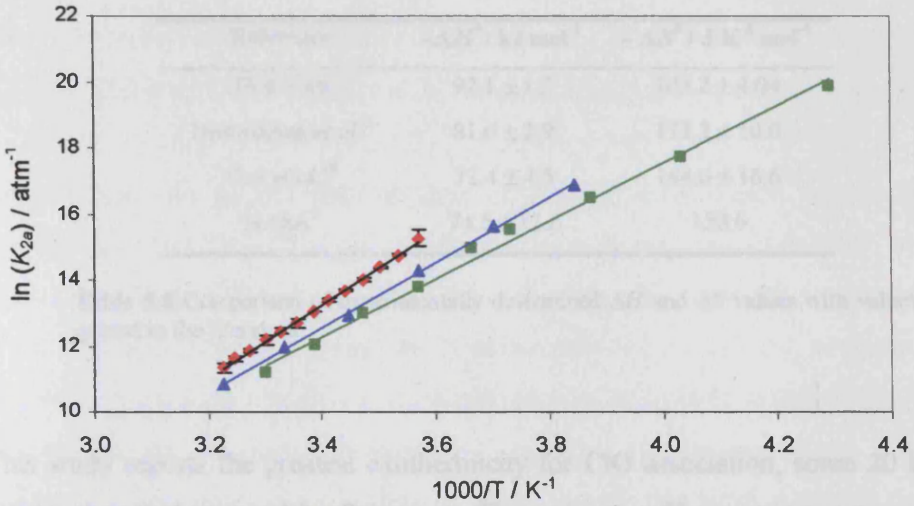

Figure 5.38: Van't Hoff plots of data from this work (red), and previously reported data of Nickolaisen *et al.*[7] (blue) and Cox *et al.*[18] (green) over full reported temperature range.

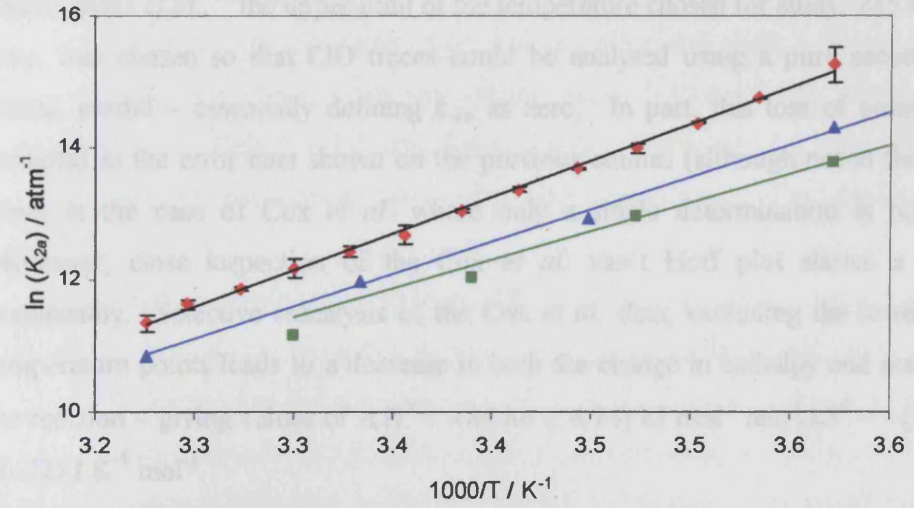

Figure 5.39: Van't Hoff plots of data from this work (red), and previously reported dataof Nickolaisen *et al.*7 (blue) and Cox *et al.*18 (green) over temperature range used in thiswork (280-310 K).

As can be seen, whilst the figures are in broad agreement, subtle differences in the gradients of the plots, are evident, reflected in the thermochemical parameters compared in Table 5.7 below.

Reference	$-\Delta_r H^0$ / kJ mol^{-1}	$-\Delta_r S^0$ / J K^{-1} mol^{-1}
This work	92.1 ± 1.2	203.2 ± 4.04
Nickolaisen *et al.*[7]	81.6 ± 2.9	173.2 ± 10.0
Cox *et al.*[18]	72.4 ± 4.5	144.0 ± 16.6
NASA[5]	74.5 ± 12.6	150.6

Table 5.8 Comparison of experimentally determined ΔH and ΔS values with values quoted in the literature.

This study reports the greatest exothermicity for ClO association, some 20 kJ mol^{-1} greater than that reported by Cox *et al.* The inclusion of lower temperature points in the thermochemical analyses of Nickolaisen *et al.* and especially Cox *et al.* (to 233 K) is surprising. In this work, the sensitivity of ClO traces to Cl_2O_2 decomposition becomes very small below 280 K, the lower limit of temperature chosen in this work. Furthermore, in some previous studies of the ClO association rate constant, such as that of Bloss *et al.*,[17] the upper limit of the temperature chosen for study, 245 K in this case, was chosen so that ClO traces could be analysed using a pure second order kinetic model – essentially defining k_{-2a} as zero. In part, this loss of sensitivity is reflected in the error bars shown on the previous studies (although not at the 248 K point in the case of Cox *et al.* where only a single determination is reported). Moreover, close inspection of the Cox *et al.* van't Hoff plot shows a distinct nonlinearity. Selective reanalysis of the Cox *et al.* data, excluding the lowest three temperature points leads to a decrease in both the change in enthalpy and entropy of the reaction – giving values of $\Delta_r H^0$ = -(84.84 ± 4.74) kJ mol^{-1} and $\Delta_r S^0$ = –(187.3 ± 16.72) J K^{-1} mol^{-1}.

5.5.4 Atmospheric Implications

The results of this study indicate that the exothermicity of association of two ClO radicals is somewhat greater than that determined by the two previous studies, most notably that of Cox *et al.*[18] As argued above, the very low temperature determinations of K_{2a} carried out by Cox *et al.* are potentially flawed due to a loss of sensitivity

arising from slow decomposition of the ClO dimer. Thus, for atmospheric purposes, a $\Delta_r H^0$ for ClO association lower than -80 kJ mol^{-1} is probably appropriate.

Simplistically, the greater exothermicity of the ClO dimerisation implies a greater stability for the ClOOCl molecule in the atmosphere, and potentially a shift in partitioning from ClO towards ClOOCl. This, coupled with the recently reported (from our laboratory) increased rate of association of ClO radicals, suggests that the ozone loss cycle *via* the ClO association reaction in sunlight is more efficient than current atmospheric models account for. In terms of stratospheric ozone loss, this would of course imply a greater loss of ozone through this cycle, although the change in ClO_x partitioning also implies that fewer ClO radicals would be available for participation in other ozone destroying cycles such as those involving ClO + BrO or ClO + HO_2 which would offset this effect. The verification, or otherwise of these predictions rely upon high quality measurements of stratospheric composition during ozone loss events. Specifically, the measurements of speciated composition within a chemical family are now becoming more commonplace and allow a thorough test of our understanding of the chemistry taking place. Atmospheric model studies incorporating new kinetic and thermochemical data available are also needed to assess the likely impact of new results such as these on the composition of the stratosphere.

One final point concerning the role of the ClO association reaction is the nature of the ClO dimer, which has been the subject of previous experimental and ab initio studies.[27,28] Following the work of Birk *et al.*[29] who reported that this molecule possesses chlorine atoms in identical chemical environments, the form of Cl_2O_2 has been assumed to be chlorine peroxide, ClOOCl. However, very recent theoretical work has suggested that the asymmetrical ClOClO isomer could form in a minor channel.[30] If the ClOClO molecule did form in the stratosphere, the likely photolysis products would be Cl + OClO. Subsequent OClO photolysis would then liberate an oxygen atom, with the effect of offsetting ozone (odd-oxygen) loss through the ClO + ClO cycle. In our studies, the existence of a secondary ClO association channel (with different $\Delta_r H^0$ to the ClOOCl formation channel) might manifest as a change in

gradient of the van't Hoff plot as a function of temperature. No such deviations from linearity were observed in the course of this work, and this work cannot conclusively confirm or deny the existence of a ClOClO forming reaction.

5.6 Summary

This chapter has described a kinetic and thermochemical study of an atmospherically important reaction using photolytic generation and real time monitoring of the reactive species involved. For the first time, the time resolved UV absorption spectroscopy used in this study has been simultaneously wavelength resolved, owing to the CCD, and unique monitoring of free radicals with an excellent signal to noise ratio has been achieved. As discussed in the concluding chapter, the success of this study indicates more generally the value of using novel, state of the art detection systems in chemical kinetics – an ultimate aim of the mass spectrometric developments detailed in previous chapters.

The ClO + ClO dimerisation reaction has been thoroughly characterised. As discussed above this is a very important process in stratospheric chemistry and this study adds to our knowledge of ozone depletion. In time, given the Montreal protocol and subsequent amendments, the atmospheric loading of anthropogenic chlorine containing gases is expected to decrease. However, this decrease seems likely to occur against a backdrop of increased carbon dioxide loading in the atmosphere. Increased atmospheric CO_2 levels are expected to cause a general warming of the Earth system at low altitudes, owing to the increased trapping and re-radiation of outgoing terrestrial radiation. This, however, is also expected to lead to a cooling of the atmosphere at higher altitudes, including the stratosphere, and stratospheric chemistry would consequently adjust with this change in environmental conditions. Given this, reactions such as the ClO association which show a negative temperature dependence, are liable to become more efficient in the stratosphere if it cools, with the effect of offsetting any reduction in absolute chlorine concentrations. Thus, in

conclusion, the ClO + ClO reaction, an elementary gas phase process which perhaps uniquely manifests itself globally as a geographically massive ozone hole each polar springtime, might yet become even more important in the future atmosphere.

5.7 References

(1) "Scientific Assessment of Ozone Depletion: Report No. 44," World Meterological Organisation Global Ozone Research and Monitoring Project, 1998.

(2) Molina L.T.; Molina M.J. *Journal of Physical Chemistry* **1987**, *91*, 433.

(3) Cox S.D.; Wagman D.D.; Medvedev V.A. *CODATA Key Values for Thermodynamics*; Hemisphere Publishing Corp.: New York, 1989.

(4) Chase M.W. *Journal of Physical Chemistry Reference Data,* **1998**, *Monograph 9.*

(5) Sander, S. P.; Friedl R.R.; Demore W.B.; Golden D.M.; Kurylo M.J.; Hampson R.F.; Huie R.E.; Moortgat G.K.; Ravishankara, A. R.; Kolb C.E.; Molina M.J. "Chemical Kinetics and Photochemical Data for use in Stratosphere Modeling - Evaluation No. 14," NASA JPL, Pasadena, CA, 2003.

(6) Boakes G., University College London, 2003.

(7) Nickolaisen S.L.; Friedl R.R.; Sander, S. P. *Journal of Physical Chemistry* **1994**, *98*, 155.

(8) Rowley, D. M.; Harwood, M. H.; Freshwater, R. A.; Jones, R. L. *Journal of Physical Chemistry* **1996**, *100*, 3020-3029.

(9) Wayne R.P.; Poulet G.; Biggs P.; Burrows J.P.; Cox R.A.; Crutzen P.J.; Hayman G.D.; Jenkin M.E.; Le Bras G.; Moortgat G.K.; Platt U.; Schlinder R.N. *Halogen oxides: radicals, sources and reservoirs in the laboratory and in the atmosphere*; European Commission, 1995.

(10) Porter G.; Wright F.J. *Discussions of the Faraday Society* **1953**, *14*, 23.

(11) Cox R.A.; Derwent R.G.; Eggleton A.E.J.; Reid J.H. *Journal of the Chemical Soceity; Faraday Transactions I* **1979**, *75*, 1648.

(12) Basco N.; Hunt J.E. *International Journal of Chemical Kinetics* **1979**, *61*, 649.

(13) Ellerman T.; Johnsson K.; Lund A.; Pagsberg P. *Acta Chemica Scandinavica* **1995**, *49*, 28.

(14) Hayman G.D.; Davies J.M.; Cox R.A. *Geophysical Research Letters* **1986**, *13*, 1347.

(15) Sander, S. P.; Friedl R.R.; Yung Y.L. *Science* **1989**, *145*, 1095.

(16) Trolier M.; Mauldin III R.L.; Ravishankara, A. R. *Journal of Physical Chemistry* **1990**, *94*, 4896.

(17) Bloss W.J.; Nickolaisen S.L.; Salawitch, R. J.; Friedl R.R.; Sander, S. P. *Journal of Physical Chemistry A* **2001**, *105*, 11226.

(18) Cox R.A.; Hayman G.D. *Nature* **1988**, *332*, 796.

(19) "Chemical Kinetics and Photochemical Data for use in Stratospheric Modelling, Evaluation No. 12," NASA JPL, Pasadena, U.S.A, 1997.

(20) Hinshelwood C.N.; Pritchard C.R. *Journal of the Chemical Society* **1923**, *123*, 2730.

(21) Knauth H.D.; Alberti H.; Clausen H.J. *Journal of Physical Chemistry* **1979**, *83*, 1604.

(22) Molina L.T.; Molina M.J. *Journal of Physical Chemistry* **1978**, *82*, 2401.

(23) Lin C.L. *Journal of Chemical Engineering Data* **1976**, *21*, 411.

(24) Simon F.G.; Schneider W.; Moortgat G.K.; Burrows J.P. *Journal of Photochemistry and Photobiology A: Chemistry* **1990**, *55*, 1.

(25) Mandelman M.; Nicholls R.W. *Journal of Quantum Spectroscopy and Radiative Transfer* **1977**, *17*, 483.

(26) Troe, J. *Journal of Physical Chemistry* **1977**, *66*, 4745.

(27) McGrath P.H.; Clemitshaw K.C.; Rowland F.S; Hehre W.J. *Journal of Physical Chemistry* **1990**, *94*, 6126.

(28) McGrath P.H.; Clemitshaw K.C.; Rowland F.S.; Hehre W.J. *Geophysical Research Letters* **1988**, *15*, 883.

(29) Birk M.; Friedl R.R.; Cohen E.A.; Pickett H.M.; Sander, S. P. *Journal of Chemical Physics* **1989**, *91*, 6588-6597.

(30) Zhu R.S.; Lin M.C. *Journal of Physical Chemistry* **2003**, *118*, 4094.

Chapter 6 Concluding Remarks

Following a summary of the appropriate theory and experimental principles, the preceding chapters have described the development of instrumentation (a chemical ionisation mass spectrometer coupled to a flow tube) for the sensitive, specific detection of trace gas species. This system has been tested, and the ultimate aim of this detection is the investigation of gas phase kinetics of species such as free radicals, which is now being pursued. In Chapter 5, a pre-existing instrument (a flash photolysis apparatus incorporating CCD detection) has been exploited for just such an (extensive) investigation. The particular advantages of using the CCD in real time monitoring of unequivocal free radical absorption signals demonstrates the immense value of improving the availability of highly sensitive and specific instrumentation for the measurement of trace concentrations of gaseous species, which has been the main aim of the instrument development work.

As described in Chapter 2, whilst the ultimate goal of developing such new detection systems is the same – in this case to pursue studies relevant to the atmosphere – the specific requirements of the detection systems are slightly different. The mass spectrometric detection system designed and constructed in this study needs to be able to specifically ionise and monitor a variety of trace gas phase species at low concentrations, but without gas kinetic time resolution which is accounted for by the steady – state nature of the flow system. By contrast, the flash photolysis/ time resolved broad-band UV absorption system needs to be able to generate and then detect species on the timescale of the reaction taking place, whilst retaining the advantages of specificity and selectivity. Fortunately, photolytic generation of reactive gas phase species is well-established, and many of these trace species do absorb in the ultraviolet, and do indeed have spectrally structured absorption spectra making their specific detection somewhat easier.

The two different experimental approaches described in this thesis also operate under different physical conditions which are to an extent imposed upon the techniques.

The flow tube/ mass spectrometric apparatus necessarily works at low pressures (typically below 10 Torr) to achieve fast linear gas flow velocities and therefore short contact times. By contrast, the flash photolysis apparatus operates at higher pressures (typically 100-760 Torr) largely to ensure that a sufficient number density of reactive species are produced in the optical absorption path. These restrictions on, in this case, pressure limits present additional practical considerations which must be addressed. In the case of flow tube work, wall loss of reactive species owing to the efficient diffusion of reactive species to the surfaces on the inside of the flow tube and the outside of the injector need to be minimised. Furthermore, the mixing of the reactive species in the two gas flows must be rapid compared to their contact time. By contrast, no such wall effects are usually significant in the higher pressures of a flash photolysis reaction cell, although other issues, associated with the larger absolute mixing ratios of precursor species and their consequent possible photolysis and secondary chemistry must be addressed.

In terms of temperature, both the discharge flow cell and the flash photolysis cell may be heated or cooled using a thermostatting envelope, as used in the flash photolysis studies detailed in Chapter 5. In discharge flow, the key to this thermostatting is to ensure that the fast moving gases are thermally equilibrated – hence heated or cooled to the requisite temperature – before their mixing and reaction. In flash photolysis cells, where a slow gas flow is simply used to replenish reagent gases for the next flash, such thermostatting issues are less problematic. However, for work at very low temperatures, such as those encountered in the polar stratosphere, issues of vapour pressure and potential in-cell condensation limit the maximum concentrations of gases that can be used as reactive species precursors. The additional flash photolytic need for rapid species generation often implies that an excess of one reagent is needed to rapidly scavenge the initial photoproduct and this may not always be possible at low temperature using low vapour pressure gases.

The fundamental approach to generating the trace species of interest in flow tube studies and flash photolysis studies also differ somewhat. In flow tubes, the key is that reactive species are prepared individually, using direct microwave dissociation or

such dissociation followed by a rapid reaction. In flash photolysis studies both reactive species need to be prepared from the same gas mixture in the same photolysis flash. The nature of this difference immediately suggests that flow tubes are more suitable for reactions of different reactive species (*e.g.* radical-radical reactions) or the reaction of a reactive species with a stable molecule. Indeed, since using flow tubes studies of bimolecular reactions are often conveniently operated in pseudo first order mode, where one species needs to be kept in excess over the other, they are especially suited to reactive species – stable molecule reactions, or reactions between two transient species where one of the species has an inherent lower reactivity than the other.

By contrast, flash photolysis studies are especially suited to the investigation of reactive species self-reactions, such as the ClO + ClO reaction detailed in Chapter 5. Flash photolysis studies of radical cross-reactions can be carried out. This requires, however, very careful design of the initial conditions, to ensure in this case that both transient species are produced in a fixed ratio upon photolysis. Furthermore, the monitoring of different transient species in flash photolysis presents a challenge. Usually, UV absorption traces at a single wavelength are monitored, and such traces may contain contributions from multiple absorbing species, which must be accounted for. A particular advantage of the charge coupled device monitoring of UV absorption, which is unique to the apparatus used in this work, is that multiple wavelengths are monitored simultaneously. This enables reactive species to be monitored unequivocally. This also enables multiple reactive species to be monitored in real time in the same experiment. Furthermore, as exploited in this work in the calibration of ClO absorption cross-sections, since both the spectrally structured part of the spectrum and the spectral continuum are recorded simultaneously, the continuum spectrum can be used to calibrate spectra. Once again, this specific advantage highlights in general terms the benefits of development of new instrumental capability for the detection of trace species in the gas phase, which has been one of the main aims of this work.

Appendix 1 ClO Dimerisation Study: Preliminary Results

Kinetic parameters (k_{2a}, k_{-2a} and K_{2a}) of the ClO + ClO self reaction were recorded as a function of temperature (280 – 310 K) and as a function of molecular bromine concentration ($0.5 - 2.5 \times 10^{-16}$ molecules cm^3) at 5 temperatures encompassing the total experimental temperature range, as discussed in Chapter 5. The following table lists the determinations of the kinetic parameters with their associated errors (2σ statistical error) for each experiment undertaken using the preliminary analysis as described in Section 5.4.1. Numbers in bold indicate the average values at each temperature.

T / K	$[Br_2]$ / 10^{16} molec cm^{-3}	$[ClO]_0$ / 10^{14} molec cm^{-3}	K_{2a} / 10^{-13} $molec^{-1}$ cm^3 s^{-1}	k_{-2a} / s^{-1}	K_{2a} / 10^{-14} cm^3 $molec^{-1}$
280	0.44	1.78	6.66	3.51	18.97
280	0.44	1.74	6.64	3.57	18.59
280	0.44	1.72	6.66	3.47	19.17
280	0.44	1.71	6.64	3.38	19.63
280	0.96	3.37	6.47	4.06	15.93
280	0.96	3.33	6.46	3.91	16.51
280	0.96	3.31	6.48	3.98	16.26
280	0.96	3.30	6.44	3.90	16.51
280	1.47	4.58	6.55	4.52	14.49
280	1.47	4.60	6.52	4.46	14.61
280	1.47	4.60	6.52	4.46	14.61
280	1.47	4.65	6.56	4.44	14.77
280	1.47	4.78	6.19	4.30	14.40
280	1.47	4.77	6.22	4.29	14.51
280	1.47	4.77	6.19	4.29	14.40
280	1.47	4.76	6.20	4.36	14.22
280	1.47	4.58	6.36	4.14	15.37
280	1.47	4.57	6.36	4.11	15.50
280	1.47	4.58	6.35	4.26	14.93
280	1.47	4.55	6.34	4.25	14.91
280	1.98	5.69	6.18	4.46	13.84
280	1.98	5.69	6.18	4.48	13.80
280	1.98	5.72	6.18	4.48	13.78
280	1.98	5.69	6.18	4.41	14.04
280	2.49	6.79	6.11	4.51	13.53
280	2.49	6.76	6.13	4.46	13.73
280	2.49	6.79	6.10	4.50	13.54
280	2.49	6.78	6.12	4.54	13.47
280	–	–	**6.36 ± 0.38**	**4.20 ± 0.70**	**15.3± 3.6**
283	1.47	4.55	6.27	6.83	9.19

T / K	$[Br_2]$ / 10^{16} molec cm^{-3}	$[ClO]_0$ / 10^{14} molec cm^{-3}	K_{2a} / 10^{-13} $molec^{-1}$ cm^3 s^{-1}	k_{-2a} / s^{-1}	K_{2a} / 10^{-14} cm^3 $molec^{-1}$
283	1.47	4.55	6.25	6.69	9.33
283	1.47	4.59	6.22	6.72	9.26
283	1.47	4.59	6.24	6.66	9.37
283	1.47	4.54	6.19	6.72	9.21
283	1.47	4.59	6.19	6.64	9.32
283	1.47	4.61	6.16	6.71	9.18
283	1.47	4.61	6.16	6.66	9.25
283	–	–	**6.21 ± 0.09**	**6.70 ± 0.12**	**9.26 ± 0.14**
285.5	1.47	4.47	6.19	9.33	6.64
285.5	1.47	4.48	6.18	9.22	6.70
285.5	1.47	4.47	6.15	9.30	6.61
285.5	1.47	4.49	6.19	9.41	6.58
285.5	1.47	4.52	6.01	9.64	6.23
285.5	1.47	4.54	6.01	9.26	6.49
285.5	1.47	4.56	6.01	9.27	6.48
285.5	1.47	4.58	6.03	9.30	6.48
285.5	–	–	**6.10 ± 0.18**	**9.34 ± 0.26**	**6.53 ± 0.29**
288	0.44	1.73	6.04	13.2	4.59
288	0.44	1.74	5.94	12.9	4.62
288	0.44	1.75	5.93	12.7	4.68
288	0.44	1.75	5.92	12.9	4.58
288	0.96	3.24	5.77	12.5	4.62
288	0.96	3.26	5.77	12.4	4.66
288	0.96	3.26	5.73	12.4	4.61
288	0.96	3.25	5.71	12.4	4.60
288	1.47	4.41	6.18	12.1	5.10
288	1.47	4.38	6.17	12.3	5.03
288	1.47	4.37	6.15	12.5	4.91
288	1.47	4.40	6.17	12.2	5.06
288	1.47	4.51	5.89	12.9	4.56
288	1.47	4.50	5.86	12.6	4.66
288	1.47	4.51	5.87	12.7	4.64
288	1.47	4.52	5.87	12.5	4.69
288	1.47	4.63	5.62	12.6	4.47
288	1.47	4.61	5.61	12.6	4.47
288	1.47	4.60	5.62	12.6	4.45
288	1.47	4.59	5.60	12.6	4.45
288	1.98	5.77	5.48	12.8	4.27
288	1.98	5.76	5.48	12.9	4.25
288	1.98	5.80	5.46	12.9	4.23
288	1.98	5.83	5.48	12.8	4.29
288	2.49	6.81	5.40	13.2	4.10
288	2.49	6.78	5.40	13.2	4.08
288	2.49	6.81	5.37	13.3	4.05
288	2.49	6.82	5.40	13.3	4.08
288	–	–	**5.75 ± 0.52**	**12.7 ± 0.6**	**4.53 ± 0.58**
290.5	1.47	4.30	5.85	17.5	3.35
290.5	1.47	4.33	5.85	17.2	3.40
290.5	1.47	4.30	5.88	17.2	3.42
290.5	1.47	4.30	5.83	17.1	3.40
290.5	1.47	4.44	5.75	16.6	3.47
290.5	1.47	4.41	5.72	17.1	3.35
290.5	1.47	4.45	5.75	17.1	3.37
290.5	1.47	4.44	5.75	17.0	3.38

T / K	$[Br_2]$ / 10^{16} molec cm^{-3}	$[ClO]_0$ / 10^{14} molec cm^{-3}	K_{2a} / 10^{-13} molec^{-1} cm^3 s^{-1}	k_{-2a} / s^{-1}	K_{2a} / 10^{-14} cm^3 molec^{-1}
290.5	–	–	**5.80 ± 0.12**	**17.1± 0.5**	**3.39 ± 0.08**
293	1.47	4.22	5.79	22.5	2.58
293	1.47	4.21	5.78	22.2	2.61
293	1.47	4.25	5.77	22.4	2.58
293	1.47	4.23	5.76	22.4	2.58
293	1.47	4.25	5.56	22.7	2.45
293	1.47	4.27	5.62	22.2	2.53
293	1.47	4.29	5.56	22.2	2.51
293	1.47	4.28	5.59	22.4	2.50
293	–	–	**5.68 ± 0.21**	**22.4 ± 0.4**	**2.54 ± 0.11**
295.5	1.47	4.19	5.51	29.1	1.89
295.5	1.47	4.16	5.50	29.0	1.90
295.5	1.47	4.17	5.48	28.9	1.90
295.5	1.47	4.18	5.51	28.9	1.90
295.5	1.47	4.19	5.44	29.1	1.87
295.5	1.47	4.18	5.43	29.0	1.87
295.5	1.47	4.19	5.45	29.2	1.86
295.5	1.47	4.14	5.42	29.2	1.86
295.5	–	–	**5.47 ± 0.07**	**29.0 ± 0.2**	**1.88 ± 0.04**
298	0.44	1.72	5.12	36.6	1.40
298	0.44	1.69	5.16	36.2	1.43
298	0.44	1.68	5.12	37.0	1.39
298	0.44	1.67	5.11	36.7	1.39
298	0.96	3.14	5.02	36.9	1.36
298	0.96	3.12	4.94	37.1	1.33
298	0.96	3.13	4.96	36.9	1.34
298	0.96	3.12	4.97	36.6	1.36
298	1.47	4.22	4.84	35.9	1.35
298	1.47	4.26	4.84	36.4	1.33
298	1.47	3.84	5.51	36.5	1.51
298	1.47	3.95	5.49	36.7	1.50
298	1.47	4.15	5.14	37.2	1.38
298	1.47	4.17	5.14	36.9	1.39
298	1.47	4.17	5.11	36.7	1.39
298	1.47	4.16	5.09	36.4	1.40
298	1.47	4.36	4.86	37.2	1.31
298	1.47	4.33	4.84	37.1	1.30
298	1.47	4.32	4.81	37.1	1.30
298	1.47	4.30	4.83	37.3	1.30
298	1.98	5.46	4.70	38.1	1.23
298	1.98	5.44	4.69	37.9	1.24
298	1.98	5.48	4.71	38.2	1.23
298	1.98	5.49	4.69	37.8	1.24
298	2.49	6.39	4.61	39.1	1.18
298	2.49	6.44	4.63	39.0	1.19
298	2.49	6.45	4.63	39.0	1.19
298	2.49	6.44	4.62	38.9	1.19
298	–	–	**4.93 ± 0.49**	**37.3 ± 1.8**	**1.33 ± 0.18**
300.5	1.47	4.00	5.16	48.4	1.07
300.5	1.47	3.95	5.03	52.4	0.960
300.5	1.47	3.99	5.13	46.4	1.11
300.5	1.47	3.98	5.14	45.9	1.12
300.5	1.47	4.07	4.98	46.7	1.07
300.5	1.47	4.07	4.97	46.4	1.07

T / K	$[Br_2]$ / 10^{16} molec cm^{-3}	$[ClO]_0$ / 10^{14} molec cm^{-3}	K_{2a} / 10^{-13} molec^{-1} cm^3 s^{-1}	k_{-2a} / s^{-1}	K_{2a} / 10^{-14} cm^3 molec^{-1}
300.5	1.47	4.09	4.99	46.6	1.07
300.5	1.47	4.05	4.99	46.8	1.07
300.5	–	–	**5.05 ± 0.16**	**47.4 ± 4.2**	**1.07 ± 0.09**
303	0.44	1.47	5.19	56.0	0.926
303	0.44	1.46	5.32	57.4	0.926
303	0.44	1.45	5.26	55.4	0.949
303	0.44	1.45	5.30	56.7	0.934
303	0.96	2.74	5.05	55.8	0.906
303	0.96	2.74	5.12	56.6	0.906
303	0.96	2.74	5.12	56.1	0.912
303	0.96	2.72	5.09	56.4	0.902
303	1.47	3.87	4.84	63.0	0.769
303	1.47	3.90	4.98	57.0	0.873
303	1.47	3.88	4.93	57.1	0.864
303	1.47	3.88	4.94	57.0	0.867
303	1.47	3.96	4.81	57.3	0.839
303	1.47	3.93	4.74	62.3	0.760
303	1.47	3.96	4.81	57.2	0.842
303	1.47	3.95	4.80	57.2	0.840
303	1.47	3.84	4.90	58.0	0.844
303	1.47	3.83	4.88	58.1	0.839
303	1.47	3.83	4.87	58.1	0.839
303	1.47	3.84	4.92	58.3	0.843
303	1.98	4.85	4.75	57.8	0.821
303	1.98	4.85	4.73	57.9	0.816
303	1.98	4.84	4.69	58.7	0.799
303	1.98	4.84	4.74	58.4	0.812
303	2.49	5.71	4.57	59.5	0.768
303	2.49	5.67	4.50	60.1	0.749
303	2.49	5.76	4.54	60.0	0.758
303	2.49	5.74	4.54	59.5	0.763
303	–	–	**4.89 ± 0.46**	**58.0 ± 3.6**	**0.845 ± 0.119**
305.5	1.47	3.83	4.59	75.0	0.613
305.5	1.47	3.82	4.63	71.7	0.646
305.5	1.47	3.85	4.64	71.2	0.652
305.5	1.47	3.92	4.47	71.2	0.628
305.5	1.47	3.91	4.49	70.9	0.633
305.5	1.47	3.91	4.46	71.0	0.629
305.5	1.47	3.89	4.49	71.2	0.631
305.5	1.47	3.89	4.49	71.7	0.626
305.5	–	–	**4.53 ± 0.15**	**71.7 ± 2.7**	**0.632 ± 0.024**
308	1.47	3.74	4.59	88.8	0.517
308	1.47	3.78	4.64	88.4	0.525
308	1.47	3.76	4.69	88.8	0.528
308	1.47	3.76	4.72	88.6	0.533
308	1.47	3.82	4.27	88.9	0.480
308	1.47	3.80	4.28	86.2	0.496
308	1.47	3.82	4.34	86.1	0.504
308	1.47	3.84	4.36	85.3	0.511
308	–	–	**4.49 ± 0.39**	**87.6 ± 3.0**	**0.512 ± 0.036**
310	0.44	1.55	4.25	99.7	0.426
310	0.44	1.50	4.25	98.7	0.430
310	0.44	1.49	4.41	102.6	0.429
310	0.44	1.49	4.42	100.7	0.439

T / K	$[Br_2]$ / 10^{16} molec cm^{-3}	$[ClO]_0$ / 10^{14} molec cm^{-3}	K_{2a} / 10^{-13} molec^{-1} cm^3 s^{-1}	k_{-2a} / s^{-1}	K_{2a} / 10^{-14} cm^3 molec^{-1}
310	0.96	2.75	4.20	100.8	0.417
310	0.96	2.71	4.16	99.9	0.416
310	0.96	2.70	4.08	100.0	0.408
310	0.96	2.72	4.17	101.0	0.413
310	1.47	3.80	4.05	103.0	0.394
310	1.47	3.77	4.02	102.4	0.393
310	1.47	3.77	4.00	102.1	0.391
310	1.47	3.76	3.98	102.1	0.390
310	1.47	3.65	4.26	100.5	0.424
310	1.47	3.60	4.14	110.3	0.376
310	1.47	3.65	4.26	100.5	0.424
310	1.47	3.65	4.27	101.2	0.422
310	1.47	3.72	4.11	104.6	0.393
310	1.47	3.68	3.99	111.0	0.360
310	1.47	3.75	4.19	101.1	0.414
310	1.47	3.71	4.18	101.4	0.412
310	1.98	4.76	3.83	104.2	0.367
310	1.98	4.76	3.85	104.0	0.371
310	1.98	4.78	3.82	104.3	0.367
310	1.98	4.72	3.78	103.9	0.364
310	2.49	5.62	3.79	106.3	0.356
310	2.49	5.61	3.80	106.7	0.356
310	2.49	5.62	3.83	106.9	0.358
310	2.49	5.59	3.80	107.2	0.354
310	–	–	**4.07 ± 0.39**	**103.1 ± 6.3**	**0.395 ± 0.055**

Table A1: Kinetic parameters determined using the preliminary analysis described in Section 5.4.1 for each experiment undertaken, with their associated errors (2σ statistical error). Numbers in bold indicate the average values for each temperature.

Appendix 2 ClO Dimerisation Study: Final Results

Kinetic parameters (k_{2a}, k_{-2a} and K_{2a}) of the ClO + ClO self reaction were recorded as a function of temperature (280 – 310 K) and as a function of molecular bromine concentration (0.5 – 2.5 × 10^{-16} molecules cm^3) at 5 temperatures encompassing the total experimental temperature range, as discussed in Chapter 5. The following table lists the determinations of the kinetic parameters with their associated errors (2σ statistical error) for each experiment undertaken using the refined analysis as described in Section 5.4.2. Numbers in bold indicate the average values at each temperature.

T / K	$[Br_2]$ / 10^{16} molec cm^{-3}	$[ClO]_0$ / 10^{14} molec cm^{-3}	k_{2a} / 10^{-13} molec^{-1} cm3 s^{-1}	k_{-2a} / s^{-1}	K_{2a} / 10^{-13} cm^3 molec^{-1}
280	0.44	1.60	7.06	3.43	2.06
280	0.44	1.61	7.08	3.52	2.01
280	0.44	1.63	7.05	3.58	1.97
280	0.44	1.66	7.07	3.54	2.00
280	0.96	3.08	6.81	3.84	1.77
280	0.96	3.09	6.85	3.93	1.74
280	0.96	3.11	6.84	3.85	1.78
280	0.96	3.15	6.85	4.00	1.71
280	1.47	4.26	6.69	4.17	1.60
280	1.47	4.28	6.71	4.02	1.67
280	1.47	4.29	6.71	4.06	1.65
280	1.47	4.29	6.92	4.45	1.55
280	1.47	4.29	6.53	6.53	1.00
280	1.47	4.31	6.88	4.39	1.57
280	1.47	4.34	6.92	4.29	1.61
280	1.47	4.35	6.92	4.36	1.59
280	1.47	4.46	6.54	4.28	1.53
280	1.47	4.47	6.56	4.21	1.56
280	1.47	4.47	6.53	4.22	1.55
280	1.47	4.48	6.53	4.22	1.55
280	1.98	5.34	6.51	4.38	1.49
280	1.98	5.34	6.51	4.37	1.49
280	1.98	5.35	6.52	4.32	1.51
280	1.98	5.37	6.51	4.39	1.48
280	2.49	6.36	6.44	4.35	1.48
280	2.49	6.38	6.44	4.42	1.46
280	2.49	6.39	6.42	4.40	1.46
280	2.49	6.39	6.41	4.39	1.46
280	–	–	**6.71 ± 0.44**	**4.21 ± 1.10**	**1.62 ±0.44**
283	1.47	4.31	6.54	6.74	0.97
283	1.47	4.31	6.51	6.61	0.99

T / K	$[Br_2]$ / 10^{16} molec cm^{-3}	$[ClO]_0$ / 10^{14} molec cm^{-3}	k_{2a} / 10^{-13} molec^{-1} cm3 s^{-1}	k_{-2a} / s^{-1}	K_{2a} / 10^{-13} cm^3 molec^{-1}
283	1.47	4.35	6.49	6.64	0.98
283	1.47	4.35	6.50	6.58	0.99
283	1.47	4.30	6.45	6.63	0.97
283	1.47	4.34	6.45	6.53	0.99
283	1.47	4.36	6.41	6.59	0.97
283	1.47	4.36	6.42	6.56	0.98
283	–	–	**6.47 ± 0.10**	**6.61 ± 0.12**	**0.98 ± 0.02**
285.5	1.47	4.28	6.39	9.21	0.69
285.5	1.47	4.28	6.37	9.11	0.70
285.5	1.47	4.27	6.34	9.20	0.69
285.5	1.47	4.29	6.39	9.31	0.69
285.5	1.47	4.32	6.20	9.54	0.65
285.5	1.47	4.34	6.20	9.16	0.68
285.5	1.47	4.36	6.20	9.19	0.67
285.5	1.47	4.38	6.22	9.20	0.68
285.5	–	–	**6.29 ± 0.18**	**9.24 ± 0.26**	**0.68 ± 0.04**
288	0.44	1.66	6.20	13.25	0.47
288	0.44	1.67	6.10	12.97	0.47
288	0.44	1.68	6.09	12.71	0.48
288	0.44	1.68	6.08	12.98	0.47
288	0.96	3.12	5.91	12.46	0.47
288	0.96	3.13	5.84	12.39	0.47
288	0.96	3.14	5.86	12.40	0.47
288	0.96	3.14	5.91	12.36	0.48
288	1.47	4.22	6.28	12.42	0.51
288	1.47	4.23	6.30	12.16	0.52
288	1.47	4.25	6.30	12.09	0.52
288	1.47	4.25	6.31	12.00	0.53
288	1.47	4.35	5.98	12.45	0.48
288	1.47	4.35	6.01	12.79	0.47
288	1.47	4.36	5.99	12.54	0.48
288	1.47	4.37	5.99	12.42	0.48
288	1.47	4.43	5.71	12.49	0.46
288	1.47	4.44	5.73	12.54	0.46
288	1.47	4.45	5.73	12.46	0.46
288	1.47	4.47	5.74	12.49	0.46
288	1.98	5.57	5.58	12.72	0.44
288	1.98	5.58	5.58	12.67	0.44
288	1.98	5.61	5.56	12.76	0.44
288	1.98	5.64	5.58	12.63	0.44
288	2.49	6.57	5.49	13.03	0.42
288	2.49	6.59	5.49	12.99	0.42
288	2.49	6.60	5.46	13.06	0.42
288	2.49	6.61	5.49	13.05	0.42
288	–	–	**5.87 ± 0.53**	**12.62 ± 1.02**	**0.47 ± 0.06**
290.5	1.47	4.19	5.91	17.36	0.34
290.5	1.47	4.22	5.91	17.13	0.34
290.5	1.47	4.20	5.94	17.09	0.35
290.5	1.47	4.20	5.89	17.05	0.35
290.5	1.47	4.33	5.80	16.46	0.35

T / K	$[Br_2]$ / 10^{16} molec cm^{-3}	$[ClO]_0$ / 10^{14} molec cm^{-3}	k_{2a} / 10^{13} molec^{-1} cm3 s^{-1}	k_{-2a} / s^{-1}	K_{2a}, / 10^{13} cm^3 molec^{-1}
290.5	1.47	4.30	5.77	16.98	0.34
290.5	1.47	4.34	5.81	16.99	0.34
290.5	1.47	4.33	5.80	16.88	0.34
290.5	–	–	**5.85 ± 0.12**	**16.99 ± 0.52**	**0.34 ± 0.01**
293	1.47	4.15	5.79	22.38	0.26
293	1.47	4.14	5.78	22.11	0.26
293	1.47	4.18	5.76	22.29	0.26
293	1.47	4.16	5.76	22.29	0.26
293	1.47	4.18	5.56	22.66	0.25
293	1.47	4.20	5.61	22.14	0.25
293	1.47	4.22	5.56	22.11	0.25
293	1.47	4.21	5.59	22.30	0.25
293	–	–	**5.68 ± 0.20**	**22.28 ± 0.36**	**0.25 ± 0.02**
295.5	1.47	4.16	5.45	29.11	0.19
295.5	1.47	4.14	5.44	28.97	0.19
295.5	1.47	4.14	5.42	28.91	0.19
295.5	1.47	4.16	5.45	28.95	0.19
295.5	1.47	4.17	5.38	29.16	0.18
295.5	1.47	4.16	5.37	29.06	0.18
295.5	1.47	4.16	5.39	29.22	0.18
295.5	1.47	4.12	5.36	29.19	0.18
295.5	–	–	**5.41 ± 0.08**	**29.07 ± 0.24**	**0.19 ± 0.01**
298	0.44	1.67	5.02	37.19	0.13
298	0.44	1.68	5.04	37.57	0.13
298	0.44	1.69	5.07	36.61	0.14
298	0.44	1.72	5.04	37.19	0.14
298	0.96	3.13	4.85	37.47	0.13
298	0.96	3.13	4.87	37.03	0.13
298	0.96	3.14	4.86	37.28	0.13
298	0.96	3.16	4.92	37.33	0.13
298	1.47	3.84	5.51	36.46	0.15
298	1.47	3.95	5.49	36.65	0.15
298	1.47	4.15	5.14	37.24	0.14
298	1.47	4.16	5.09	36.41	0.14
298	1.47	4.17	5.11	36.71	0.14
298	1.47	4.17	5.14	36.86	0.14
298	1.47	4.22	4.84	35.92	0.13
298	1.47	4.26	4.84	36.36	0.13
298	1.47	4.32	4.72	37.53	0.13
298	1.47	4.34	4.70	37.40	0.13
298	1.47	4.35	4.73	37.35	0.13
298	1.47	4.38	4.75	37.44	0.13
298	1.98	5.48	4.58	38.06	0.12
298	1.98	5.50	4.59	38.25	0.12
298	1.98	5.51	4.59	38.39	0.12
298	1.98	5.53	4.58	38.02	0.12
298	2.49	6.44	4.49	39.24	0.11
298	2.49	6.49	4.51	39.00	0.12
298	2.49	6.49	4.51	39.11	0.12
298	2.49	6.50	4.51	39.04	0.12

T / K	$[Br_2]$ / 10^{16} molec cm^{-3}	$[ClO]_0$ / 10^{14} molec cm^{-3}	k_{2a} / 10^{-13} molec^{-1} cm3 s^{-1}	k_{-2a} / s^{-1}	K_{2a} / 10^{-13} cm^3 molec^{-1}
298	–	–	**4.86 ± 0.56**	**37.47 ± 1.78**	**0.130 ± 0.020**
300.5	1.47	4.07	5.00	48.82	0.10
300.5	1.47	4.02	4.88	52.99	0.092
300.5	1.47	4.05	4.97	46.80	0.11
300.5	1.47	4.04	4.99	46.37	0.11
300.5	1.47	4.13	4.83	47.25	0.10
300.5	1.47	4.14	4.82	46.93	0.10
300.5	1.47	4.15	4.84	47.10	0.10
300.5	1.47	4.11	4.83	47.31	0.10
300.5	–	–	**4.89 ± 0.16**	**47.94 ± 0.96**	**0.102 ± 0.010**
303	0.44	1.48	5.13	58.19	0.088
303	0.44	1.49	5.09	56.87	0.089
303	0.44	1.50	5.14	58.77	0.087
303	0.44	1.50	5.02	57.47	0.087
303	0.96	2.79	4.90	57.52	0.085
303	0.96	2.81	4.93	57.63	0.086
303	0.96	2.81	4.87	56.89	0.086
303	0.96	2.81	4.93	57.19	0.086
303	1.47	3.93	4.69	59.15	0.079
303	1.47	3.94	4.68	59.08	0.079
303	1.47	3.94	4.70	59.00	0.080
303	1.47	3.94	4.73	59.32	0.080
303	1.47	3.97	4.66	64.18	0.073
303	1.47	3.98	4.74	58.00	0.082
303	1.47	3.99	4.75	57.98	0.082
303	1.47	4.01	4.78	57.93	0.083
303	1.47	4.04	4.56	63.58	0.072
303	1.47	4.06	4.62	58.21	0.079
303	1.47	4.06	4.62	58.15	0.079
303	1.47	4.07	4.62	58.34	0.079
303	1.98	4.98	4.50	59.62	0.075
303	1.98	4.98	4.55	59.25	0.077
303	1.98	4.98	4.53	58.78	0.077
303	1.98	4.99	4.55	58.67	0.078
303	2.49	5.84	4.32	61.03	0.071
303	2.49	5.88	4.37	60.31	0.073
303	2.49	5.93	4.35	60.82	0.072
303	2.49	5.93	4.35	60.82	0.072
303	–	–	**4.70 ± 0.46**	**59.03 ± 3.56**	**0.080 ± 0.012**
305.5	1.47	3.99	4.39	77.17	0.057
305.5	1.47	3.97	4.42	73.64	0.060
305.5	1.47	4.00	4.43	73.11	0.061
305.5	1.47	4.08	4.27	73.27	0.058
305.5	1.47	4.07	4.29	72.95	0.059
305.5	1.47	4.06	4.26	73.02	0.058
305.5	1.47	4.05	4.29	73.28	0.059
305.5	1.47	4.05	4.29	73.80	0.058
305.5	–	–	**4.33 ± 0.14**	**73.78 ± 2.80**	**0.059 ± 0.002**
308	1.47	3.91	4.27	89.89	0.047
308	1.47	3.95	4.32	89.45	0.048

T / K	$[Br_2]$ / 10^{16} molec cm^{-3}	$[ClO]_0$ / 10^{14} molec cm^{-3}	k_{2a} / 10^{-13} molec^{-1} cm3 s^{-1}	k_{-2a} / s^{-1}	K_{2a} / 10^{-13} cm^3 molec^{-1}
308	1.47	3.93	4.35	89.72	0.049
308	1.47	3.92	4.39	89.43	0.049
308	1.47	4.02	4.06	92.66	0.044
308	1.47	4.00	4.06	89.72	0.045
308	1.47	4.03	4.12	89.56	0.046
308	1.47	4.04	4.14	88.62	0.047
308	–	–	**4.21 ± 0.26**	**89.88 ± 2.38**	**0.047 ± 0.004**
310	0.44	1.57	4.22	109.41	0.039
310	0.44	1.58	4.23	107.19	0.039
310	0.44	1.59	4.06	105.33	0.039
310	0.44	1.64	4.07	106.30	0.038
310	0.96	2.87	3.90	106.27	0.037
310	0.96	2.89	3.96	105.93	0.037
310	0.96	2.89	3.98	107.12	0.037
310	0.96	2.92	4.00	106.79	0.037
310	1.47	3.84	3.96	117.13	0.034
310	1.47	3.88	4.03	110.68	0.036
310	1.47	3.88	4.04	105.76	0.038
310	1.47	3.89	4.06	106.47	0.038
310	1.47	3.93	3.82	118.22	0.032
310	1.47	3.95	3.97	106.87	0.037
310	1.47	3.96	3.92	110.70	0.035
310	1.47	4.00	3.98	106.61	0.037
310	1.47	4.00	3.79	108.09	0.035
310	1.47	4.01	3.81	108.17	0.035
310	1.47	4.02	3.83	108.36	0.035
310	1.47	4.06	3.86	108.85	0.035
310	1.98	5.05	3.60	110.34	0.033
310	1.98	5.08	3.67	110.08	0.033
310	1.98	5.09	3.64	110.40	0.033
310	1.98	5.11	3.64	110.55	0.033
310	2.49	5.99	3.62	113.48	0.032
310	2.49	6.01	3.61	112.83	0.032
310	2.49	6.02	3.64	112.99	0.032
310	2.49	6.03	3.60	112.41	0.032
310	–	–	**3.88 ± 0.38**	**109.4 ± 6.68**	**0.035 ± 0.004**

Table A2: Kinetic parameters determined using the refined analysis described in Section 5.4.2 for each experiment undertaken with their associated errors (2σ statistical error). Numbers in bold indicate the average values for each temperature.